Investigating the mechanical and behavioral heterogeneity in the tumor microenvironment

By

Paul Vanisi Taufalele

Dissertation
Submitted to the Faculty of the
Graduate School of Vanderbilt University
in partial fulfillment of the requirements
for the degree of

DOCTOR OF PHILOSOPHY
in
Biomedical Engineering
May 12, 2024
Nashville, Tennessee

Approved:

Cynthia A. Reinhart-King, Ph.D. (chair)
W. David Merryman, Ph.D.
Marjan Rafat, Ph.D.
Ken S. Lau, Ph.D.
Jin Chen, M.D./Ph.D.

I dedicate this thesis to my family.

Acknowledgments

Thank you to my advisor Dr. Cynthia A. Reinhart-King. I am extremely grateful for the opportunity to come to Vanderbilt and work in your lab. My experience in the lab and under your mentorship has helped me develop a tremendous amount academically, professionally, and scientifically. Thank you for believing and trusting in me these past few years. I would also like to thank my committee members – Dr. Jin Chen, Dr. Ken Lau, Dr. W. David Merryman, and Dr. Marjan Rafat for contributing their guidance and wisdom to the oversight of my dissertation.

Thank you to my current and previous labmates. Science is not performed in a vacuum and the day-to-day interactions, assistance, guidance, support, camaraderie, and leadership have helped me greatly succeed. I certainly would not have survived without you all. Thank you to Dr. Francois Bordeleau, Dr. Kayla Goliwas, Dr. Lauren Griggs, Dr. Jian Zhang, Dr. Aniqua Rahman-Zaman, Dr. Jacob VanderBurgh, Dr. Lauren Hapach, Dr. Matthew Zanotelli, Dr. Samantha Schwager, Dr. Jenna Mosier, Adam Munoz, Andrew Johnson, Ethan Oseas, Curtis Schunk, Sunny Wu, Matthew Rowe, Emily Berestesky, Hannah Kirkham, Dr. Katie Young, Dr. Georgii Vasiukov, Dr. Sarah Libring, Wenjun Wang, Ismael Ortiz, Kyra Smart, Chelsea Mariano, Madison Bates, Emily Fabiano, Santiago Lopez, Lindsey Sabo, Hannah Kirkham and Victor Dunagan.

Thank you to my past mentors at the University of Iowa. Thank you to Dr. E. Dale Abel for allowing me to volunteer in your lab as a freshman and providing me with the opportunity to gain critical research experience. Thank you to Dr. Yuan Zhang for your direct guidance and mentorship in the lab and especially your patience. Working with you is one of my fondest memories of Iowa and you gave me the foundational skills to become a scientist.

Lastly, I want to deeply thank my family, friends, and partner. To my parents, Denise and Amanaki, and to my siblings, David and Kalisi, I am forever grateful for having your love and support in my life. The friends I made back home, at Iowa and in Nashville were incredibly important parts of my support system and I want to thank you all. And I want to thank my incredible partner, Kyra Smart, for being my best friend through the challenging times and the fun times.

Table of Contents

List Of Figures

Abbreviations

ANOVA	Analysis of variance
BSA	Bovine Serum Albumin
cDNA	Complementary DNA
Ct	Cycle threshold
DAC	Division of Animal Care
DAPI	4′,6-diamidino-2-phenylindole
DMSO	Dimethyl sulfoxide
ECM	Extracellular matrix
EDTA	Ethylenediaminetetraacetic acid
EMT	Epithelial to mesenchymal transition
FACS	Fluorescence-activated cell sorting
FAK	Focal adhesion kinase
FBS	Fetal bovine serum
HBSS	Hank’s Balanced Salt Solution
HUVEC	Human umbilical vein endothelial cell
IACUC	Institutional Animal Care and Use Committee
KO	Knockout
LSM	Laser Scanning Microscope
mRNA	Messenger RNA
MW	Molecular weight
PBS	Phosphate-buffered saline
PDMS	Polydimethylsiloxane
PFA	Paraformaldehyde
RT	Room temperature
RT-PCR	Reverse transcription polymerase chain reaction
SD	Standard deviation
SDS	Sodium dodecyl sulfate
SEM	Standard error of the mean
WB	Western blot

Chapter 1:

Introduction

1.1 Solid Tumors

Cancer is a disease broadly characterized by uncontrolled growth and spread of abnormal cells harboring genetic mutations throughout the body. According to the National Cancer Institute (NCI), there will be approximately 1.8 million new cases of cancer in 2023 [1]. Out of these new cases, roughly 90% will be solid cancers such as breast, lung, prostate, colorectal, and melanoma cancers [1]. Solid cancers, as opposed to liquid cancers, form contiguous masses of abnormal cells known as tumors in particular anatomic sites throughout the body. These solid tumors may be further characterized and defined by the type of tissue they arise from. For example, carcinomas represent solid tumors originating from the epithelium while sarcomas arise from connective tissues [2]. Thus within the category of solid tumors, there are numerous subdivisions based on anatomic site and original tissue of the cancer cells. A large effort has been directed towards the classification of cancers and the targeting of specific treatment regimens to each cancer subtype. However, a remaining challenge is to understand the heterogeneity within and between tumors even within the same classification. Here I will briefly detail several key components of the tumor microenvironment, such as the cellular and extracellular composition, tumor mechanics, and tumor vasculature. Then the following chapters will investigate key components of heterogeneity within tumors.

1.2 Cellular make-up

There are numerous types of cells that reside within the tumor microenvironment. Here I will detail several of the major cell types and briefly review the roles they play in the tumor microenvironment and examples of how they contribute to cancer progression.

<u>Cancer cells</u>

Cancer cells often make up one of the largest portions of cells residing in the tumor microenvironment [3–8]. As such, cancer cells play a central role in shaping the dynamics of the tumor microenvironment and cancer progression. A defining feature of cancer cells are their abnormalities relative to the normal tissue they are derived from. In particular, genetic mutations are thought to be the primary cause of cancer and cancer cells typically carry multiple mutations [9]. As such, many therapies are being developed that actively target the mutations found in cancer cells [10]. Additionally, cancer cells differ in appearance [11]. For example, aneuploidy, genomic alterations, and protein alterations in cancer cells have been shown to contribute to altered nuclear morphologies [12].

In addition to different appearances and genetic mutation, recent work has defined hallmarks of cancer which denote abnormal cell behaviors that ultimately contribute to cancer progression and have become targets for therapeutic intervention [13]. Several of the hallmarks identify behaviors cancer cells exhibit which can be utilized to continue to grow without regulation, including proliferative signaling, evading growth suppressors, enabling replicative immortality, and resisting cell death [13]. Cancer cell proliferation is a significant component of tumor growth and cancer mortality [14]. As such, many chemotherapy agents act through cytotoxic effects on rapidly proliferating cells [15].

Another important hallmark of cancer is the activation of invasion and subsequent metastasis [13]. Metastasis is a complex multistep process by which cancer cells acquire a migratory phenotype, invade through the primary tumor, intravasate into the vasculature, travel throughout the vasculature, extravasate from the vasculature to a secondary site, and colonize the secondary site. As metastasis significantly contribute to disease progression, much work has gone towards understanding the processes of metastasis and the mechanisms by which cancer cells are able to achieve such a journey [16]. The epithelial-to-mesenchymal transition is a mechanism by which epithelial cancer cells alter their phenotype to lose cell-cell contacts and become more migratory [17]. EMT has been implicated in the process of metastasis and as such has become a large area within cancer research working to develop potential therapeutic targets [18].

As cancer cells must intravasate into the vasculature in order to metastasize, the tumor vasculature is a critical component of the tumor microenvironment [13]. Importantly, cancer cells have developed mechanisms to interact with the tumor vasculature in order to facilitate tumor growth and metastasis [19,20]. For example, cancer cells can secrete soluble factors such as VEGF to induce angiogenesis and increase tumor vascularity [21].

Additionally, cancer cells can secret specialized vesicles known as exosomes containing angiogenic factors to enhance angiogenesis [22,23].

The immune system also plays a critical role in the tumor microenvironment. Importantly, cancer cells have developed mechanisms to avoid immune destruction and mechanisms to perpetuate tumor promoting inflammation [13]. For example, cancer cells may secrete immunosuppressive factors such as TGF-beta to avoid immune detection and destruction [24]. Immune cells detect potential objects for destruction via antigens. Thus another mechanism cancer cells utilize to escape recognition by cytotoxic t-cells is through antigen loss [25]. Furthermore, mutations in the class I presentation pathway can result in significant reduction in MHC class I expression on the surface of cancer cells which further aids in avoiding cytotoxic t-cell destruction [26]. In addition to avoiding from the immune system, cancer cells may also contribute to pro-tumor inflammation which may promote tumorigenesis [27]. For example, recent work has demonstrated that cancer cells can express high levels of the inflammatory gene iNOS which contributes to pro-tumor inflammation [28].

The metabolism of cancer cells is abnormal. Importantly, it was noted in the 1920s by Otto Warburg that cancer cells have heightened levels of glycolysis compared to respiration [29]. This Warburg effect has important consequences for the tumor microenvironment and cancer progression. For example, the increased levels of lactic acid due to enhanced glycolysis can accumulate in the extracellular matrix and an acidic environment is favorable for tumor invasion [30]. Furthermore, the increased levels of glycolytic intermediates can be utilized to promote further cell proliferation and growth [30]. Metabolic reprogramming research in cancer has expanded to cover even more pathways including the pentose phosphate pathway, glutaminolysis, glutathione synthesis and more [31]. As altered cancer metabolism contributes to cancer progression, it remains an attractive area of research for identifying novel therapeutic targets.

A major reason chemotherapies fail is the ability of cancer cells to acquire chemoresistance [32]. Currently, it is believed that cancer cells exposed to a chemotherapy have a chance of developing resistance to the drug given the right circumstances. For example, aneuploidy-driven changes in gene copy number have been implicated in development of chemoresistance [33]. Furthermore, TP53 mutation-associated genomic instability in an ovarian cancer model has been shown to promote chemoresistance and recurrence [34].

In summary, cancer cells are key players in the tumor microenvironment and significantly contribute to cancer progression. Cancer cells develop mechanisms to promote abnormal growth, metastasize to secondary sites, recruit vasculature, modulate the immune system, alter their metabolism, and become resistant to chemotherapies.

Macrophages

Macrophages are an important part of the innate immune system dealing with host defense and inflammation [35]. Macrophages are derived myeloid precursors in the bone marrow which differentiate into monocytes upon entering the blood and further differentiate into macrophages upon exiting the vasculature and entering tissues [36]. Macrophages are phagocytic cells which can engulf foreign substances, microbes, and cellular debris [37]. As such, macrophages additionally play important roles in wound healing and tissue remodeling [38,39].

Macrophages found in the tumor microenvironment may either be tissue resident macrophages, meaning they exist in the tissue prior to tumor development, or can be recruited into the tumor microenvironment [40]. Macrophages polarize into different phenotypes based upon activation factors and canonically exist on a multidimensional spectrum between M1 and M2 phenotypes [41]. M1 macrophages are referred to as classically activated and are associated with type I inflammation while M2 macrophages are referred to as alternatively activated macrophages and are associated with type II inflammation [42,43]. The M2 phenotype is associated with pro-tumor behaviors while the M1 phenotype is associated with anti-tumor behaviors [43]. Polarization towards M1 or M2 is plastic and depends on numerous signals derived from soluble factors and the tissue microenvironment [41].

In the tumor microenvironment, macrophages play numerous roles interacting directly with other cell types and remodeling the extracellular matrix [44]. Macrophages residing in the M1 phenotype are associated with anti-tumor effects and M1 macrophage density has been positively correlated with survival time [45]. The M1 macrophages may produce anti-tumor effects by releasing tumor killing molecules or utilizing antibody-dependent cell-mediated cytotoxicity [46]. Thus inducing an M1 polarization has become a therapeutic strategy to induce the tumoricidal activity of macrophages residing in the tumor microenvironment [47]. Macrophages residing closer to the M2 phenotype are associated with tumor promoting effects [46]. For example, M2-like tumor macrophages may promote cancer cell proliferation, invasion, and metastasis [46,47]. Furthermore, tumor associated macrophages have been shown to contribute to tumor vascularization by secreting pro-angiogenic factors such as VEGF, PlGF, and ANGs which promote tumor angiogenesis [48].

In summary, macrophages are an important subset of immune cells with numerous roles in the tumor microenvironment. Macrophages in the tumor microenvironment may be derived from tissue-resident macrophages or monocyte recruitment and differentiation. Once in the tumor microenvironment, macrophages may become polarized towards different phenotypes associated with anti- and pro-tumor effects. The M1 phenotype is associated with anti-tumor effects which include different mechanisms to kill cancer cells. The M2 phenotype is associated with pro-tumor effects which include mechanisms to promote cancer cell proliferation, invasion, metastasis and the induction of tumor angiogenesis.

Cancer Associated Fibroblasts

Cancer-associated fibroblasts (CAFs) are fibroblasts residing in the tumor microenvironment. The term CAF is often used to denote fibroblasts residing within the tumor microenvironment which have been activated and express myofibroblast markers [49]. These CAFs may express alpha smooth muscle actin, produce extracellular matrix components, and actively contract to generate mechanical forces [50]. CAFs may originate from resident fibroblasts, trans-differentiation of epithelial or endothelial cells into mesenchymal cells, or recruitment from remote sources such as bone-marrow derived precursors or mesenchymal stem cells [51].

There are numerous ways CAFs contribute to the TME and cancer progression. CAFs can directly promote tumor growth through expression of tumor promoting factors such as EGF, TGF-beta, HGF, and others [52]. Moreover, secreted factors from CAFs and ECM remodeling aid cancer cells to invade tumor stroma and ultimately metastasize [53]. CAFs also interact with the tumor vasculature and may secrete or interact with pro-angiogenic factors such as VEGF, SF-1, TGF-beta, HGF, or PDGF to promote tumor angiogenesis [54]. Crosstalk between CAFs and the immune system may also promote cancer progression by mediating immunosuppression in the tumor microenvironment [55]. For example, ECM remodeling by CAFs may perturb immune cell infiltration [56]. Additionally, CAFs may directly inhibit immune cells such as dendritic cells, cytotoxic T-cells, and NK cells [56]. Furthermore, CAFs may secrete factors which can affect macrophage polarization and monocyte and T-cell differentiation [56].

In summary, CAFs are a subset of fibroblasts that may be activated and reside in the tumor microenvironment. CAFs are able to remodel the extracellular matrix, exert mechanical forces, and secrete signaling factors. Through these mechanisms, CAFS can induce tumor growth, cancer invasion and metastasis, tumor angiogenesis, and immunosuppression. As such, therapeutic strategies are being developed to target the pro-tumorigenic activities of CAFs to improve cancer outcomes [57].

Endothelial Cells

Endothelial cells are specialized cells within the circulatory system which line the inside of blood vessels. Endothelial cells play a critical role in the circulatory system by regulating blood flow and the exchange of nutrients, oxygen, and waste products to surrounding tissues [58]. However, tumor endothelial cells have several abnormalities compared to normal endothelial cells. For example, tumor endothelial cells express specific transcripts, are more contractile, have larger nuclei and karyotypic abnormalities, overexpress pro-angiogenic factors and stemness genes, and secrete angiocrine factors [59–62]. Most solid tumors recruit vasculature through the process of angiogenesis where novel blood vessels sprout from pre-existing vessels nearby [63]. However, there are various sources of tumor endothelial cells in addition to angiogenesis. Tumor endothelial cells may be derived from vasculogenesis, recruitment of endothelial progenitor cells, vasculogenic mimicry, and trans-differentiation of cancer cells [63].

Tumor endothelial cells possess an elevated angiogenic phenotype. For example, tumor endothelial cells are more migratory, proliferative, and secrete angiogcrine factors which stimulate angiogenesis [64]. Enhanced angiogenesis promotes the vascularization of the tumor microenvironment and the tumor vasculature in turn enables tumor growth and metastasis [65,66]. Poor vessel structure due to tumor endothelial cell abnormalities and secreted growth factors enables cancer cell metastasis by aiding and facilitating cancer cell migration and intravasation [65]. Furthermore, tumor endothelial cells interact with the immune system to further contribute to cancer progression. Tumor endothelial cells can alter gene expression of cell adhesion molecules to regulate immune cell infiltration, express immune checkpoint ligands to inhibit T-cell activation, express pathways to induce T-cell apoptosis, and present processed antigens to T-cells via MHC molecules without activating naïve T-cells [67].

As tumor endothelial cells exhibit abnormal phenotypes and contribute to cancer progression by enhancing tumor vascularization, promoting and facilitating metastasis, and interacting with the immune system, tumor endothelial cells have become attractive therapeutic targets [68]. Such work aims to find ways to specifically target the tumor endothelium and find targets that may inhibit or normalize the tumor vasculature to improve cancer outcomes [69,70].

1.3 Extracellular make-up

The extracellular matrix (ECM) is a complex and dynamic network of non-cellular components found in tissues. The ECM provides physical support and harbors chemical and mechanical cues for normal tissue function [71]. The major components of the ECM are typically proteoglycans or fibrous proteins [71]. Proteoglycans have core proteins which are heavily glycosylated with chains of glycosaminoglycans and major proteoglycans found in the tumor microenvironment include versican, decorin, glypican, and syndecan among others [72,73]. Fibrous proteins found in the tumor microenvironment include fibrillar collagens, fibronectin, and laminins [73].

The tumor ECM is highly deregulated and varies in ECM composition, organization, and post-translational modification relative to normal ECM [73]. CAFs play a major role in ECM deposition in the tumor microenvironment and can excessively deposit ECM proteins such as collagens and elastin [74]. Additionally, cancer cells and macrophages can produce and deposit ECM components to alter the tumor ECM [75,76]. Matrix degradation plays a key role in ECM remodeling in the tumor microenvironment and cancer and stromal cells can take advantage of enzymes such as matrix metalloproteinases, the plasminogen activation system, and cathepsins to degrade the matrix [77]. Degradation of ECM proteins may also release ECM fragments which act as signals which can be transduced by cancer cells to promote migration, proliferation, invasion, or apoptosis [78]. Furthermore, the ECM components can be modified by post-translational modifications such as cross-linking, hydroxylation, nitrosylation, isomerization, glycosylation or citrullination [79].

The deregulated tumor ECM plays an important role in cancer progression and has been shown to contribute to the different hallmarks of cancer. For example, ECM proteins such as collagen, fibronectin, and laminin may trigger intracellular signaling through cell-surface receptors to influence tissue invasion and metastasis, cell growth, and evasion of apoptosis [80]. Proteolytic enzymes can activate tumor-derived ECM proteins and promote tumor angiogenesis by stimulating endothelial cell migration, proliferation, angiogenic sprouting and tube formation [81]. Excessive ECM deposition can increase matrix density which may inhibit invasion of certain immune cells into the tumor microenvironment [82].

As the tumor ECM varies significantly contributes to cancer progression, there are efforts to identify and characterize tumor ECM biomarkers and signatures to determine if they hold prognostic value [83]. Furthermore, there are numerous studies working on destabilizing the tumor ECM as a therapeutic strategy [73]. Examples include targeting collagen and hyaluronan synthesis directly, interfering with pathways responsible for ECM production such as TGF-beta or Hif1-alpha, or targeting CAFs with anti-fibrotic drugs [73].

1.4 Matrix Stiffness

Tissue stiffness is a material property defined by the ratio of deformation under a particular load [84]. In most solid tumors, the cancerous tissue is significantly stiffer than the normal tissue counterpart [85]. In the extracellular matrix, tumor stiffening is often attributed to excess ECM deposition and ECM crosslinking [85]. Cells residing in the tumor microenvironment also contribute to total tissue stiffness and cellular contractility and cytoskeletal remodeling contribute to enhanced cellular stiffening [86]. Tissue stiffness is typically measured by macro or micro-indenters, such as an Atomic Force Microscope, where the stress and strain relationship can be determined [87]. In medical research, shear wave elastography by ultrasound or magnetic resonance can be used to assess tissue stiffness [88].

Tumor stiffness is a well-studied area and has profound effects on many facets of cancer progression. For example, matrix stiffness modulate cancer cell spreading and morphology, enhance cancer cell proliferation, migration, and invasion [88]. The effects of matrix stiffness also affect the stromal components of the tumor microenvironment. Elevated matrix stiffness has been shown to increase angiogenesis and reduce endothelial barrier function [85]. CAFs both contribute and respond to matrix stiffness and elevated matrix stiffness can activate CAFs to enhance contractility and induce a reciprocal feedback loop of stiffness mediated contractility and contractility mediated matrix stiffening [89]. Furthermore, enhanced matrix stiffness may prevent T-cell infiltration and hinder anti-tumor behavior or immunotherapies [88].

As matrix stiffness contributes to numerous aspects of cancer progression, matrix stiffness has become an attractive target for developing novel therapeutics. There are some efforts to directly reduce matrix stiffening by targeting CAF fibrotic and contractility, or reducing cross-linking from advanced glycation end-products, lysyl oxidase, or tissue transglutaminase [90]. Additionally, other strategies aim to interrupt the cellular response to matrix stiffness by targeting integrins, Rho GTPase, Rho GEFs, Rho-associated kinase, Focal adhesion kinase, Yes-associated protein/transcriptional coactivator with PDZ-binding motif, myocardin-related transcription factor-A, nuclear factor NF-κB, mitogen-activated protein kinase, alternative splicing, and nuclear mechanics [90].

1.5 Tumor vasculature.

In order for tumors to grow beyond a particular size, they must recruit blood vessels to support further growth [63]. Work from Judah Folkman’s lab demonstrated that if a piece of tumor was inoculated into the eye of a rabbit beyond a particular distance from existing blood vessels, the tumor would stay viable but not expand past a particular size [91,92]. However, if the tumor was placed within reach of existing blood vessels, the tumor would recruit the surrounding blood vessels into the tumor and the tumor would rapidly expand [91,92]. This work paved the way for further research in the field of tumor angiogenesis, studying how tumors develop vasculature systems by recruiting new blood vessels from preexisting blood vessels [93].

While tumors utilize angiogenesis to develop a vasculature system, the tumor blood vessels do not develop normally and have several pathological features. Normal blood vessels are highly organized and exist in hierarchies with large vessels leading into smaller vessels and eventually into capillaries and then back out through progressively larger vessels [94]. However, the vasculature system that develops within tumors is tortuous and lacks clear hierarchy [95]. Normal vasculature matures with a complete lining of endothelial cells and is surrounded uniformly by pericytes [96]. Tumor vessels are immature and lack full pericyte coverage and have gaps between endothelial cells lining the blood vessels [96]. In addition to gaps in the endothelium, the endothelial cell-cell junctions themselves are abnormal and produce weaker barrier function [95]. Altogether, these abnormal features of the tumor vasculature ultimately lead to decreased tumor perfusion [97]. Decreased tumor perfusion can create zones of hypoxia which have been shown to promote cancer progression [97]. Furthermore, decreased tumor perfusion may reduce drug delivery making systemic therapeutics less viable and possibly leading to chemoresistance in areas where lower concentrations are delivered [98,99].

Due to the consequences of abnormal tumor vasculature, vascular normalization has emerged as an attractive therapeutic target that aims to normalize the abnormal features of the tumor vasculature to reduce hypoxia and improve drug delivery [100]. Excessive tumor angiogenesis contributes to the development of the abnormal tumor vasculature [100]. As such, vascular normalizing strategies aim to restore the balance of pro and anti-angiogenic factors by either inhibiting pro-angiogenic factors or delivering anti-angiogenic factors [100]. Additional strategies aim to enhance pericyte recruitment, improve endothelial cell-cell junctions, or modulating perfusion and hypoxia [98].

1.6 Conclusions

In summary there are numerous cellular and non-cellular components of the tumor microenvironment which contribute to cancer progression. Importantly, there exists significant heterogeneity and variation in these tumor microenvironmental features which further contribute to difficulty in treating cancer. In this thesis, I will explore several pertinent examples in heterogeneity found within the tumor microenvironment and investigate the impact of these variations in tumor microenvironment features. First, I will investigate how collagen architectural features can confound other architectural and mechanical properties that affect cell behavior. Then I will investigate how differences in matrix stiffness affect the tumor microenvironment composition and endothelial epigenetics. Lastly, I will investigate how transcriptional landscapes underlying migratory phenotypes compares across different cancer cell lines. Altogether this work will further our understanding of how heterogeneities in mechanical properties and cellular behaviors observed in the tumor microenvironment contribute to cancer progression.

Chapter 2:

Fiber alignment drives changes in architectural and mechanical features in collagen matrices

Paul V. Taufalele, Jacob A. VanderBurgh, Adam Munoz, Matthew R. Zanotelli, Cynthia A. Reinhart-King

This chapter is adapted from *Fiber alignment drives changes in architectural and mechanical features in collagen matrices* published in *Plos One* and has been reproduced with permission of the publisher and co-authors.

Taufalele, P. V., VanderBurgh, J. A., Muñoz, A., Zanotelli, M. R., & Reinhart-King, C. A. (2019). Fiber alignment drives changes in architectural and mechanical features in collagen matrices. *Plos one*, *14*(5), e0216537.

2.1 Abstract

Aligned collagen architecture is a characteristic feature of the tumor extracellular matrix (ECM) and has been shown to facilitate cancer metastasis using 3D in vitro models. Additional features of the ECM, such as pore size and stiffness, have also been shown to influence cellular behavior and are implicated in cancer progression. While there are several methods to produce aligned matrices to study the effect on cell behavior in vitro, it is unclear how the alignment itself may alter these other important features of the matrix. In this study, we have generated aligned collagen matrices and characterized their pore sizes and mechanical properties at the micro- and macro-scale. Our results indicate that collagen alignment can alter pore-size of matrices depending on the polymerization temperature of the collagen. Furthermore, alignment does not affect the macro-scale

stiffness but alters the micro-scale stiffness in a temperature independent manner. Overall, these results describe the manifestation of confounding variables that arise due to alignment and the importance of fully characterizing biomaterials at both micro- and macro-scales.

2.2 Introduction

The extracellular matrix (ECM) contains chemical and physical cues that guide cellular behavior [101]. During tumor progression, the tumor ECM becomes deregulated resulting in altered chemical and physical cues [102]. These ECM transformations contribute to abnormal cell behavior and ultimately help to drive cancer progression [102]. Thus, the ECM plays a critical role in cancer and it is important to fully understand its properties. Recently, attention has been drawn to the altered physical properties of the tumor ECM, as it has been an understudied aspect of cancer that has proven to display increasingly more control over cellular function [103]. Due to increased collagen deposition and cross-linking, tumors are characteristically stiffer than healthy ECM [104,105]. This enhanced matrix stiffness has been shown to regulate cellular proliferation [106], migration [107], and tissue morphogenesis [108] which have many implications in tumor growth [105] and metastasis [109]. In addition to increased matrix stiffness, excess collagen deposition leads to reduced pore sizes in the ECM [110,111]. Reduced pore sizes have been shown to hinder 3D cell migration [111] and may require cells to remodel the ECM via matrix degrading enzymes such as matrix metalloproteinases (MMPs) to navigate the ECM [112].

In addition to depositing and cross-linking matrix, cancer cells are also capable of remodeling collagen in the ECM to generate regions of highly aligned collagen fibers [113,114]. This feature is often seen at the tumor periphery[113] and has been identified as a prognostic marker in human breast cancer [115]. Aligned collagen matrices provide guidance cues for migrating cancer cells and promote migration direction persistence [114]. Furthermore, collagen alignment has been shown to reduce the energy required for cancer cell migration [116] and may facilitate intravasation *in vivo* during tumor progression [117]. While it is known that enhanced collagen deposition leads to a significantly stiffer ECM with smaller pore sizes, and collagen matrices can be stiffened via cross-linking without altering the network architecture, it is unclear how aligning collagen matrices affects other architectural and mechanical features. Stylianopoulos et al. computationally predict that pore sizes are larger in aligned regions while Ray et al. reports smaller pores in matrices aligned by cells [118,119]. Because architectural features and mechanical properties of the ECM are crucial regulating factors during tumor progression, it is important to understand their relationship relative to alignment. Moreover, previous work has shown that macro-scale properties, such as bulk density of collagen gels, may not accurately reflect the effective property that the cells experience at the micro-scale [110]. However, many studies report mechanical properties at either the micro- or macro-scale but not both [107,120–122]. Thus, we measured and compared the micro- and macro-scale mechanical properties of the collagen matrices.

In this study, we investigated the architectural and micro- and macro-scale mechanical properties between aligned and randomly oriented collagen matrices. We quantified matrix pore size as well as micro- and macro-scale mechanical properties of aligned collagen matrices compared to randomly oriented matrices. We used two different polymerization temperatures to account for confounding matrix parameters such as network architecture [123] and fibril morphology [111,124]. Our data indicate that collagen alignment significantly alters pore size in gels polymerized at higher temperatures. Mechanical characterization reveals that macro-scale stiffness is not affected by alignment or polymerization temperature while the micro-scale stiffness decreases as polymerization temperature increases. Together these findings reveal that collagen alignment can induce confounding architectural and mechanical differences that are also known to affect cell behavior, and macro-scale measurements of stiffness may not be reflective of stiffness at the micro-scale.

2.3 Materials and Methods

2.3.1 Collagen gel preparation

Type I collagen was acid solubilized in 0.1% glacial acetic acid (Macron, V193-14) from rat tail tendons to obtain 10 mg/ml type I collagen stock solution. Each collagen gel was mixed as a separate solution of stock collagen diluted to 1.5 mg/ml with 0.1% glacial acetic acid, 10X HEPES buffer, 1X PBS, and neutralized with 1N NaOH. Gels were allowed to polymerize at 37ºC for 1 hr or 25ºC for 1.5 hr prior to usage.

Collagen gels were loaded into a custom polydimethylsiloxane (PDMS) devices, as previously described [125]. To create the custom PDMS device used for collagen matrix alignment, a 15 mm x 15 mm x 5 mm PDMS square was formed, from which a 10 mm x 10 mm section was then removed (S1 Fig). A no. 1.5 glass slide was attached to the front side of the PDMS mold using silicon to enclose the 10 mm opening and create the fourth wall of the chamber (S1 Fig). The PDMS molds were then attached to large glass slides using vacuum grease to seal the bottom of the chambers onto the glass slide. To achieve collagen alignment, paramagnetic polystyrene beads (PM-20-10; Spherotech, Lake Forest, IL) were incorporated into a collagen solution at 1% (vol/vol). Collagen solution containing paramagnetic polystyrene beads was loaded into the custom PMDS device and placed next to a neodymium magnet (BZX0Y0X0-N52; K&J Magnetics, Pipersville, PA) while the collagen polymerized. Collagen gels without paramagnetic polystyrene beads were created to serve as randomly-oriented controls.

2.3.1 Confocal reflectance microscopy

Collagen fiber architecture was visualized via confocal reflectance using a Zeiss Axio Examiner.Z1 equipped with a LSM700 confocal module using a 405-nm laser, and a W Plan-Apochromat 20x/1.0 N.A. water immersion objective operated by Zen 2010 software. Images were taken throughout the gels and at least 150 μm above the glass-gel interface.

2.3.1 Analysis of collagen microstructure

Collagen fiber orientation was analyzed in ImageJ using the Orientation J plugin to generate pseudocolor visual representations and fiber orientation distributions. An orientation index was generated from the orientation distribution by implementing a previously described method as a custom Matlab script [126]. In brief, the orientation index, S, is defined by

$$S = 2 < cos^2\alpha > -1 \qquad (1)$$

where α represents the angle between an individual fiber and the average fiber orientation and $<cos^2\alpha>$ represents the averaged square cosine of all α per image. An orientation index of 0 represents a perfectly random distribution, and an orientation index of 1 represents a perfectly aligned distribution. To further quantify fiber alignment, a custom Matlab script was used to assess anisotropy based of the Fourier transform of confocal reflectance images. In brief, the 2D fast Fourier transform was computed for each image and an ellipse was fit to the subsequent power spectrum. A measure of anisotropy was obtained by calculating the aspect ratio of the fit ellipse from the long and short axes.

To measure pore size from confocal reflectance images, two methods were employed as custom Matlab scripts (MathWorks, R2018a). The 2D autocorrelation function in Matlab was used to quantify the characteristic pore size in an image as previously described [110]. Images were uploaded into Matlab and preprocessed to remove background noise using an adaptive Weiner filter (0.625 μm filtering window) and a TopHat filter (0.94 μm strel disk diameter) and finally converted to a binary image. The 2D autocorrelation was computed for each image and the characteristic pore size was derived from the decay measured in the autocorrelation. An erosion-based algorithm was also used to measure pore size, as described previously [127]. In brief, confocal images were uploaded into Matlab and preprocessed to remove background noise as described above. Images were then converted to binary and eroded with progressively larger disk sizes until a threshold of 50% image erosion was crossed. Clusters of adjacent pixels with the same value were grouped together and labeled as objects. The objects containing ‘on’ pixels represented pores, while the objects containing ‘off’ pixels represented collagen fibers. The area of each object representing a pore (objects containing ‘on’ pixels) was measured and the average area was used to calculate an average pore diameter.

To measure fiber diameter from confocal reflectance images, we adapted a previous method utilizing line scans [128]. In brief, line scans were computed over confocal reflectance images and fiber diameter was determined for each image as the average peak width at half prominence.

2.3.1 Macro-Scale stiffness

Macro-scale stiffness was determined by confined compression as previously described [95]. Collagen gels were loaded onto a TA Electroforce Model 3100 (TA Instruments) that performed 5% stepwise indentations and used a 250g load cell to measure the resulting forces. The stress relaxation data was then fit to a standard linear solid model of viscoelastic behavior via a custom Matlab script. The equilibrium modulus was then calculated from the slope of the resulting stress-strain curve.

2.3.1 Micro-Scale stiffness

The micro-scale stiffness was determined by atomic force microscopy (AFM). The Young's modulus of each collagen gel was measured using AFM in contact mode (MFP-3D, Asylum Research, CA). Indentations were performed at a minimum of 3 regions within each collagen gel. Force-displacement curves were taken at 30 points within each region within a 120 by 120 µm grid (6 x 5), for a total of 90 indentations for each collagen gel. Indentations were made at a loading rate of 1 µm/s and trigger force of 2 nN with silicon nitride cantilevers with a nominal spring constant of 0.01 N/m and a 4.5 µm diameter spherical polystyrene bead (Novascan, Boone, IA). AFM tips were calibrated before use and had a mean spring constant of 0.015 ± 0.002 N/m. Force-displacement curves were fit to the Hertz model assuming a Poisson's ratio of 0.5 using the Asylum curve fitting software to determine the elastic modulus.

2.3.1 Statistical analysis

Statistical analyses were performed using GraphPad Prism 7.0 (GraphPad Software, La Jolla, CA, USA). Ordinary two-way ANOVA followed by Tukey's multiple comparison test were performed on all image analysis and macro-scale mechanical testing results. The non-parametric Kruskal-Wallis test followed by Dunn's multiple comparison test was applied to the micro-scale mechanical testing. 'N' represents the number of independent samples while 'n' represents the number of measurements taken.

2.4 Results

2.4.1 Temperature alters the degree of collagen alignment

Network architecture, specifically network connectivity, pore size, and fiber diameter, are heavily influenced by polymerization temperature [124,129]. By increasing polymerization temperature, others have shown an increase in network connectivity and decreases in pore size [124,129]. To investigate matrix alignment under varied network architectures, we characterized collagen matrices polymerized at 25ºC and 37ºC. To measure the alignment of the collagen matrices, confocal reflectance images were analyzed via the OrientationJ plugin in ImageJ (Fig 1A and 1B). Pseudocolor images generated by OrientationJ reveal strong coherency of fiber colors in the aligned matrices compared to the random matrices at both temperatures (Fig 1C). Furthermore, fiber orientation histograms show a robust peak around 0 degrees in the aligned collagen matrices compared to the random matrices at both temperatures (Fig 1C). The fiber orientation distributions were used to calculate an orientation index as described in the methods. To further confirm the alignment and provide a quantitative measure of alignment in each matrix, we calculated the aspect ratio of 2D Fourier transform spectra derived from confocal reflectance images. At both temperatures, the orientation index and aspect ratio were significantly higher in aligned matrices compared to random matrices indicating significant alignment occurred at both temperatures (Fig 1D). Interestingly, the aspect ratio of aligned collagen matrices is significantly higher at 25ºC compared to aligned matrices at 37ºC, indicating a higher degree of anisotropy at the lower temperature. However, there is no significant difference between the orientation indexes of aligned collagen matrices at 25ºC and 37ºC, indicating similar percentages of aligned fibrils at both conditions. Together, these data indicate that fiber alignment is possible at both temperatures but may be more perceptible at 25ºC compared to 37ºC.

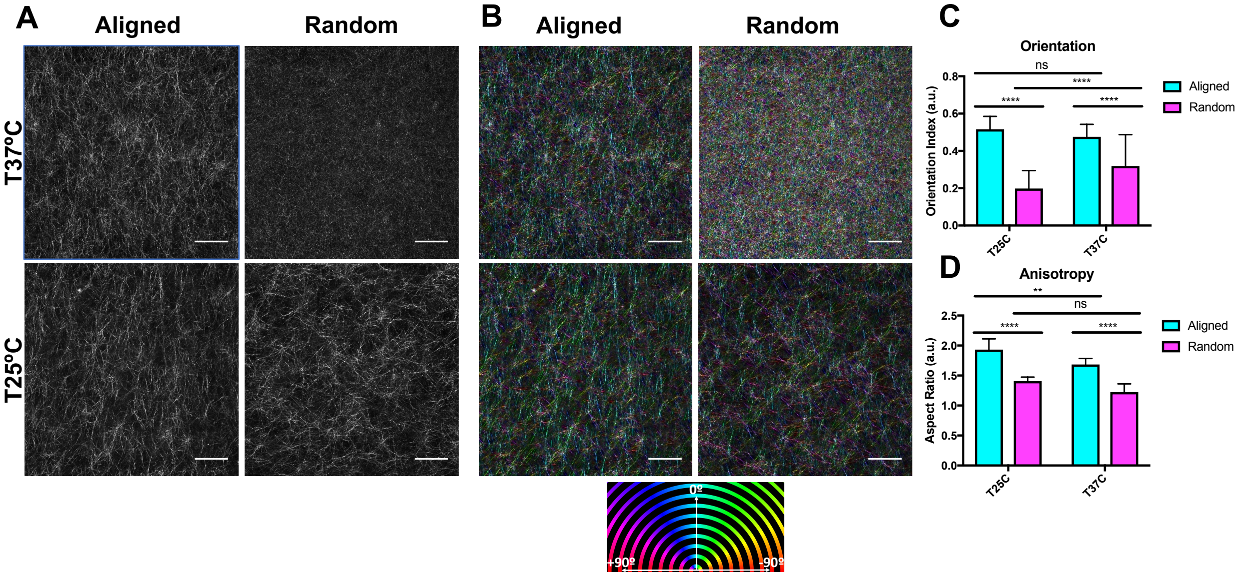

Figure 2.1. The effects of temperature on collagen alignment. (A) Representative confocal reflectance images. (B) Pseudo-color confocal reflectance images depicting fiber orientations. The 0º mark indicates the direction the beads were pulled to induce alignment. (C) Representative histograms depicting fiber orientation distributions generated from the OrientationJ plugin in ImageJ. (D) Quantifications of the collagen alignment via 2 methods: aspect ratio and orientation index. N = 6-7; n = 36-42. Data presented as mean ± s.d.

2.4.2 Collagen alignment alters pore size in a temperature dependent manner

Prior studies have utilized temperature to control pore size of collagen matrices independently of collagen density [130] and have demonstrated that decreasing polymerization temperature induces larger pore sizes [111,130]. To investigate the effects of matrix alignment under different temperatures on collagen pore size, confocal reflectance images were captured (Fig 2A) and analyzed using custom Matlab scripts to quantify pore size. Here, we utilized both a 2D autocorrelation (Fig 2B) and erosion-based algorithm (Fig 2C and 2D) originally designed to quantify the microarchitecture of randomly aligned collagen matrices to ensure that our findings were robust as well as to mitigate any possible technical aberrations. As expected, the random gels polymerized at 25ºC have significantly larger pores than random gels polymerized at 37ºC (Fig 2B and 2C). Interestingly, there was no difference in pore size between aligned and random matrices at 25ºC, whereas the aligned matrices had significantly larger pore size than the random matrices at 37ºC (Fig 2B and 2C). These findings were evident in pore size measurements from both the autocorrelation and erosion-based methods.

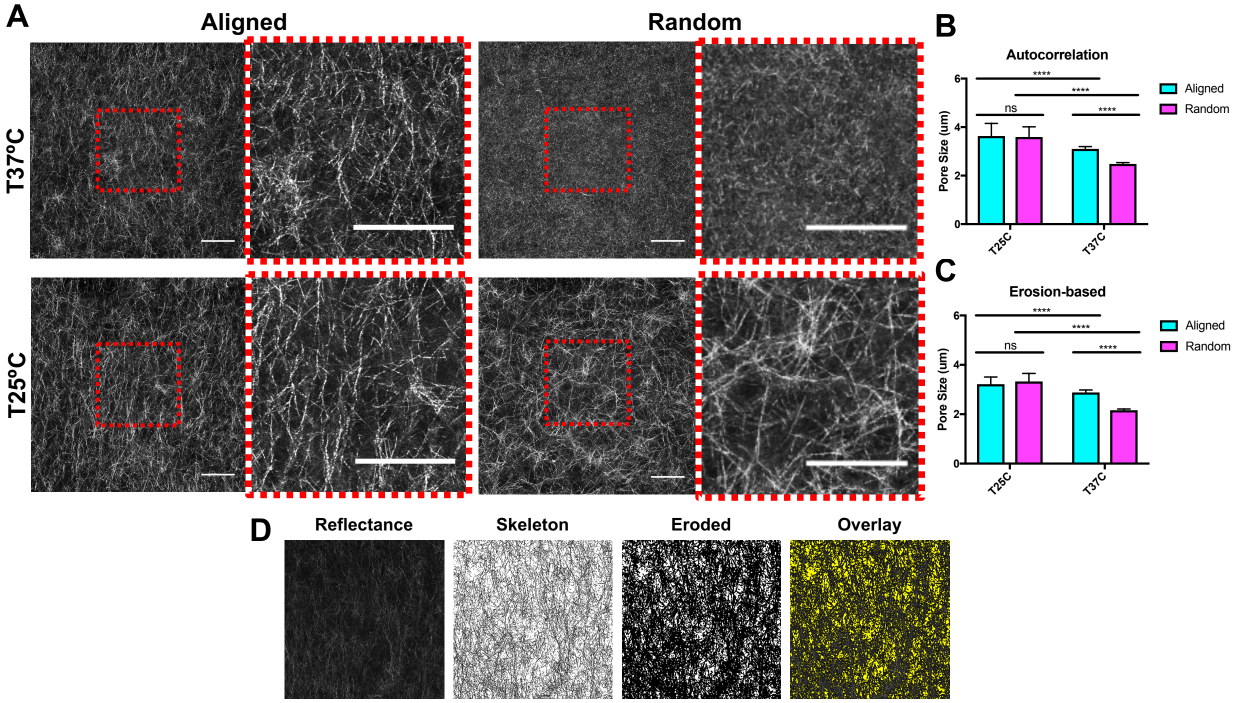

Figure 2.2. The effects of collagen alignment at different temperatures on pore size. (A) Representative confocal reflectance images of aligned & random collagen gels gelled at 25ºC and 37ºC. Cropped and magnified images are included to the right of the images. Scale bars = 50 μm. Collagen pore size quantified by autocorrelation methods (B) and erosion-based methods (C). N = 6-7; n = 36-42. Data presented as mean ± s.d. (D) Erosion-based quantification process. Representative confocal reflectance image of collagen architecture is transformed into a skeletonized binary image with black pixels depicting fibers. Pores are produced by erosion of the skeletonized binary image.

2.4.3 Collagen alignment decreases stiffness at the micro-scale but not at the macro-scale

Collagen fiber architecture plays a significant role in determining the mechanical properties of collagen matrices [129]. Thus, to investigate the mechanical properties of the aligned collagen matrices, we utilized confined compression testing and atomic force microscopy to measure the micro- and macro-scale mechanical properties. Interestingly, confined compression measurements show that there were no significant differences in equilibrium modulus between aligned and randomly oriented matrices at 25ºC or 37ºC (Fig 3A). However, AFM measurements revealed a significant difference in stiffness between aligned and randomly oriented matrices at both temperatures, as well as significant differences in stiffness between matrices polymerized at 25ºC or 37ºC (Fig 3B). Notably, 25ºC aligned and random matrices were significantly stiffer than their 37ºC counterparts. Together, these findings reveal that macro-scale stiffness is not affected by collagen alignment; however, at the micro-scale, alignment affects stiffness independently of temperature.

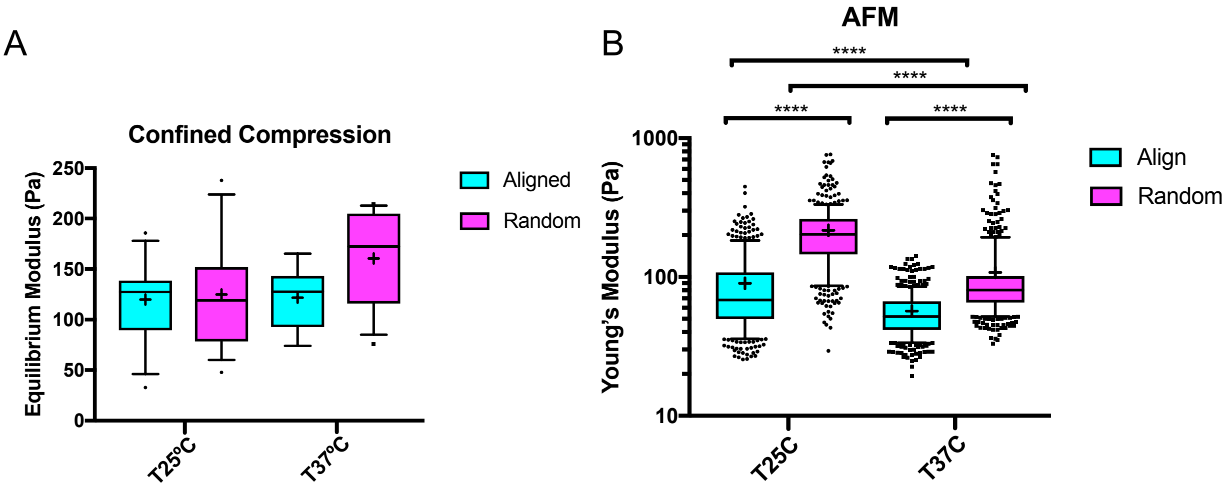

Figure 2.3. Mechanical properties of aligned and random collagen matrices at different temperatures. (A) Equilibrium modulus of gels measured by confined compression. Data presented as mean ± SEM. N = 8-16; n = 8-16. (B) Young's modulus of gels measured by AFM. Data presented as median ± interquartile range (box), 10th-90th percentile (whiskers), and mean (+) with outliers represented as points. N = 4; n = 335-379.

2.5 Discussion

Tumor progression brings about profound ECM remodeling, leading to distorted chemical and physical properties [102]. Importantly, physical properties of the tumor ECM, such as stiffness, have shown to be increasingly important during cancer progression [103]. As previously shown, physical properties of the ECM are highly dependent upon the architecture of the matrix [129,131–133]. A perturbed collagen architecture has been observed at the tumor periphery where cells have remodeled the ECM to form regions of highly aligned collagen fibers [115]. Furthermore, this architectural feature has been shown to have prognostic value in breast cancers [115] and provides guidance cues for cells escaping the primary tumor site [114]. As such, there have been significant efforts to investigate the role of collagen alignment during cancer progression and the underlying mechanisms by which aligned collagen accelerates cancer progression using 3D *in vitro* models [118,120,125,134]. However, the effects of collagen alignment on other features of the matrix that have known consequences, such as pore sizes and mechanical properties, have not been directly studied.

In this study, we used magnetic beads to align collagen matrices and assess the effects on pore size and macro- vs micro-scale mechanical properties. Quantification of collagen alignment revealed significant alignment at both 25ºC and 37ºC. However, there was disagreement between the quantification methods employed. The orientation index indicates no significant difference between alignment at 25ºC and 37ºC. In contrast, the aspect ratio indicates a higher degree of alignment at 25ºC. We attribute this discrepancy to the underlying features each method uses to quantify the degree of alignment. In calculating the aspect ratio, the Fourier transform-based method evaluates the anisotropy of an entire image, while the orientation index is based on weighting the distribution of fiber angles. Our orientation index measurements indicate that a similar portion of aligned fibers at both temperatures are created, whereas aspect ratio measurements indicate that the aligned matrices are more anisotropic at 25ºC compared to 37ºC. This is likely due to lower polymerization temperatures inducing longer collagen fibers and thus enhancing the anisotropy of the images. These results illustrate a critical distinction between alignment quantification methods and emphasize the importance of understanding limitations of what can be concluded from the alignment analysis methods.

Architectural analysis revealed that collagen alignment resulted in temperature-dependent pore size differences. Specifically, we found that aligned collagen matrices at 37ºC had significantly larger pore sizes than random matrices at 37ºC. However, there was no significant difference in pore size between aligned and random gels at 25ºC.

Additionally, collagen matrices polymerized at 25ºC were significantly stiffer than those polymerized at 37ºC. Our results are in agreement with computational predictions by Stylianopolous et al. but disagree with experimental results from Ray et al [118]. However, the results reported by Ray et al. [118] are based on matrices aligned by cells, and it is possible that these matrices underwent additional remodeling aside from fiber alignment. Previous studies have shown that both alignment and pore size affect cancer cell migration [111,118]. Higher alignment has been shown to promote migration in the direction of alignment [118] and smaller pore sizes have been shown to hinder migration [111]. Thus, it is vital to fully understand the architectural properties of any experimental model being used to account for confounding architectural features, with our system displaying altered pore size with collagen alignment at 37ºC.

Mechanical analysis revealed no significant differences in macro-scale stiffness but temperature independent differences in micro-scale stiffness. To measure macro- and micro-scale stiffness, we utilized confined compression and AFM, respectively. Confined compression revealed no difference in compressive moduli between aligned and random matrices at both temperatures (Fig 3A). This result is in agreement with Shannon et al. who used strong magnetic fields to align collagen matrices (35). While they were unable achieve significant alignment at 37ºC, they found no differences in compressive moduli between aligned and random gels across a range of lower temperatures [135]. It has been previously shown that macro-scale stiffness (as measured by unconfined compression) modulates epithelial cell behavior and induce a malignant phenotype (36). However, macro-scale compression testing is not sufficient to detect mechanical differences in our system.

Micro-scale mechanical analysis via AFM revealed that aligned collagen matrices were significantly more compliant than their random counterparts at both temperatures (Fig 3B). Additionally, our AFM results also showed that matrices polymerized at 37ºC were more compliant than their 25ºC counterparts (Fig 3B). Strikingly, this contrasts our confined compression data (Fig 3A) that shows no differences between conditions. This is likely due to how compressive measurements at the macro- and micro-scale reflect different properties of the matrices. Macro-scale compressive testing is more dependent upon bulk architectural features such as density [95]. Micro-scale compressive testing via

AFM measurements is more dependent upon features of individual collagen fibers or local fiber architecture. Prior studies have reported that polymerization temperature regulates fibril diameter, with lower temperatures creating larger diameter fibers and vice versa [124]. Thus, thicker fibers generated at lower temperatures may explain why our AFM measurements indicate both random and aligned collagen matrices polymerized at 25ºC are significantly stiffer than their 37ºC counterparts. Utilizing line scans from confocal reflectance images, we did not detect significant differences between fiber diameter amongst any of the conditions (S2 Fig). However, because this method is limited by the wavelength of light used to capture the confocal reflectance images, it is unable to accurately quantify features under 0.405 µm and prior reports indicate collagen fiber diameters under this constraint in the range of approximately 60-220 nm measured by scanning electron microscopy [124]. Nonetheless, our data is consistent with previous results indicating that larger diameter fibers are formed at lower temperatures [124] and larger fiber diameters lead to increased stiffness as measured by AFM [137].

While altered fiber diameter may explain the differences in stiffness between matrices polymerized at different temperatures, the change in stiffness observed between aligned and random matrices at a given temperature may be due to another local architecture parameter. Interconnectivity of the collagen network describes the extent of overlapping fibers in a cross-section and is a critical determinant of a network's mechanical integrity [138]. Our data suggests alignment may reduce local network interconnectivity and thus explain our observed decreased stiffness in aligned matrices compared to their random counterparts at the same temperature [138]. While pore size was significantly larger in matrices polymerized at 25ºC compared to their 37ºC counterpart, there was only a significant difference between aligned and random matrices polymerized at 25ºC. Thus, pore size does not appear to correlate with macro or micro-scale mechanics.

While it has become widely accepted that mechanical properties of the ECM drive cellular behavior that can contribute to cancer progression [136], it is less clear how architectural and mechanical properties at the micro- and macro-scale are related and how much each actually contribute to these phenomena. While it has become routine to measure the mechanical properties of 3D scaffolds, they do not report both micro- or macro-scale measurements [107,120–122]. Our experiments have revealed significant differences between micro- and macro-scale mechanical properties of aligned collagen matrices in addition to altered pore sizes. Collagen alignment is a prominent tumor associated collagen signature [113] and its full contribution to tumor progression is still unknown. Thus, as more aligned collagen scaffolds and tumor associated collagen signatures are investigated, it will be important to measure and consider the contribution of varying micro-scale mechanics and architecture and choose the scaffold conditions which hold the highest number of parameters constant. In our study, for example, it would be ideal to use collagen matrices polymerized at 25ºC as they have similar pore sizes. These studies underscore the need to fully characterize all architectural and mechanical parameters of 3D culture systems to correctly identify the features responsible for driving cellular behavior without confounding variables.

2.6 Supporting Information

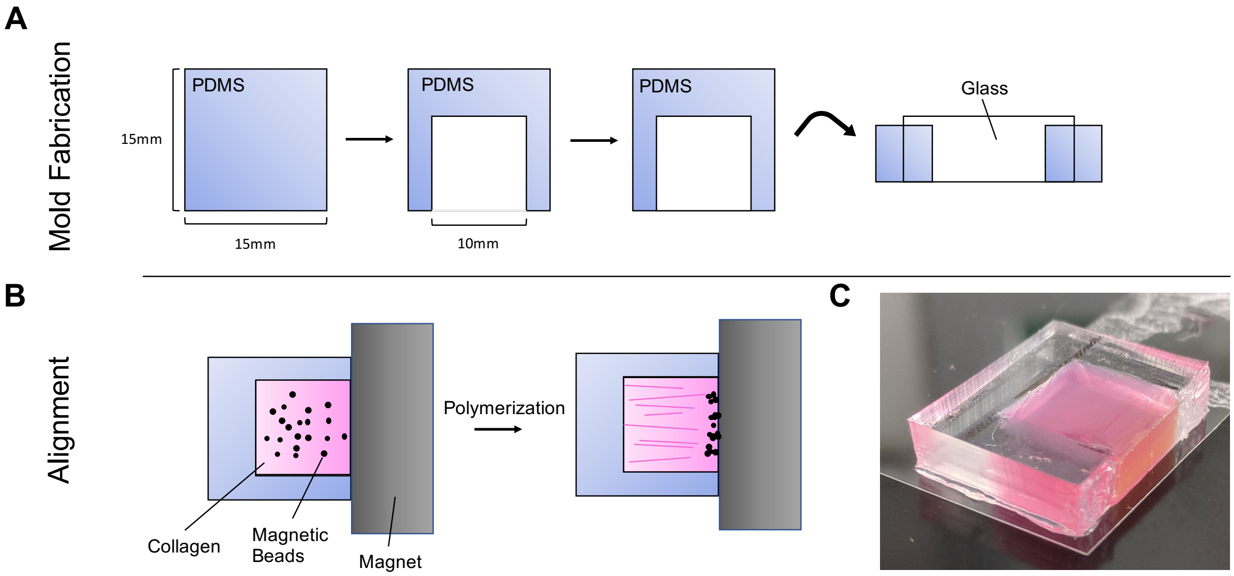

Supplementary Figure 2.1. Collagen alignment system. (A) Fabrication of PDMS mold used to fabricate collagen matrices. **(B)** Schematic depicting the alignment of collagen fibers via magnetic beads. **(C)** An image of an aligned collagen gel in a fabricated PDMS mold.

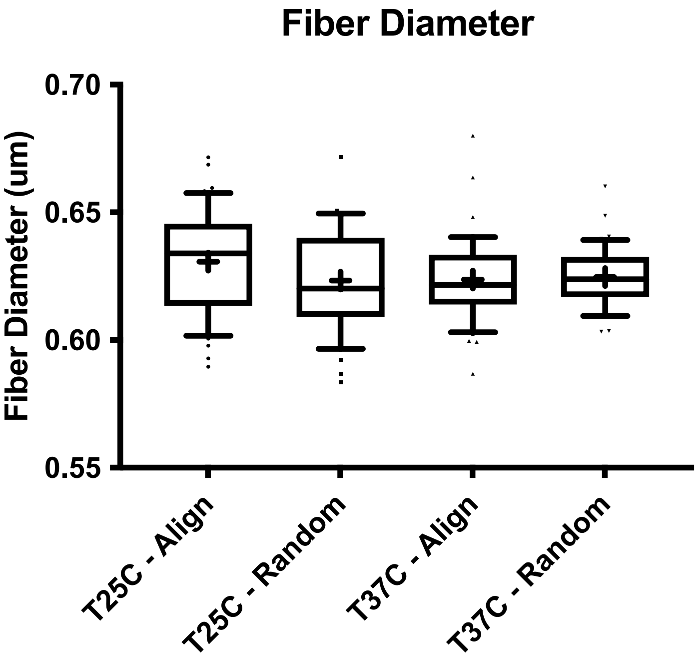

Supplementary Figure 2.2. Collagen fiber diameters. Fiber diameter of matrices measured using line scans from confocal reflectance images. Data presented as median +/- interquartile range (box), 10th-90th percentile (whiskers), and mean (+) with outliers represented as points. N = 6-7; n = 36-42.

2.7 Acknowledgements

This work was funded by the NIH NHLBI (Award number HL127499 and GM131178) to CAR. Francois Bordeleau provided technical assistance on this work.

Chapter 3:

Matrix stiffness enhances cancer-macrophage interactions and M2-like macrophage accumulation in the breast tumor microenvironment

*Paul V. Taufalele, *Wenjun Wang, Alan J. Simmons, Austin N. Southard-Smith, Bob Chen, Joshua D. Greenlee, Michael R. King, Ken S. Lau, Duane C. Hassane, Francois Bordeleau, Cynthia A. Reinhart-King

*co-first authors

This chapter is adapted from *Matrix stiffness enhances cancer macrophage interactions and M2-like macrophage accumulation in the breast tumor microenvironment* published in *Acta Biomaterialia* and has been reproduced with permission of the publisher and co-authors. This work was completed in collaboration with co-first author Wenjun Wang.

Taufalele, P. V., Wang, W., Simmons, A. J., Southard-Smith, A. N., Chen, B., Greenlee, J. D., King, M. R., Lau, K. S., Hassane, D. C., Bordeleau, F., & Reinhart-King, C. A. (2022). Matrix stiffness enhances cancer-macrophage interactions and M2-like macrophage accumulation in the breast tumor microenvironment. *Acta Biomaterialia*.

3.1 Abstract

The role of intratumor heterogeneity is becoming increasingly apparent in part due to expansion in single cell technologies. Clinically, tumor heterogeneity poses several obstacles to effective cancer therapy dealing with biomarker variability and treatment responses. Matrix stiffening is known to occur during tumor progression and contribute to pathogenesis in several cancer hallmarks, including tumor angiogenesis and metastasis. However, the effects of matrix stiffening on intratumor heterogeneity have not been

thoroughly studied. In this study, we applied single-cell RNA sequencing to investigate the differences in the transcriptional landscapes between stiff and compliant MMTV-PyMT mouse mammary tumors. We found similar compositions of cancer and stromal subpopulations in compliant and stiff tumors but differential intercellular communication and a significantly higher concentration of tumor-promoting, M2-like macrophages in the stiffer tumor microenvironments. Interestingly, we found that cancer cells seeded on stiffer substrates recruited more macrophages. Furthermore, elevated matrix stiffness increased Colony Stimulating Factor 1 (CSF-1) expression in breast cancer cells and reduction of CSF-1 expression on stiffer substrates reduced macrophage recruitment. Thus, our results demonstrate that tissue phenotypes were conserved between stiff and compliant tumors but matrix stiffening altered cell-cell interactions which may be responsible for shifting the phenotypic balance of macrophages residing in the tumor microenvironment towards a pro-tumor progression M2 phenotype.

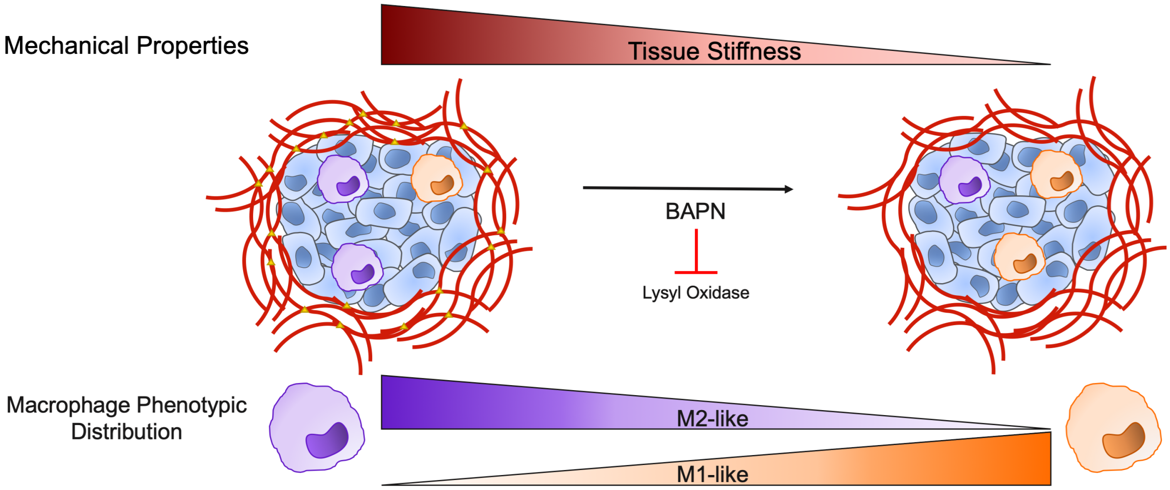

Figure 3.0. Graphical Abstract.

3.2 Statement of significance

Cells within tumors are highly heterogeneous, posing challenges with treatment and recurrence. While increased tissue stiffness can promote several hallmarks of cancer, its effects on tumor heterogeneity are unclear. We used single-cell RNA sequencing to investigate the differences in the transcriptional landscapes between stiff and compliant

MMTV-PyMT mouse mammary tumors. We found similar compositions of cancer and stromal subpopulations in compliant and stiff tumors but differential intercellular communication and a significantly higher concentration of tumor-promoting, M2-like macrophages in the stiffer tumor microenvironments. Using a biomaterial-based platform, we found that cancer cells seeded on stiffer substrates recruited more macrophages, supporting our in vivo findings. Together, our results demonstrate a key role of matrix stiffness in affecting cell-cell communication and macrophage recruitment.

3.3 Introduction

The extracellular matrix (ECM) contributes both structure and signaling cues to the tumor microenvironment. Over the past decade, extensive work has demonstrated how the mechanics of ECM structure itself can provide physical signals to cells. Importantly, matrix stiffness has emerged as a critical parameter of the tumor microenvironment having substantial effects on cellular behavior across many different cell types. Matrix stiffening primarily occurs through excess matrix deposition and cross-linking by either cancer or stromal cells[102]. In cancer cells, elevated matrix stiffness has been shown to regulate cell morphology and cell spreading, and promote critical cancer cell behaviors such as proliferation, migration, and epithelial-to-mesenchymal transition[139–141]. Increased matrix stiffness also affects stromal cell types including cancer-associated fibroblasts, endothelial cells, and an assortment of immune cells. Cancer associated fibroblasts are more activated on stiffer matrices which may contribute to a positive feedback loop resulting in additional matrix stiffening and fibroblast activation[142,143]. Endothelial cells are widely known to be mechanosensitive, displaying enhanced angiogenic behaviors on stiffer matrices[95]. Interestingly, matrix stiffening alone has been shown to induce tumor vasculature phenotypes *in vivo*[95,144,145]. The immune component of the tumor microenvironment, composed of numerous cell types and phenotypes, is also affected by matrix stiffness. Immune cell infiltration has been correlated with matrix stiffness and macrophages have demonstrated mechanosensitive behaviors such as cell spreading, migration, and phenotypic polarization[146–148].

While matrix stiffening can affect cell behavior, the effect of matrix stiffening on the overall composition of the tumor microenvironment is incompletely understood. Given that matrix stiffening is known to influence the behavior of numerous cells in the tumor microenvironment, and the tumor microenvironment is complex, we implemented single cell RNA sequencing (scRNAseq) to analyze cells isolated from stiff and compliant breast tumors from the MMTV-PyMT mouse model. Our results indicate that similar cell types and phenotypes exist within both stiff and compliant tumors with a similar degree of transcriptional diversity, but stiff and compliant tumors differ in specific cell-cell signaling and altered the distribution of macrophage subsets. Specifically, we found stiffer tumors contain a higher proportion of macrophages residing in the more tumor-promoting M2-like phenotype. Additionally, we found that matrix stiffening enhances CSF-1 expression, a protein associated with M2 macrophage polarization[149], in breast cancer cells. We further demonstrated that matrix stiffness-mediated CSF-1 expression was responsible for enhanced macrophage recruitment *in vitro* by breast cancer cells seeded on stiffer substrates. Thus, our data indicates that stiffer tumors promote the accumulation of M2-like macrophages and this may be in part due to matrix stiffness induced secretion of the macrophage polarizing and attracting factor CSF-1 by cancer cells.

3.4 Methods

3.4.1 MMTV-PyMT mouse studies

All animals experiments were conducted following a protocol approved by the Vanderbilt University Institutional Animal Care and Use Committee (IACUC). MMTV-PyMT mice of the FVB strain background were acquired from Jackson Laboratories (Stock No:002374) and housed in a facility with controlled temperature, humidity, and light (12 hr light/dark cycle). Standard rodent chow and water were provided ad libitum. Hemizygous MMTV-PyMT females began BAPN treatment (3mg/kg body weight) at the age of 4 weeks and continued treatment until 12-14 weeks of age to produce more compliant tumors as previously described[95,105,150–156]. Mice were euthanized with CO_2 prior to tumor removal and subsequent processing.

3.4.1 *Tumor dissociation*

Fresh tumors were isolated in a sterile biosafety cabinet and placed in ice cold HBSS during transit from mouse facility to laboratory. Tumors were rinsed several times in ice cold HBSS and minced with sterile scalpels. Minced tumor was then enzymatically digested using the Human Tumor Dissociation Kit from Milytenyi Biotec (130-095-929). Post-enzymatic digestion, cells were passed through 100µm and 70 µm strainers (Miltenyi Biotec 130-110-916) to remove debris and undigested fragments. Cell suspensions then underwent several brief rounds of washing in 1X PBS with 3mM EDTA and an incubation in TrypLE (ThermoFisher Scientific 12604013) for 10 min to break apart cell clusters. Cells were suspended in PBS without EDTA and diluted to a concentration of 150k cells/ml for encapsulation.

3.4.1 *Single cell RNA-sequencing*

Single cell encapsulation and barcoding was performed as previously described[157]. Samples were sequenced in 3 batches, with 1 control and 1 BAPN tumor per batch, via Illumina NextSeq 500. Raw counts underwent quality control in Python (supplementary code) and were further analyzed in R using Seurat v3(supplementary code). Diversity scores were calculated as previously described to measure intratumoral heterogeneity[158]. Briefly, the diversity score was calculated by calculating the average distance between individual cells and the centroid within the principal component space. The centroid was calculated as the arithmetic mean of all the principal components calculated. Potential intercellular communication events were predicted using CellPhoneDB[159].

3.4.1 *Flow cytometry*

Cells were fixed in 4% paraformaldehyde (Electron Microscopy Sciences) in Hank's Balanced Salt Solution (HBSS) (Gibco) for 15 min at RT, then blocked in 100 µL of FACS Buffer (HBSS without calcium, 2% FBS and 1mM EDTA) with 1% bovine serum albumin (BSA) (Sigma) for 20 min at 4°C. Cells were washed with FACS buffer between each step. Cells suspensions of 50 µL were incubated for 15 min at RT with 0.5 µL Mouse TruStain FcX (Biolegend, 101319) to prevent nonspecific Fc receptor binding. Samples were immediately stained with the following primary antibodies for 30 min at 4°C: 0.125μg/100μL eFlour 450 anti-mouse CD11b (Thermo Fisher Scientific, Clone M1/70), 0.5μg/100μL FITC anti-mouse F4/80 (Thermo Fisher Scientific, Clone BM8), 0.5μg/100μL PE anti-mouse CD86 (BD Biosciences Clone GL1), and 0.5μg/100μL APC anti-mouse CD206 (BioLegend, Clone C068C2). Cells were washed 2x with FACS buffer and analyzed using a Guava EasyCyte 12HT benchtop flow cytometer (MilliporeSigma). Flow cytometry plots were analyzed using FlowJo v10.7.1 software. Macrophages were characterized as CD11b+ F4/80+ populations. Within the gated macrophage population, M1/M2 gates were made using a control sample for each tumor, stained only for CD11b and F4/80 in the absence of M1/M2 markers to account for background fluorescence. M1 macrophages were characterized as CD86+ while M2 macrophages were CD206+.

3.4.1 Immunofluorescence staining

Fresh tumors were excised and snap frozen. 8 micron sections were obtained from the VUMC Translational Pathology Shared Resource. Tumor sections were fixed with 4% (v/v) paraformaldehyde, washed with PBS, and permeabilized with 1% (v/v) triton X-100 in PBS. After permeabilization, samples were then blocked with 10% (v/v) FBS and 5% (v/v) donkey serum in PBS. Samples were stained with primary antibody (VE-Cadherin: eBioScience, eBioBV13) at 1:50 diluted in blocking solution overnight at 4°C, washed with PBS supplemented with 0.02% tween, and then incubated with secondary antibody (donkey anti-rat Alexa Fluor 594, A21209; Thermo Fisher Scientific) at 1:100 diluted in blocking solution for 1 h at room temperature in the dark. Samples were then washed, stained with DAPI, and incubated with either eFluor 660 CD68 pre-conjugated antibody (Thermo Fisher 50-0681-82) or APC CD206 (Biolegend 141708) at 1:50 diluted in blocking solution overnight at 4°C in the dark. Immunofluorescent images were taken with a Zeiss LSM800 microscope using a x40/1.1 NA water immersion objective and 488 excitation laser line.

3.4.1 Cell culture

MDA-MB-231 cells (ATCC), were cultured in DMEM media (Gibco) supplemented with 10% Fetal Bovine Serum and 1% penicillin-streptomycin. BAC1.2F5 cells (generously provided by Dr. Richard Stanley, Albert Einstein College of Medicine) were cultured in MEM supplemented with 10% FBS, 1% penicillin-streptomycin, and 3000 U/ml of purified CSF-1 (R&D System, Minneapolis, MN, USA). Medium was replaced every 48 h and cells were maintained in a 37°C humidified incubator of 5% (v/v) CO_2. HUVECs (Lonza) between passage 3 and 5 were cultured in EBM (CC-3121; Lonza) supplemented with EGM Endothelial Cell Growth Medium SingleQuots Supplements (CC-4133; Lonza) and 1% penicillin-streptomycin.

3.4.1 Polyacrylamide gel synthesis

Polyacrylamide (PA) gels were synthesized as previously described. PA gels with stiffness of 1kPa and 10kPa were prepared by mixing 3%:0.1% or 7.5%:0.35% acrylamide [40% (w/v) stock solution] to bis-acrylamide [2% (w/v) stock solution], respectively, in Mili-Q water with HEPES and tetramethylethylenediamine (TEMED; Bio-rad) at pH 6. Ammonium persulfate was dissolved in Mili-Q water at 10% (w/v) and used to initiate polymerization. PA gels were functionalized with N-6- [(acryloyl)amido]hexanoic acid, succinimidyl ester. Type 1 rat tail collagen (Corning, Corning, NY, USA) was then covalently bound to the PA gel surfaces at 4°C in 50mM HEPES solution at pH 8. Unreacted N-6- [(acryloyl)amido]hexanoic acid, succinimidyl ester was quenched with 1:1000 ethanolamine in 50mM HEPES solution at pH8. PA gels were washed in 1X PBS and stored at 4°C in PBS with 4% penicillin-streptomycin prior to seeding. PA gels were exposed to UV light for 1 h prior to seeding to sterilize.

3.4.1 Cytokine assay

MDA-MB-231 cells were cultured on either compliant (1kPa) or stiff (10kPa) PA gels coated with 0.1 mg/mL Type 1 rat tail collagen. After 24 h culture on PA gels, cell culture medium was collected and utilized as directed by the Proteome Profiler Human XL Cytokine Array Kit (ARY022B; R&D Systems).

3.4.1 qPCR

mRNA was isolated from cells cultured on either compliant (1kPa) or stiff (10kPa) PA gels using the RNeasy Mini Kit (Qiagen). The iScript Select cDNA Synthesis Kit (Bio-

Rad) was used to generate cDNA from the isolated mRNA. Quantitative PCR was performed using SYBR green (Thermo Fisher Scientific) according to the manufacturer's instructions. Relative expression was calculated using the 2 $^{-\Delta\Delta CT}$ method using B2M as a housekeeping gene. The primers used were CSF-1: forward: 5’-CCA GTG TCA TCC TGG TCT TG-3’, reverse: 5’-CCA CCT GTC TGT CAT CCT GA-3’; B2M: forward: 5′-CAC CCC CAC TGA AAA AGA TGA G-3′, reverse: 5′-CCT CCA TGA TGC TGC TTA CAT G-3’.

3.4.1 *Western blot*

MDA-MB-231 cells were seeded on top of either compliant (1kPa) or stiff (10kPa) gels for 24 h and treated with or without the FAK inhibitor PF573228 (MilliporeSigma). Cells were rinsed with 1X PBS and lysed with 4X SDS sample buffer (4X Tris-Cl/SDS, pH6.8, 30% v/v glycerol, 10% w/v SDS, 0.09% v/v 2-mercaptoethanol, and 0.012% w/v Bromophenol Blue). Standard SDS-PAGE was conducted usingBio-Rad Any kD Mini-PROTEAN (4569035; Bio-Rad gels and PVDF membranes (Bio-rad). Membrane washing steps were performed with 0.1% polyoxyethylene 20 sorbitan monolaurate (Tween; JT Baker, Phillipsburg, NJ) in Tris-buffered saline. Blocking was performed with 5% milk in the washing buffer. Primary antibodies (GAPDH Biolegend poly6314; CSF-1 Santa Cruz sc-365779) were diluted in blocking buffer at 1:1000 dilution and applied to the membranes overnight at 4°C. Horseradish-peroxidase conjugated secondary antibodies were applied to the membranes in blocking buffer at 1:2000 dilution for 1 h at room temperature. Membranes were imaged using SuperSignal chemiluminescent substrate and a FujiFilm ImageQuant LAS-4000. Quantification of protein expression was normalized to GAPDH loading control and densitometry was performed using Fiji.

3.4.1 *Macrophage recruitment assay*

In the macrophage recruitment assay, we utilized a modified trans-endothelial transwell migration assay. Transwells were coated with neutralized 1mg/mL collagen and allowed to polymerize before hydration and seeding. HUVECs were then seeded on top of polymerized collagen coated transwell inserts at 300,000 cells/well and cultured for 3 days to allow a monolayer to form. MDA-MB-231 cells were cultured on compliant (1kPa) or stiff (10kPa) PA gels in the bottom of the transwells below the inserts. BAC1.2F5 macrophages stained with CellTracker Green CMFDA Dye (C7025; ThermoFisher) were then seeded in the medium above the transwell insert and allowed to transmigrate through the HUVEC monolayer, collagen coating, and transwell insert pores towards the MDA-MB-231 cells cultured on PA gels in the bottom of the well. The number of recruited macrophages were measured via laser scanning confocal reflectance imaging and quantified as the number of macrophages per defined region of interest in the bottom of the transwell chamber.

3.4.1 Statistical analysis

Statistical analyses were performed using GraphPad Prism 9 (GraphPad Software, La Jolla, CA, USA). Where appropriate, data were compared using unpaired t-tests with Welch's Correction, a two-way analysis of variance (ANOVA) with Sidak multiple comparison test, or a nested t-test. Statistical significance was determined if the tested p-value was smaller than 0.05 (*), 0.01(**), 0.001 (***), or 0.0001 (****). ‘N’ represents the number of independent samples while ‘n’ represents the number of measurements taken.

3.5 Results

3.5.1 Single cell RNA sequencing reveals similar cell type composition of compliant and stiff breast tumor microenvironments

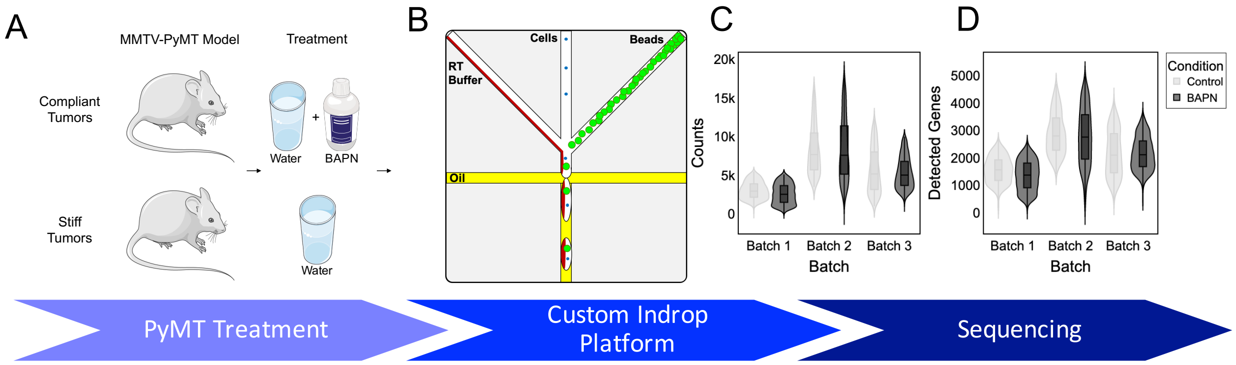

Figure 3.1. Single cell RNA-seq reveals similar transcriptional landscapes between stiff and compliant MMTV-PyMT tumors.

Schematic of (A) experimental treatment regime and (B) custom Indrop platform. Violin plot of (C) raw counts per cell and (D) detected genes per cell across the 6 samples. N = 3.

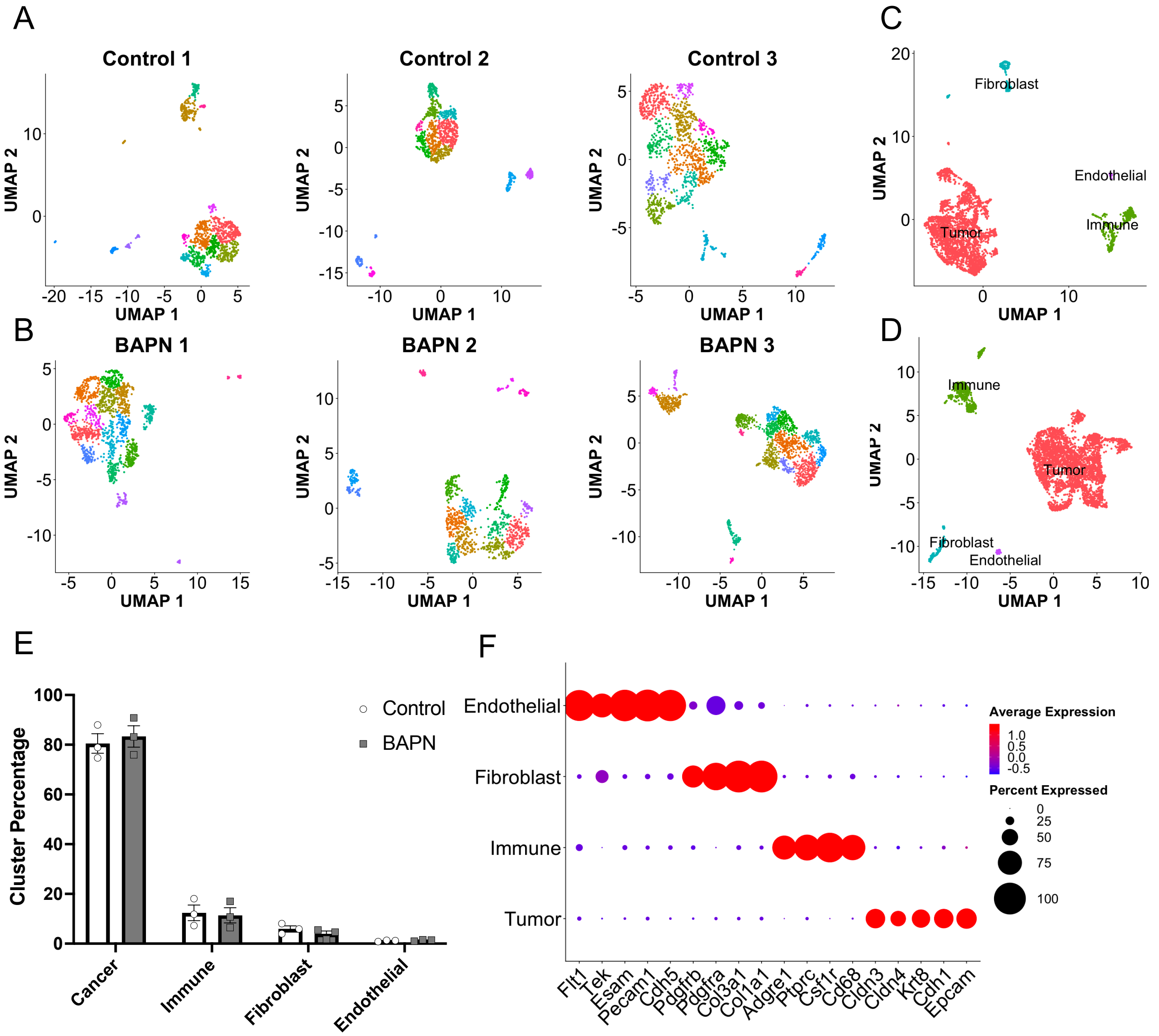

Figure 3.2. Single cell RNA-seq reveals similar transcriptional landscapes between stiff and compliant MMTV-PyMT tumors.

Individual UMAP projections of each individual sample from (A) stiff and (D) compliant tumors integrated onto a single UMAP projection and clusters labeled by cell type determined by expression of canonical markers below. (E) Distribution of libraries across the 4 main cell types. Data plotted as mean +/- SEM. N =3. (F) Gene expression of the canonical cell type markers.

To investigate the architectural effects of matrix stiffness on the tumor microenvironment, we performed scRNAseq on stiff and compliant MMTV-PyMT mammary tumors. To obtain compliant and stiff tumors, MMTV-PyMT mice were treated with BAPN, a lysyl oxidase inhibitor, or vehicle control, respectively (**Fig. 1A**). Tumors were dissociated to form single cell suspensions and encapsulated using a custom inDrop platform (**Fig. 1B**). Tumors were excised, encapsulated, and sequenced pairwise in 3 batches on separate days and sequencing runs. All sequencing results were filtered using several quality control methods prior to analysis. Inflection point gating for total counts per cell was applied to each sample individually to remove cells with low library size and an upper threshold was applied to remove droplets that may have contained more than 1 cell[160]. Additionally, cells containing a high proportion of mitochondrial genes were removed. A total of 8,523 cells passed quality control metrics from 6 tumors with an average of ~5200 counts per cell over ~2100 genes (**Fig. 1C,D**). While there was batch to batch variation in preprocessed library quality, there was no difference between compliant and stiff tumors sequenced within the same batch (**Fig. 1C,D**).

Lower dimensional embedding via UMAP revealed similar numbers of clusters in both compliant and stiff tumors detected by k-means clustering both on individual sample landscapes and samples integrated by condition using sctransform method[161](**Fig. 2A,B,C,D**). Using the expression of a manually curated list of marker genes, cells were assigned to 4 major cell types: cancer, immune, fibroblast, or endothelial (**Fig. 2E,F,G**). Cancer cells were defined as non-stromal cells that expressed epithelial markers. Both landscapes were composed of similar distributions of cell types with cancer cells being largest population of ~80% and immune cells being the next largest population at ~12% followed by fibroblasts at ~5% and endothelial cells at ~1% (**Fig. 2E**).

As the integration of all cell types onto a single projection is dominated by variability in cell type marker expression, we parsed cells by cell type and re-integrated all samples together for further analysis of heterogeneity. Cells were isolated on a cell type basis and re-analyzed via Seurat to integrate the samples based on highly variable genes that exist within the specific cell type under investigation. After integration, cells were again visualized via lower dimensional embeddings and displayed thorough mixing between conditions and samples (**Supplemental Fig. 1A,E,I**). Several distinct subpopulations were evident from lower dimensional embeddings and clustering via Louvain algorithm with Seurat (**Supplemental Fig. 1B,F,J**) and were defined by distinct gene expression profiles (**Supplemental Fig. 1C,G,K**). Importantly, these subpopulations were composed of cells from both stiff and compliant tumors (**Supplemental Fig. 1A,E,I**). Interestingly, the majority of Louvain clusters detected in the cancer cells were contiguous while the clusters detected in the immune and CAF cells were more separated. Contiguous clustering suggests a spectrum of related cell states while the separation in the stromal subpopulations suggests more distinct phenotypes. To further quantify the intratumoral heterogeneity we utilized a previously published method to compute transcriptomic diversity scores based on principal component embeddings[158]. These scores were calculated for cancer cells, immune cells, and fibroblasts individually using each tumor as an independent sample. In agreement with the thorough mixing of cells between conditions and samples (**Supplemental Fig. 1A,E,I**), the diversity scores displayed no significant difference between cell types in stiff versus compliant tumors (**Supplemental Fig. 1D,H,L**). Thus, this indicates that there is significant heterogeneity that exists within the cancer and stromal cells and that this heterogeneity is conserved between stiff and compliant tumors.

3.5.2 Macrophages constitute the largest portion of immune cells and exhibit phenotypic heterogeneity

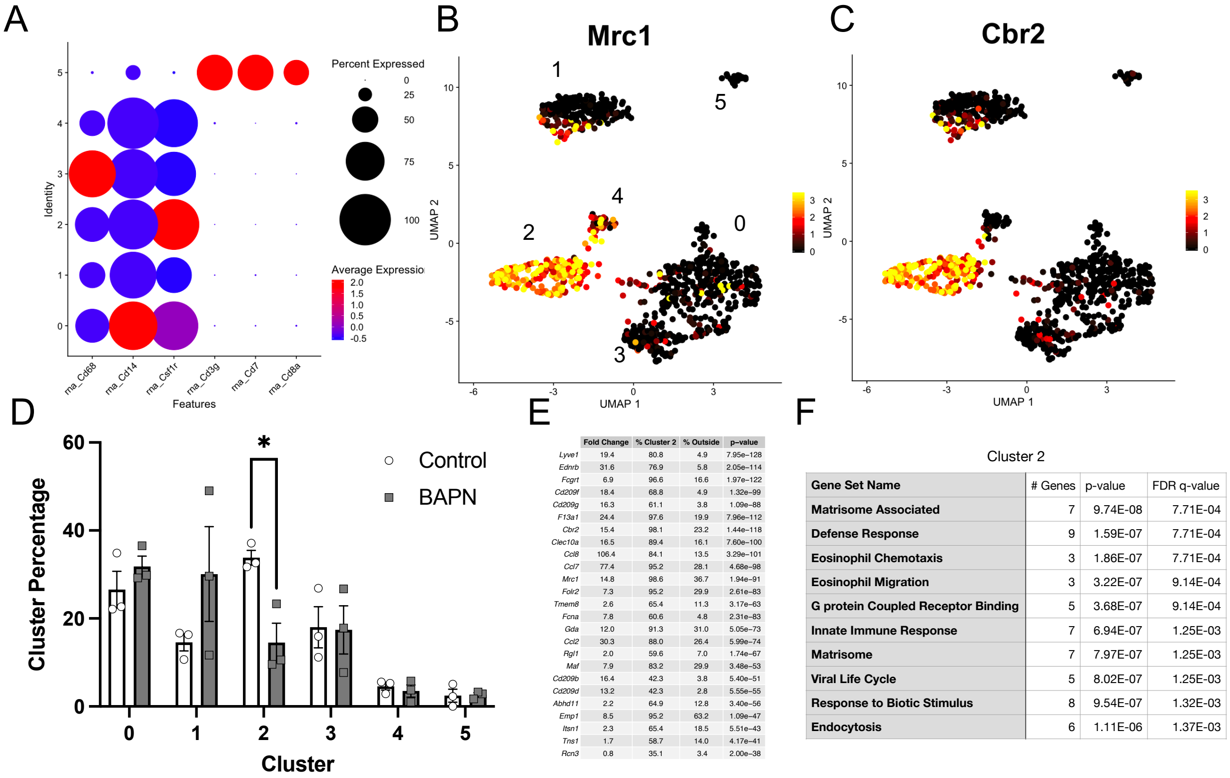

	Fold Change	% Cluster 2	% Outside	p−value
Lyve1	19.4	80.8	4.9	7.95e−128
Ednrb	31.6	76.9	5.8	2.05e−114
Fcgrt	6.9	96.6	16.6	1.97e−122
Cd209f	18.4	68.8	4.9	1.32e−99
Cd209g	16.3	61.1	3.8	1.09e−88
F13a1	24.4	97.6	19.9	7.96e−112
Cbr2	15.4	98.1	23.2	1.44e−118
Clec10a	16.5	89.4	16.1	7.60e−100
Ccl8	106.4	84.1	13.5	3.29e−101
Ccl7	77.4	95.2	28.1	4.68e−98
Mrc1	14.8	98.6	36.7	1.94e−91
Folr2	7.3	95.2	29.9	2.61e−83
Tmem8	2.6	65.4	11.3	3.17e−63
Fcna	7.8	60.6	4.8	2.31e−83
Gda	12.0	91.3	31.0	5.05e−73
Ccl2	30.3	88.0	26.4	5.99e−74
Rgl1	2.0	59.6	7.0	1.74e−67
Maf	7.9	83.2	29.9	3.48e−53
Cd209b	16.4	42.3	3.8	5.40e−51
Cd209d	13.2	42.3	2.8	5.55e−55
Abhd11	2.2	64.9	12.8	3.40e−56
Emp1	8.5	95.2	63.2	1.09e−47
Itsn1	2.3	65.4	18.5	5.51e−43
Tns1	1.7	58.7	14.0	4.17e−41
Rcn3	0.8	35.1	3.4	2.00e−38

Cluster 2

Gene Set Name	# Genes	p-value	FDR q-value
Matrisome Associated	7	9.74E-08	7.71E-04
Defense Response	9	1.59E-07	7.71E-04
Eosinophil Chemotaxis	3	1.86E-07	7.71E-04
Eosinophil Migration	3	3.22E-07	9.14E-04
G protein Coupled Receptor Binding	5	3.68E-07	9.14E-04
Innate Immune Response	7	6.94E-07	1.25E-03
Matrisome	7	7.97E-07	1.25E-03
Viral Life Cycle	5	8.02E-07	1.25E-03
Response to Biotic Stimulus	8	9.54E-07	1.32E-03
Endocytosis	6	1.11E-06	1.37E-03

Figure 3.3. Immune cell annotation reveals immune cells are predominantly composed of macrophages and enrichment of M2-like macrophages in stiffer tumors. (A) Expression of canonical macrophage and T-cell markers across cells in the immune category. (B,C) Expression of canonical M2-like macrophage markers overlaid on UMAP projections of the cells in the immune group. (D) Comparison of the distribution of immune cells to each subpopulation plotted as mean +/- SEM. N = 3. (E) Top 25 conserved marker genes for immune cell cluster 2. Table displays the average fold expression within cluster 2 compared to the rest of the cells, the percentage of cells expressing each transcript in cluster 2 versus the remaining clusters, and the adjusted p-value for the transcript. (F) GO Term enrichment of the top 25 marker genes for the M2-like macrophage subpopulation. *p<0.05.

The tumor microenvironment is home to numerous types of immune cells with important pro- and anti-tumor functions. To determine the identity of immune cells captured in this study, we assessed the expression of a panel of canonical immune cell specific markers. Broad expression of macrophage markers (CD68, CD14, CSF1R) were seen in 5 of the 6 subpopulations of immune cells, approximately 97% of total immune cells, with some variation in expression levels between the clusters (**Fig. 3A**). The remaining small subpopulation in cluster 5, approximately ~3% of the immune cells, were identified as T-cells based on expression of CD3g, CD7, and CD8a (**Fig. 3A**).

Macrophages are a heterogeneous cell type containing complex phenotypic and functional variation[162,163]. We performed differential expression analyses between each of the macrophage subpopulations to identify marker genes for each cluster and investigate the observed heterogeneity (**Supplemental Fig. 2**). Examination of the top 25 marker genes in each cluster revealed heterogeneous expression of several macrophage phenotypic markers. Cluster 0 represented one of the larger clusters with approximately 30% of the total immune cells in both stiff and compliant tumor landscapes. Macrophages in this subpopulation displayed transcripts associated high expression of macrophage genes associated with both canonical polarization states, such as an important anti-inflammatory M2 polarization regulator Tlr2[164,165], the pro-inflammatory (M1-like) factor Aif1[166], and the monocyte differentiation regulator transcript Runx3[167], suggesting they may represent an intermediate polarization state (**Supplemental Fig. 2**). GO term analysis of the top markers revealed significant enrichment for transcripts in cell activation, cell adhesion, and secretion (**Supplemental Fig. 2**). Cluster 1 was composed of a subpopulation defined by high expression of transcripts traditionally involved in epithelium development and differentiation (Epcam, Cldn3, and Krt8) (**Supplemental Fig. 2**). Additionally, transcripts associated with both pro- and anti-inflammatory macrophage behaviors were significantly expressed in cluster 1 (Ccn1[168] and Lcn2[169], respectively). High expression of epithelial markers alongside Cd24a suggests these cells may actually represent Langerhans cells, a specialized antigen-presenting macrophage subtype[170–172] typically found in epidermal tissue but have been shown to infiltrate breast tumors[173] (**Supplemental Fig. 2**). Interestingly, macrophages in cluster 2 had significantly higher expression of several canonical anti-inflammatory M2 macrophage markers (Cd209, Mrc1, Cbr2, and Folr2)[174–177] and resident-like macrophage markers (F3a1, Lyve1)[176] (**Fig. 3B,C,E** and **Supplemental Fig. 2**). Due to the high expression of canonical M2 markers, we designated these macrophages as ‘M2-like’. Significant GO terms in the M2-like macrophages included categories related to the matrisome, with several C-C motif ligand chemokines (Ccl2, Ccl7, Ccl8), and eosinophil migration and chemotaxis (**Fig. 3E,F**). Cluster 3 was contiguous with the macrophages in cluster 0 and also significantly expressed a few pro-inflammatory transcripts associated with the M1 phenotype (Slc7a2[177], Fcgbr2[177], and Npc2[178]) and several anti-inflammatory transcripts typically associated with the M2 phenotype (Adam8[179], Spp1[180], Ctsl[177], Ctsb[177], Arg1[174,175]) (**Supplemental Fig. 2**), suggesting macrophages in this subpopulation may reside in an intermediate polarization state. Furthermore, cluster 3 GO terms included cell activation and secretion, similarly to cluster 0 (**Supplemental Fig. 2**). Cluster 4 was contiguous with cluster 2 (M2-like macrophages) and highly expressed several anti-inflammatory transcripts associated with the M2-like phenotype (Ccr2[175], Retnla[181], and Mgl2[181]) suggesting this cluster may represent a subset of M2-like macrophages, possibly M2b due to presence of Il6[182]. Altogether, these data indicate that the majority of the immune cells captured are of macrophage lineage and cluster similarly to previously defined macrophage phenotypic subsets.

3.5.3 M2-like macrophages are enriched in stiffer tumors

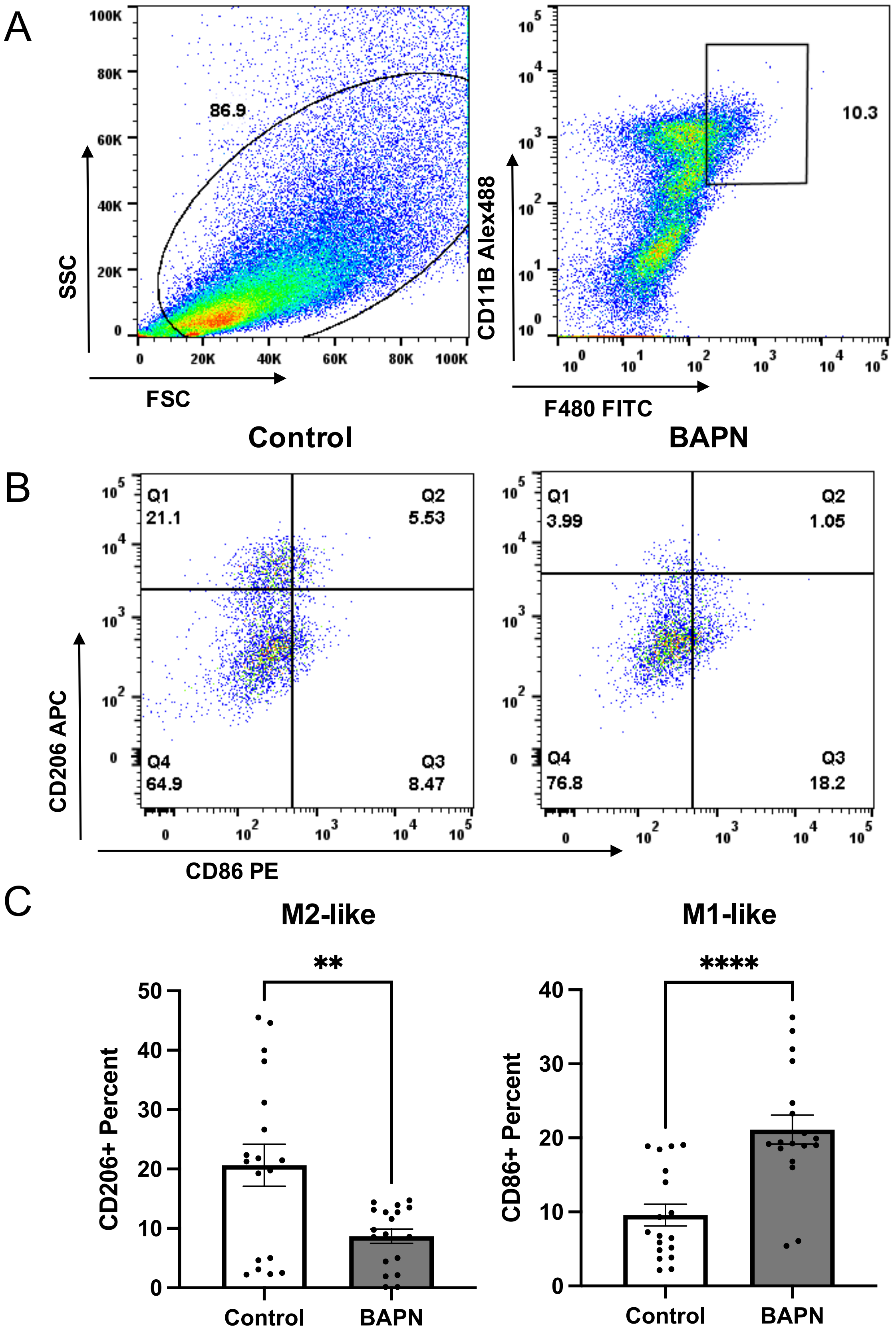
A
SSC
FSC
86.9
CD11B Alex488
F480 FITC
10.3
Control
BAPN
B
CD206 APC
CD86 PE
Q1 21.1
Q2 5.53
Q4 64.9
Q3 8.47
Q1 3.99
Q2 1.05
Q4 76.8
Q3 18.2
C
M2-like
M1-like
**
****
CD206+ Percent
CD86+ Percent
Control
BAPN

Figure 3.4. Quantifying macrophage polarization in the MMTV-PyMT breast tumor microenvironment via flow cytometry. (A) Flow cytometry gating based on side-light vs forward light scatter intensity and double positive CD11B and F4/80 staining. (B) CD206 expression (M2 marker) and CD86 expression (M1 marker) in isolated macrophages. (C) Quantification of CD11b and F4/80 positive macrophages in total cell populations. (D) Quantification of CD206 (left), and CD86 (right) positive macrophages in the total gated macrophage populations. Data plotted as mean +/- SEM. N = 3 (number of mice), n = 18 (number of data points). **p<0.01, ****p<0.0001.

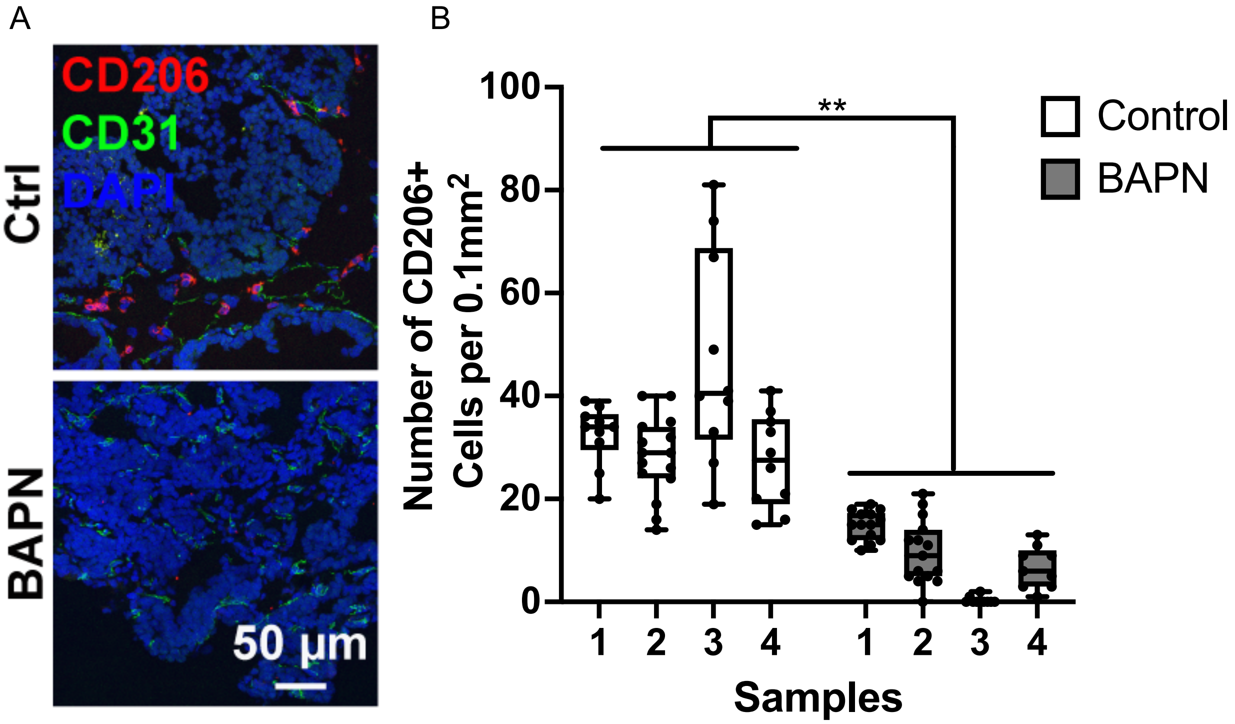

Figure 3.5. Quantifying macrophage polarization in the MMTV-PyMT breast tumor microenvironment. (A) Representative images of MMTV-PyMT tumor sections stained for DAPI (blue), CD31 (green), and CD206 (red). (B) Quantification of stained tumor sections. Number of CD206+ cells per field of interest. N=4 (number of mice), n = 9-15 (number of data points). **p<0.01. This figured was generated by co-first author Wenjun Wang.

Differential expression analysis between macrophages from stiff and compliant tumors for each subpopulation yielded very few differentially expressed transcripts. However, analyzing the distribution of the macrophages in each subset identified in stiff and compliant tumors revealed significant enrichment of an M2-like macrophage subpopulation in stiffer tumors, with ~30% of macrophages in stiffer tumors mapping to the M2-like phenotype compared to ~14% in the more compliant tumors (**Fig. 3D**). To quantify the phenotypic distribution of macrophages in vivo and validate our scRNAseq data, we obtained stiff and compliant tumors from our MMTV-PyMT model. Tumors were dissociated and subjected to flow cytometry analysis using CD11b and F4/80 as general macrophage markers (**Fig. 4A**), CD86 as an M1 macrophage marker[183] (**Fig. 4B**), and CD206 as an M2 macrophage marker[183] (**Fig. 4B**). Flow cytometry revealed no significant difference between total macrophage content (**Fig. 4C**) but a significant increase in CD206$^+$ macrophages in the stiffer tumors compared to compliant tumors as well as a concomitant decrease in CD86$^+$ macrophages (**Fig. 4D**). Furthermore, immunofluorescence staining of tumor sections also confirmed an increase in the number of CD026+ cells per field of interest in stiff tumors compared to compliant tumors (**Fig. 5A,B**). This data confirms that stiff tumors contain a higher proportion of M2-like macrophages compared to compliant tumors.

3.5.4 Intercellular communication differs between stiff and compliant tumors

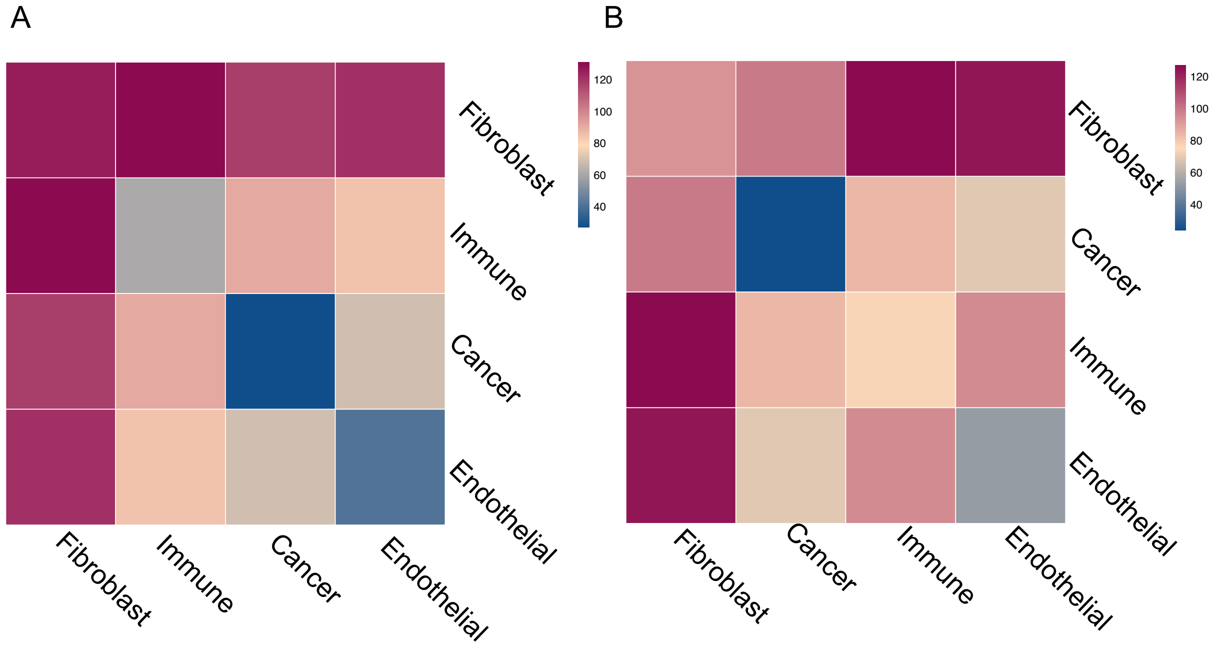

Figure 3.6. Quantification of cell-cell interactions between cell-types in the MMTV-PyMT tumor microenvironment. Heat map summarizing the number of significant ligand-receptor interactions in (A) control or (B) BAPN treated tumors.

To investigate the source of M2-like macrophage enrichment in stiffer tumors, we utilized CellPhoneDB to infer cell-cell interactions in the scRNAseq data using the expression of ligands and receptors across cell types[159]. Analysis using CellPhoneDB revealed numerous potential cell-cell interactions between all the cell types in both stiff and compliant tumors (**Fig. 6A,B**). While many of the cell-cell interactions were shared between treatment groups, there were 45 significant interactions specific to the stiff tumors and only 7 significant interactions specific to the compliant tumors (**Supplemental Fig. 3A,B)**. Interestingly, the network of cell-cell interactions in stiffer tumors shifted towards an increase in communication involving fibroblasts (**Fig. 6A,B**), with many of the ligand-receptor interactions specific to stiffer tumors involving collagen-integrin interactions with fibroblasts (**Supplemental Fig. 3A,B)**. However, significant interactions between other cell types were present, particularly in interactions involving immune cells. Notably, the several cancer-to-immune ligand-receptor interactions were found significant only in the stiffer tumors; including TYRO3-GAS6, SPP1-PTGER4, CSF3-CSF3R, and PLXNB1-SEMA4D (**Supplemental Fig. 3A,B**). Furthermore, CelllPhoneDB analysis indicates that there are more immune cell-cell interactions with other cell types than cancer cell-cell interactions in stiffer tumors but the inverse is true within compliant tumors (Fig. 6A,B). Altogether, this data suggests that stiff and compliant tumors have similar degrees of heterogeneity in regards to the presence (**Supplemental Fig. 1A,E,I**) and diversity (**Supplemental Fig. 1D,H,L**) of cell states but significantly differ in the intercellular communication with stiffer tumors displaying more integrin-based fibroblast signaling and potentially more immune cell interactions with other cell types (**Fig. 6A,B**).

3.5.5 Matrix stiffness regulates cytokine expression in MDA-MB-231 cells

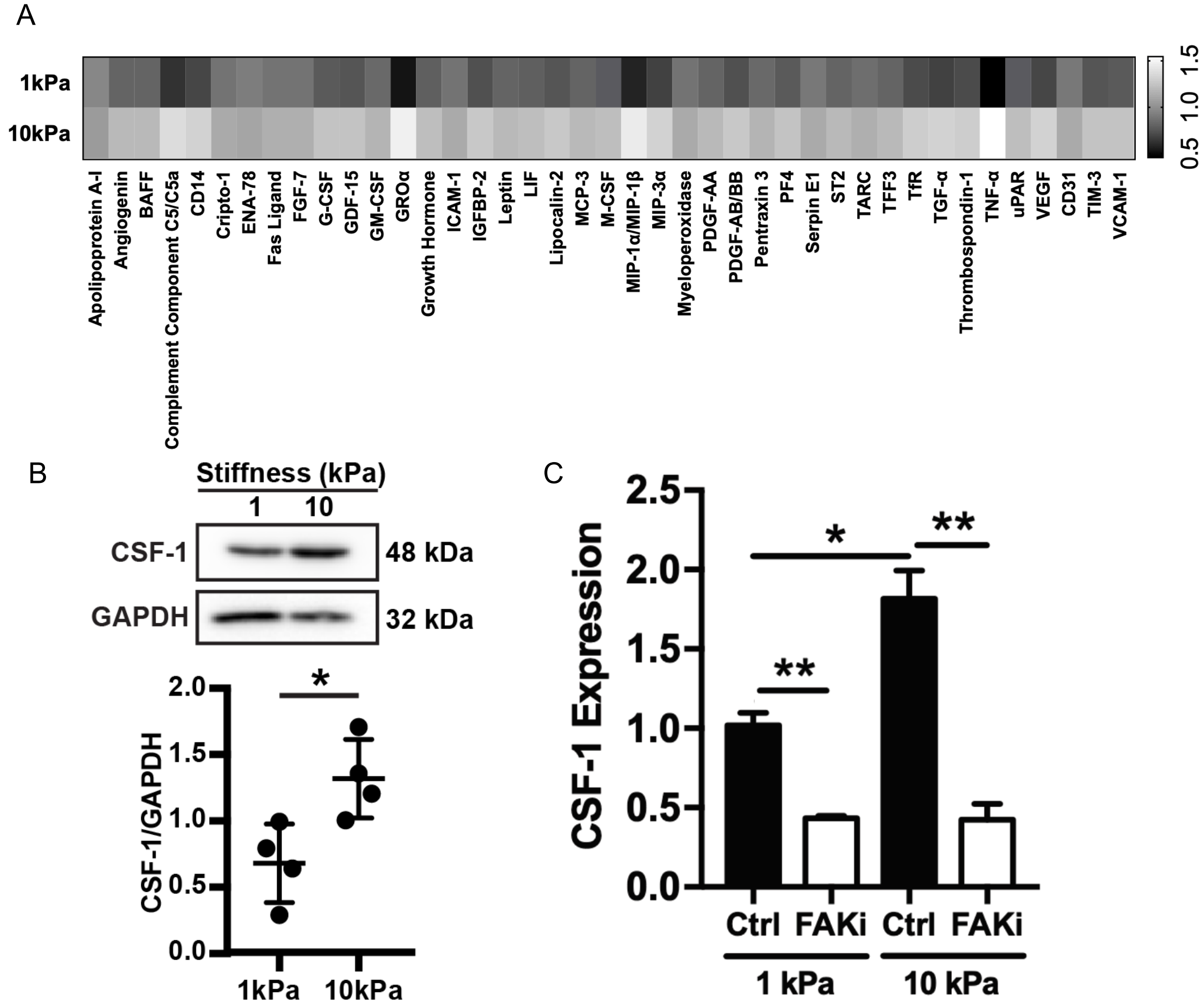

Figure 3.7. Matrix stiffness mediates cytokine expression in MDA-MB-231 cells. (A) Heat map displaying significantly differentially expressed cytokines between MDA-MB-231 cells on compliant (1kPa) or stiff (10kPa) gels. (B) Western blot image and quantification of CSF-1 in compliant (BAPN) or stiff (ctrl) PyMT tumors. (C) Western blot image and quantification of CSF-1 in MDA-MB-231 cells cultured on compliant or stiff PA gels. (D) qPCR of CSF-1 expression in MDA-MB-231 cells cultured on compliant or stiff PA gels and treated with a FAK inhibitor (FAKi). All data represented as mean +/- SEM. *p<0.05, **p<0.01. This figure was generated by co-first author Wenjun Wang.

While there were several statistically significant cell-cell interactions based on CellPhoneDB, differential expression testing revealed very few significantly expressed transcripts between stiffer and compliant tumors when comparing the same cell types. This may stem from technical limitations of our scRNAseq data resulting from the low mRNA capture efficiency of InDrop platforms as well as lower sequencing depth compared to bulk RNA sequencing. Thus, to further investigate potential cell-cell interactions responsible for M2-like macrophage enrichment, we transitioned into in vitro models using the human breast cancer cell line MDA-MB-231, a highly metastatic cell line. To determine how matrix stiffness may induce cancer-macrophage interactions to promote M2-like macrophage accumulation, we assessed how matrix stiffness regulates cytokine expression in MDA-MB-231 cells. MDA-MB-231 cells were seeded on either compliant (1kPa) or stiff (10kPa) collagen coated polyacrylamide (PA) gels. Cell lysates were collected and assayed using a human cytokine array kit which detected 105 different cytokines. 41 cytokines were found to be significantly differentially regulated by substrate stiffness (**Fig. 7A**). Interestingly, 3 members of the colony-stimulating factor (CSF) family, secreted glycoproteins with important roles in regulating immune cell functions and differentiation, were significantly upregulated in MDA-MB-231 cells cultured on stiff (10kPa) PA gels (**Fig. 7A**). This data indicates that the cancer cell cytokine secretome is affected by matrix stiffness and suggests matrix stiffening may affect intercellular signaling between cancer cells and immune cells.

3.5.6 Increased matrix stiffness upregulates CSF-1 in MDA-MB-231 cells and is dependent on FAK-mediated mechanotransduction

To further investigate how matrix stiffness may mediate intercellular communication between cancer and immune cells, we focused on the CSF family of cytokines as CSF1, CSF2, and CSF3 were upregulated in MDA-MB-231 cells cultured on stiff (10kPa) PA gels (**Fig. 7A**), and they are known to regulate macrophage function and polarization[184]. As our scRNAseq data only revealed appreciable expression of the CSF-1 receptor on our macrophage populations, we hypothesized that mechanical regulation of CSF-1 in the MDA-MB-231 cells may regulate macrophage recruitment. To determine if CSF-1 protein expression is higher in stiffer MMTV-PyMT tumors, we performed western blotting on lysates derived from compliant (BAPN) and stiff (control) MMTV-PyMT tumors and found that CSF-1 expression was significantly higher in stiffer tumors (**Fig. 7B**). To confirm that increased substrate stiffness upregulates CSF-1, we cultured MDA-MB-231 cells on compliant (1kPa) and stiff (10kPa) PA gels and performed western blotting on cell lysates. As expected, western blotting revealed protein expression of CSF-1 on stiff PA gels compared to compliant PA gels (**Fig. 7C**). Prior work shows that the focal adhesion kinase (FAK) is an important protein in the mechanotransduction of substrate stiffness in cancer cells[185]. To determine if mechanical regulation of CSF-1 in MDA-MB-231 cells is regulated by FAK, we treated MDA-MB-231 cells cultured on compliant (1kPa) and stiff (10kPa) gels with PF573228, a small molecule FAK inhibitor. Western blotting revealed that inhibition of FAK via PF573228 significantly reduced the expression of CSF-1 in MDA-MB-231 cells (**Fig. 7D**). Together, this data indicates that matrix stiffness regulates CSF-1 expression via FAK in MDA-MB-231 cells.

3.5.7 Matrix stiffness regulates macrophage recruitment through CSF-1

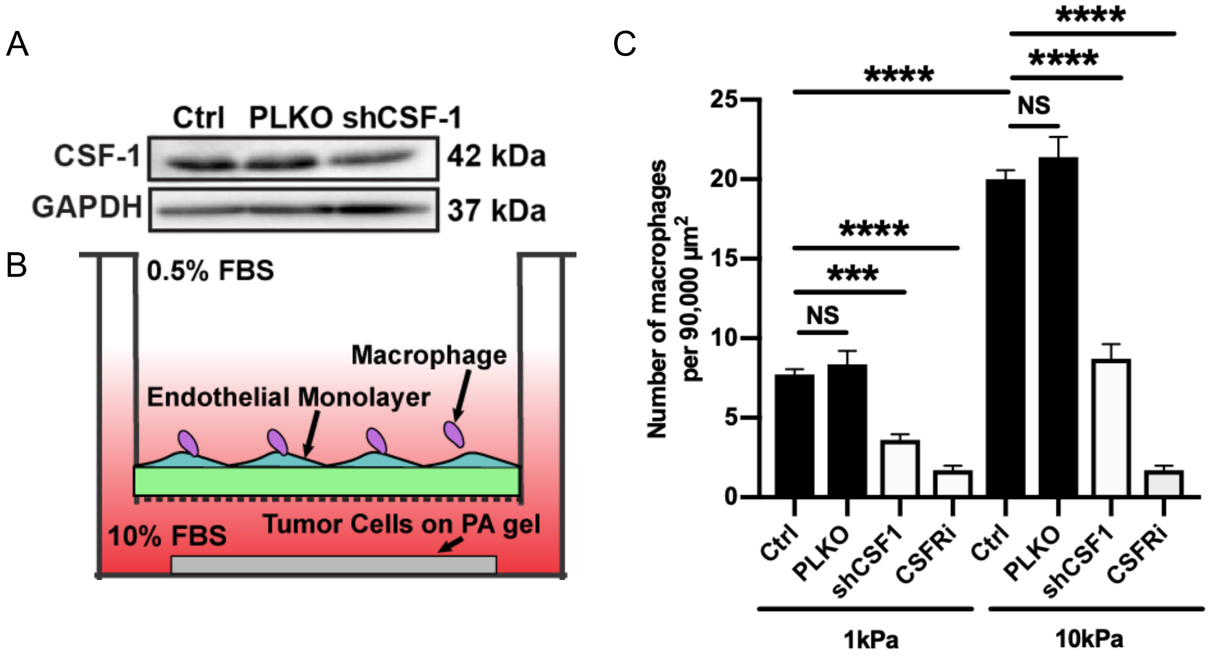

Figure 3.8. Stiffness mediated CSF-1 expression promotes macrophage recruitment. (A) Representative western blot confirming CSF-1 knockdown via shCSF-1. (B) Schematic diagram of modified transwell assay used to measure macrophage recruitment. (C) Quantification of the number of macrophages that migrated through the transwell towards MDA-MB-231 cells cultured on compliant or stiff PA gels with or without CSF-1 knockdown or with or without a CSF-1R inhibitor (CSF1Ri). Data plotted as mean +/- SEM. N=3, n=25-30. ***p<0.001, ****p<0.0001. This figure was generated by co-first author Wenjun Wang.

To confirm the functional importance of tumor derived CSF-1 in cancer-macrophage intercellular communication, we utilized an in vitro transwell-based assay to determine how stiffness mediated CSF-1 expression effects macrophage recruitment. In brief, BAC1.2F5 macrophages were seeded on top of a transwell insert with a Human Umbilical Vein Endothelial Cell (HUVEC) monolayer and MDA-MB-231 cells were seeded in the bottom of the well on compliant (1kPa) or stiff (10kPa) PA gels (**Fig. 8B**). Macrophage recruitment was quantified as the number of macrophages that migrated through the HUVEC monolayer and transwell insert membrane towards the MDA-MB-231 cells that were imaged 24 hours after seeding. As expected, MDA-MB-231 cells cultured on stiffer PA gels recruited significantly more macrophages than those on compliant PA gels (**Fig. 8C**). Furthermore, reduction of CSF-1 expression in MDA-MB-231 cells via shRNA knockdown resulted in significantly less macrophage recruitment (**Fig. 8A,C**). Similarly, inhibition of CSF-1 receptor on macrophages using a CSF-1 receptor inhibitor resulted in significantly less macrophage recruitment (**Fig. 8C**). Thus, our data suggests matrix stiffness facilitates a cancer-macrophage intercellular interaction by increasing CSF-1 expression in cancer cells.

3.6 Discussion

To profile the transcriptional landscapes and investigate phenotypic differences caused by tumor stiffness, we performed scRNAseq on all cells isolated from stiff and compliant PyMT mammary tumors. Both stiff and compliant tumors exhibit significant intratumor heterogeneity in the cancer and stromal cells (**Supplemental Fig. 1A,E,I**). Interestingly, much of the heterogeneity was conserved between conditions with both stiff and compliant tumors containing roughly the same subpopulations of cells with similar diversity of transcriptional profiles (**Supplemental Fig. 1D,H,L**). However, there were differences in cell-cell interactions between stiff and compliant tumors with stiffer tumor interaction networks increasing the number of ECM-component and integrin-based fibroblast receptor-ligand interactions (**Fig. 6**) as expected in stiffer more fibrotic tumors[105]. Furthermore, a significantly higher percentage of M2-like macrophages reside in the stiffer tumor microenvironment. Thus, while matrix stiffness does not induce novel cell phenotypes, it may affect intercellular signaling and adjust the phenotypic balances within the tumor microenvironment.

Our findings synergize well with recent reports using scRNAseq showing stromal subpopulations from different patients were highly similar in their expression states but varied in their proportions[186] and CAF subsets were highly similar between primary tumor and lymph node metastases[187]. Together, these studies suggest stromal subpopulations may be highly conserved between tumors, and the intertumoral heterogeneity may predominantly come in the form of intercellular communication and varying tumor composition.

Our scRNAseq (**Fig. 3D**), flow cytometry (**Fig. 4**), and immunostaining (**Fig. 5**) data indicate an elevation in M2-like macrophage presence in stiffer tumors. Additionally, while not evident in the scRNAseq data (**Fig 3D**), our flow cytometry data indicate a significant decrease in M1-like macrophages in stiffer tumors (**Fig. 4**). This discrepancy is likely due to the fact that our scRNAseq data did not resolve any specific M1-like clusters according to canonical markers (such as CD86) which could arise from technical aberrations or the actual complexity of macrophage polarization phenotypes[163,188]. It is known that tumor associated macrophages specifically contribute to tumor progression by promoting angiogenesis, facilitating cancer cell invasion, and repressing anti-tumor immunity[189–193]. The presence of macrophages within the tumor microenvironment has prognostic value in several cancers, with higher macrophage density being correlated with worse outcomes[194–196]. Traditionally, tumor associated macrophages exhibiting an alternatively activated M2 phenotype exert pro-tumoral effects while the classically activated M1 phenotype may exert tumor suppressing effects[45,197,198]. Furthermore, previous studies have revealed that BAPN treatment in the MMTV-PyMT model delays primary tumor development and metastatic lung burden[156]. As the M2 phenotype is associated with tumor progression and elevated matrix stiffening is associated with delayed primary tumor development and metastasis, this finding suggests another mechanism by which matrix stiffening may reshape the tumor microenvironment to further cancer progression. However, the mechanism by which matrix stiffness drives M2-like macrophage enrichment remains unknown.

Macrophage accumulation could occur through several mechanisms. Stiffer matrices may 1.) preferentially recruit M2-like macrophages, 2.) promote proliferation and survival of M2-like macrophages, 3.) shift macrophages towards an M2-like phenotype, or 4.) decrease infiltration, proliferation, or survival of M1-like macrophages. Extracellular matrix stiffness could induce expression of chemokines or other attractants by either cancer or stromal cells that lead to infiltration of M2-like macrophages. For example, previous work has demonstrated that hypoxia in the breast cancer microenvironment may induce intercellular signaling between that ultimately leads to increased macrophage recruitment via cancer secreted CSF-1[199]. Interestingly, while a large portion of significant cell-cell interactions detected specifically in stiffer tumors were focused between fibroblasts to fibroblasts, we detected cancer-to-immune cell ligand-receptor interactions which could contribute to M2-like accumulation. Another interesting possibility could be differential macrophage infiltration due to changes in the tumor endothelium. We have previously shown that matrix stiffening leads to significant permeability in the tumor endothelium [95]. Thus, it may be possible for more macrophages to enter the stiffer tumor microenvironment, bypassing a more permissive vasculature than in compliant tumors. However, this does not completely explain the enrichment for M2-like macrophages as similar amount of total macrophages were observed in the stiff and compliant tumors.

It is highly possible that matrix stiffness in the tumor microenvironment polarizes macrophages towards the M2-like phenotype. Macrophages are mechanosensitivity to substrate stiffness[147,200] and the effect of matrix stiffness on macrophage polarization has been studied numerous times, with some mixed findings [201–206]. There is evidence for increased M2 polarization on both stiff [201,204,205] or soft [203] matrices. To further complicate these conflicting findings, the studies employed different macrophage sources coupled with systems possessing different dimensionality (2D vs 3D), ligand availability, and stiffness ranges. Additionally, these studies were completed on macrophages cultured in vitro using methods developed to polarize macrophages with a chemical stimulus. Importantly, our data provides indirect evidence for macrophage polarization towards an M2 phenotype under stiffer conditions and, to our knowledge, is the only study to use an *in vivo* model of matrix stiffening.

Importantly, we have shown that MDA-MB-231 cells alter their cytokine secretome in response to increased matrix stiffness. Notably, CSF-1 is upregulated in stiffer MMTV-PyMT tumors and MDA-MB-231 cells cultured on stiffer substrates (**Fig. 7**). CSF-1, also known as macrophage CSF (M-CSF), is a member of the family of the colony stimulating factors[184]. CSF members are regulatory cytokines that facilitate intercellular communication, paracrine, autocrine, or endocrine, via binding to extracellular CSF receptors [184]. In particular, CSF-1 promotes macrophage polarization towards the M2 phenotype and CSF1-R inhibition has been shown to reduce M2 gene expression in vivo[149]. In cancer, CSF-1 has been correlated with worse prognosis[207]. As such, there has been a recent focus on targeting CSF-1 in cancer patients as a therapeutic strategy and there have been two clinical trials completed utilizing an anti-CSF-1 antibody in combination with additional chemotherapy agents in patients with various types of breast cancer[208,209]. Thus Our findings suggest that matrix stiffness may induce M2-like macrophage accumulation via a cancer-macrophage intercellular communication through CSF-1. Thus the anti-CSF-1 drugs may also be effective in inhibiting the accumulation of tumor promoting M2-like macrophages in stiffer tumors.

3.7 Conclusion

Therapies targeting extracellular matrix stiffness have become increasingly popular due to the known effects of matrix stiffness on cellular behavior, however, these therapies are unlikely to work as standalone treatments and it will be important to understand what additional therapies will be viable if matrix stiffening can be attenuated[90]. Our results indicate that while the overall cell populations close resemble each other in stiff and compliant tumor microenvironments, the cell-cell interactions between cell types and the distribution of phenotypic cell subtypes are different. Specifically, more integrin-based fibroblast cell-cell interactions exist in stiffer tumors and a higher proportion of the tumor promoting M2-like macrophages reside within stiffer tumors. Furthermore, our data suggests that matrix stiffening in the tumor microenvironment may drive M2-like macrophage accumulation through intercellular cross-talk between cancer cells and macrophages via cancer secreted CSF-1. Given that tumor angiogenesis and metastasis are affected by both matrix stiffening[95,140,210] and M2-like macrophage interactions[193,211], accumulation of M2-like macrophages may represent an alternative or reinforcing mechanism by which matrix stiffness alters tumor angiogenesis and metastasis.

3.8 CRediT authorship contribution statement

Paul V. Taufalele: Conceptualization, Visualization, Methodology, Data curation, Formal analysis, Writing – review & editing. **Wenjun Wang:** Conceptualization, Visualization, Methodology, Data curation, Formal analysis, Writing – review & editing. **Alan J. Simmons:** Conceptualization, Visualization, Methodology, Data curation, Formal analysis. **Austin N. Southard-Smith:** Conceptualization, Visualization, Methodology, Data curation, Formal analysis. **Bob Chen:** Conceptualization, Visualization, Methodology, Data curation, Formal analysis. **Joshua D. Greenlee:** Conceptualization, Visualization, Methodology, Data curation, Formal analysis. **Michael R. King:** Conceptualization, Visualization. **Ken S. Lau:** Conceptualization, Visualization, Methodology, Data curation, Formal analysis. **Duane C. Hassane:** Conceptualization, Visualization. **François Bordeleau:** Conceptualization, Visualization. **Cynthia A. Reinhart-King:** Conceptualization, Visualization, Data curation, Writing – review & editing.

3.9 Acknowledgments

This work was funded by the NIH NHLBI (Award number HL127499 and GM131178) and the W.M. Keck Foundation to CAR. PVT was funded by a Diversity Supplement for the NIH NHLBI R01(Award number HL127499) and an NIH F31 Predoctoral Fellowship (1F31HL154727). WW was funded by an AHA Predoctoral Fellowship (917613). JDG was funded by an NSF Graduate Research Fellowship. KSL, ANS, BC, and AJS were funded by R01DK103831 and P50CA236733. We would like to thank the Vanderbilt Technologies for Advanced Genomics (VANTAGE) core facility for their help with this work. The BAC1.2F5 cells were graciously donated by Dr. Richard Stanley, Albert Einstein College of Medicine.

3.10 Supplementary materials

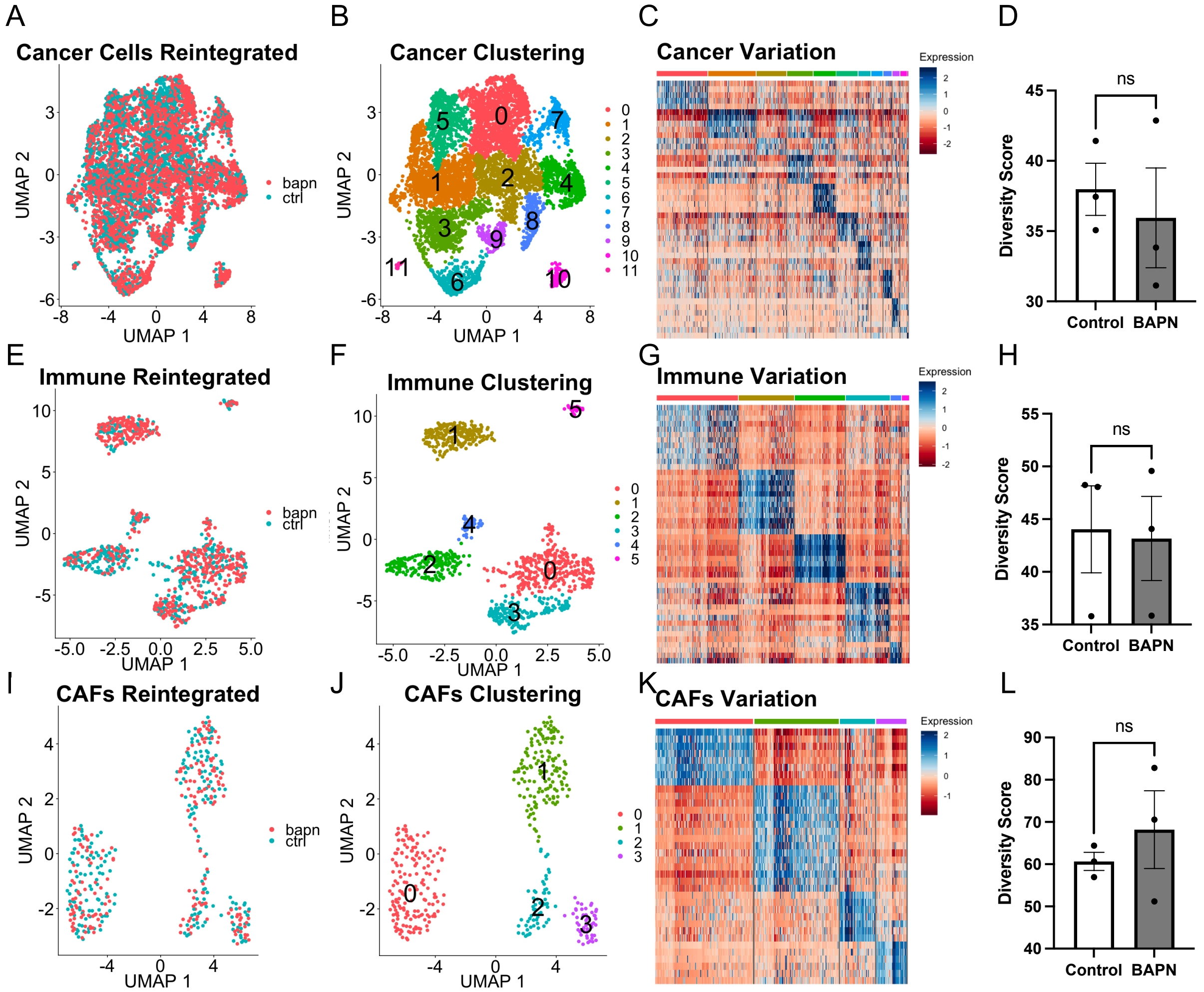

Supplementary Figure 3.1. Intratumoral heterogeneity within cell types in the MMTV-PyMT tumor microenvironment. UMAP projection of all (A) cancer, (E) immune, and (I) CAF cells integrated via Seurat and colored by treatment. Clustering via Louvain algorithm in Seurat for (B) cancer, (F) immune, and (J) CAF cells. (C,G,K) Heat map of top marker gene expression profiles for the different subpopulations across the cell types. Heterogeneity score calculated from PCA embeddings for (D) cancer, (H) immune, and (L) CAF cells.

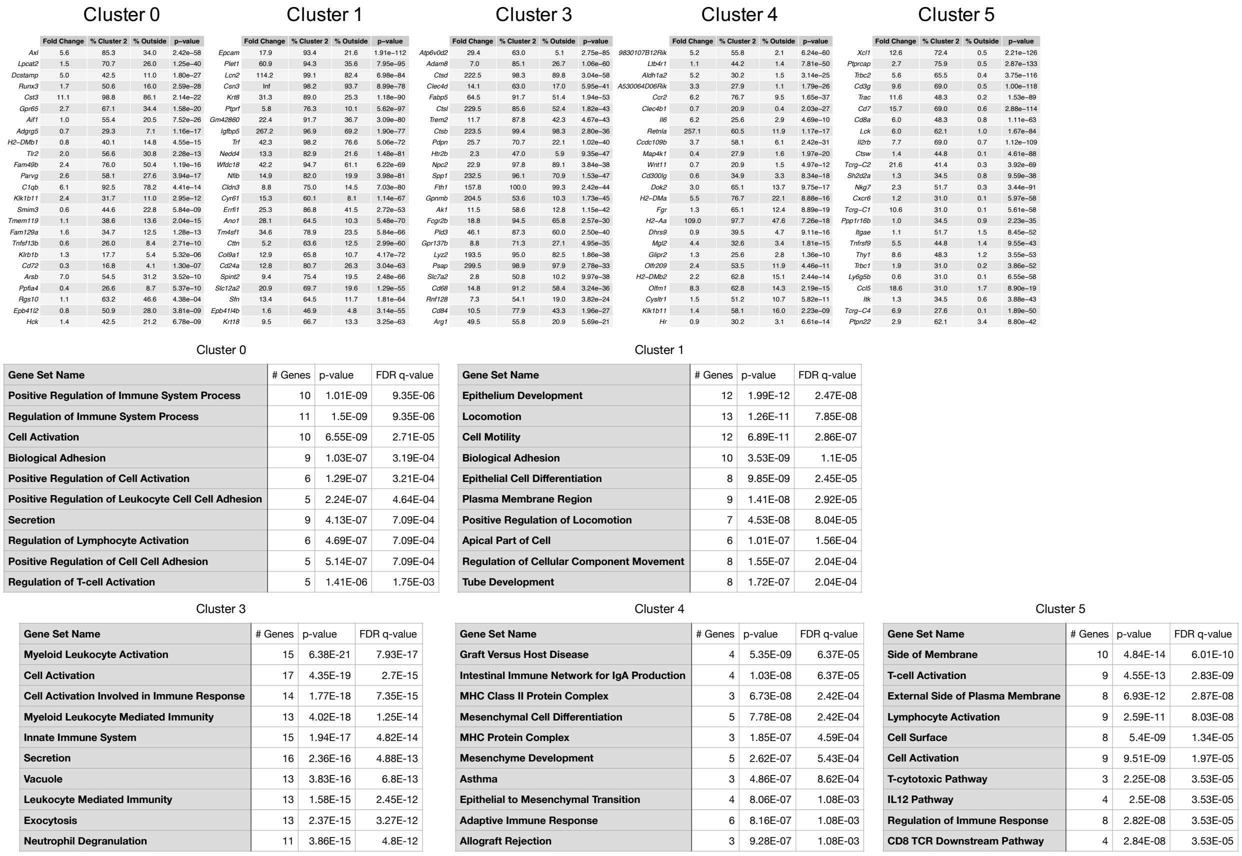

Cluster 0

	Fold Change	% Cluster 2	% Outside	p–value
Axl	5.6	85.3	34.0	2.42e–58
Lpcat2	1.5	70.7	26.0	1.25e–40
Dcstamp	5.0	42.5	11.0	1.80e–27
Runx3	1.7	50.6	16.0	2.59e–28
Cst3	11.1	98.8	86.1	2.14e–22
Gpr65	2.7	67.1	34.4	1.58e–20
Aif1	1.0	55.4	20.5	7.52e–26
Adgrg5	0.7	29.3	7.1	1.16e–17
H2–DMb1	0.8	40.1	14.8	4.55e–15
Tlr2	2.0	56.6	30.8	2.28e–13
Fam49b	2.4	76.0	50.4	1.19e–16
Parvg	2.6	58.1	27.6	3.94e–17
C1qb	6.1	92.5	78.2	4.41e–14
Klk1b11	2.4	31.7	11.0	2.95e–12
Smim3	0.6	44.6	22.8	5.84e–09
Tmem119	1.1	38.6	13.6	2.04e–15
Fam129a	1.6	34.7	12.5	1.28e–13
Tnfsf13b	0.6	26.0	8.4	2.71e–10
Klrb1b	1.3	17.7	5.4	5.32e–06
Cd72	0.3	16.8	4.1	1.30e–07
Arsb	7.0	54.5	31.2	3.52e–10
Ppfia4	0.4	26.6	8.7	5.37e–10
Rgs10	1.1	63.2	46.6	4.38e–04
Epb41l2	0.8	50.9	28.0	3.81e–09
Hck	1.4	42.5	21.2	6.78e–09

Cluster 1

	Fold Change	% Cluster 2	% Outside	p–value
Epcam	17.9	93.4	21.6	1.91e–112
Plet1	60.9	94.3	35.6	7.95e–95
Lcn2	114.2	99.1	82.4	6.98e–84
Csn3	Inf	98.2	93.7	8.99e–78
Krt8	31.3	89.0	25.3	1.18e–90
Ptprf	5.8	76.3	10.1	5.62e–97
Gm42860	22.4	91.7	36.7	3.09e–80
Igfbp5	267.2	96.9	69.2	1.90e–77
Trf	42.3	98.2	76.6	5.06e–72
Nedd4	13.3	82.9	21.6	1.48e–81
Wfdc18	42.2	94.7	61.1	6.22e–69
Nfib	14.9	82.0	19.9	3.98e–81
Cldn3	8.8	75.0	14.5	7.03e–80
Cyr61	15.3	60.1	8.1	1.14e–67
Errfi1	25.3	86.8	41.5	2.72e–53
Ano1	28.1	64.5	10.3	5.48e–70
Tm4sf1	34.6	78.9	23.5	5.84e–66
Cttn	5.2	63.6	12.5	2.99e–60
Col9a1	12.9	65.8	10.7	4.17e–72
Cd24a	12.8	80.7	26.3	3.04e–63
Spint2	9.4	75.4	19.5	2.48e–66
Slc12a2	20.9	69.7	19.6	1.29e–55
Sfn	13.4	64.5	11.7	1.81e–64
Epb41l4b	1.6	46.9	4.8	3.14e–55
Krt18	9.5	66.7	13.3	3.25e–63

Cluster 3

	Fold Change	% Cluster 2	% Outside	p–value
Atp6v0d2	29.4	63.0	5.1	2.75e–85
Adam8	7.0	85.1	26.7	1.06e–60
Ctsd	222.5	98.3	89.8	3.04e–58
Clec4d	14.1	63.0	17.0	5.95e–41
Fabp5	64.5	91.7	51.4	1.94e–53
Ctsl	229.5	85.6	52.4	1.82e–43
Trem2	11.7	87.8	42.3	4.67e–43
Ctsb	223.5	99.4	98.3	2.80e–36
Pdpn	25.7	70.7	22.1	1.02e–40
Htr2b	2.3	47.0	5.9	9.35e–47
Npc2	22.9	97.8	89.1	3.84e–38
Spp1	232.5	96.1	70.9	1.53e–47
Fth1	157.8	100.0	99.3	2.42e–44
Gpnmb	204.5	53.6	10.3	1.73e–45
Ak1	11.5	58.6	12.8	1.15e–42
Fcgr2b	18.8	94.5	65.8	2.57e–30
Pld3	46.1	87.3	60.0	2.50e–40
Gpr137b	8.8	71.3	27.1	4.95e–35
Lyz2	193.5	95.0	82.5	1.86e–38
Psap	299.5	98.9	97.9	2.78e–33
Slc7a2	2.8	50.8	10.2	9.97e–38
Cd68	14.8	91.2	58.4	3.24e–36
Rnf128	7.3	54.1	19.0	3.82e–24
Cd84	10.5	77.9	43.3	1.96e–27
Arg1	49.5	55.8	20.9	5.69e–21

Cluster 4

	Fold Change	% Cluster 2	% Outside	p–value
9830107B12Rik	5.2	55.8	2.1	6.24e–60
Ltb4r1	1.1	44.2	1.4	7.81e–50
Aldh1a2	5.2	30.2	1.5	3.14e–25
A530064D06Rik	3.3	27.9	1.1	1.79e–26
Ccr2	6.2	76.7	9.5	1.65e–37
Clec4b1	0.7	20.9	0.4	2.03e–27
Il6	6.2	25.6	2.9	4.69e–10
Retnla	257.1	60.5	11.9	1.17e–17
Ccdc109b	3.7	58.1	6.1	2.42e–31
Map4k1	0.4	27.9	1.6	1.97e–20
Wnt11	0.7	20.9	1.5	4.97e–12
Cd300lg	0.6	34.9	3.3	8.34e–18
Dok2	3.0	65.1	13.7	9.75e–17
H2–DMa	5.5	76.7	22.1	8.88e–16
Fgr	1.3	65.1	12.4	8.89e–19
H2–Aa	109.0	97.7	47.6	7.26e–18
Dhrs9	0.9	39.5	4.7	9.11e–16
Mgl2	4.4	32.6	3.4	1.81e–15
Glipr2	1.3	25.6	2.8	1.36e–10
Olfr209	2.4	53.5	11.9	4.46e–11
H2–DMb2	2.2	62.8	15.1	2.44e–14
Olfm1	8.3	62.8	14.3	2.19e–15
Cysltr1	1.5	51.2	10.7	5.82e–11
Klk1b11	1.4	58.1	16.0	2.23e–09
Hr	0.9	30.2	3.1	6.61e–14

Cluster 5

	Fold Change	% Cluster 2	% Outside	p–value
Xcl1	12.6	72.4	0.5	2.21e–126
Ptprcap	2.7	75.9	0.5	2.87e–133
Trbc2	5.6	65.5	0.4	3.75e–116
Cd3g	9.6	69.0	0.5	1.00e–118
Trac	11.6	48.3	0.2	1.53e–89
Cd7	15.7	69.0	0.6	2.88e–114
Cd8a	6.0	48.3	0.8	1.11e–63
Lck	6.0	62.1	1.0	1.67e–84
Il2rb	7.7	69.0	0.7	1.12e–109
Ctsw	1.4	44.8	0.1	4.61e–88
Tcrg–C2	21.6	41.4	0.3	3.92e–69
Sh2d2a	1.3	34.5	0.8	9.59e–38
Nkg7	2.3	51.7	0.3	3.44e–91
Cxcr6	1.2	31.0	0.1	5.97e–58
Tcrg–C1	10.6	31.0	0.1	5.61e–58
Ppp1r16b	1.0	34.5	0.9	2.23e–35
Itgae	1.1	51.7	1.5	8.45e–52
Tnfrsf9	5.5	44.8	1.4	9.55e–43
Thy1	8.6	48.3	1.2	3.55e–53
Trbc1	1.9	31.0	0.2	3.86e–52
Ly6g5b	0.6	31.0	0.1	6.55e–58
Ccl5	18.6	31.0	1.7	8.90e–19
Itk	1.3	34.5	0.6	3.88e–43
Tcrg–C4	6.9	27.6	0.1	1.89e–50
Ptpn22	2.9	62.1	3.4	8.80e–42

Cluster 0

Gene Set Name	# Genes	p-value	FDR q-value
Positive Regulation of Immune System Process	10	1.01E-09	9.35E-06
Regulation of Immune System Process	11	1.5E-09	9.35E-06
Cell Activation	10	6.55E-09	2.71E-05
Biological Adhesion	9	1.03E-07	3.19E-04
Positive Regulation of Cell Activation	6	1.29E-07	3.21E-04
Positive Regulation of Leukocyte Cell Cell Adhesion	5	2.24E-07	4.64E-04
Secretion	9	4.13E-07	7.09E-04
Regulation of Lymphocyte Activation	6	4.69E-07	7.09E-04
Positive Regulation of Cell Cell Adhesion	5	5.14E-07	7.09E-04
Regulation of T-cell Activation	5	1.41E-06	1.75E-03

Cluster 1

Gene Set Name	# Genes	p-value	FDR q-value
Epithelium Development	12	1.99E-12	2.47E-08
Locomotion	13	1.26E-11	7.85E-08
Cell Motility	12	6.89E-11	2.86E-07
Biological Adhesion	10	3.53E-09	1.1E-05
Epithelial Cell Differentiation	8	9.85E-09	2.45E-05
Plasma Membrane Region	9	1.41E-08	2.92E-05
Positive Regulation of Locomotion	7	4.53E-08	8.04E-05
Apical Part of Cell	6	1.01E-07	1.56E-04
Regulation of Cellular Component Movement	8	1.55E-07	2.04E-04
Tube Development	8	1.72E-07	2.04E-04

Cluster 3

Gene Set Name	# Genes	p-value	FDR q-value
Myeloid Leukocyte Activation	15	6.38E-21	7.93E-17
Cell Activation	17	4.35E-19	2.7E-15
Cell Activation Involved in Immune Response	14	1.77E-18	7.35E-15
Myeloid Leukocyte Mediated Immunity	13	4.02E-18	1.25E-14
Innate Immune System	15	1.94E-17	4.82E-14
Secretion	16	2.36E-16	4.88E-13
Vacuole	13	3.83E-16	6.8E-13
Leukocyte Mediated Immunity	13	1.58E-15	2.45E-12
Exocytosis	13	2.37E-15	3.27E-12
Neutrophil Degranulation	11	3.86E-15	4.8E-12

Cluster 4

Gene Set Name	# Genes	p-value	FDR q-value
Graft Versus Host Disease	4	5.35E-09	6.37E-05
Intestinal Immune Network for IgA Production	4	1.03E-08	6.37E-05
MHC Class II Protein Complex	3	6.73E-08	2.42E-04
Mesenchymal Cell Differentiation	5	7.78E-08	2.42E-04
MHC Protein Complex	3	1.85E-07	4.59E-04
Mesenchyme Development	5	2.62E-07	5.43E-04
Asthma	3	4.86E-07	8.62E-04
Epithelial to Mesenchymal Transition	4	8.06E-07	1.08E-03
Adaptive Immune Response	6	8.16E-07	1.08E-03
Allograft Rejection	3	9.28E-07	1.08E-03

Cluster 5

Gene Set Name	# Genes	p-value	FDR q-value
Side of Membrane	10	4.84E-14	6.01E-10
T-cell Activation	9	4.55E-13	2.83E-09
External Side of Plasma Membrane	8	6.93E-12	2.87E-08
Lymphocyte Activation	9	2.59E-11	8.03E-08
Cell Surface	8	5.4E-09	1.34E-05
Cell Activation	9	9.51E-09	1.97E-05
T-cytotoxic Pathway	3	2.25E-08	3.53E-05
IL12 Pathway	4	2.5E-08	3.53E-05
Regulation of Immune Response	8	2.82E-08	3.53E-05
CD8 TCR Downstream Pathway	4	2.84E-08	3.53E-05

Supplementary Figure 3.2. Immune cell annotation. Tables including the top 25 genes significantly upregulated within each cluster and GO Term analysis of these top marker genes.

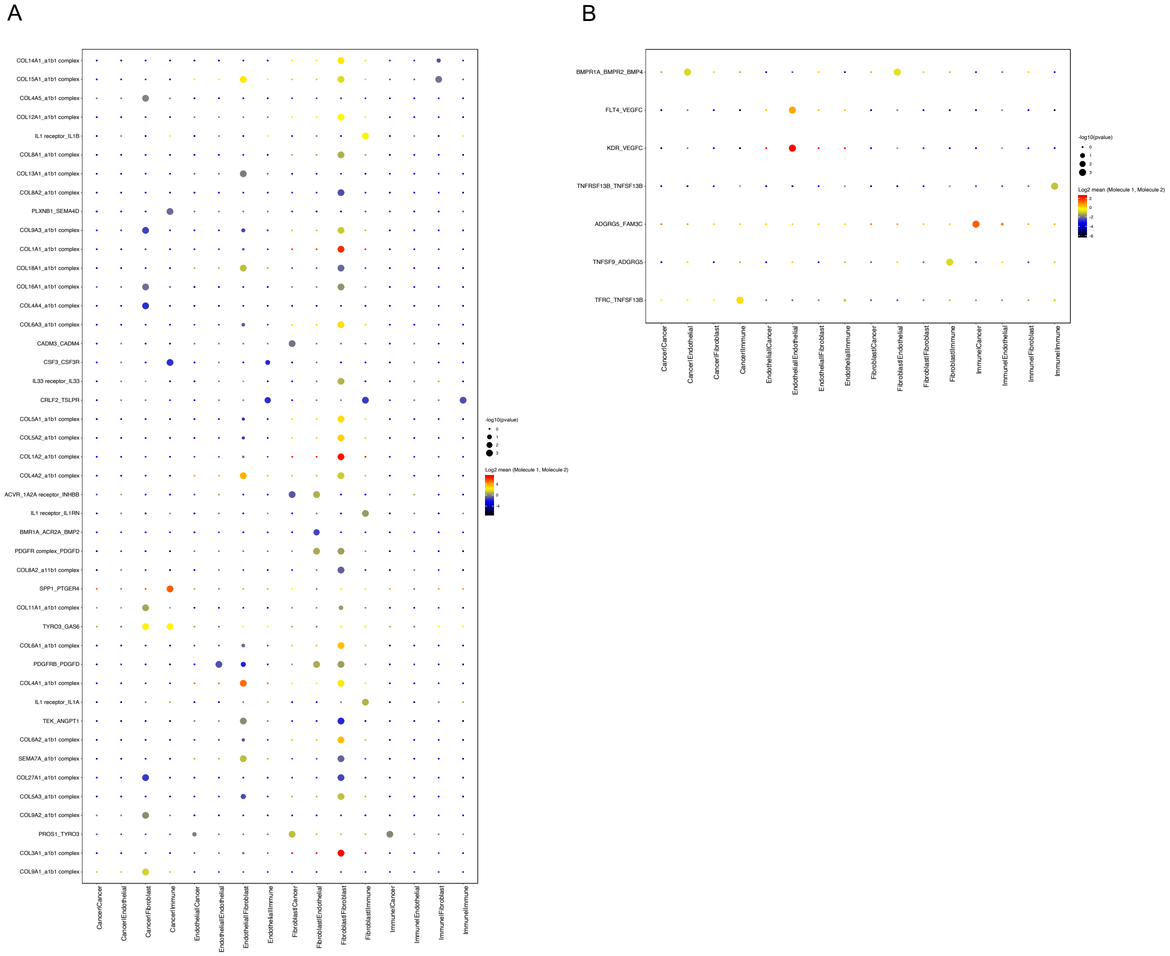

Supplementary Figure 3.3. Significant cell-cell interactions in the MMTV-PyMT tumor microenvironment. Dot plots displaying cell-cell interactions that were specifically found to be significant in only (A) stiff or (B) compliant tumors.

Chapter 4:

Matrix stiffness-mediated DNA methylation in endothelial cells

Paul V. Taufalele, Hannah Kirkham, Cynthia A. Reinhart-King

This chapter is in preparation for submission and has been reproduced with the permission of my co-authors.

4.1 Abstract

Purpose

Altered tissue mechanics is a prominent feature of many pathological conditions including cancer. As such, much work has been dedicated towards understanding how mechanical features of tissues contributes to pathogenesis. Interestingly, previous work has demonstrated that the tumor vasculature acquires pathological features in part due to enhanced tumor stiffening. To further understand how matrix mechanics may be translated into altered cell behavior and ultimately affect tumor vasculature function, we have investigated the effects of substrate stiffening on endothelial epigenetics. Specifically, we have focused on DNA methylation as recent work indicates DNA methylation in endothelial cells can contribute to aberrant behavior in a range of pathological conditions.

Methods

Human umbilical vein endothelial cells (HUVECs) were seeded on stiff and compliant collagen coated polyacrylamide gels and allowed to form monolayers over 5 days. DNA methylation was assessed via 5-methylcytosine ELISA assays and immunofluorescent staining. Gene expression was assessed via qPCR on RNA isolated from HUVECs seeded on collagen coated polyacrylamide gels of varying stiffness.

Results

Our work demonstrates that endothelial cells cultured on stiffer substrates exhibit lower levels of global DNA methylation relative to endothelial cells cultured on more compliant substrates. Interestingly, gene expression and DNA methylation dynamics suggest stiffness-mediated gene expression may play a role in establishing or maintaining differential DNA methylation levels in addition to enzyme activity. Additionally, we found that the process of passaging induced higher levels of global DNA methylation.

Conclusions

Altogether, our results underscore the importance of considering cell culture substrate mechanics to preserve the epigenetic integrity of primary cells and obtain analyses that recapitulate the primary environment. Furthermore, these results serve as an important launching point for further work studying the intersection tissue mechanics and epigenetics under pathological conditions.

4.2 Introduction

The vasculature system is a critical component of the tumor microenvironment. To grow, tumors must recruit blood vessels from pre-existing blood vessels through angiogenesis [212,213]. However, tumor vasculature is characteristically unorganized, tortuous, and leaky [100]. Interestingly, physical cues such as extracellular matrix stiffness have been shown to play an important role in regulating endothelial cell behavior [152,214,215]. Furthermore, there is ample evidence demonstrating that many solid tumors are significantly stiffer than their normal tissue counterparts [85], in part due to excess matrix deposition or matrix cross-linking [88]. Our lab has previously demonstrated that several features of the tumor vasculature can be rescued by reducing matrix stiffening [95]. Specifically, reducing matrix stiffness decreases excessive angiogenesis and decreases vascular permeability [95]. As such targeting mechanotransduction and mechanical effects could be leveraged as a therapeutic strategy [90]. Here we seek to understand how mechanical properties may drive contribute to aberrant endothelial cell behavior in the tumor microenvironment.

The intersection of epigenetics with mechanobiology has been gaining interest [216,217]. Epigenetics is the study of phenomena by which chromosomal regions are altered to register, signal, or perpetuate altered activity states [218]. One of the main epigenetic systems is DNA methylation [218]. In DNA methylation, a methyl group is covalently attached to a cytosine base in DNA [219]. In mammalian cells, this methylation occurs preferentially at ‘CG’ sequences [220]. DNA methylation traditionally has been shown to regulate gene expression by recruiting methyl binding proteins or directly inhibiting the binding of transcription factors [219]. Much attention has been placed onto the study of DNA methylation as it has found usage as a possible prognostic marker [221–225].

Interestingly, DNA methylation plays an important role in endothelial cells and disease progression. Recent work demonstrated that disturbed fluid flow induces changes in endothelial cell DNA methylation and gene expression which can contribute to atherosclerosis development [226–228]. Additional work has revealed endothelial cells exhibit decreased global DNA methylation levels during angiogenic programs, with corresponding specific correlations between changes in gene promoter methylation and RNA abundance [229]. Furthermore, Maishi et al. have shown that tumor endothelial cells, which are abnormal and exhibit pathological characteristics [230,231], have altered levels of DNA methylation [232]. Specifically, tumor endothelial cells exhibited decreased DNA methylation at promoter region of biglycan resulting in higher expression [232].

As recent work in the field has demonstrated a link between mechanical cues and DNA methylation [217], we specifically focused on the effects of matrix stiffness on DNA methylation in endothelial cells. Utilizing collagen-coated polyacrylamide substrates, our data indicate endothelial cells cultured on increased stiffnesses display decreased levels of global DNA methylation, a decrease in the RNA abundance of DNMT1 which plays a role in propagating DNA methylation. Furthermore we find that global levels of DNA methylation decrease over time and the process of passaging increases global levels of DNA methylation.

4.3 Results

4.3.1 DNA methylation levels are responsive to substrate stiffness

To investigate the effect of substrate stiffness on global DNA methylation levels in endothelial cells, we seeded Human Umbilical Vein Endothelial Cells (HUVECs) atop collagen-coated polyacrylamide (PA) gels of 2.5kPa and 20kPa to mimic the range of heterogeneous stiffness observed in the tumor microenvironment[233]. After 5 days, global DNA methylation levels were assessed via immunofluorescent staining of fixed cells (Fig. 1A,B) and ELISA performed on isolated genomic DNA (Fig. 1C). Immunofluorescent staining of 5-methylcytosine revealed signal was predominantly localized to the nucleus (Fig. 1A). Interestingly, HUVECs seeded on stiffer substrates had significantly lower 5-methylcytosine signal in the nucleus (Fig. 1B). Furthermore, this result was confirmed by performing an ELISA on isolated DNA demonstrating significantly lower 5-methylcytosine levels in HUVECs cultured on stiffer substrates (Fig. 1C). Altogether, this data suggests that increased substrates stiffness induces lower levels of global DNA methylation.

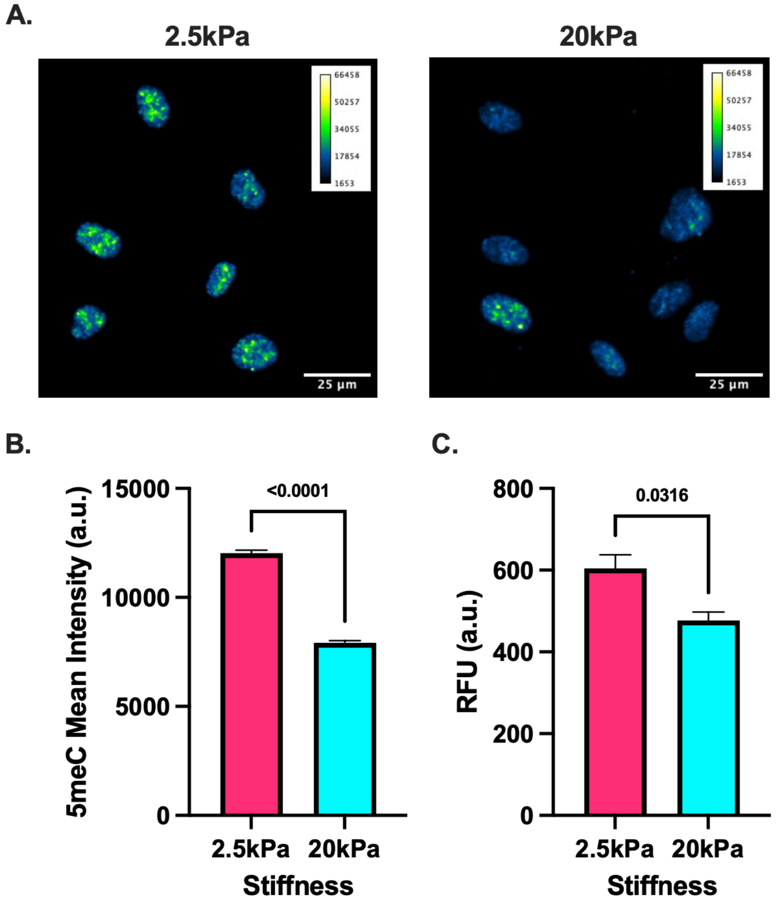

Figure 4.1. Stiffness mediated global DNA methylation levels. (**A**) Representative images of 5-methylcytosine immunofluorescent staining. (**B**) Quantification of 5-methylcytosine immunofluorescent staining in HUVECs cultured on PA gels. Mann Whitney test. N = 6, n =1936-2039; (**C**) Quantification of 5-methylcytosine ELISA fluorescent intensity. Unpaired t-test. N = 3, n = 3;

4.3.2 mRNA abundance of DNMT1 is reduced on stiffer substrates

DNA methylation and demethylation can be accomplished by several known enzymes. To determine if substrate stiffness induces changes in overall abundance of these enzymes, we cultured HUVECs on compliant (2.5kPa) and stiff (20kPa) PA gels for 5 days and performed qPCR to measure RNA abundance. We performed qPCR on DNMT1, DNMT3a, DNMT3b, TET1, and TET2. Interestingly, qPCR revealed DNMT1 levels were significantly lower on stiffer substrates (Fig. 2). DNMT3a, TET1, and TET2 remained not significantly different (Fig. 2) and DNMT3b expression was not detected (data not shown). Altogether our results suggest that increased substrate stiffness induces lower levels of DNMT1 expression while the remaining enzymes involved in DNA methylation remain unchanged.

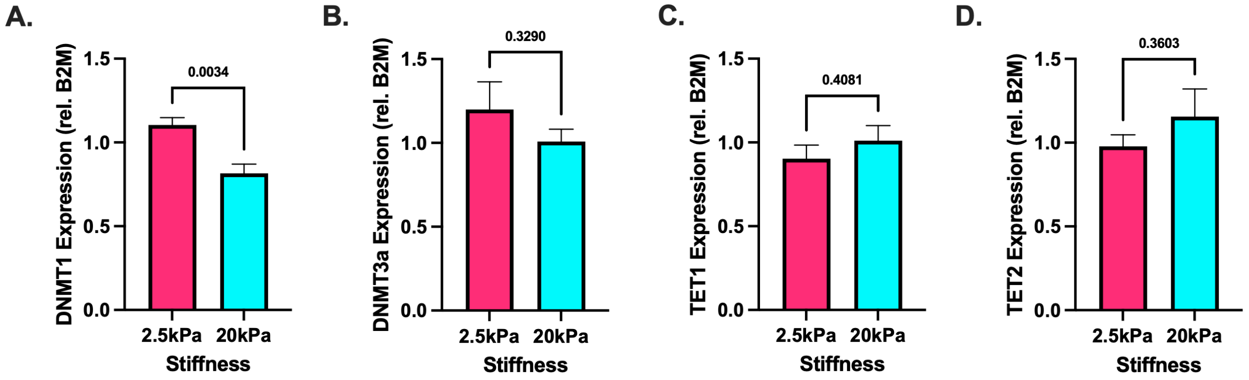

Figure 4.2. Stiffness mediated gene expression. Quantification of (**A**) DNMT1, (**B**) DNMT3a, (**C**)TET1, and (**D**) TET2 RNA abundance measured by qPCR. Unpaired t-test. N = 4, n = 4-5;

4.3.3 Dynamics of stiffness responsive DNA methylation

To investigate the dynamics of DNA methylation in response to substrate stiffness, we seeded HUVECs on top of compliant (2.5kPa) and stiff (20kPa) PA gels and measured global DNA methylation levels via 5-methylcytosine staining every 24 hours for 5 days (Fig. 3). Interestingly, our results demonstrate that DNA methylation levels are significantly lower on stiffer substrates after only 24 hours of culture (Fig. 3). Furthermore, the data suggests that DNA methylation levels decreases over time in both stiffness conditions while the difference between stiff and compliant substrates remains significant. To assess the contribution of passaging to the changes in DNA methylation, we measured the DNA methylation levels of HUVECs cultured on glass slides prior to seeding on PA gels (Fig. 4). Additionally we added a glass slide condition at the 24 hour time point to isolate specifically the effects of passaging on DNA methylation levels (Fig. 4). Interestingly, our results demonstrate that DNA methylation levels are significantly higher after passaging onto all 3 conditions compared to the HUVECs cultured on glass slides before passaging (Fig. 4). Altogether, these results indicate that DNA methylation levels may be responsive to substrate stiffness within 24 hours of exposure and that the process of passaging cells increases DNA methylation levels.

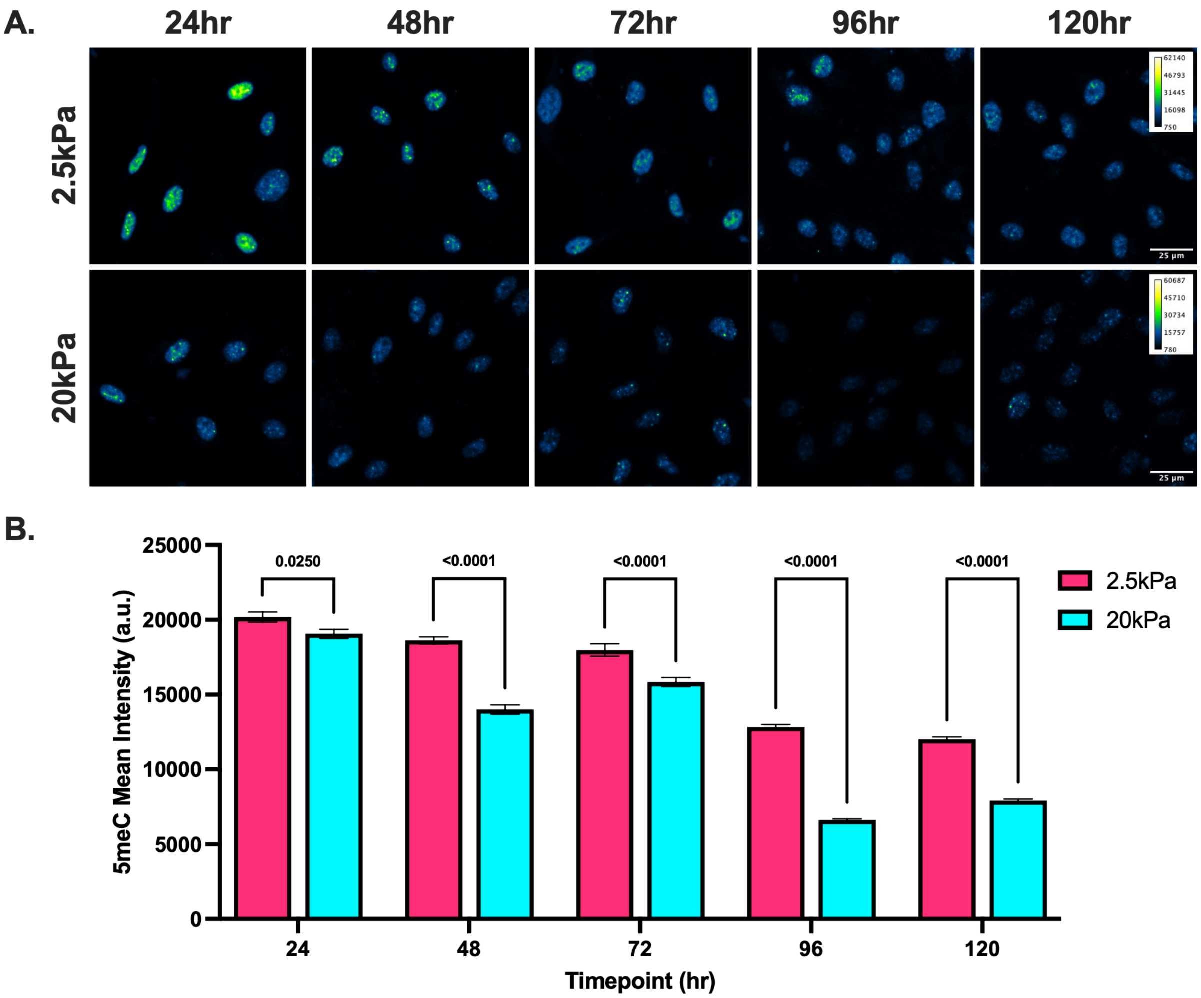

Figure 4.3. DNA methylation over time. (**A**) Representative 5-methylcytosine immunofluorescent staining of HUVECs cultured on PA gels over 5 days and (**B**) quantification of fluorescent intensity. Two-way ANOVA. N = 4-7, n=523-2039;

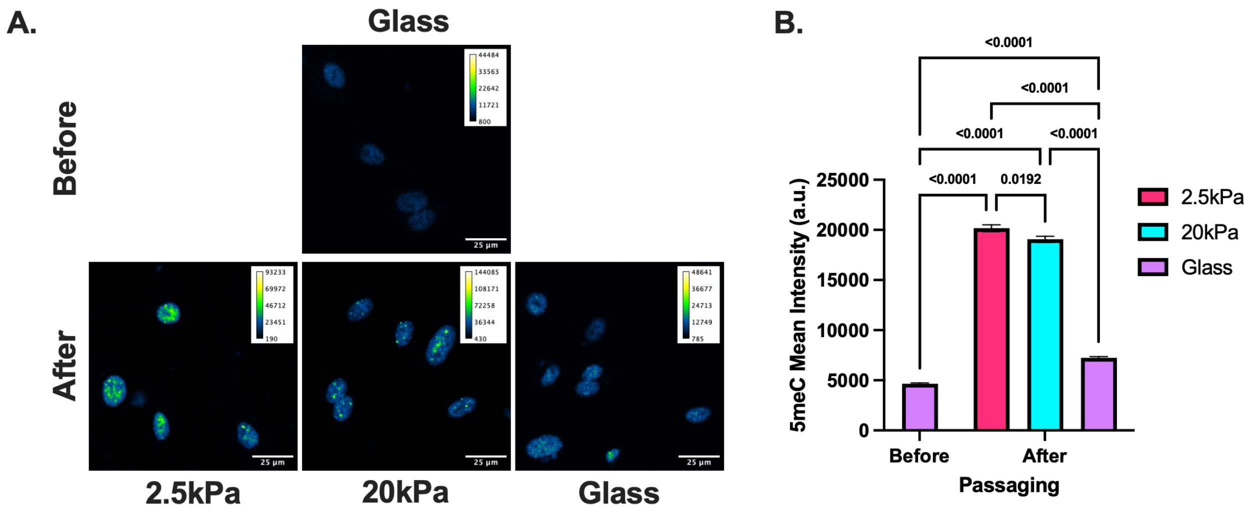

Figure 4.4. DNA methylation before and after passaging. (**A**) Representative 5-methylcytosine immunofluorescent staining of HUVECs seeded on PA gels or glass slides before or after passaging and (**B**) quantification of fluorescent intensity. Two-way ANOVA. N = 3-6, n=339-596;

4.4 Discussion

Here, we demonstrate that global DNA methylation in endothelial cells is responsive to substrate stiffness. Specifically our data indicates increased substrate stiffness decreases global DNA methylation levels. Additionally, we show that levels of DNMT1, an enzyme responsible for methylating DNA, are congruent with global DNA methylation levels. Finally, our data suggests this difference in global DNA methylation level is evident as early as 24 hours of exposure to substrates of varying stiffness and global DNA methylation levels decrease over time on both substrate stiffnesses while maintaining a significant different compared to each other.

Recent studies investigating the effects matrix stiffness on DNA methylation have reported mixed results [234–238]. Two have demonstrated that increased substrate stiffness has no significant effect on global DNA methylation levels [235,237], while one group has shown significant decreases [234] and two groups have shown significant increases [236,238]. Other groups have focused on the methylation of a single promoter region in the genome, where some have demonstrated that increased substrate stiffness is associated with decreases in DNA methylation in a specific promoter region [239–241] while others have demonstrated a significant increase [242]. Interestingly, our work examines global DNA methylation levels (Fig. 1) and is in alignment with Xie et al. who show vascular smooth muscle cells decrease global DNA methylation on stiffer substrates [234]. There are several possibilities as to the discrepancy in the literature regarding the relationship between substrate stiffness and DNA methylation, including cell-type specific mechanisms. The studies cited above include the use of smooth muscle cells, various cancer cells, stem cells, epithelial cells, chondrocytes, and fibroblasts [234–242]. Different cell types vary not only in their compositions but in their functions. As such, much work has revealed the different ways in which different cell types respond to matrix stiffness [243,244]. Thus, the differential change in global DNA methylation in response to substrate stiffness may be tied to the particular cell behaviors and internal mechanisms in each cell type. Furthermore, the range of stiffnesses used varies between studies. This is likely due to the particular context in which the cells were studied. We selected 2.5kPa and 20kPa to reflect the range of stiffnesses observed in the breast tumor microenvironment[233]. The mechanical properties of different tissues and pathologies vary and likely contribute to the selection of stiffnesses used in the studies [87]. Furthermore, cellular responses to stiffness may be non-linear [87] and biphasic [245–247]. Thus this suggests a limitation on extrapolating mechanoresponsive observations to different mechanical settings.

To investigate potential mechanisms underlying stiffness-mediated DNA methylation, we measured the RNA abundance to estimate the expression of the several key enzymes involved in DNA methylation. After culture on PA gels for 5 days, we measured the RNA abundance of several enzymes involved in methylating [248–250] and de-methylating DNA [251], and found DNMT1 significantly downregulated on stiffer substrates (Fig. 2). DNMT1 is a member of the DNA methyltransferase family of enzymes which can methylate DNA [248,249]. Interestingly, DNMT1 is particularly involved in the maintenance of DNA methylation patterns through cell divisions [248–250], whereas its other family members DNMT3a and DNMT3b can carry out *de novo* methylation [248,249]. Our data demonstrates that changes in DNA methylation occur as early as 24 hours after seeding (Fig. 3). As HUVECs have doubling times of approximately 36 hours [252], this stiffness-mediated DNA methylation may not be completely induced by

DNMT1, as decreased propagation of DNA methylation would only be evident after cell division. Thus, it is likely that decreased DNMT1 levels on stiffer substrates contribute to the lower levels of global DNA methylation.

Interestingly, our data demonstrates that DNA methylation levels prior to seeding on PA gels are significantly lower than after seeding on both 2,5kPa and 20kPa stiffness PA gels (Fig. 3B). Furthermore, our data demonstrates that simply passaging cells induces a significant increase in DNA methylation levels (Fig. 3B). Intriguingly, a group has recently demonstrated that once cancer cells detach from the ECM, they exhibit increased global DNA methylation levels [253]. However, in our data, the increase solely from passaging is significantly less than the passaging onto both PA gel conditions. These results suggest that passaging cells increases their DNA methylation levels but cannot explain the increase seen on PA gels or the significant difference between the 2 PA gel conditions. DNA methylation levels are a balance of 1. *de novo* methylation, 2. maintenance methylation, 3. replication-coupled passive methylation loss, and 4. active demethylation [254]. Since we observe differences in DNA methylation levels 24 hours after passaging, which is likely prior to the division of most of the cells, we suspect that the initial passage mediated DNA methylation changes may occur due to either *de novo* methylation or active demethylation. The exact mechanisms remain to be elucidated.

Although our time series data demonstrates that differences in DNA methylation between stiff and compliant conditions persist over a 5-day period, the levels in both conditions appear to decrease over time (Fig. 3). As noted above, we observed a subtle but significant increase in DNA methylation after passaging HUVECs and this is congruent with another observation by Nur et al. 2022 that cancer cells exhibit higher levels of global DNA methylation after detachment from the matrix [253]. Thus, it is possible that this anchorage dependent phenomena may be reversible after restoration of adhesion contacts. However, this likely can only attribute to a portion of the decrease, as DNA methylation levels are significantly higher after passage from glass onto PA gels compared to passage from glass onto glass. Another factor to consider is the confluence of the cell cultures. In this study, cells were first seeded at a sub-confluent level and allowed to grow to confluence over the 5 days. As endothelial cells undergo internal changes as they reach confluence, such as VE-cadherin phosphorylation [255], Weibel-

Palade body formation[256], and cell cycle withdrawal [257], another effect may be due to the cellular changes that occur during progression from sub-confluent to confluent monolayers.

Our work may be of interest to the field studying mechanical memory. Cells may be exposed to numerous mechanical forces and environments during development and disease [258]. For example, during metastasis, a cancer cells may traverse a heterogeneous primary tumor environment and to a secondary location [103,259]. Additionally, tumors can progressively stiffen over time which exposes all cells residing in the tumor to more mechanical forces [136]. Tumor angiogenesis entails the recruitment of vascular cells from surrounding healthy tissue into the tumor, in which the tumor tissue is typically stiffer than the healthy tissue counterpart [85]. Furthermore, time to initial cancer treatment in the United States after diagnosis ranges between 0 and 50 days [260]. As many drugs in development are targeting tissue stiffening, it will be important to understand how cells will respond to new mechanical properties or mechanical signaling after initiation of drug treatment [90]. Importantly, epigenetic regulation has been demonstrated to play a key role in mechanical memory. Particularly, nuclear deformation and actomyosin contractility can induce epigenetic effects such as histone acetylation, histone methylation, and DNA methylation [261]. Our work indicates that global DNA methylation levels are significantly altered by substrate stiffness and the effects emerge after 24 hours and persist at least 120 hours. Importantly, this demonstrates that substrate mechanics can induce epigenetic effects. As the majority of cell culture platforms vary from the mechanical environment of primary tissue, our work highlights the important need to consider mechanical properties of cell culture platforms to ensure *in vitro* results faithfully recapitulate *in vivo* phenomena. Future work should address the particular loci where methylation events occur due to differences in effects based on the particular location of DNA methylation [262]. Furthermore, links between altered DNA methylation states and functional consequences in gene expression or cell behavior remain a prime area of interest due to the development and implication of drugs targeting DNA methylation and other epigenetic marks [263].

4.5 Methods

4.5.1 Cell culture

Human Umbilical Vein Endothelial cells (HUVECs) were purchased from Lonza [Lonza; C2519A]. HUVECs were maintained in Endothelial Cell Growth Medium-2 BulletKits (EGM-2) [Lonza; CC-3162] with 1% penicillin-streptomycin [Gibco; 15140122] and HUVECs cultured on PA gels or glass slides were cultured in M199 medium [Gibco; 11150067] supplemented with Endothelial Cell Growth Medium SingleQuots Supplements [CC-4133] and 1% penicillin-streptomycin. HUVECs were maintained at 37C and 5% CO2 incubators and utilized up to passage 5 for all experiments.

4.5.1 Polyacrylamide gel preparation

Polyacrylamide gels (PA gels) were fabricated as previously described. In brief, glass slides were activated by plasma treatment [Harrick Plasma; Plasma Cleaner PDC-001] for 2 minutes, incubated in 1% polyethyleneimine [Sigma-Aldrich; P3143] for 10 minutes, washed 3 times in DI water, incubated in 0.1% glutaraldehyde [Sigma-Aldrich; G7776] in phosphate buffered saline without calcium or magnesium (PBS) [Gibco; 14200166 (10X stock)], washed 3 times in DI water, and allowed to air dry overnight. To generate PA gels of varying stiffness, the ratio of acrylamide [BioRad; 1610140] to bis-acrylamide [BioRad; 1610142] was varied in solution containing 70mM HEPES pH6 and 0.1% v/v TEMED. For 2.5kPa and 20kPa PA gels, the ratio of acrylamide to bis-acrylamide was 5%:0.1% and 12%:0.19%, respectively. The pH of the PA gel mixes were adjusted to pH6 using 2M HCl and degassed prior to polymerization with 10% ammonium persulfate [BioRad; 1610700]. The gels were functionalized with N-6-((acryloyl)amido)hexanoic acid (N6) (synthesized by lab) to allow covalent attachment of 0.1mg/ml rat tail type I collagen [Corning; 354236] in 50mM HEPES pH8. Excess N6 was neutralized with 1:1000 ethanolamine in 50mM HEPES pH8. Polymerized gels were incubated in PBS supplemented with 4% penicillin-streptomycin overnight and exposed to UV light for 1 hour in a biosafety cabinet prior to cell seeding.

4.5.1 Immunohistochemistry

Prior to fixing, samples were briefly washed 2x with 1X PBS. Samples were fixed in 3.2% PFA in 1X PBS for 5 minutes at room temperature. After fixation, samples were washed 3X with 1X PBS, permeabilized in 0.1% Triton-X100 [JT Baker; X198-07 (Octyl Phenol Ethoxylate)] in 1X PBS for 5 minutes and then washed 3x with 0.02% tween 20 [Fisher Scientific; BP337-100 (Polysorbate 20)] in 1X PBS. For methylated cytosine antigen retrieval, samples were incubated in 2M HCl in PBS for 30 minutes at 37C. Directly after, samples were neutralized with 0.1M Tris-HCl pH8 for 5 minutes at room temperature. Samples were washed 3X in 0.02% tween 20 in 1X PBS and then placed in blocking solution for 1 hour at room temperature. Blocking solution was composed of 10% donkey serum [Sigma-Aldrich; S30-100ML] and 10% fetal bovine serum [Corning; 35010CV] in 0.02% tween 20 in 1X PBS. After blocking, samples were incubated with primary antibodies in blocking solution overnight at 4C. To measure DNA methylation, primary antibodies against 5-methylcytosine were used. OptimAb Anti-5-methylcytosine (33D3) [Eurogentec; BI-MECY-0100 (mouse)] was used at a dilution of 1:450 for staining HUVECs and recombinant anti-5methylcytosine (RM231) [Abcam; ab214727 (rabbit)] was used at a dilution of 1:450 for staining mouse tumor sections. After primary staining overnight, samples were washed 3x with 0.02% tween 20 in 1X PBS and placed in secondary antibodies and DAPI for 1 hour at room temperature. For secondary staining 1:100 dilution of donkey anti-mouse secondary antibodies were used and 1:300 dilution of DAPI was used. After secondary staining, samples were washed 2x with 0.02% tween 20 in 1X PBS and 2x in 1X PBS before mounting on glass slides in vectashield antifade mounting medium [Vector Laboratories; H100010] and imaged on an LSM700 confocal microscope.

4.5.1 Confocal microscopy

Immunofluorescence stained samples were visualized using a Zeiss Axio Examiner.Z1 equipped with a LSM700 confocal module using a W Plan-Apochromat 20x/1.0 N.A. water immersion objective operated by Zen 2010 software. For each image, 3 z-stacks were captured at 3.785 micron intervals. Images were captured with a size of 1024x1024 pixels with a resolution of 3.1991 pixels per micron.

4.5.1 Image Analysis

Images were analyzed in Fiji (Fiji is just imageJ) with the aid of custom scripts. In brief, z-stacks were combined using SUM projections and a threshold was used on the channel containing signal from DNA methylation. Then the ‘analyze particles’ function was utilized to obtain ROI’s for every nucleus within the field of view. Quality control was performed manually to ensure debris or noise was not included as an ROI and mean intensities were measured for every ROI. Then a simple background subtraction was performed to obtain a mean fluorescent intensity.

4.5.1 DNA isolation and methyl-cytosine quantification

We utilized TRIZOL [Invitrogen; 155966026] to isolate genomic DNA followed by ethanol precipitation to obtain high purity genomic DNA. In brief, PA gels with HUVECs were turned over onto a droplet of TRIZOL and incubated at room temperature for 5 minutes. Then the PA gels were rinsed with the TRIZOL carefully by pipette and the TRIZOL solution containing the cell material was transferred into a microcentrifuge tube and allowed to incubate at room temperature for another 5 minutes. Then chloroform was added to the TRIZOL per manufacturer’s instructions (0.2mL chloroform for every 1mL TRIZOL) and vigorously shaken. Samples were centrifuged at 4C for 30 minutes at 12,000xg. The clear aqueous phase at the top was removed for subsequent RNA isolation. 100% ethanol was added to the remaining organic and interphase to precipitate the DNA. Samples were centrifuged at 4C for 5 minutes at 4000xg to pellet the DNA. The pellet was washed twice with 0.1M sodium citrate in 10% ethanol, pH 8.5 for 30 minutes. Then the pellet wash washed with 75% ethanol before allowing to dry and resuspended in 8mM NaOH. To clean up the DNA, we utilized ethanol precipitation as described previously. In brief, 2 volumes of ice-cold ethanol and 2mM ammonium acetate were added to the resuspended DNA and stored overnight at 4C. DNA was recovered by centrifugation at 4C at max speed for 10 minutes. Then the pellets were washed 2x in 70% ethanol and resuspended in 8mM NaOH. DNA concentration and purity was measured via nanodrop [Mettler Toledo; UV5 Nano]. To quantify methylcytosine levels in isolated genomic DNA, we utilized the Methylated DNA Quantification Kit (Fluorometric) [Abcam; ab117129] as per manufacturer's instructions.

4.5.1 RNA isolation

A combination of TRIZOL and RNeasy Micro Kits [Qiagen; 74004] were used to isolate RNA from HUVECs cultured on top of PA gels. In brief, the clear aqueous phase from the DNA isolation section above was added to 0.5mL of 70% ethanol and mixed by pipetting. This mixture was then applied to the RNeasy columns by centrifugation at 10,000xg for 30 seconds. The samples were washed with 0.7 mL of RW1 buffer followed by 2 washes with RPE buffer. Samples were centrifuged without any wash buffer to allow for drying and then eluted in 35 microliters of DNase-RNase free water. RNA concentration and purity was measured via nanodrop.

4.5.1 RT-qPCR

To perform reverse-transcription quantitative PCR, we utilized the iScript cDNA synthesis kits [BioRad; 1708890] and iQ SYBR green supermix [BioRad; 1708882] according to manufacturer's instructions. DNA oligo primers were ordered from Sigma Genosys through the Vanderbilt Molecular Biology Core. The following sequences were used for qPCR: DNMT1: fwd:GTCTGCTCCTGCGTGGAAG and rev: TTGGTGACGGTTGTGCTGAA. DNMT3a fwd: TCTTCGTTGGAGGAATGTGC and rev: AAAAGCACCTGCAGCAGTTG. DNMT3b fwd: AATAAGTCGAAGGTGCGTCG and rev: TTCATCCCCTCGGTCTTTGC. TET1 fwd: AATGGAAGCACTGTGGTTTG and rev: ACATGGAGCTGCTCATCTTG. TET2: GTGAGATCACTCACCCATCG and rev: CAGCATCATCAGCATCACAG. B2M: CACCCCCACTGAAAAAGATGAG and rev: CCTCCATGATGCTGCTTACATG. B2M served as housekeeping control gene. Samples were run on a Biorad thermocycler [CFX96 Real-Time System] and analyzed via the Biorad CFX Maestro Software.

4.5.1 Statistical analysis

Statistical analysis was performed using GraphPad Prism 9.0 [GraphPad Software; La Jolla, CA, USA]. The non-parametric unpaired Mann-Whitney test was performed on image analysis results from immunofluorescence staining of DNA methylation. Unpaired two-tailed t-tests with Welch's correction were performed on ELISA and qPCR results. An ordinary two-way ANOVA with Sidak's multiple comparison test was performed on timeseries methylation data. 'N' represents the number of independent biological replicates and 'n' represents the number of measurements made.

4.6 Acknowledgments

PVT was funded by an NIH F31 Predoctoral Fellowship (F31HL154727).

Chapter 5:

Assessment of transcriptomic networks underlying highly and weakly migratory cancer cell subpopulations

Paul V. Taufalele*, Ismael Ortiz*, Victor Dunagan, Lauren A. Hapach, Jing Wang, Qiu Liu, and Cynthia A. Reinhart-King

This chapter is in preparation for submission and has been reproduced with the permission of my co-authors. This work was completed in collaboration with co-first author Ismael Ortiz.

5.1 Abstract

Cancer cells can exhibit phenotypic heterogeneity even within the same tumor. Cell migration is a hallmark of cancer and a requirement for metastasis to occur. To investigate molecular underpinnings of heterogeneity in cancer cell migration phenotype, highly and weakly migratory subpopulations were transcriptionally profiled across 5 different cancer cell lines. Interestingly, we found significant but inconsistent differences in morphologies between highly and weakly migratory subpopulations within the same cancer cell line. While only a single gene was observed to be significantly upregulated in all 5 highly migratory subpopulations, many GO terms were significantly enriched across all 5 cell lines. Moreover, many of the common GO terms were enriched for by cell specific gene signatures, suggesting the cells utilize similar biological processes through cell specific pathways. Furthermore, TEAD4 activity was predicted to be a potential upstream regulator in highly migratory subpopulations and increased TEAD4 nuclear-to-cytosolic ratio was observed in 4 out of the 5 highly migratory subpopulations. While increased levels of EVA1A were observed in tumor tissue compared to normal tissue, correlation to survival outcomes was cancer type dependent. Altogether, our results demonstrate that there are few commonly upregulated genes across all cancer cell lines but GO-term and

upstream regulator prediction analysis indicate that numerous biological processes and pathways are being shared. Thus future biomarkers based on gene expression may require cancer specific panels to predict cancer phenotypes.

5.2 Introduction

Cancer metastasis is a complex process whereby cells from a primary tumor relocate to a new region in the body. Cell migration is a fundamental cell behavior and is exploited by cancer cells during the process of metastasis [264]. As such, cell migration is recognized as a hallmark of cancer and has been at the forefront of cancer biology [13,265,266]. Importantly, there are numerous contexts and modes of migration a cancer cell. Collective migration refers to the coordinated movement of a collection of cells which are connected through cell-cell contacts [267]. Single cell migration refers to the migration of an individual cell free of cell-cell contacts [268]. Interestingly, there are numerous phenotypes associated with single cell migration based on morphology and cell markers. The epithelial-to-mesenchymal transition (EMT) refers to a process by which cells transition into a de-differentiated phenotype characterized by loss of cell-cell contacts and enhanced migratory and invasive behaviors [17]. As most solid tumors are epithelial, the EMT phenotype is a critical concept in cancer cell migration [17]. Additionally, single cancer cells may adopt an ameboid migratory phenotype characterized by protease independent movement through mechanically displacing matrix fibrils and an ameboid-like cell shape [269]. Interestingly, there have been several genes associated with the different migratory phenotypes and establishing additional markers for these migratory phenotypes remains an important task [17,270].

Heterogeneity is another established feature of cancer that exists among many dimensions. For example, there is inter and intra tumoural heterogeneity. Inter tumoural heterogeneity refers to the variation between different tumors while intra tumoural heterogeneity refers to the variation observed within a single tumor. The intra tumoural heterogeneity may refer to variance observed between individual tumor cells and may occur spatially and temporally [271]. This intratumoral heterogeneity is observed at numerous levels including genetics, epigenetics, and the tumor microenvironment [272]. The sources of heterogeneity include cancer stem cells, phenotypic plasticity, and clonal evolution [273]. Importantly, tumor heterogeneity may have profound implications in developing and utilizing cancer therapies. Recent work has shown that higher levels of intratumoral heterogeneity are linked with worse clinical outcomes [271]. Furthermore, several targeted therapeutics exhibit significant clinical improvements compared to previous treatments but not every molecularly selected patient responds [274]. For example, addition of a specific PIK3CA inhibitor to a luminal breast cancer treatment regimen improved response rates from 12.6% to 26.6% and a combination of BRAF/MEK inhibitors and monoclonal antibodies against EGFR utilized in metastatic colon cancer patients with BRAF-V600E mutation improved response rates from 2% to 26% [274]. Thus investigating tumor heterogeneity is critical to understand why some patients respond and others do not.

To identify additional markers of cell migration, numerous groups have utilized large library genomic screens in combination with high throughput migration assays. The majority of these studies have utilized either a genome wide or curated RNA interference screening assays followed by high throughput migration assays to determine how knock-out of particular genes affect migration [275–284]. However, there are some studies that transfect cells with cDNA to induce expression of a curated list of genes to determine how overexpression of particular genes affect migration [285,286]. The strength of these types of genetic and functional screens lies in their alignment with functional translation. Specifically for a marker to be functional, targeting the marker must afford a degree of controllability. Essentially, genetic modulation of marker expression must have a functional consequence on cell migration. Thus, these genetic screens identify genes that afford a degree of controllability. However, cancer cells exhibit a high degree of heterogeneity and particularly in their migratory abilities. For example, we have previously demonstrated that there exist highly and weakly migratory subpopulations within cancer cell lines [287]. Thus, we utilized a migratory sorting technique to obtain highly and weakly migratory cancer cell subpopulations followed by RNA sequencing to gain further insight into heterogeneity affecting cancer cell migration ability.

Here we subjected 5 cancer cell lines to a transwell sorting procedure to obtain highly and weakly migratory subpopulations. To investigate molecular underpinnings to the highly migratory phenotypic subpopulations, we performed bulk RNA sequencing and differential expression analysis to determine genes and pathways associated with either phenotype. Interestingly we found a single gene, EVA1A, upregulated in all 5 highly migratory subpopulations. Gene ontology analysis revealed numerous biological processes regulated in all 5 cell lines despite substantial heterogeneity in underlying gene expression profiles. Additionally, TEAD4 was predicted to be an activated upstream regulator in all highly migratory subpopulations and immunostaining confirmed elevated TEAD4 activity in 4 out of 5 highly migratory subpopulations. Altogether, this work highlights the extent of transcriptional heterogeneity underlying migratory cancer phenotypes.

5.3 Methods

5.3.1 Cell Culture

A375 [ATCC; CRL-1619], MDA-MB-231 cells [ATCC; HTB-26], MCF10CA1a cells [Barbara Ann Karmanos Cancer Institute, Detroit, MI], SUM159PT cells (BioIVT; HUMANSUM-0003006), and SW480 [ATCC; CCL-228] cultured according to manufacturer's instruction at 37°C and 5% CO_2.

5.3.2 Transwell sorting assay

Selected cell lines MDA-MB-231 (ATCC, Catalog No. HTB-26), MCF10CA1a (Barbara Ann Karmanos Cancer Institute, Detroit, MI) , SUM159PT (BioIVT) were sorted in Hapach et al. SW480 (ATCC, Catalog No. CCL-228), A375 (ATCC, Catalog No. CRL-1619) cell lines were sorted utilizing consecutive transwell assays. Desired cell populations were seeded on an 8 μm pore transwell (Corning) with a 1mg/mL collagen gel with an approximate thickness of 10 μm. Cells were supplied with DMEM + 0.5% FBS and placed into a 6-well plate containing DMEM + 10% FBS. After 2 days of culture the top reservoir was refreshed. On day 4 of culture, the mediums were collected, cells were washed with PBS and trypsonized with 0.25% Trypsin-EDTA. Cells that migrated through were collected and reseeded as were cells that did not migrate through the transwell. Consecutive transwell assays were conducted to collect the migratory cells from the initial migratory population and the non-migratory cells from the non-migratory cell population. After the invasive fraction plateaued at 25 sorts we collected the final cells, giving us a Highly Migratory and Weakly Migratory subpopulation for each desired cell line.

5.3.3 RNA isolation

Prior to bulk RNA sequencing, cells were cultured in tissue culture plastic 6-well plates. To isolate RNA, we utilized the QIAshredder [Qiagen; 79656] and RNeasy Micro kits [Qiagen; 74004] with the on-column DNase I digest [Qiagen; 79254]. In brief, buffer RLT, buffer RPE, and DNase I stock solution were prepared according to manufacturing instructions prior to RNA isolation. Cells were disrupted by adding 350 µL of Buffer RLT directly onto the cells in the well. The cells in Buffer RLT were then homogenized by adding the lysate directly to the QIAshredder spin column and centrifugation at max speed for 2 minutes. Then 350 µL of 70% ethanol was added to the lysate and applied directly to the RNeasy MinElute spin column. Then the samples were centrifuged at 10,000 x g for 15 seconds to bind the sample to the spin column. The samples were washed with 350 µL of Buffer RW1 and centrifuged at 10,000 x g for 15 seconds. To digest genomic DNA, 10 µL of DNase I stock solution in 70 µL Buffer RDD was added directly to each spin column and allowed to incubate for 15 minutes at room temperature. Then samples were washed with 350 µL Buffer RW1 and 500 µL Buffer RPE, centrifuging at 10,000 x g for 15 seconds for each wash. Then a final wash with 500 µL Buffer RPE was performed at 10,000 x g for 2 minutes followed by centrifugation at 10,000 x g for 1 minute with a new empty collection tube. To elute the RNA, 35 µL of RNase free water was added directly to the spin column and allowed to incubate at room temperature for 1 minute prior to centrifugation at max speed. RNA concentrations and purity were measured via Nanodrop instrument [Mettler Toledo; UV5 Nano] and RNA with 260/280 values > 1.7 were proceeded with for bulk RNA sequencing.

5.3.4 Bulk RNA sequencing

RNA samples were submitted to the VANTAGE core facility at Vanderbilt University for bulk RNA sequencing. The VANTAGE core facility provided RNA quality control, stranded mRNA library preparation, and sequencing on the Illumina NovaSeq6000. Samples were utilized with an RNA integrity number equivalent (RINe) greater than 8. RNASeq libraries were prepared using 500 ng of total RNA and the NEBNext® Ultra™ II RNA Library Prep [NEB, Cat: E7765S] per manufacturer's instructions, with mRNA enriched via poly-A-selection using oligoDT beads. The RNA was then thermally fragmented and converted to cDNA, adenylated for adaptor ligation and PCR amplified. The libraries were sequenced using the NovaSeq 6000 with 150 bp paired end reads. RTA [version 2.4.11; Illumina] was used for base calling and analysis was completed using MultiQC v1.7.

5.3.5 Bioinformatics

RNA-Seq reads were aligned to hg19 using STAR [PMID: 23104886] and quantified by featureCounts [PMID: 24227677]. Differential analysis was performed by DESeq2 [PMID: 25516281]. FDR < 0.05 and |log2FoldChange|>1 were used to identify significantly changed genes. To get the gene sets that significantly enriched in the differentially expressed genes between highly migratory subpopulations of cancer cells compared to their weakly migratory counterparts, Gene Set Enrichment Analysis (GSEA) was run on MSigDB gene sets of hallmark, curated gene set, regulatory target gene sets, ontology gene sets, and oncogenic signature gene sets (Subramanian, Tamayo, et al. (2005, PNAS) and Mootha, Lindgren, et al. (2003, Nature Genetics)). For survival clinical features, logrank test in univariate Cox regression analysis with proportional hazards model (Andersen and Gill 1982) was used to estimate the P values comparing high and low expression groups using the 'coxph' function in R. Kaplan-Meier survival curves were plotted using high [median, maximum] and low expression [minimum, median] groups. We used the 'Benjamini and Hochberg' method of 'p.adjust' function in R to convert p-values into FDRs. The 'upstream regulator' tool was used from the Qiagen IPA software package.

5.3.6 Transcription factor prediction

To identify transcription factors that may regulate all 3 genes found to be significantly upregulated in all 5 highly migratory subpopulations, we utilized the hTFtarget online resource found at http://bioinfo.life.hust.edu.cn/hTFtarget. EVA1A, GGT5, and TM4SF18 were input into the 'Co-regulation' function and all transcription factors with potential to regulate at least 2 of the 3 genes were retained. Qiagen Ingenuity Pathway Analysis software (IPA, Qiagen, Redwood City, CA, USA) was utilized to predict potential upstream regulators based on differential gene expression data.

5.3.7 Quantitative polymerase chain reaction (qPCR)

Previously isolated RNA was converted to cDNA via the first-strand iScript cDNA synthesis kit [Biorad; 1708890]. qPCR was performed using the iQ SYBR Green Supermix [Biorad; 1708880]. The following sequences were used for qPCR: EVA1A: fwd: AGATGGCTTTGCTCAGCAACA and rev: GATGCACACGCCAGAAACAA.

5.3.8 TEAD4 immunostaining

Cells were seeded overnight on an activated coverslip and cultured in complete medium. Next day they were rinsed with PBS and exposed to PFA for 10 minutes. After 2 five-minute PBS washes the cells were permeabilized with Triton for 10 minutes. Then 3 five-minute washes were performed with 0.02% Tween before blocking with a 3% BSA solution for 1 hour. Finally, the rabbit-anti-TEAD4 primary antibody (abcam AB155244) was added at a concentration of 1:100 overnight. 3 five-minute washes with a 1% BSA solution. Cells were stained with secondary antibodies AF488 phalloidin (1:500) AF568 donkey-anti-rabbit (1:250) and DAPI (1:500) for one hour at room temperature in the dark. Cells were washed 3 times for 5 minutes with 0.02% Tween.

5.4 Results

5.4.1 Repeated application of transwell migration assay enables the capture of cancer cell subpopulations with heterogeneous migration ability

To investigate the transcriptional landscapes underlying highly migratory cancer cell phenotypes, we utilized a previously described repetitive transwell sorting assay (**Fig. 1A)** [287]. The breast cancer cell lines MCF10CA1a, MDA-MB-231, and SUM159-PT were previously sorted [287]. The melanoma cancer cell line A375 and the colorectal cancer cell line SW480 were additionally subjected to the transwell sorting assay. Prior to subsequent experimentation, subpopulations from all 5 cell lines were subjected to a transwell invasion assay to confirm differences in migratory behavior. Our results indicate that we successfully obtained highly migratory (HM) subpopulations with invasive fractions greater than 0.4 and (WM) weakly migratory subpopulations with invasive fractions less than 0.2 from all 5 cancer cell lines (**Fig. 1B)**.

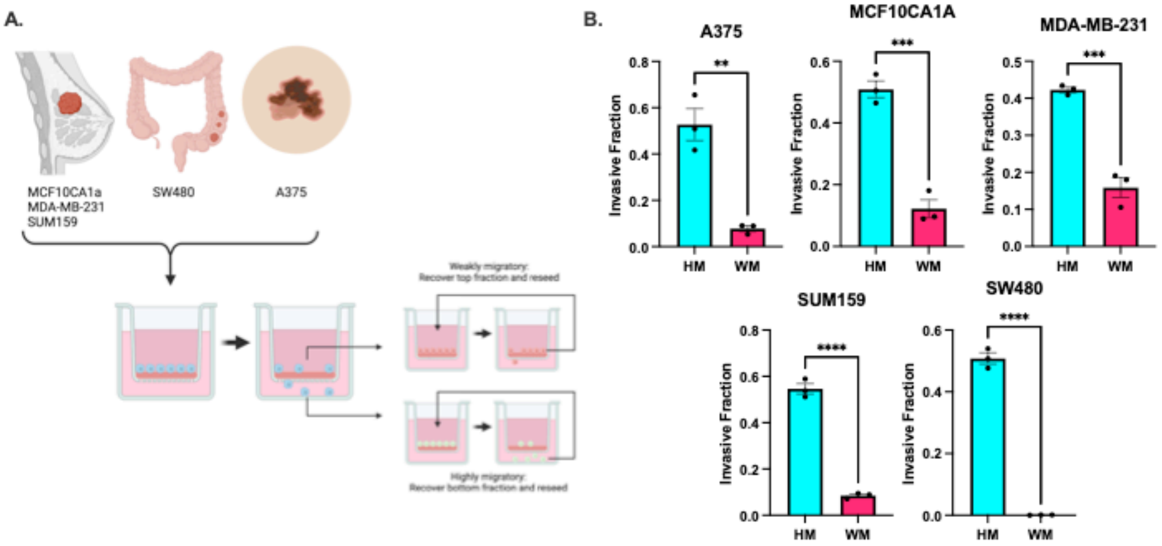

Figure 5.1. Repetitive transwell sorting overview. (**A**) Schematic depicting repetitive transwell sorting assay procedure. (**B**) Quantification of invasive fractions for HM and WM subpopulations. This data for panel (B) in this figure was generated by co-first author Ismael Ortiz.

5.4.2 Differences in cell morphology between highly and weakly migratory subpopulations vary among the 5 cell lines

Cell migration is tightly connected to cell morphology and the cytoskeleton [277]. To determine if cell morphology broadly reflects migratory phenotype, we compared the cell area and aspect ratio between HM and WM subpopulations. Interestingly, there were no consistent trends among the 5 cancer cell lines. The HM subpopulations were significantly larger in the A375, MCF10a-CA1a, SUM159, and SW480 cell lines while the WM subpopulations were significantly larger in the MDA-MB-231 cell line (**Fig. 2A)**. The HM subpopulations had significantly increased aspect ratios relative to WM subpopulations in the MCF10a-CA1a, MDA-MB-231, and SW480 cell lines while the opposite was true for the A375 cell line and there was no significant trend observed in the SUM159 cell line. Our data indicates that cell morphology is not a reliable predictor of migratory phenotype in our system. Notably, there is morphological variation even within the 3 breast cancer cell lines.

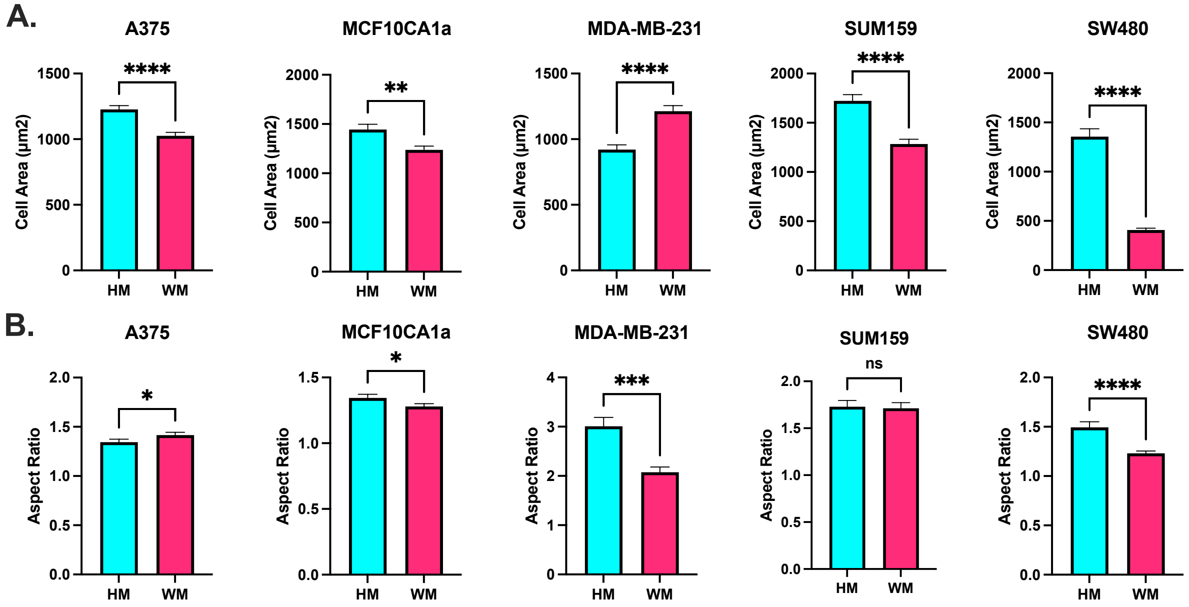

Figure 5.2. Morphological differences between HM and WM subpopulations. Quantification of cell area (**A**) and aspect ratio (**B**) for HM and WM subpopulations. This data in this figure was generated by co-first author Ismael Ortiz.

5.4.3 Bulk RNA sequencing reveals numerous transcriptional differences between highly and weakly migratory subpopulations across all 5 cell lines

To determine if there are common transcriptomic changes underlying migratory phenotypes, we conducted bulk RNA sequencing on the HM and WM subpopulations for all 5 cell lines. Comparing the gene expression between HM and WM subpopulations within the same cell line revealed numerous significantly differentially expressed genes (**Fig. 3A)**. We detected approximately 1,000-1,800 differentially expressed transcripts in each cell line (**Fig. 3B)**. Interestingly, across all 5 cell lines, there were more significantly upregulated genes in the HM subpopulation relative to upregulated genes in the WM subpopulation (**Fig. 3B)**.

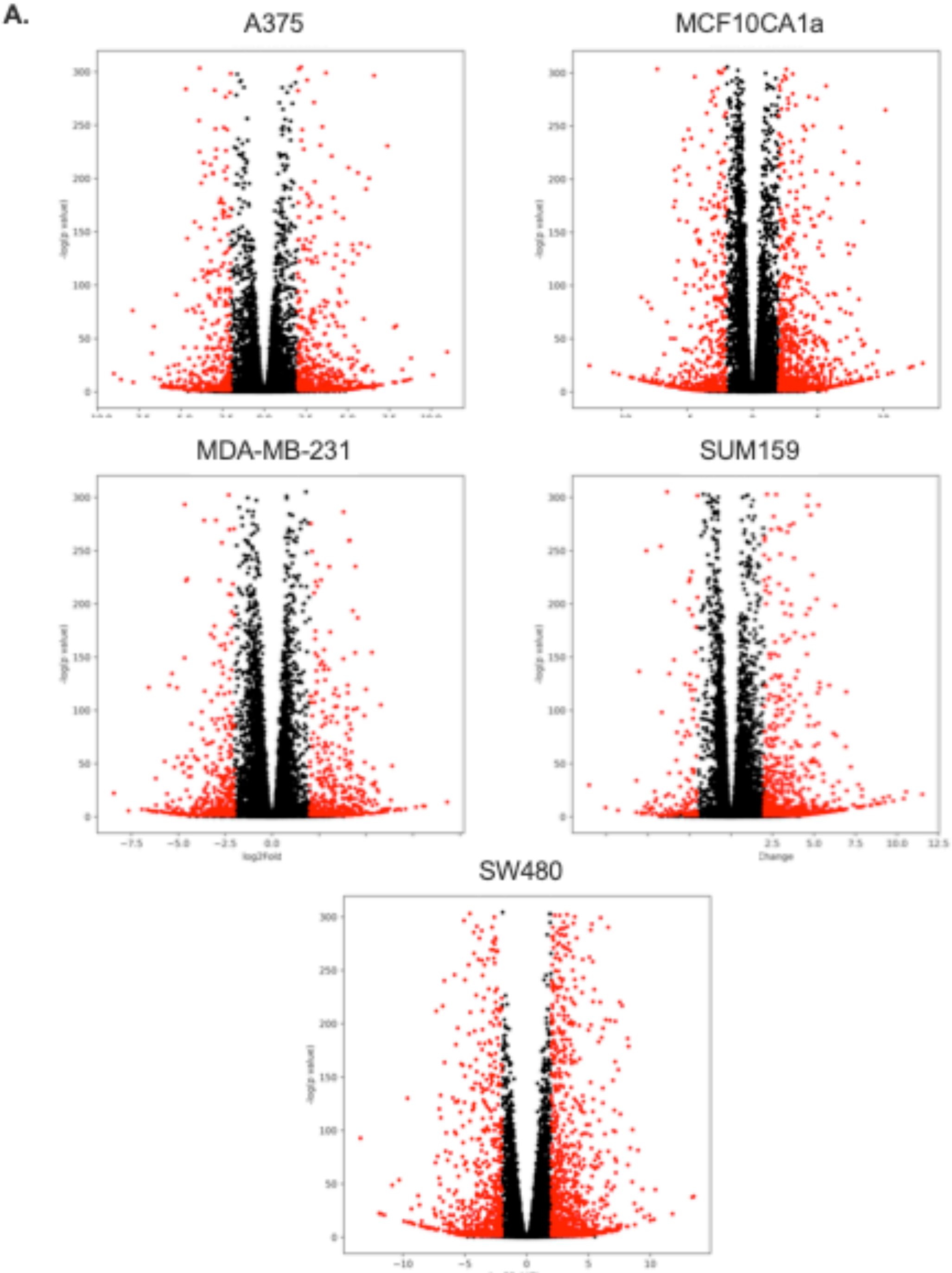

B.

Cell Line	Total SDE	Up in HM	Up in WM
A375	1017	606	411
MCF10CA1a	1578	1010	568
MDA-MB-231	1002	515	487
SUM159	1055	898	157
SW480	1848	1122	726

Figure 5.3. Bulk RNA sequencing reveals numerous transcriptional differences. (**A**) Volcano plots representing differentially expressed genes (red dots). (**B**) Summary of total number of genes significantly upregulated in each cell line and direction of upregulation.

To determine the relationship between different HM or WM subpopulations, we investigated shared genes upregulated in all the HM (**Fig. 4A**) or WM (**Fig. 4B**) subpopulations. Interestingly, there were only 3 genes that were upregulated in all 5 HM subpopulations (**Fig. 4A**) and 0 genes that were upregulated in all 5 WM subpopulations (**Fig. 4B**). Furthermore, the majority of differentially expressed genes were only detected in a single cell line (**Fig 4A,B**). The 3 upregulated genes detected in all 5 HM subpopulations included EVA1A, GGT5, and TM4SF18. Notably, the upregulation of EVA1A was confirmed via qPCR while GGT5 and TM4SF18 expression where not detected via qPCR. Altogether, this data suggests that there is significant heterogeneity in the transcriptional signatures associated with migratory phenotypes between cell types and only a single gene is associated with all 5 highly migratory subpopulations.

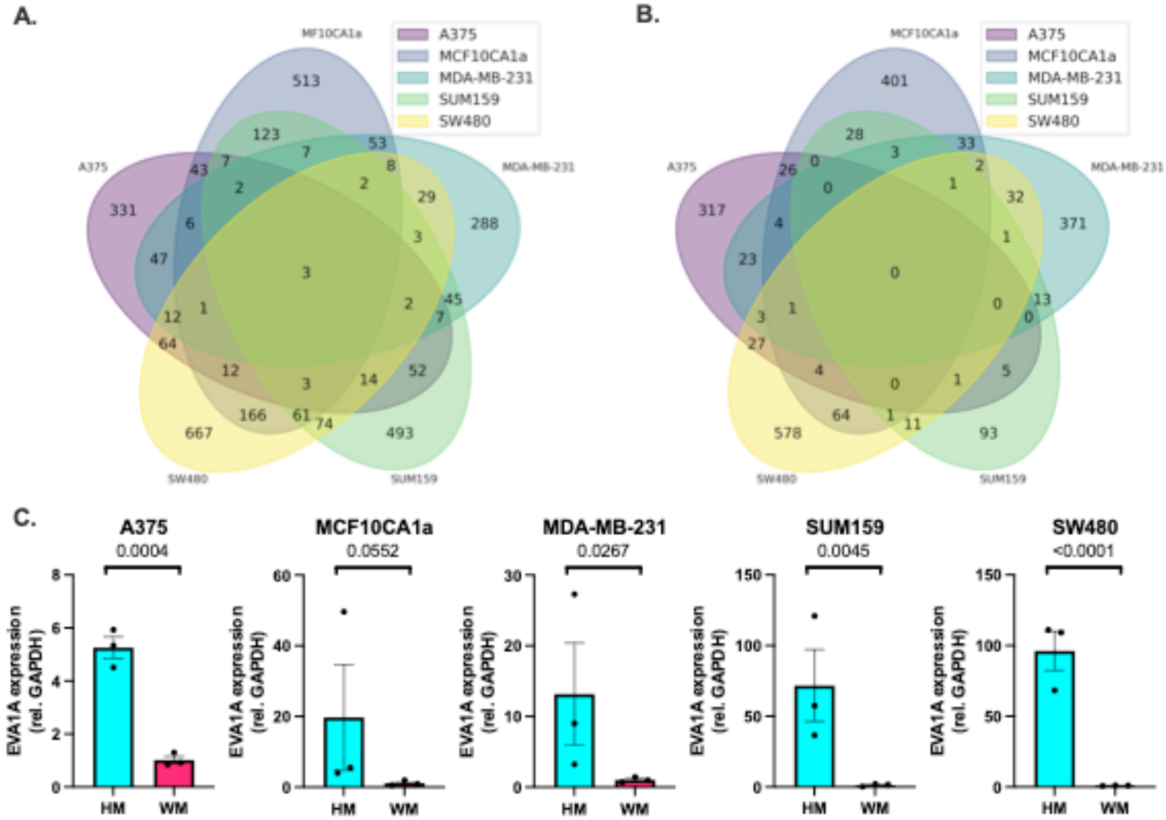

Figure 5.4. Shared differentially expressed genes across the 5 cell lines. Venn diagrams depicting number of significantly differentially expressed genes that are upregulated in the (**A**) HM and (**B**) WM subpopulations. (**C**) Quantification of EVA1A expression via qPCR. The data in panel (C) for this figure was generated by co-first author Ismael Ortiz.

5.4.4 Most highly migratory subpopulations display higher EMT score

Mesenchymal and ameboidal phenotypes are well described modes of migration associated with cancer cells [288,289]. Furthermore, recent work has detailed gene expression signatures associated with these phenotypes [270,290–293]. Thus we computed EMT and ameboid scores for each subpopulation utilizing previously described signatures [270,287]. Interestingly, 4 out of the 5 HM subpopulations had significantly higher EMT scores compared to their respective WM counterpart. There was no statistical difference between EMT scores in the HM and WM A375 subpopulations. The ameboid score revealed the HM subpopulation in the MCF10a-CA1a cells had significantly higher ameboid score relative to their WM counterpart. However, there was no significant difference detected in the ameboid scores for the remaining 4 cell lines. Importantly, our results demonstrate heterogeneity in migratory mode phenotypes derived from transcriptional scores among the 5 cell lines.

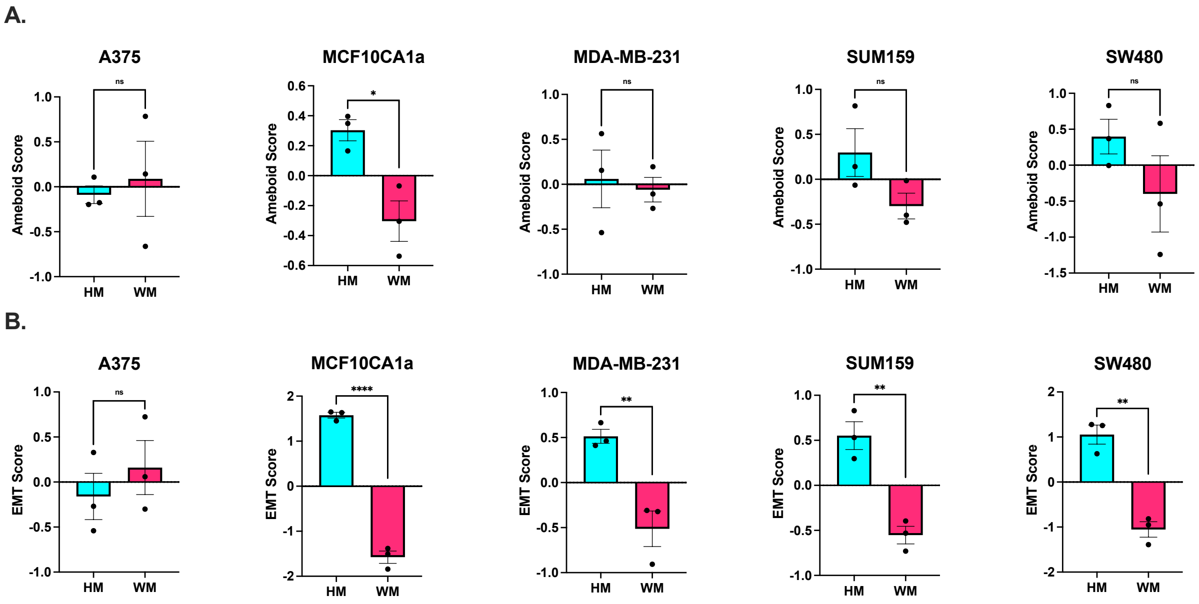

Figure 5.5. Migratory phenotype scores. Quantification of (**A**) ameboid and (**B**) EMT scores derived from RNA sequencing data.

5.4.5 Numerous biological processes are regulated across all 5 cell lines

As few universal upregulated transcripts existed amongst the subpopulations from the 5 cell lines, we sought to investigate if common biological processes were consistently upregulated in all of the subpopulations or consistently over-enriched in differentially expressed transcripts. Gene Set Enrichment Analysis (GSEA) revealed numerous biological processes significantly enriched in each of the subpopulations (**Fig. 6A,B**). However, there were 0 biological processes that were significantly enriched in all 5 HM or WM subpopulations (**Fig. 6A,B**). Over representation analysis revealed numerous significantly enriched biological processes between HM and WM subpopulations in each of the 5 cell lines (**Fig. 6C**). Interestingly, there were 90 biological processes that were significantly over-represented in all 5 cell lines (**Fig. 6C**). Furthermore, the number of shared biological processes was higher than any of the biological processes unique to a single cell line (**Fig. 6C**). This data suggests that while there are no biological processes enriched in all 5 HM or WM subpopulations, there are numerous biological processes that are potentially being regulated in all 5 cell lines between HM and WM subpopulations.

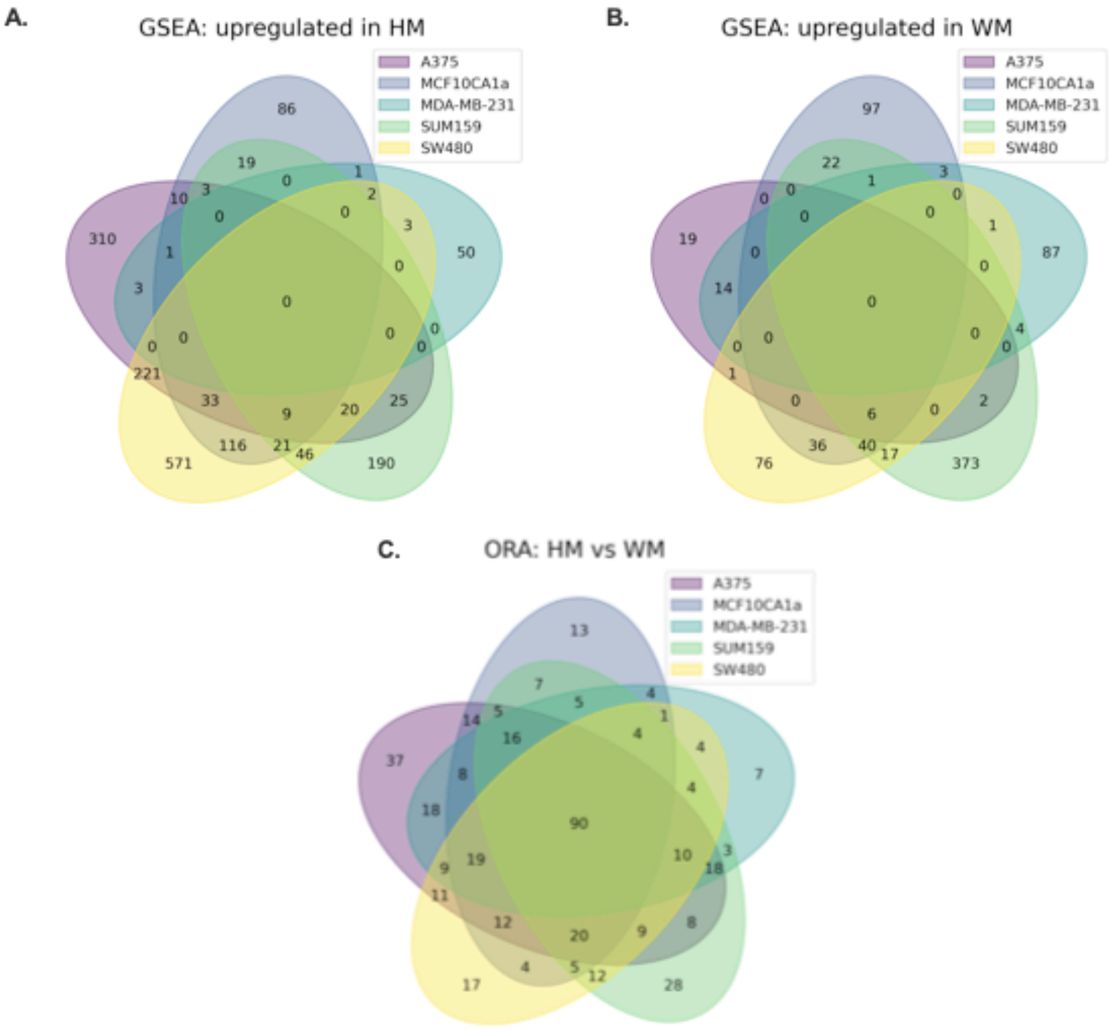

Figure 5.6. GO term ontology analysis. Venn diagram depicting significantly enriched GO terms detected via GSEA and upregulated in either (**A**) HM or (**B**) WM subpopulations. (**C**) Venn diagram depicting significantly enriched GO terms detected in all cell lines via over representation analysis.

To further investigate the shared biological processes, we defined a cell specific GO-term signature (**Fig. 7A**). The cell specific GO-term signatures comprise GO-terms that were found to be significantly over-represented in all 5 cell lines but were at least partly comprised by genes that were only significantly differentially expressed in a single cell line (**Fig. 7A**). We found numerous biological processes that had cell specific GO-term signatures such as positive regulation of cell motility, ameboidal-type cell migration, ERK1 and ERK2 cascade, and regulation of cell-cell adhesion (**Fig. 7B**). Altogether this data suggests that numerous biological processes are potentially regulated across all 5 cell lines despite distinct gene expression profiles.

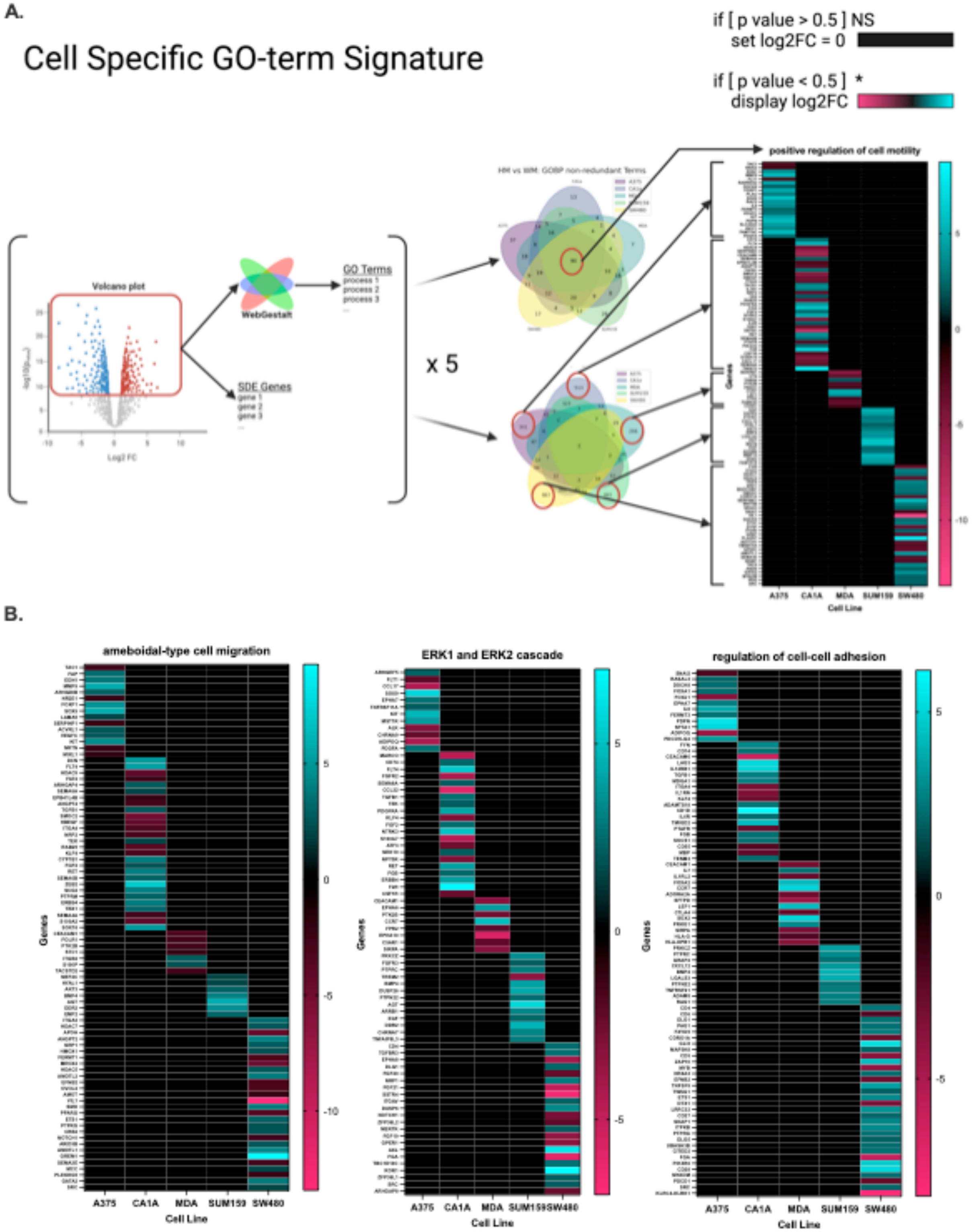
A.
Cell Specific GO-term Signature
if [p value > 0.5] NS
set log2FC = 0
if [p value < 0.5] *
display log2FC
Volcano plot
-log10(p_adj)
Log2 FC
WebGestalt
GO Terms
process 1
process 2
process 3
SDE Genes
gene 1
gene 2
gene 3
x 5
HM vs WM: GOBP non-redundant Terms
positive regulation of cell motility
Genes
A375
CA1A
MDA
SUM159
SW480
Cell Line
5
0
-5
-10
B.
ameboidal-type cell migration
Genes
A375
CA1A
MDA
SUM159
SW480
Cell Line
5
0
-5
-10
ERK1 and ERK2 cascade
Genes
A375
CA1A
MDA
SUM159SW480
Cell Line
5
0
-5
regulation of cell-cell adhesion
Genes
A375
CA1A
MDA
SUM159
SW480
Cell Line
5
0
-5

Figure 5.7. Cell specific GO-term signatures. (**A**) Overview schematic depicting cell specific GO-term signature derivation. (B) Representative heatmaps representing cell-specific GO-term signatures.

5.4.6 TEAD4 is a potential upstream regulator active in 4 out of 5 highly migratory subpopulations

Gene expression data can also be utilized to infer upstream regulators based on known causal interactions [294]. We utilized the Ingenuity Pathway Analysis software to determine if there are potential upstream regulators shared among all HM or WM subpopulations. Interestingly, we found numerous potential upstream regulators that were activated in all 5 HM subpopulations such as MRTFB, TGFB1, and TEAD4 (**Fig. 8**). Using the Database of Human Transcription Factor Targets (hTFtarget), we found further evidence supporting TEAD4 as a possible regulator of EVA1A (data not shown). Thus we sought to confirm upregulation of TEAD4 activity in the HM subpopulations. We measured the TEAD4 nuclear-to-cytosolic ratio via TEAD4 immunostaining and found that TEAD4 nuclear-to-cytosolic ratio was significantly higher in 4 of the 5 HM subpopulations relative to their WM counterpart (**Fig. 9**). There was no significant difference detected in the TEAD4 nuclear-to-cytosolic ratio in the A375 cell line. Our data suggests that increased TEAD4 activity may be a potential upstream regulator in 4 of the 5 HM subpopulations.

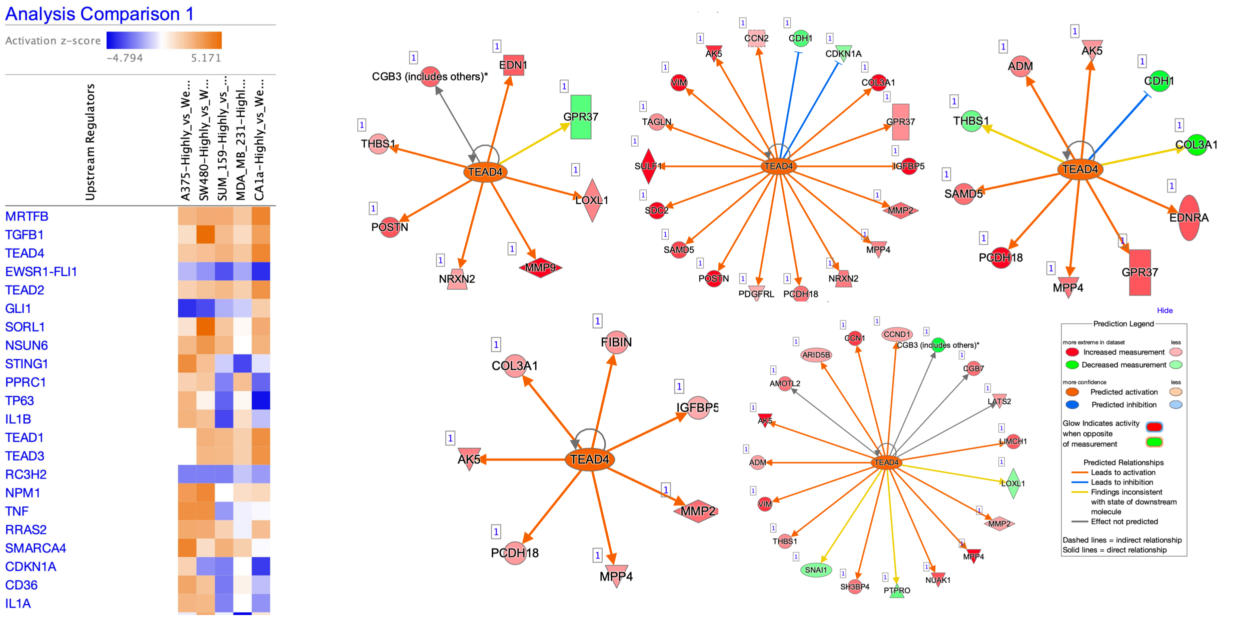

Figure 5.8. Qiagen IPA upstream regulator prediction. (**A**) Heatmap representing potential upstream regulators predicted via Qiagen IPA upstream regulator analysis. (B) Genes significantly contributing to detection of upstream regulators in each cell line.

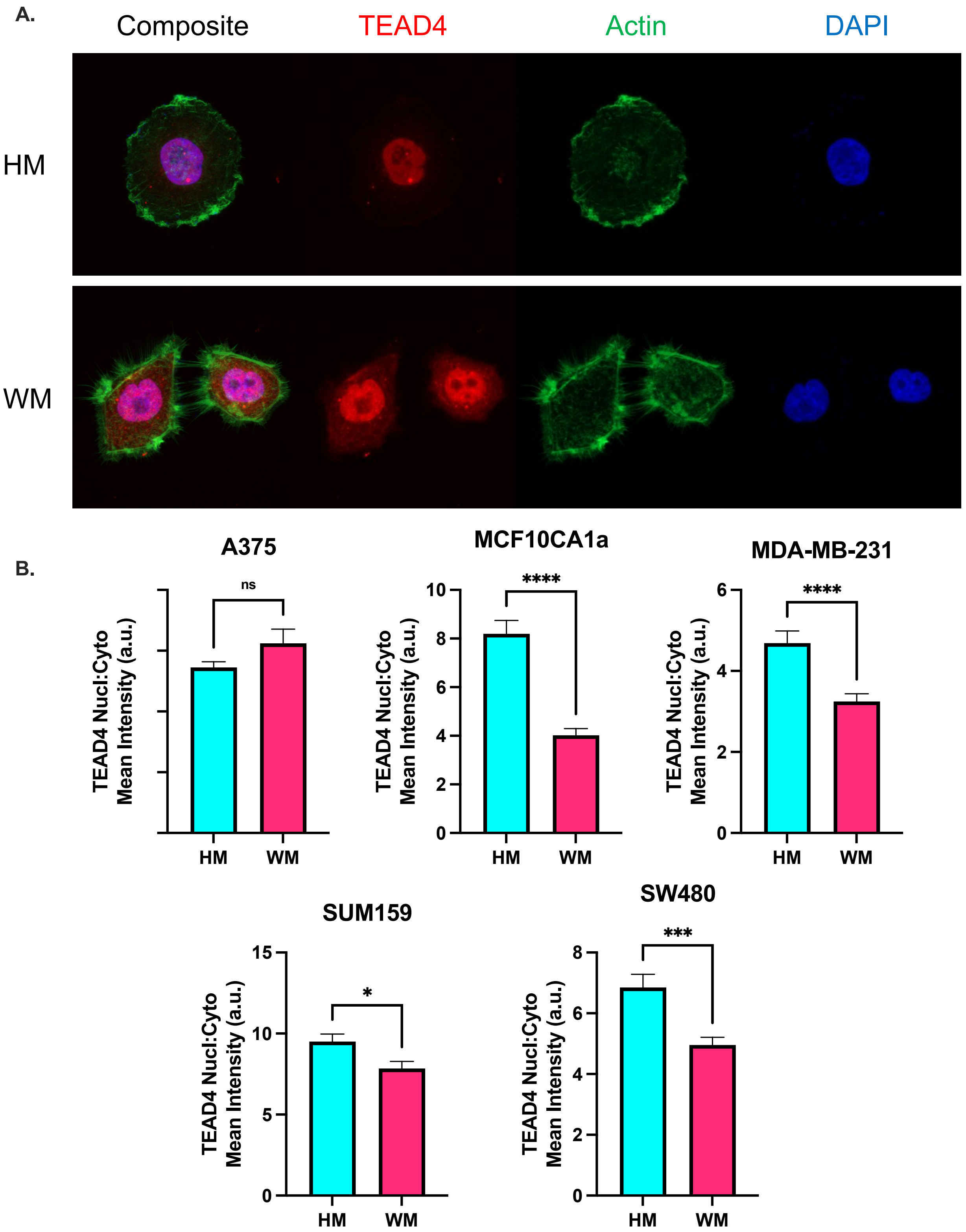
A.
Composite
TEAD4
Actin
DAPI
HM
WM
B.
A375
ns
TEAD4 Nucl:Cyto Mean Intensity (a.u.)
HM
WM
MCF10CA1a
****
10
8
6
4
2
0
TEAD4 Nucl:Cyto Mean Intensity (a.u.)
HM
WM
MDA-MB-231
****
6
4
2
0
TEAD4 Nucl:Cyto Mean Intensity (a.u.)
HM
WM
SUM159
*
15
10
5
0
TEAD4 Nucl:Cyto Mean Intensity (a.u.)
HM
WM
SW480
***
8
6
4
2
0
TEAD4 Nucl:Cyto Mean Intensity (a.u.)
HM
WM

Figure 5.9. TEAD4 nuclear localization. (**A**) Representative images for MCF10CA1a HM and WM subpopulations fixed and stained for phalloidin, DAPI, and TEAD4. (**B**) Quantification of nuclear-to-cytosolic ratio in HM and WM subpopulations via immunostaining. The data in this figure was generated by co-first author Ismael Ortiz.

5.4.7 Clinical correlation depends on cancer type

To determine the potential clinical utility of EVA1A expression, we compared EVA1A expression in normal and tumor tissue in patients with breast cancer, colon adenocarcinoma, and melanoma. Interestingly we found that EVA1A expression was significantly increased in tumor tissue compared to normal tissue in all 3 cancers (**Fig. 10A**). To evaluate the prognostic utility of EVA1A expression, we further investigated the relationship between EVA1A expression and survival. High expression of EVA1A was not significantly correlated with survival outcomes in breast cancer and melanoma (**Fig. 10A**). However, high expression of EVA1A was significantly correlated with better survival in colon adenocarcinoma (**Fig. 10B**). Additionally, we utilized muTarget to evaluate mutation status with EVA1A expression. In breast cancer, we only found a single mutation associated with a significant increase in EVA1A expression. Interestingly, we found 222 mutations associated with lower EVA1A expression and 1 mutation associated with higher EVA1A expression. There were 42 mutations associated with higher EVA1A expression in melanoma and only 5 mutations associated with lower EVA1A expression. Altogether, our data demonstrates that EVA1A is significantly upregulated in breast, colon adenocarcinoma, and melanoma solid tumors relative to normal tissue. However, EVA1A expression is only significantly correlated with survival in colon adenocarcinoma and higher EVA1A expression is associated with better survival outcomes. Furthermore, EVA1A expression is associated with the most mutations in colon adenocarcinoma and almost all mutations are correlated with lower EVA1A expression.

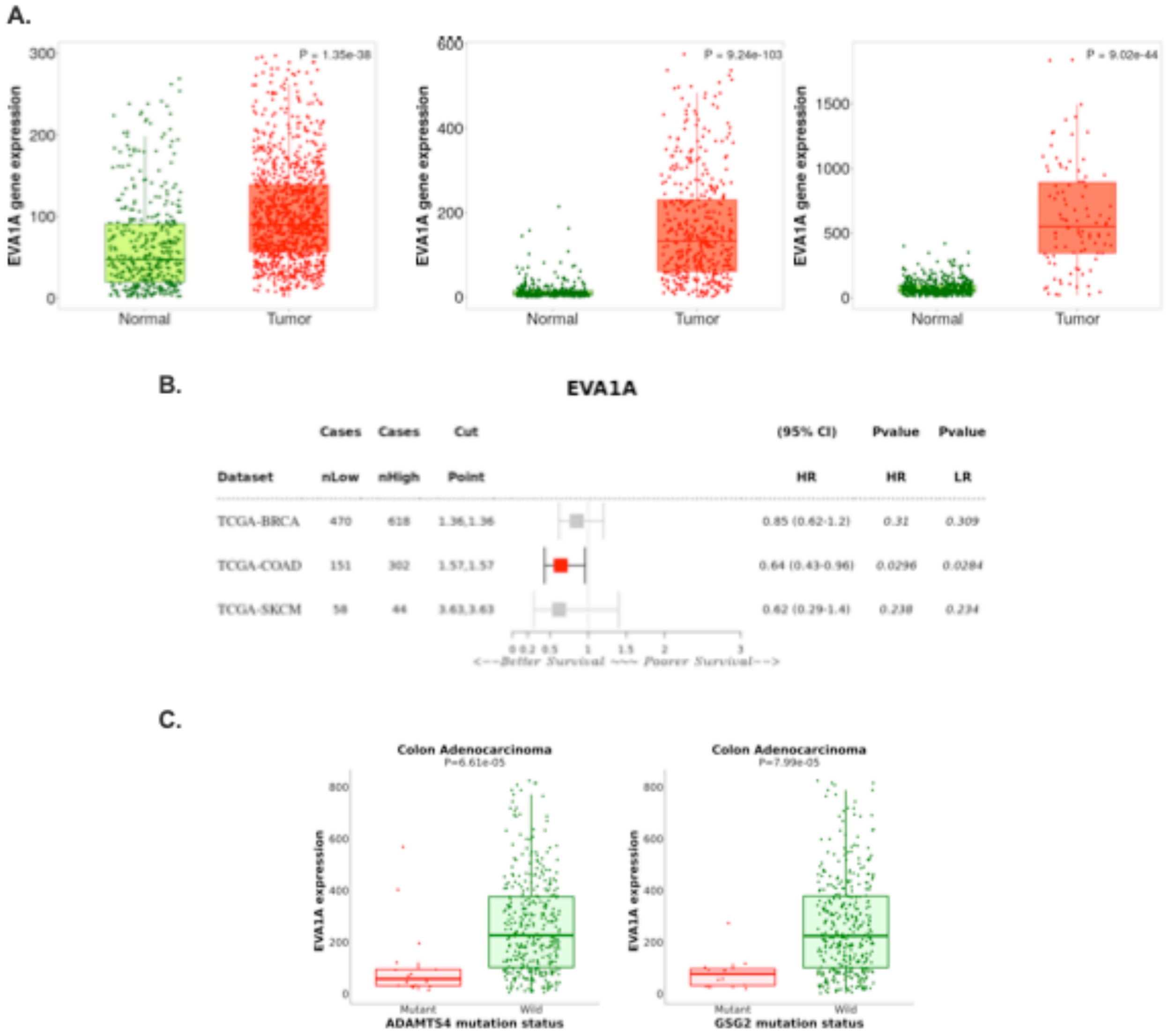

Cancer	MUT –> UP	MUT –> DOWN
BREAST	1	0
COLON	1	222
MELANOMA	42	5

Figure 5.10. Clinical correlations with EVA1A expression. (**A**) Quantification of EVA1A expression in normal vs tumor tissue. (B) Quantification of survival analysis for EVA1A expression. (C) Representative quantification of EVA1A expression in colon tumors with ADAMTS4 or GSG2 mutations. (D) Summary of genes associated with significant up or down regulation of EVA1A.

5.5 Discussion

Altogether our data highlights the extent of heterogeneity that exists between migratory cancer subpopulations. All 5 subpopulations were obtained through the same repetitive transwell sorting assay and displayed similar migratory ability. Cell morphology measurements revealed no consistent trend in cell size or aspect ratio across all 5 HM or WM subpopulations. Furthermore, migratory scores for EMT and ameboid migration modes derived from bulk sequencing revealed inconsistent trends across the 5 cell lines. Additionally, bulk RNA sequencing analysis revealed numerous significant transcriptional differences between HM and WM subpopulations but only a single gene was confirmed to be upregulated in all 5 HM subpopulations relative to their WM counterparts. EVA1A was significantly upregulated in all 5 HM subpopulations in the RNA sequencing analysis and via qPCR. Interestingly, while there was only a single gene commonly upregulated in HM subpopulations, there were numerous biological processes commonly regulated across all 5 cell lines between HM and WM subpopulations. Furthermore, each cell line had a unique signature of genes contributing to many of the biological processes, suggesting that different cell lines accomplish similar biological processes through distinct transcriptional networks. Upstream regulator prediction via Qiagen IPA software revealed TEAD4 activity as a potential mediator of the transcriptional changes observed in all 5 cell lines via RNA sequencing and elevated TEAD4 activity measured via TEAD4 nuclear-to-cytosolic ratio confirmed increased TEAD4 activity in 4 out of the 5 HM subpopulations relative to their WM counterpart. While EVA1A expression appears to be elevated in breast, colon, and melanoma cancers relative to normal tissue, there were no consistent trends in survival correlations. High EVA1A expression was significantly correlated with better survival in colon cancer but not significantly correlated with outcomes in breast cancer or melanoma. Thus, the molecular mechanisms that drive migration phenotypes may differ significantly across different cancer types and individual patients.

In cancer, EMT is linked to highly migratory phenotype. In our experiments we find that most of the HM subpopulations displayed higher EMT scores compared to their WM counterparts. In addition to transcriptional changes, EMT is associated with morphological changes. Specifically, EMT is associated with cellular elongation with cells typically being associated with higher aspect ratios after undergoing EMT. While we find that 4 out of the 5 HM subpopulations have higher EMT scores, we find that only 3 out of the 5 HM subpopulations have significantly higher aspect ratios compared to their WM counterparts. The SUM159 cells display no significant differences in aspect ratio while the A375s display higher aspect ratios in the WM subpopulations. The A375 subpopulations did not have significantly different EMT scores, which may explain why the subpopulation aspect ratios do not follow the expected trend associated with EMT. However, the SUM159 cells have higher EMT scores but do not have significantly higher aspect ratios. Our data suggests EMT status may not necessarily predict cell morphology.

We only observed a singular gene consistently upregulated across all 5 HM subpopulations. Previous research has established a link between chromosomal abnormalities and alterations in gene expression [295]. Given the variety of karyotypic abnormalities present within our cell lines, it's plausible that these genetic variances significantly influence the transcriptional landscapes, leading to a diverse expression profile across the different cancer cell lines (Supplemental Table 1). Epigenetic modifications have also been shown to be a source of heterogeneity within cancer cells [296,297]. As such, heterogeneity in epigenetic modifications across cancer cell lines likely have a role in shaping the unique gene expression patterns observed. However, despite karyotypic differences and possible epigenetic modifications, our GO-term and upstream regulator analysis suggests that different cancer cells may still manage to utilize similar cellular programs to achieve the same behavior. We found numerous biological processes shared across all 5 cancer cell lines and increased TEAD4 activity was confirmed in 4 out of the 5 cancer cell lines. Interestingly, we found a unique set of genes for each subpopulation which contributes to the shared biological processes. Altogether, this suggests that these biological processes are driven by robust gene expression networks that contain redundancies which allows flexibility across genetic and epigenetic heterogeneities.

Our data has shown EVA1A upregulation in all 5 HM subpopulations relative to their WM counterparts. EVA1A is associated with the lysosome and endoplasmic reticulum with roles in autophagy and apoptosis [298]. Prior work has observed conflicting correlations between EVA1A expression and cancer migration. For example, increased

EVA1A expression is associated with decreased migration in hepatocellular carcinoma and breast cancer cell lines [299–301]. However, increased EVA1A expression is associated with increased migration in human aortic endothelial cells and repression of EVA1A expression is associated with reduced migration in papillary thyroid cancer cells [302,303]. Interestingly, we observed increased EVA1A expression associated with higher migratory ability in 3 breast cancer cell lines (MDA-MB-231, MCF10A-CA1a, SUM159) while previous work observed increased EVA1A expression associated with lower migratory ability in MDA-MB-231, MDA-MB-468, and MCF-7 breast cancer cell lines [299,300]. This discrepancy may be due to the contexts of EVA1A upregulation. Specifically, Zhen et al. treat breast cancer cell lines with flubendazole, an anthelmintic drug traditionally used to treat parasitic worms, and observe increased autophagic death and increased EVA1A expression alongside decreases in migration [299]. Thus, the flubendazole treatment likely affects additional pathways contributing to the decrease in migration. Altogether this suggests EVA1A is likely not a universal marker of enhanced migration ability and remains dependent upon cell, cancer, and environment specific contexts.

Prior work has also shown that EVA1A contributes to cancer progression [298]. Evidence in hepatocellular carcinoma, pancreatic cancer, and papillary thyroid cancer suggests EVA1A is associated with effects that contribute to cancer progression [298]. However, additional evidence in breast cancer, glioblastoma, hepatocellular carcinoma, and non-small lung cell carcinoma suggests EVA1A is associated with inhibiting effects that contribute to cancer progression [298]. In our study, we find that while EVA1A expression is elevated in tumor tissue relative to normal tissue in breast, colon, and melanoma cancers, EVA1A expression is only significantly correlated with positive survival in colon cancer. Our work demonstrates EVA1A is associated with increased migratory phenotype in cancer cells but is significantly correlated with better survival outcomes. This result is unexpected as cell migration is a key step in the metastatic cascade and increased migration is typically assumed to be associated with increased metastasis and thus worse survival [287,304]. However, we have recently demonstrated that increased migration does not necessarily correlate with increased metastasis using breast cancer HM and WM subpopulations [287]. Thus our data further corroborates that genes correlated with increased cancer cell migration do not necessarily correlate with metastasis and poorer survival outcomes.

While we only confirmed a single overexpressed gene shared by the 5 HM subpopulations, we found numerous shared biological processes via GO term over representation analysis. Interestingly, it appeared many of the GO terms over-enrichment was driven by unique cell specific sets of genes which contributed to the same GO term but were only significantly differentially expressed in a single cell line. To identify common drivers, we utilized the Qiagen IPA analysis to infer potential upstream regulators and identified TEAD4, a transcription factor with canonical roles in the Hippo pathway [305]. We further confirmed increased TEAD4 in 4 out of the 5 HM subpopulations with the A375 cell line being the only HM subpopulation to not have a significantly higher nuclear-to-cytosolic ratio of TEAD4 staining. In the context of cancer, prior work has demonstrated TEAD4 can promote EMT in colorectal and head-neck squamous cell carcinoma and contribute to metastasis in gastric, breast, lung, and colorectal cancers [305]. As EMT is associated with increased migration, our data is in alignment with work demonstrating TEAD4 activity may promote cancer cell migration as our 4 out of our 5 HM subpopulations had significantly higher EMT scores and higher TEAD4 nuclear-to-cytosolic ratios [306].

5.6 Acknowledgments

The SW480 cells were graciously provided by the King lab.

Chapter 6:

Conclusions and Future Work

6.1 Conclusions

This thesis has investigated mechanical and behavioral heterogeneities observed in the tumor microenvironment and has identified effects at multiple levels. Collagen alignment methods *in vitro* may introduce temperature dependent confounding changes in pore size and stiffness. Stiffer tumors alter tumor composition by increasing M2-like macrophage accumulation and cell-cell communication by increasing cancer-macrophage signaling. Global levels of DNA methylation are mechanoresponsive and exhibit lower levels on stiffer substrates. And highly migratory cancer subpopulations exhibit numerous transcriptional differences in comparison to their weakly migratory counterparts. The highly and weakly migratory subpopulation across various cell lines have few shared common differentially regulated transcripts but share several common pathways and upstream regulators.

6.1.1 Pore size and stiffness may confound collagen alignment systems

In Chapter 2, I investigated the an *in vitro* collagen alignment system. I utilized confocal reflectance microscopy to visualize and analyze collagen architecture. Collagen alignment was be induced by pulling magnetic beads through a collagen matrix towards a strong magnet during self-assembly at 25C and 37C. Significant alignment was achieved at both temperatures, but I found temperature dependent effects on pore size. First, decreasing temperature increased pore size within aligned and non-aligned collagen matrices. However, pore size was only significantly different between aligned and non-aligned matrices at 37C. At 37C the aligned collagen matrices had significantly larger pore sizes while at 25C the aligned and non-aligned matrices were not significantly different. Furthermore, I compared the mechanical properties of aligned and non-aligned matrices produced at different temperatures. There were no significant differences measured by confined compression testing. However, there were several significant differences found by atomic force microscopy (AFM). Non-aligned matrices were significantly stiffer than their aligned counterparts at the same temperature. Furthermore, collagen matrices produced at 25C were significantly stiffer than their counterparts produced at 37C. Thus the stiffest matrices were non-aligned matrices produced at 25C and the softest matrices were aligned matrices produced at 37C. Together, these results indicate that collagen alignment methods may impart temperature dependent confounding architectural and mechanical changes in matrix pore size and stiffness, respectively.

6.1.2 Increased cancer-macrophage interactions and M2-like macrophage accumulation found in stiffer tumor microenvironments

Chapter 3 utilized the MMTV-PyMT spontaneous breast cancer mouse model to investigate the effects of matrix stiffness on the tumor microenvironment. The lysyl oxidase inhibitor beta-aminopropionitrile (BAPN) and tap water control were utilized to obtain compliant and stiff tumors from MMTV-PyMT mice, respectively. Single cell RNA sequencing via a custom InDrop platform was performed on dissociated stiff and compliant tumors from the MMTV-PyMT mice in 3 separate batches. A panel of canonical cell type markers identified cancer, immune, fibroblast, and endothelial cells captured in the single cell RNA sequencing. There were no significant differences in cell type distribution between stiff and compliant tumors. However, further analysis of the immune cells revealed macrophages were the predominant immune cell and there was an increase proportion of M2-like macrophages captured in stiffer tumors compared to compliant tumors. Flow cytometry using CD11B and F480 as general macrophage markers, CD86 as an M1-like marker, and CD206 as an M2-like marker confirmed an increase in M2-like macrophages and a decrease in M1-like macrophages in stiffer tumors. This finding was further confirmed via immunostaining of tumor sections with CD206. CellphoneDB was used to quantify potential cell-cell interactions between cell types in the MMTV-PyMT tumor microenvironment and revealed numerous possible interactions between all cell types. Interestingly, there were several unique cancer-to-immune ligand-receptor interactions and more total immune cell-cell interactions in stiffer tumors.

To further analyze potential intercellular communication, MDA-MB-231 breast cancer cells were seeded on stiff and compliant substrates and subjected to a cytokine profiling assay. The colony stimulating factor 1 (CSF-1) was significantly upregulated on stiffer substrates and confirmed via Western blot. CSF-1 protein levels were also found to be upregulated in stiffer tumors via Western blot. Treatment with FAK inhibitor PF573228 decreased CSF-1 expression detected via qPCR in MDA-MB-231 cells seeded on substrates of varying stiffness. As the single cell RNA sequencing data revealed CSF-1 receptor expression on macrophage populations, we sought to determine if stiffness mediated CSF-1 expression in cancer cells can affect macrophage recruitment. MDA-MB-231 cells were transduced with lentiviral shRNA targeting CSF-1 to knockdown CSF-1 expression. To determine the effect of MDA-MB-231 secreted factors to attract macrophages, we adopted a transwell migration assay in which macrophages migrate through collagen and an endothelial monolayer in response to stiffness mediated MDA-MB-231 secreted factors. MDA-MB-231 cells seeded on stiffer substrates attracted a significantly increased number of macrophages compared to softer substrates. Additionally, CSF-1 knockdown and CSFR significantly decreased the number of macrophages recruited, suggesting stiffness mediated MDA-MB-231 secretion of CSF-1 contributes to macrophage recruitment. Altogether this work demonstrates that increased numbers of M2-like macrophages accumulate in stiffer tumors and stiffness mediated CSF-1 may play a role in increased cancer-macrophage intercellular signaling in stiffer tumors.

6.1.3 Decreased global DNA methylation levels in endothelial cells seeded on stiffer substrates

In Chapter 4, I investigated the role of mechanical signaling on global DNA methylation levels in endothelial cells. Human umbilical vein endothelial cells (HUVECs) were seeded on stiff and complaint substrates and allowed to grow over 5 days to form monolayers. Subsequently, cells were fixed and stained for 5-methylcytosine (5meC) levels in the nucleus. Immunostaining revealed decreased global 5meC levels on stiffer substrates compared to compliant substrates. As DNA methylation levels are controlled by enzymes which methylate or de-methylate DNA, we assessed stiffness mediated expression of DNA methylation enzymes. Analysis of RNA abundance via qPCR indicated a significant decrease in DNMT1 levels but not DNMT3a, TET1, or TET2.

To further investigate stiffness DNA methylation dynamics *in vitro*, DNA methylation levels were assessed every 24 hours over 120 hours in HUVECs seeded on stiff and compliant substrates. Interestingly, there was a significant decrease in 5meC levels at 24 hours that persisted until 120 hours. Furthermore, the overall levels of 5meC continuously decreased over the 120 hours while maintaining a significant difference based on substrate stiffness. To assess the effects of passaging on global DNA methylation levels, 5meC levels were measured prior to seeding on PA gels of varying stiffness and 24 hours after seeding on a glass slide. The 5meC levels prior to seeding on PA gels were significantly lower than 5meC levels on both stiff and compliant substrates. Additionally, the 5meC levels significantly increased after passaging onto a glass slide, indicating that passaging may have an effect on global DNA methylation levels. Altogether this work demonstrates global DNA methylation levels are mechanosensitive in endothelial cells with response times as early as 24 hours and minor contributions from cell passaging.

6.1.4 Highly migratory cancer cell subpopulations exhibit diverse transcriptional profiles

In Chapter 5, I investigated the molecular similarities among highly and weakly migratory subpopulations derived from 5 different cancer cell lines. Morphological analysis revealed migratory subpopulations exhibit significant differences in cell area. However, the cell area was not consistently increased in all highly or weakly migratory subpopulations. Bulk RNA sequencing revealed numerous significantly differentially expressed genes between highly and weakly migratory subpopulations. Comparing the overlaps between differentially expressed genes among the 5 cancer cell lines revealed only a single gene upregulated consistently in the same subpopulation. Specifically, we found EVA1A expression was upregulated across all 5 highly migratory subpopulations and validated this finding via qPCR. Over representation analysis revealed numerous biological processes significantly enriched across all 5 cell lines. Furthermore, analysis of the significantly differentially expressed genes contributing to the over enrichment scores demonstrated that different cell lines contain unique cell-specific GO-term signatures.

Upstream regulator prediction analysis revealed several potential regulators, including TEAD4, and we observed increased TEAD4 activity in 4 out of the 5 highly migratory subpopulations relative to their weakly migratory counterparts. Survival analysis revealed increased EVA1A expression is only correlated with positive survival in colon cancer and not significantly correlated with survival in breast or melanoma cancers. Altogether, our data suggests significant heterogeneity exists in the underlying transcriptional programs that may drive migration heterogeneity in cancer cells.

6.2 Future Work

6.2.1 Further quantification of collagen alignment systems

In Chapter 2, we utilize magnetic beads pulled by a strong magnet to align collagen fibrils. As the magnetic beads physically interact with the collagen while passing through the solution, it is possible that the pore size obtained via our system described in Chapter 2 is dependent upon the size of the beads. However, there exists other methods to align collagen matrices which should be assessed for confounding architectural features such as pore size. Three additional methods of collagen alignment include utilizing a strong magnetic field in the absence of magnetic beads, utilizing shear flow during gel deposition, and applying strain to collagen gels. Magnetic collagen alignment without beads can be achieved with strong magnetic fields on the order of 1.9T to 5.6T [307]. Shear flow induced alignment requires the collagen to be quickly pipetted into a narrow channel prior to incubation. Strain-induced alignment requires collagen gels to be uniaxially deformed or stretched in a single direction [308]. These methods provide reliable collagen alignment but do not require the addition of magnetic beads to the system. The degree of alignment, pore size, and stiffness should be measured in these systems across the same range of temperatures used in Chapter 2. These results will determine how the relationships between alignment, pore size, and stiffness vary across currently used *in vitro* alignment platforms.

In addition to quantifying non-cellular *in vitro* alignment platforms, further work should examine the architectural and mechanical features of cell-aligned collagen. Numerous studies have reported that cells such as fibroblasts can align collagen matrices *in vitro* [309–314]. As such, it is important to compare the architectural and mechanical features of cell-aligned collagen with artificially aligned collagen. There two techniques for obtaining cell-induced collagen alignment which produce large scale alignment suitable for pore size and mechanical assessments. The first method entails seeding a fibroblast laden collagen matrix into a toroid shaped mold with a central inner peg [310]. After 2 weeks of cell culture within the collagen toroids, significant collagen alignment via fibroblast contractility and remodeling [310]. The second method requires an interstitial flow chamber which can direct radial flow of cell culture medium through a collagen gel seeded with fibroblasts [309]. After 48 hours of interstitial flow, significant collagen alignment via active fibroblast remodeling and interstitial flow are observed [309]. These gels may be decellularized after their respective time requirements for alignment via Triton X-100 and sodium deoxycholate for alignment, pore size, and mechanical testing. Importantly, this work will help to determine optimal *in vitro* settings for artificial alignment systems and allow us to interrogate cellular mechanisms controlling cell-induced collagen architectural and mechanical properties.

6.2.2 Determine the effects of collagen alignment on migration with fewer confounding effects

Studies have shown that both alignment and pore size can affect cell migration [315,316]. However, as shown in Chapter 2, the process of collagen alignment via magnetic beads may also affect the pore size of the matrix depending on the temperature during self-assembly. Specifically, at 37C the pore size of aligned collagen was significantly larger than the non-aligned counterpart while at 25C the pore sizes were not significantly different between aligned and non-aligned. Thus, the 25C alignment system should be utilized to determine the effects of collagen alignment on cell migration without the confounding effects due to pore size alterations. As cancer cells encounter matrix alignment, the highly motile MDA-MB-231 cancer cell line should be utilized to investigate the effects of alignment on migration [315]. MDA-MB-231 cells should be embedded in aligned and non-aligned collagen matrices prepared at 25C and 37C to compare how alignment induced effects are modulated by confounding effects from pore size changes. Alignment induced effects may be assessed by time-lapse microscopy capturing the matrix structure via confocal reflectance and the cell body with either brightfield or a fluorescent cell-tracker dye. Then the fraction of motile cells, the average cell migration speed, the distribution of stepwise movements in a direction relative to the matrix alignment, and the relationship between cell migration speed and direction of movement relative to matrix alignment may be calculated using image analysis software such as FIJI.

While this work will further refine the effect sizes of collagen alignment induced cell migration behavior, the mechanical stiffness may still be a confounding variable. In Chapter 2, I demonstrated that at both 25C and 37C, the aligned matrix was significantly softer than the random matrix. As matrix stiffness also plays a role in cell migration, further work should explore methods to create matrices with different architectural arrangements but similar mechanical features [317]. Non-enzymatic glycation via ribose may be used to stiffen the extracellular matrix without inducing effects in overall structure of the collagen [318]. Thus a dose curve of varying ribose concentrations should be utilized on aligned matrices to determine the optimal concentration to needed to match the stiffness of non-aligned matrices. Then MDA-MB-231 cells may be subjected to the same migration assay described above to determine the contribution of stiffness on alignment induced migration behavior.

6.2.3 Investigate additional methods for targeting matrix stiffening to determine effects on M2-like macrophage accumulation in the tumor microenvironment

In Chapter 3, we utilized beta aminopropionitrile (BAPN), a lysyl oxidase inhibitor, to decrease tumor stiffness. However, BAPN has toxic side effects in humans which limits the utility of the molecule [319]. Thus it is important to determine if additional methods which target matrix stiffening will have similar effects on the tumor microenvironment as BAPN. Our lab has previously demonstrated that advanced glycation end-products (AGEs) contribute to tumor stiffness and drugs which disrupt AGEs can reduce tumor stiffness [320]. As such, MMTV-PyMT mice should be treated with the glycation inhibitor aminoguanidine and the glycation breaker alagebrium to validate their ability to decrease tumor stiffness [320]. In addition to methods directly targeting matrix stiffness, some methods aim to inhibit the cellular response to matrix stiffening [90]. The focal adhesion kinase (FAK) inhibitor PF573228 disrupts a major component of the cellular mechanosensory machinery and has demonstrated safety and efficacy in a diabetic hyperglycemic mouse model of breast cancer [320]. Thus future work should also include treating the MMTV-PyMT model with PF573228. The M2-like macrophage levels after treatment should be measured via immunofluorescence staining with CD68 as a general macrophage marker and CD206 as a M2-like macrophage marker.

There are several subtypes of breast cancer which include the luminal, ErbB2 associated, and triple negative [321]. The MMTV-PyMT model utilized in Chapter 3 recapitulates many features of the luminal B subtype of breast cancer [322]. To determine if our findings are applicable to the other subtypes of breast cancer, future work should explore additional mouse models of breast cancer which represent all the breast cancer subtypes. Genetically engineered mice typically have functional immune systems and develop from intact native tissues [323]. As such, it is preferable to utilize genetically engineered mouse models particularly when studying the extracellular matrix. The MMTV-ErbB2 model on the FVB strain represent a model that resembles the ErbB2 associated human breast cancer subtype and the BLG-Cre;Brca1$^{F22-24/F22-24}$;p53$^{+/-}$ mouse model on the C57BL/6 strain represent a model that resembles the triple negative human breast cancer subtype. These additional models should be subjected to BAPN, aminoguanidine, alagebrium, and PF573228 treatment to determine the extent of matrix softening and M2-like macrophage levels should be measured after treatment as described above. These experiments will determine how broad the phenomena of matrix stiffness driven M2-like macrophage accumulation is in breast cancer models.

6.2.4 Investigate mechanisms driving M2-like macrophage accumulation in stiffer tumors

In Chapter 3, we show that M2-like macrophages accumulate at higher levels in stiffer tumors relative to softer tumors. However, the mechanism governing M2-like macrophage accumulation remains unknown. There are several hypotheses whereby matrix stiffness could directly influence the levels of M2-like macrophages. Matrix stiffness could promote the proliferation and survival of M2-like macrophages, shift macrophages toward the M2-like phenotype, or inhibit M1-like macrophage proliferation or survival.

There have been numerous studies investigating the effects of matrix stiffness on macrophage polarization, however these studies typically utilize *in vitro* fabricated matrices [4]. To better recapitulate the *in vivo* microenvironment, future work should explore the effects of matrix stiffness on macrophage behavior in decellularized tumor tissue. MMTV-PyMT mice can be treated with or without BAPN to produce compliant and stiff tumors, respectively. Tumors can be excised and decellularized via Triton X-100 and sodium deoxycholate and used for reseeding. Decellularization can be confirmed via DAPI staining to confirm lack of cellular material. Tumor stiffness can be determined via confined compression and AFM to confirm decellularized tumors derived from BAPN treated mice remain softer than non-treated counterparts.

To determine if stiffer tumor matrices promote proliferation or survival of M2-like macrophages, future work should utilize bone-marrow derived monocytes (BMDMs) and the decellularized tumor matrices. The BMDMs can be treated with IL-4 and IL-13 to induce an M2 macrophage phenotype. To determine proliferation effects, the Click-iT EdU cell proliferation kit can be used to compare the levels of DNA synthesis in M2 macrophages seeded in stiff and compliant decellularized tumor matrices. Previous work has shown that 3D intestinal organoids can be stained with propidium iodide and Hoechst to detect cell death [324]. As such, M2 macrophages seeded in stiff and compliant decellularized tumor matrices can be monitored for cell viability via propidium iodide and Hoechst staining. Thus proliferation rates and viability can be compared in M2-like macrophages seeded in stiff and compliant tumor matrices to determine the contribution of stiffness mediated proliferation and survival in M2-like macrophage accumulation in stiffer tumors.

To determine if stiffer tumor matrices promote polarization towards the M2-like macrophage phenotype, future work should measure polarization efficiency of BMDMs or macrophages seeded in decellularized tumor matrices. Monocytes differentiate into macrophages upon exiting the blood and entering the tissue. Thus to determine if stiffer tumor matrices enhance M2-like macrophage polarization, BMDMs can be seeded into stiff and compliant decellularized tumor matrices and be treated with IL-4 and IL-13. The efficiency of polarization can be measured via decellularized tissue dissociation and flow cytometry of isolated macrophages. The percent of CD206 positive macrophages and mean fluorescent intensity of CD206 can be compared between macrophages polarized in stiff and compliant tumor matrices to determine the contribution of stiffness enhanced M2 polarization on M2-like accumulation in stiffer tumors. Furthermore, recent work demonstrates that M1 macrophages can be repolarized towards the M2 phenotype z. As such BMDMs should be polarized towards an M1 phenotype via LPS. M1 macrophages can be seeded in decellularized tumor matrices and treated with IL-4 and IL-13 to induce an M2 repolarization. The extent of repolarization towards the M2 phenotype can be measured as described above via tissue dissociation and flow cytometry based quantification of CD206 expression.

To determine if stiffer tumor matrices inhibit M1 macrophage proliferation or survival, BMDMs should be polarized towards an M1 phenotype via LPS and seeded in stiff and compliant decellularized tumor matrices. Macrophage proliferation can be measured via the Click-iT EdU cell proliferation kit and survival can be measured via propidium iodide and Hoechst staining. Altogether, comparing M2 and M1 macrophage proliferation, survival, polarization, and repolarization in stiff and compliant tumor matrices could provide evidence for direct mechanisms linking matrix stiffness and M2-like macrophage accumulation in the tumor microenvironment.

6.2.5 Investigate cell-cell signaling with spatial resolution

In Chapter 3, I utilized the cellphoneDB to investigate cell-cell signaling in the single-cell RNA sequencing dataset and found numerous significant interactions between various cell types in the tumor microenvironment. However, the cellphoneDB analysis is limited due to lack of spatial information of cells. As such, it remains unknown whether such cell-cell interaction actually exist without further investigation. However, there have been numerous developments in generating spatial ‘omics’ tools that allow spatial RNA profiling of tissue sections [325]. To further investigate matrix stiffness mediated cell-cell signaling, MMTV-PyMT mice should be treated with or without BAPN to generate compliant or stiff tumors, respectively. Tumors can be excised, embedded in OCT and flash frozen. The 10X Visium platform can be used to perform spatial transcriptomics on ten micron sections mounted on Visium slides. According to the standard Visium protocol, hematoxylin and eosin staining will be imaged via brightfield prior to RNA profiling. Tissue sections are permeabilized on special tissue slides where mRNA released from cells binds to spatially barcoded oligonucleotides. Reverse transcription reactions produce barcoded cDNA from captured RNA and can be pooled for downstream processing to generate a sequencing-ready library and subsequent standard NGS sequencing. Visium provides software for remaining bioinformatic analyses. With spatially resolved transcriptomics analyses provided by Visium, we can assess colocalization of varying cell types within the tumor microenvironment to determine particular niches [326]. Furthermore we can perform colocalization analysis between ligand and receptor interactions detected in the cellphoneDB scRNAseq analysis to provide additional evidence for particular cell-cell interactions [326].

6.2.6 Evaluate stiffness mediated endothelial DNA methylation at base-resolution

In Chapter 4, I have demonstrated that endothelial cells seeded on stiffer substrates exhibit lower levels of global DNA methylation relative to endothelial cells seeded on more compliant substrates. To further examine the effects of stiffness mediated DNA methylation on endothelial cell behavior, reduced representation bisulfite sequencing should be performed on genomic DNA isolated via the Qiagen DNeasy kit from endothelial cells seeded on stiff and compliant substrates. The Ovation RRBS Methyl-seq kit can be utilized to perform MspI digestion, adapter ligation, end repair, bisuflite conversion, and PCR amplification required to generate a sequencing library. Sequencing can be performed on the NovaSeq6000 targeting approximately 30 million reads per sample. The Bismark software can be utilized to quantify methylation at each genomic locus using Bowtie2 for alignment [327]. Chen et al. 2018 have developed a workflow utilizing edgeR to perform differential methylation analysis of RRBS data which can test for differential methylation by CpG loci, chromosome, gene promoters, and transcriptional start sites [327]. To further explore the differential methylation identified in gene promoters or near transcriptional start sites, the methylation analysis can be correlated with bulk RNA sequencing to determine if differences in methylation correspond to alterations in gene expression. Genes identified by altered methylation status and corresponding transcriptional changes may be analyzed via qPCR and Western blot to confirm stiffness mediated changes in expression. To identify functional consequences for stiffness mediated gene expression, the corresponding genes can be knocked-out or overexpressed in endothelial cells and seeded on polyacrylamide gels of varying stiffness and subjected to proliferation, migration, and permeability assays. Altogether this work will help determine the contribution of stiffness mediated DNA methylation in stiffness driven aberrant endothelial cell behaviors.

The RRBS methylation data may also be used to determine possible mechanisms of stiffness mediated DNA methylation. Increased matrix stiffness drives numerous cell behaviors through increased cell contractility [87,328,329]. Furthermore, the contractile cytoskeleton is directly to the nuclear envelope which is composed of nuclear lamina which can interact with the genome through lamina-associated domains [330–332]. As such, future work should determine if force transmitted from stiffness mediated cytoskeletal contractility to chromatin via nuclear lamina is correlated with altered methylation at nearby CpG loci. Chromatin immunoprecipitation-sequencing (ChIP-seq) of A- and B-type lamins can be performed to on endothelial cells seeded on stiff or compliant substrates to compare correlation between methylation levels and lamin binding. Thus, ChIP-seq analysis paired with RRBS methylation analysis can help determine if mechanical forces transmitted to chromatin play a role in stiffness mediated DNA methylation.

6.2.7 Investigate additional stiffness mediated epigenetic effects in endothelial cells

Chapter 4 demonstrated endothelial global DNA methylation levels are responsive to substrate stiffness. However, there are additional epigenetic pathways that contribute to endothelial cell behaviors. In particular, histone post-translational modifications can modulate chromatin accessibility to modulate transcription [333]. For example, histone deacetylase 7 (HDAC7) and sirtuin 1 (SIRT1) are histone modifying enzymes which have been shown to regulate endothelial function [333–336]. To determine if HDAC7 or SIRT1 are implicated in stiffness mediated epigenetic changes, HDAC7 and SIRT1 protein levels can be compared between endothelial cells seeded on stiff and compliant substrates via Western blot. Furthermore, as HDAC7 and SIRT1 have been shown to acetylate H3, HDAC7/SIRT1 activity can be compared between endothelial cells seeded on stiff and compliant substrates via pan acetylated H3 Western blot [337]. To further explore the contribution HDAC7 and SIRT1 mediated epigenetic modifications, ChIP-seq can be performed on endothelial cells seeded on stiff and compliant substrates using HDAC7 and SIRT1 antibodies to determine if there are differential binding patterns induced by substrate stiffness. This work should discern whether important endothelial specific epigenetic enzymes are also regulated by matrix stiffness.

6.2.8 Investigate EVA1A expression and TEAD4 activity on migratory behavior

In Chapter 5, we found increased EVA1A expression in all 5 highly migratory subpopulations and increased TEAD4 activity in 4 highly migratory subpopulations. To determine if EVA1A expression is required for increased migratory ability, future work should modulate EVA1A expression in migratory subpopulations and evaluate transwell migration ability. EVA1A should be knocked down in highly migratory subpopulations via lentiviral shRNA targeting EVA1A and EVA1A should be overexpressed in weakly migratory subpopulations via lentiviral transduction of EVA1A containing expression plasmid. Knock-down of EVA1A in highly migratory subpopulations should decrease transwell migration while overexpression of EVA1A in weakly migratory subpopulations should increase transwell migration. As we did not detect significant differences in TEAD4 expression, TEAD4 activity should be targeted to determine its contribution to migratory phenotype. TEAD4 activity can be disrupted by mimicking the TEAD4 binding domain of VGLL4 to interrupt YAP-TEAD4 interactions with Super-TDU [338]. Highly migratory subpopulations should be treated with Super-TDU and subjected to transwell migration assays. Altogether this work will demonstrate the role of EVA1A expression and TEAD4 activity on the highly migratory phenotype.

6.2.9 Examine intracellular signaling pathway activity in highly and weakly migratory subpopulations

In Chapter 5, highly and weakly subpopulations exhibited numerous transcriptional differences. Gene ontology, GSEA, and IPA upstream regulator analysis provide predictions for cellular pathways which are being modulated between conditions. However, the predictions have limitations and are established on canonical signaling pathways which may be affected in abnormal and dysregulated cancer cells. Thus, to gain further insight into differential pathway activation, highly and weakly migratory subpopulations should be subjected to the Proteome Profiler Human Phospho-Kinase Array Kit. The Proteome Profiler kit detects the phosphorylation of 37 human kinases with known implications in cancer cell migration such as Akt, beta-Catenin, c-Jun, EGFR, ERK1/2, Lck, and Src [339–345]. This work will complement the transcriptomic profiling and possibly confirm or uncover additional molecular differences between highly and weakly migratory cancer cells.

6.2.10 Investigate heterogeneity in organotropic metastasis

In chapter 6, we utilized a transwell migration assay to phenotypically sort cells that preferentially migrated through a transwell in the direction of an FBS gradient. We successfully captured highly and weakly motile cells that maintained their migration phenotypes for long time periods which allowed us to identify molecular similarities across different cancer cell lines that contribute to migratory phenotype. Thus our work has demonstrated the capability of this technique to investigate molecular underpinnings of phenotypic heterogeneity. Another important feature of cancers is the organ-specific metastasis known as metastatic organotropism [346]. In particular for breast cancer, metastasis is widely observed in the bone, liver, lung, and axial lymph nodes [347]. While this phenomena is observed, the mechanism driving organotropism remains incompletely understood. The ‘seed and soil’ hypothesis generated by Stephen Paget states that metastasis requires the seed (cancer cell) and soil (metastatic site) to be compatible with one another [348]. Recent work has demonstrated that signals from the primary tumor and cancer cells can work to prime the secondary site for metastasis [349]. However, the secondary site may also release signals to attract metastasis. Thus, future work should expand upon our phenotypic sorting assay to address the hypothesis that soluble signals from the secondary site attract particular subsets of cancer cells.

Previous work investigating metastatic organotropism has utilized MDA-MB-231 subpopulations derived from organ specific metastases typically in mouse models [347]. However, our *in vitro* sorting model provides several advantages over collecting metastatic subpopulations from *in vivo* experiments. By sorting *in vitro*, we reduce usage of animals and costs. Furthermore, by selecting the soluble factor to form the chemogradient, we can ensure the specificity of the organ specific attractant. Other metastatic models which begin via orthotopic injection and primary metastasis may capture cancer cells that arrived to the metastatic site after initial seeding and were thus attracted by soluble factors released by other cancer cells as opposed to soluble factors released by the resident cells found in the secondary site.

To test the hypothesis that soluble signals from secondary site attract particular subsets of cancer cells in breast cancer, future work should subject the MDA-MB-231 metastatic cell line to our repetitive transwell sorting assay replacing the FBS gradient with a soluble factors derived from the secondary site. As breast cancer particularly metastasize to the bone, lung, lymph nodes, and liver, the soluble factors should be specific to those tissues [347]. Prior work has demonstrated that the chemokine RANKL is secreted by osteoblasts and other bone stromal cells and associated with bone metastasis [347]. Thus RANKL can be used as the chemogradient to generate a bone metastasis specific subpopulation of MDA-MB-231 cells. Prior work has demonstrated that chemokines CXCL12 and CCL21 are highly abundant in lung and lymph nodes and can be used as the chemogradient to generate lung/lymph node metastasis specific subpopulation [347]. In the liver, previous work has demonstrated that CCL20 is constitutively expressed in the liver and may promote liver metastases [350]. Thus CCL20 may be utilized to generate the liver specific metastatic subpopulation.

Future work should further identify additional tissue specific factors that may attract cancer cells to metastasize in that particular location. Several approaches can be combined to identify novel metastatic organotypic attractants. Mouse organs can be harvested and processed for bulk RNA sequencing and proteomic analysis. Additionally, the primary cell type from each tissue can be cultured *in vitro* and the secretome can be assessed by collecting spent media and subjecting the collected media to proteomic analysis. Hepatocytes may be utilized for liver, lung epithelial cells for lung, and osteocytes for bone secretome. Proteins that are detected with high abundance in all 3 measurements can then be tested via transwell sorting assay to determine if each factor can act as a chemoattractant for MDA-MB-231 cells. Furthermore, human tissue samples can be probed via immunohistochemistry to verify elevated abundance in human tissue. These experiments will identify possible targets that are highly expressed in the organ at the RNA and protein level and are secreted by the major cell type residing in that tissue.

After repetitive transwell sorting to generate MDA-MB-231 subpopulations that are attracted to tissue specific soluble factors, each subpopulation can be transfected with a lentiviral plasmid containing GFP and either injected orthotopically or via tail vein. Metastasis to the bone, lung, and liver can be assessed by fixing the tissue in PFA and embedding in paraffin. The tissue can be sectioned and assessed via immunohistochemistry for GFP positive cells, indicating metastasis to that tissue. Furthermore, the excised tissue can be viewed under a stereoscopic microscope and macro metastatic nodules can be counted by gross examination. These experiments will reveal which tissue specific factors used in our repetitive transwell sorting assay generate MDA-MB-231 subpopulations that metastasize preferentially to a single organ.

Confirmed organotropic subpopulations can be further subjected to characterization to assess the contribution of ligand-receptor interactions in organotropic metastasis. To determine the available surface receptors present on the organotropic subpopulations, proteomics analysis can be performed with modifications to enrich for surface proteins. To enrich for surface proteins, cationic colloidal silica beads can be used prior to lysis to allow for plasma membrane enrichment via differential centrifugation [351]. Proteomic analysis via mass spectroscopy following cell surface protein enrichment can be used to determine the presence and absence of cell surface receptors. Future work should focus on known and potential receptors for the soluble factors utilized in generating the organotropic subpopulations. Protein abundance can be verified via western blotting and immunohistochemistry. If soluble factors play an important role in organotropic metastasis, it is possible that subpopulations highly express receptors for the organ specific factor while lowly expressing receptors for the other organ specific factors.

To determine the contribution of receptor-ligand interactions in organotropic metastasis, the subpopulations can be subjected to *in vitro* and *in vivo* characterization following gene knock-out. Receptors for organotropic factors can be knocked out via CRISPR and subpopulations can be subjected to *in vitro* transwell migration assays using the organotropic factor to establish a chemogradient. Furthermore, genetically modified subpopulations can be subjected to tail vein injections and orthotopic injections to determine if organotropic metastasis is maintained following gene knock-out. If receptor-ligand interactions play an important role in organotropic metastasis, knock-out of receptors for organotropic factors on cancer cells should decrease organ specific metastasis or alter the distribution of metastatic sites in the generated organotropic metastatic subpopulations. Altogether, this work will build upon our phenotypic sorting platform to investigate the heterogeneity behind organotropic metastasis and reveal the contribution of receptor-ligand interactions between cancer cells and soluble factors released by secondary sites in organotropic metastasis.

Appendix A:

Matrix stiffness primes cells for future oxidative stress

This chapter is adapted from *Matrix stiffness primes cells for future oxidative stress* published in *Trends in Cancer* and has been reproduced with permission of the publisher and co-author CA Reinhart-King.

Taufalele, P. V. & Reinhart-King, C. A. (2021). Matrix stiffness primes cells for future oxidative stress. *Trends in Cancer*, *7*(10), 883-885.

A.1 Abstract

Attention on metabolic reprogramming has re-emerged in recent years due to the far reaching consequences of metabolism on nearly all cellular behaviors. In Tharp et al, adhesion-dependent mechanical signaling is shown to induce mitochondrial and metabolic reprogramming to help cells adapt to future oxidative stress.

A.2 Main Text

Cells exist within microenvironments where they interact with biochemical and physical cues from other cells as well as the extracellular matrix (ECM). In many pathological states, such as aging and tumorigenesis, the ECM becomes deregulated and can undergo compositional and structural changes[90]. Tissue stiffening is a major consequence of pathological ECM remodeling that can occur due to excessive ECM deposition and cross-linking[90]. Cells are equipped with mechanosensitive machinery to sense tissue stiffening and tune their behaviors accordingly[352]. While the specific biochemical and cellular composition vary across tissue and disease, tissue stiffening is a shared feature of many pathological states and has become a promising target for therapeutic intervention by interfering with the mechanism of tissue stiffening or the cellular responses[90].

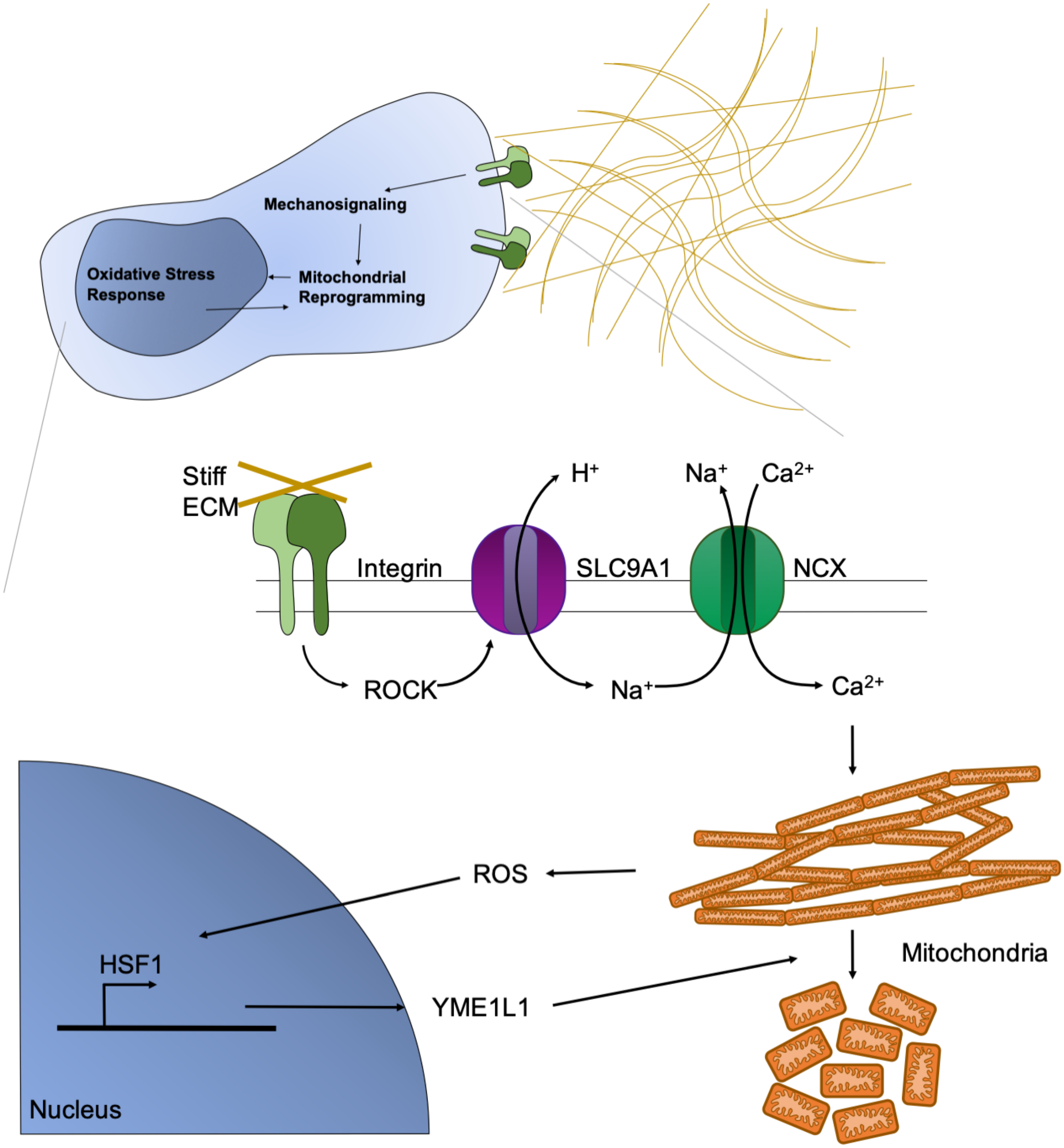

Figure A.1. Mechanical signaling through cell adhesions induce mitohormesis. Integrin-mediated cell-ECM adhesions transduce matrix stiffness to activate Rho-associated protein kinase (ROCK) signaling. ROCK signaling regulates SLC9A1 (Na^+/H^+ exchanger) to increase the influx of Na^+ ions and efflux of H^+ ions. SLC9A1 mediated efflux of H^+ ions indirectly induces mitochondrial ROS production through NCX (Na^+/Ca^{2+} exchanger) activity and mitochondrial calcium loading. Elevated mitochondrial ROS production activates a HSF1 and YME1L1 dependent oxidative stress response which leads to changes in mitochondrial morphology and metabolic reprogramming.

Recently, matrix stiffening was shown to affect metabolic reprogramming[352]. Importantly, metabolism is central to the function of the cell, and as such, metabolism is an attractive mechanosensitive therapeutic target. The mitochondria is a center for energy production and consumes oxygen to produce ATP via oxidative phosphorylation. Mitochondria also generate reactive oxygen species (ROS) as a by-product of oxidative phosphorylation. Accumulation of ROS can induce oxidative stress that damages macromolecules or initiate mitogenic signaling pathways such as PI3K/AKT/mTOR or MAPK/ERK[353]. Mitochondrial ATP and ROS production is altered in pathological settings such as cancer, and it contributes to cancer cell proliferation and migration[353]. While mitochondrial morphology and function are tied to the cytoskeleton and the cytoskeleton plays a major role in transducing mechanical signals, the relationship between mechanosignaling and mitochondrial function remains unclear[90,352,354]. Tharp et al. demonstrated that mechanosignaling activation induced changes in mitochondrial morphology, with cells cultured on stiffer substrates displaying fragmented/toroidal morphologies compared to the thin interconnected filaments displayed on softer substrates[355] (Figure 1). Mitochondrial morphology is known to be linked to its function and disrupting the dynamic fusion and fission of mitochondria leads to altered ATP production[356]. Consistent with that, the authors showed that activated mechanosignaling induced lower mitochondrial oxygen consumption [355].

The electric potential across the inner mitochondrial membrane plays an important role in mitochondrial function and is associated with altered metabolism and morphology[356]. Interestingly, while loss of mitochondrial membrane potential is a typical culprit for reduced mitochondrial function and associated with fragmentation, activated mechanosignaling increased mitochondrial membrane potential[355,356]. In search of an explanation, the authors compared the mitochondrial morphology of cells exposed to hyperglycemia, as hyperglycemia has been shown to induce mitochondrial fragmentation and increase membrane potential and alter intracellular pH[355]. Using lattice light sheet microscopy of mammary epithelial cells cultured on soft substrates and exposed to hyperglycemic conditions, the authors found the same transition of mitochondrial morphology towards fragmented and toroidal structures[355].

Intracellular pH is predominantly regulated by transmembrane proteins that regulate the flux of ions in and out of the cell. Interestingly, the Na+/H+ exchanger SLC9A1, which helps control intracellular pH, is regulated by ROCK and aids in FAK phosphorylation which facilitates mechanotransduction events downstream of cell-ECM adhesions[355]. SLC9A1 can also indirectly cause mitochondrial ROS production via mitochondrial calcium overload. Tharp et al. found that inhibition of SLC9A1 restored mitochondrial morphology[355]. Mitochondrial calcium content and ROS production[7] have been associated with mitochondrial remodeling and mitochondrial calcium concentration, and the authors found that ROS production was highest on stiff ECM but could be reduced through SLC9A1 knockout[355]. Increasing mitochondrial calcium content was sufficient to induce mitochondria fragmentation on compliant ECM[355]. Conversely, suppression of mitochondrial ROS or calcium loading prevented fragmentation on stiff ECM[355]. These findings indicate SLC9A1 activity may transduce mechanical stress at adhesion sites to increase mitochondrial calcium concentration and ROS production to drive mitochondrial remodeling (Figure 1).

Cellular ROS can inflict damage on DNA and proteins, which can disrupt important cellular functions. Elevated levels of ROS have been observed in cancer and aging cells and have been previously attributed to oncogenic signaling and enhanced metabolic output due to energetic demands[355,357]. To explore SLC9A1 and ROS production more broadly, the authors utilized an nhx-2 (SLC9A1) knockdown in *C. elegans*. Nhx-2 knockout animals displayed lower basal levels of oxidative stress and longer lifespans[355]. However, when treated with paraquat, an herbicide that promotes mitochondrial ROS production, nhx-2 knockout animals surprisingly had higher oxidative stress levels and shorter lifespans than wild types[355]. This finding suggested that SLC9A1 activity may confer some oxidative stress resilience to the animals. Furthermore, the authors discovered that adhesion-mediated oxidative stress response was mediated by HSF1 and YME1L1 transcription which are in part responsible for metabolic reprogramming and increased oxidative stress resilience[355]. This led the authors to hypothesize that adhesion-mediated production of sub-lethal mitochondrial ROS, which promotes mitochondrial reorganization, may induce an oxidative stress response that prepares cells to overcome subsequent oxidative stresses (Figure 1). A response to a non-lethal mitochondrial stress that leaves the cell less susceptible to subsequent perturbations has recently been termed mitohormesis and may be responsible for the disappointing efficacy of antioxidants clinically[358].

Together, this recent work demonstrates that the mild overproduction of ROS induced by adhesion-mediated mechanosignaling leads to metabolic reprogramming and induction of compensatory ROS quenching programs mediated by HSF1 and YME1L1[355] (Figure 1). Future work could investigate inhibition of the oxidative stress response mediated by HSF1 and YME1L1 to remove cytoprotective effects of mitohormesis or potentially enhance the efficacy of antioxidant treatments. Recent work has revealed the importance of metabolism in mechanically-regulated cellular behaviors such as cell migration and proliferation[359]. Thus mechanically-induced mitohormesis may represent a mechanism by which cancer cells resist ROS but continue to generate high levels of ATP in stiffer environments to support migration and invasion. Furthermore, this work has revealed critical insight into the overlap between aberrant mechanics and metabolic reprogramming that could reveal potential mechanomedicine targets. For example, during aging vessel wall stiffening decreases endothelial barrier function which contributes to atherosclerosis progression[360]. As increased levels of ROS are also associated with atherosclerosis[353], it is possible that vascular stiffening plays a role in endothelial and vascular smooth muscle cell-mediated ROS signaling. Likewise, diabetes involves altered tissue mechanics, metabolism, and ROS levels[90,353]. However, as hyperglycemia induces mitochondrial reprogramming, the synergy between mechanically and biochemically induced mitochondrial reprogramming will need to be dissected. Uncovering a novel mechanism by which metabolic responses are mediated by matrix stiffening to affect ROS signaling may be foundational for new discoveries in mechanomedicine across numerous diseases.

Acknowledgments

This work was supported by funding from the National Institutes of Health (GM131178) and F31 Predoctoral Individual National Research Service Award (under grant no. 1F31HL154727) to P.V.T. The authors thank Jian Zhang for thoughtful discussion.

Appendix B:

Rat tail collagen isolation protocol

B.1 Overview

This protocol is designed to solubilize Type I collagen from isolated rat tail tendons. Acid solubilized collagen is centrifuged at high speed to remove particulates and lyophilized and resuspended at a standard 10mg/ml for every day usage by the lab. The rat tails cannot be fully sterile but we still perform the dissection of the rat tails and all the other steps in the biosafety cabinets to be as sterile as possible as we use this collagen to culture cells.

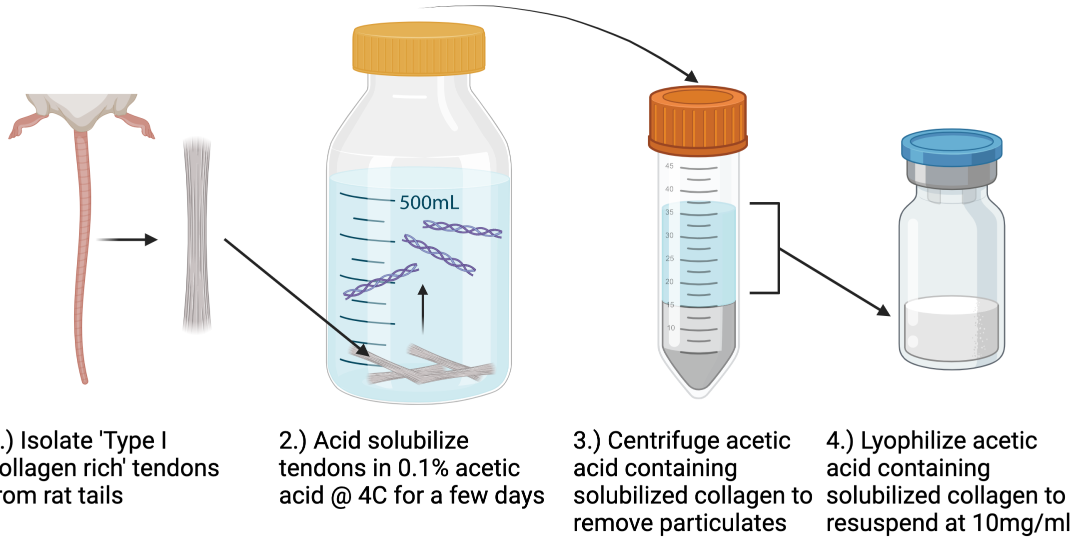

Figure B.1. Rat tail collagen isolation overview. Schematic depicting general protocol steps for isolating rat tail collagen for cell culture purposes.

B.2 Materials

- Rat tails (Sprague Dawley; M/F; age 5-7wk)
  - order from Rockland Antibodies [RT-T297] and email to ask for a quote
  - Keep in -20C; try to use within few months to a year
- Cutting board
- Scalpel
- Forceps

- Tissue forceps with 1x2 teeth (looks like tweezers with teeth)
    - Wpiinc.com → [SKU: 15918-G]
- 70% Ethanol
- Large wide glass beaker
- 2x 80ml glass beaker (any size above 80mL should be fine)
- Glacial Acetic Acid
- MiliQ water
- Centrifuge (needs to be able to spin 50mL conical tubes) as fast as possible
- 50mL conical tubes
- 250mL storage bottles
- Lyophilizer
- Kimwipes (small)
- Rubber bands
- 1L glass bottle (autoclaved)
- Sterile filter
- Scale
- Biosafety cabinet
- 4C fridge
- -20C freezer
- Lab coats (ppe)
- Nitrile gloves (ppe)

B.2 Protocol

B.2.1 Isolate type I collagen rich tendons from rat tails

1. **Open up biosafety cabinet #3 and spray these items with 70% EtOH to sterilize**
    a. Cutting board
    b. Scalpel (and blades)
    c. Forceps
    d. Tissue forceps with 1x2 teeth
    e. 2x 80mL glass beakers filled with 70% EtOH

    f. Large wide glass beaker filled half way with 70% EtOH

2. **Put ~25 rat tails into the large beaker filled halfway with 70% EtOH.**
    a. The rat tails should be frozen and stored in the -20C. I try to use the rat tails within a year of receiving them before I notice a large degree of freezer burn and worse quality of collagen.
3. **Once the rat tails have thawed [you can tell when they become less rigid and more bendy], you may begin dissecting the rat tail:**
    a. Place the tile horizontally across you on the cutting board
    b. Use the scalpel to trim the top and bottom of the tail about a ¼ in
        i. Try not to force the blade through and find the nearest ‘knuckle’ to cut through
    c. Starting at the larger end of the tail, make an incision through the rat tail skin all the way down the tail.
        i. Make sure that your incision is not on top of a tendon so you don’t ruin the tendon and make it harder to remove. There are 4 tendons spaced around the rat tail and you can see white and then brown/red sections underneath the skin. I always cut down one of the brown/red sections.
    d. Peel the skin away from the tail
        i. Works best if you use the scalpel to free up some of the skin at the large end of the tail and then peel it down from there
    e. Use the tissue forceps to lift up a part of one of the tendons
        i. I usually aim for about 1/3 of the way from the large end of the tail
    f. Use the forceps to pull the tendon down towards the small end of the tail and off the tail
    g. Place the removed tendon into small 80mL glass beaker #1 full of EtOH
    h. Repeat this for the remaining 3 tendons on the tail in front of you and then repeat for the remaining 24 rat tails
    i. Working with 2 people this process should take about 1.5 hr
4. **After all of the rat tails have been completed, wash the tails with the 2nd 80mL glass beaker of EtOH**

    a. Can pick up rat tail tendons with tweezers and simply move them from their current glass beaker to the second glass beaker
    b. The ethanol helps to clean and to dry the tendons
5. **Dry the tendons on kimwipes**
    a. Spread out kimwipes in the biosafety cabinet and spread the tendons across the kimwipes.
    b. Try to spread them out so they are not clumped together. This step is to dry the tendons to get an accurate weight
6. **While the tendons are drying, make 1L of sterile filtered 0.1% Acetic Acid using the stock Glacial Acetic Acid.**
    a. Utilize miliQ water. We have used DI water before but prefer miliQ water as a precaution.
    b. Use a 1L bottle that has been autoclaved
7. **After the tendons have dried [they are not soft anymore], use a 50mL tube to weigh the tendons.**
    a. Pre-measure weight of 50mL tube
    b. place dried tendons into 50mL tube
    c. measure weight of 50mL tube again

B.2.2 Acid solubilize tendons in 0.1% acetic acid at 4C for several days

1. **To acid solubilize the collagen from the rat tail tendons, we use a ratio of ~150-300mL 0.1% Acetic Acid for every 1 gram of dried tendons.**
    a. As long as you have between 6.6 and 3.3 g of tendons, I will just put all of them into the 1L bottle of sterile acetic acid
2. **Incubate the rat tendons in 0.1% Acetic Acid at 4C for at least 48 hrs**
    a. After 48 hrs, the type I collagen should acid solubilized and in solution
    b. I have stored the rat tendons in acetic acid at 4C for up to 6 months and it seems to be fine (based on viscosity and collagen hydrogel structure under confocal reflectance)

B.2.3 Centrifuge acetic acid containing solubilized collagen to remove particulates

1. **Take 50mL aliquots of the acid solubilized collagen solution and centrifuge at 4750RPM in our Beckman coulter centrifuge for 90 minutes @ 4C**
    a. Make sure the tubes are perfectly balanced
        i. After pipetting 50ml into each 50ml c-tube, I weigh them on the scale and arrange the 2 centrifuge buckets so that they are balanced within 0.1g of each other.
    b. It is okay if there is some rat tendons that get into the tubes
    c. Turn the centrifuge on 4C before you start aliquoting so it has time to get down to temperature
2. **Transfer the supernatant into 250mL corning storage bottles. I usually take the supernatant from 14 50ml c-tubes and transfer it to 4 250ml storage bottles.**
    a. Do not fill storage bottles above 150ml
    b. Make sure there are no particulates that are transferred into the storage tubes. Anything that is not collagen may be quite disruptive experiments. If If some particulate get transferred, either discard the whole storage bottle or re-centrifuge
3. **Store the 250 ml storage bottles at -20C until fully frozen (usually overnight is enough)**

B.2.1 Lyophilize acetic acid containing solubilized collagen to resuspend at 10mg/ml

1. **Place collagen on lyophilizer for ~72hrs**
    a. Turn on lyophilizer and vacuum pump
    b. Set lyophilizer to run and wait until temperature drops to -55C and vacuum below 0.15
    c. Remove the cap from the storage bottle
    d. Place kimwipe overtop opening
    e. Secure kimwipe with rubber band

    f. Place storage bottle into large lyophilizer glass container
    g. Place lid onto lyophilizer container
    h. Attach lyophilizer container to lyophilizer machine and open valve
    i. Wait until the vacuum pressure drops below 0.15 again
    j. Repeat steps c-i with remaining storage bottles

2. **Monitor collagen until full lyophilized**
    a. You will see a dry white sponge material.
    b. If you feel the bottom of the glass lyophilizer bottle with your hand, it should be fairly warm to touch. If it is still cold then it needs more time.
3. **Remove collagen from lyophilizer and measure weight**
    a. Take lyophilizer glass jar with collagen sponge inside directly to BSC (try to be sterile)
    b. Pre measure the weight of a sterile 50ml c-tube
    c. Using sterile tweezers and inside of the BSC, transfer the lyophilized collagen sponge into the pre measured 50ml tube
    d. Weigh the 50mL tube with the collagen inside and calculate the weight of the collagen sponge
4. **Reconstitute / resuspend at 10mg/mL in 0.1% sterile acetic acid**
    a. Add appropriate volume of 0.1% sterile acetic acid to collagen sponge to reconstitute at a concentration of 10ml/ml for the lab to use
    b. Shake the tube vigorously, then place on rocker in 4C for a few days to allow all the air bubbles to be removed
5. **Clean and shut off the lyophilizer**
    a. Run the lyophilizer and set the vacuum pump ballast to 'II' for 15-20 min. This will allow all the acetic acid and other contaminants to be removed from the vacuum pump
    b. Set the vacuum pump ballast back to "0" and turn of the lyophilizer and pump
    c. Open the valves on lyophilizer and wait for the inside to thaw
    d. Clean inside with ethanol and allow to dry until next use

Appendix C:

Tumor dissociation for single cell RNA sequencing

C.1 Overview

This protocol was developed for dissociating tumors from the MMTV-PyMT mouse model to obtain highly viable single cell suspensions with sufficient quality for single cell RNA sequencing techniques. This protocol was specifically designed to achieve greater than 90% cell viability and minimize cell clusters and debris in as little time as possible.

C.2 Materials

- Human Tumor dissociation kit (Miltenyi Biotech; 130-095-929)
- RPMI1640
- MACS Smart Strainers 70 and 30 microns
- gentleMACS C Tubes
- gentleMACS dissociator
- TrypLE
- 1X HBSS + 3mM EDTA
- 1X PBS + 3mM EDTA
- 1X PBS

C.2 Protocol

1. Prepare enzyme mix by adding 4.7 mL of RPMI 1640 with 200 uL of Enzyme H, 100 uL of Enzyme R, and 25 uL of Enzyme A in a gentle MACS tube
    a. Prepare fresh right before mouse dissection and keep on ice
2. Wash isolated tumors in ice cold HBSS + 3mM EDTA in a 15 mL conical tube
    a. Leave 1-2 mL of airspace in conical tube
    b. Invert tube 3-5 times to thoroughly

    c. Repeat step 2x with fresh conical tube
3. Place tumors into sterile petri dish
4. Mince tumor into small pieces using sterile razor
    a. Approximately 1-2 mm pieces are sufficiently small
5. Transfer minced tissue into gentleMACS C Tube containing enzyme cocktail
6. Run gentleMACS program h-tumor-01
7. Incubate sample for 30 minutes at 37C on orbital shaker set to medium
    a. Tape samples down to restrict rolling
    b. Ensure all tissue is in media and not on sides of tube
8. Run gentleMACS program h-tumor-01
9. Incubate sample for 30 minutes at 37C on orbital shaker set to medium
10. Run gentleMACS program h-tumor-01
11. Filter sample through 70 micron strainer into 50 mL conical tube
    a. Wash gentleMACS tube with additional 20 mL media and strain
12. Centrifuge at 300 xg for 5 minutes
13. Resuspend in 10-15 mL of ice cold HBSS + 3mM EDTA
    a. Depends on tumor size and amount of debris. Use enough so that cells are fully resuspended
14. Centrifuge at 300 xg for 5 minutes
    a. Repeat steps 13 and 14 up to 3 times until debris are mostly removed
    b. Check for debris by examining aliquot on hematocytometer
15. Resuspend in 10 mL of HBSS
16. Centrifuge at 100 xg for 3 minutes
    a. This step aids in removing large debris, large cell clusters, and red blood cells
    b. Repeat step up to 3 times until no red is left in pellet
17. Resuspend in 3mL of prewarmed TrypLE for 5 minutes at 37C under gentle agitation on orbital shaker
    a. Can incubate for up to 10 minutes if you have a significant amount of large cell clusters
18. Dilute sample with 7 mL of PBS + 3mM EDTA

19. Centrifuge at 300 xg for 5 minutes
20. Resuspend in 10-15 mL of PBS
    a. EDTA must be removed from all steps at this point
    b. Repeat steps 19 and 20 twice
21. Filter samples through 30 micron strainer into 15 mL conical tube
22. Centrifuge sample at 300 xg for 7 minutes
23. Resuspend in PBS and proceed to single cell RNA sequencing encapsulation

References

1. Common Cancer Sites - Cancer Stat Facts Available online: https://seer.cancer.gov/statfacts/html/common.html (accessed on 4 December 2023).
2. M.D, R.W.R. *Cancer Biology*; Oxford University Press, 2007; ISBN 978-0-19-974815-0.
3. Zhang, Y.; Narayanan, S.P.; Mannan, R.; Raskind, G.; Wang, X.; Vats, P.; Su, F.; Hosseini, N.; Cao, X.; Kumar-Sinha, C.; et al. Single-Cell Analyses of Renal Cell Cancers Reveal Insights into Tumor Microenvironment, Cell of Origin, and Therapy Response. *Proceedings of the National Academy of Sciences* **2021**, *118*, e2103240118, doi:10.1073/pnas.2103240118.
4. Taufalele, P.V.; Wang, W.; Simmons, A.J.; Southard-Smith, A.N.; Chen, B.; Greenlee, J.D.; King, M.R.; Lau, K.S.; Hassane, D.C.; Bordeleau, F.; et al. Matrix Stiffness Enhances Cancer-Macrophage Interactions and M2-like Macrophage Accumulation in the Breast Tumor Microenvironment. *Acta Biomaterialia* **2023**, *163*, 365–377, doi:10.1016/j.actbio.2022.04.031.
5. Olsson, L.T.; Williams, L.A.; Midkiff, B.R.; Kirk, E.L.; Troester, M.A.; Calhoun, B.C. Quantitative Analysis of Breast Cancer Tissue Composition and Associations with Tumor Subtype. *Human Pathology* **2022**, *123*, 84–92, doi:10.1016/j.humpath.2022.02.013.
6. Valdés-Mora, F.; Salomon, R.; Gloss, B.S.; Law, A.M.K.; Venhuizen, J.; Castillo, L.; Murphy, K.J.; Magenau, A.; Papanicolaou, M.; Rodriguez De La Fuente, L.; et al. Single-Cell Transcriptomics Reveals Involution Mimicry during the Specification of the Basal Breast Cancer Subtype. *Cell Reports* **2021**, *35*, 108945, doi:10.1016/j.celrep.2021.108945.
7. Lai, H.; Cheng, X.; Liu, Q.; Luo, W.; Liu, M.; Zhang, M.; Miao, J.; Ji, Z.; Lin, G.N.; Song, W.; et al. Single-Cell RNA Sequencing Reveals the Epithelial Cell Heterogeneity and Invasive Subpopulation in Human Bladder Cancer. *International Journal of Cancer* **2021**, *149*, 2099–2115, doi:10.1002/ijc.33794.
8. Wu, F.; Fan, J.; He, Y.; Xiong, A.; Yu, J.; Li, Y.; Zhang, Y.; Zhao, W.; Zhou, F.; Li, W.; et al. Single-Cell Profiling of Tumor Heterogeneity and the Microenvironment in Advanced Non-Small Cell Lung Cancer. *Nat Commun* **2021**, *12*, 2540, doi:10.1038/s41467-021-22801-0.
9. Loeb, L.A.; Loeb, K.R.; Anderson, J.P. Multiple Mutations and Cancer. *Proceedings of the National Academy of Sciences* **2003**, *100*, 776–781, doi:10.1073/pnas.0334858100.

10. Waarts, M.R.; Stonestrom, A.J.; Park, Y.C.; Levine, R.L. Targeting Mutations in Cancer. *J Clin Invest* **2022**, *132*, doi:10.1172/JCI154943.
11. Bignold, L.P.; Coghlan, B.L.D.; Jersmann, H.P.A. Cancer Morphology, Carcinogenesis and Genetic Instability: A Background. In *Cancer: Cell Structures, Carcinogens and Genomic Instability*; Experientia Supplementum; Birkhäuser: Basel, 2006; pp. 1–24 ISBN 978-3-7643-7378-8.
12. Fischer, E.G. Nuclear Morphology and the Biology of Cancer Cells. *Acta Cytologica* **2020**, *64*, 511–519, doi:10.1159/000508780.
13. Hanahan, D.; Weinberg, R.A. Hallmarks of Cancer: The Next Generation. *Cell* **2011**, *144*, 646–674, doi:10.1016/j.cell.2011.02.013.
14. Tubiana, M. Tumor Cell Proliferation Kinetics and Tumor Growth Rate. *Acta Oncologica* **1989**, *28*, 113–121, doi:10.3109/02841868909111193.
15. Mitchison, T.J. The Proliferation Rate Paradox in Antimitotic Chemotherapy. *MBoC* **2012**, *23*, 1–6, doi:10.1091/mbc.e10-04-0335.
16. Christofori, G. New Signals from the Invasive Front. *Nature* **2006**, *441*, 444–450, doi:10.1038/nature04872.
17. Tiwari, N.; Gheldof, A.; Tatari, M.; Christofori, G. EMT as the Ultimate Survival Mechanism of Cancer Cells. *Seminars in Cancer Biology* **2012**, *22*, 194–207, doi:10.1016/j.semcancer.2012.02.013.
18. Singh, M.; Yelle, N.; Venugopal, C.; Singh, S.K. EMT: Mechanisms and Therapeutic Implications. *Pharmacology & Therapeutics* **2018**, *182*, 80–94, doi:10.1016/j.pharmthera.2017.08.009.
19. Carmeliet, P.; Jain, R.K. Angiogenesis in Cancer and Other Diseases. *Nature* **2000**, *407*, 249–257, doi:10.1038/35025220.
20. Shenoy, A.K.; Lu, J. Cancer Cells Remodel Themselves and Vasculature to Overcome the Endothelial Barrier. *Cancer Letters* **2016**, *380*, 534–544, doi:10.1016/j.canlet.2014.10.031.
21. Liby, T.A.; Spyropoulos, P.; Buff Lindner, H.; Eldridge, J.; Beeson, C.; Hsu, T.; Muise-Helmericks, R.C. Akt3 Controls Vascular Endothelial Growth Factor Secretion and Angiogenesis in Ovarian Cancer Cells. *International Journal of Cancer* **2012**, *130*, 532–543, doi:10.1002/ijc.26010.
22. Aslan, C.; Maralbashi, S.; Salari, F.; Kahroba, H.; Sigaroodi, F.; Kazemi, T.; Kharaziha, P. Tumor-Derived Exosomes: Implication in Angiogenesis and Antiangiogenesis Cancer Therapy. *Journal of Cellular Physiology* **2019**, *234*, 16885–16903, doi:10.1002/jcp.28374.

23. He, Q.; Ye, A.; Ye, W.; Liao, X.; Qin, G.; Xu, Y.; Yin, Y.; Luo, H.; Yi, M.; Xian, L.; et al. Cancer-Secreted Exosomal miR-21-5p Induces Angiogenesis and Vascular Permeability by Targeting KRIT1. *Cell Death Dis* **2021**, *12*, 1–14, doi:10.1038/s41419-021-03803-8.
24. Gilboa, E. How Tumors Escape Immune Destruction and What We Can Do about It. *Cancer Immunol Immunother* **1999**, *48*, 382–385, doi:10.1007/s002620050590.
25. Vyas, M.; Müller, R.; Pogge von Strandmann, E. Antigen Loss Variants: Catching Hold of Escaping Foes. *Frontiers in Immunology* **2017**, *8*.
26. Dhatchinamoorthy, K.; Colbert, J.D.; Rock, K.L. Cancer Immune Evasion Through Loss of MHC Class I Antigen Presentation. *Frontiers in Immunology* **2021**, *12*.
27. Pribluda, A.; Elyada, E.; Wiener, Z.; Hamza, H.; Goldstein, R.E.; Biton, M.; Burstain, I.; Morgenstern, Y.; Brachya, G.; Billauer, H.; et al. A Senescence-Inflammatory Switch from Cancer-Inhibitory to Cancer-Promoting Mechanism. *Cancer Cell* **2013**, *24*, 242–256, doi:10.1016/j.ccr.2013.06.005.
28. Samadi, A.K.; Bilsland, A.; Georgakilas, A.G.; Amedei, A.; Amin, A.; Bishayee, A.; Azmi, A.S.; Lokeshwar, B.L.; Grue, B.; Panis, C.; et al. A Multi-Targeted Approach to Suppress Tumor-Promoting Inflammation. *Seminars in Cancer Biology* **2015**, *35*, S151–S184, doi:10.1016/j.semcancer.2015.03.006.
29. Warburg, O. The Metabolism of Carcinoma Cells1. *The Journal of Cancer Research* **1925**, *9*, 148–163, doi:10.1158/jcr.1925.148.
30. Kroemer, G.; Pouyssegur, J. Tumor Cell Metabolism: Cancer’s Achilles’ Heel. *Cancer Cell* **2008**, *13*, 472–482, doi:10.1016/j.ccr.2008.05.005.
31. Martinez-Outschoorn, U.E.; Peiris-Pagés, M.; Pestell, R.G.; Sotgia, F.; Lisanti, M.P. Cancer Metabolism: A Therapeutic Perspective. *Nat Rev Clin Oncol* **2017**, *14*, 11–31, doi:10.1038/nrclinonc.2016.60.
32. Chang, A. Chemotherapy, Chemoresistance and the Changing Treatment Landscape for NSCLC. *Lung Cancer* **2011**, *71*, 3–10, doi:10.1016/j.lungcan.2010.08.022.
33. Ippolito, M.R.; Martis, V.; Martin, S.; Tijhuis, A.E.; Hong, C.; Wardenaar, R.; Dumont, M.; Zerbib, J.; Spierings, D.C.J.; Fachinetti, D.; et al. Gene Copy-Number Changes and Chromosomal Instability Induced by Aneuploidy Confer Resistance to Chemotherapy. *Developmental Cell* **2021**, *56*, 2440-2454.e6, doi:10.1016/j.devcel.2021.07.006.
34. Zhang, M.; Zhuang, G.; Sun, X.; Shen, Y.; Wang, W.; Li, Q.; Di, W. TP53 Mutation-Mediated Genomic Instability Induces the Evolution of Chemoresistance and Recurrence in Epithelial Ovarian Cancer. *Diagnostic Pathology* **2017**, *12*, 16, doi:10.1186/s13000-017-0605-8.

35. Charles A Janeway, J.; Travers, P.; Walport, M.; Shlomchik, M.J. Principles of Innate and Adaptive Immunity. In *Immunobiology: The Immune System in Health and Disease. 5th edition*; Garland Science, 2001.
36. Johnston, R.B. Monocytes and Macrophages. *N Engl J Med* **1988**, *318*, 747–752, doi:10.1056/NEJM198803243181205.
37. Chen, S.; Lai, S.W.T.; Brown, C.E.; Feng, M. Harnessing and Enhancing Macrophage Phagocytosis for Cancer Therapy. *Frontiers in Immunology* **2021**, *12*.
38. Wynn, T.A.; Chawla, A.; Pollard, J.W. Macrophage Biology in Development, Homeostasis and Disease. *Nature* **2013**, *496*, 445–455, doi:10.1038/nature12034.
39. Kloc, M.; Ghobrial, R.M.; Wosik, J.; Lewicka, A.; Lewicki, S.; Kubiak, J.Z. Macrophage Functions in Wound Healing. *Journal of Tissue Engineering and Regenerative Medicine* **2019**, *13*, 99–109, doi:10.1002/term.2772.
40. Lahmar, Q.; Keirsse, J.; Laoui, D.; Movahedi, K.; Van Overmeire, E.; Van Ginderachter, J.A. Tissue-Resident versus Monocyte-Derived Macrophages in the Tumor Microenvironment. *Biochimica et Biophysica Acta (BBA) - Reviews on Cancer* **2016**, *1865*, 23–34, doi:10.1016/j.bbcan.2015.06.009.
41. Murray, P.J. Macrophage Polarization. *Annual Review of Physiology* **2017**, *79*, 541–566, doi:10.1146/annurev-physiol-022516-034339.
42. Alberto Mantovani; Antonio Sica; Locati, M. Macrophage Polarization Comes of Age. *Immunity* **2005**, *23*, 344–346, doi:10.1016/j.immuni.2005.10.001.
43. Sica, A.; Larghi, P.; Mancino, A.; Rubino, L.; Porta, C.; Totaro, M.G.; Rimoldi, M.; Biswas, S.K.; Allavena, P.; Mantovani, A. Macrophage Polarization in Tumour Progression. *Seminars in Cancer Biology* **2008**, *18*, 349–355, doi:10.1016/j.semcancer.2008.03.004.
44. Qian, B.-Z.; Pollard, J.W. Macrophage Diversity Enhances Tumor Progression and Metastasis. *Cell* **2010**, *141*, 39–51, doi:10.1016/j.cell.2010.03.014.
45. Ma, J.; Liu, L.; Che, G.; Yu, N.; Dai, F.; You, Z. The M1 Form of Tumor-Associated Macrophages in Non-Small Cell Lung Cancer Is Positively Associated with Survival Time. *BMC Cancer* **2010**, *10*, 112, doi:10.1186/1471-2407-10-112.
46. Pan, Y.; Yu, Y.; Wang, X.; Zhang, T. Tumor-Associated Macrophages in Tumor Immunity. *Frontiers in Immunology* **2020**, *11*.
47. Chanmee, T.; Ontong, P.; Konno, K.; Itano, N. Tumor-Associated Macrophages as Major Players in the Tumor Microenvironment. *Cancers* **2014**, *6*, 1670–1690, doi:10.3390/cancers6031670.

48. Squadrito, M.L.; De Palma, M. Macrophage Regulation of Tumor Angiogenesis: Implications for Cancer Therapy. *Molecular Aspects of Medicine* **2011**, *32*, 123–145, doi:10.1016/j.mam.2011.04.005.

49. Kalluri, R.; Zeisberg, M. Fibroblasts in Cancer. *Nat Rev Cancer* **2006**, *6*, 392–401, doi:10.1038/nrc1877.

50. Hanley, C.J.; Mellone, M.; Ford, K.; Thirdborough, S.M.; Mellows, T.; Frampton, S.J.; Smith, D.M.; Harden, E.; Szyndralewiez, C.; Bullock, M.; et al. Targeting the Myofibroblastic Cancer-Associated Fibroblast Phenotype Through Inhibition of NOX4. *JNCI: Journal of the National Cancer Institute* **2018**, *110*, 109–120, doi:10.1093/jnci/djx121.

51. Anderberg, C.; Pietras, K. On the Origin of Cancer-Associated Fibroblasts. *Cell Cycle* **2009**, *8*, 1461–1465, doi:10.4161/cc.8.10.8557.

52. Östman, A.; Augsten, M. Cancer-Associated Fibroblasts and Tumor Growth – Bystanders Turning into Key Players. *Current Opinion in Genetics & Development* **2009**, *19*, 67–73, doi:10.1016/j.gde.2009.01.003.

53. Kalluri, R. The Biology and Function of Fibroblasts in Cancer. *Nat Rev Cancer* **2016**, *16*, 582–598, doi:10.1038/nrc.2016.73.

54. Wang, F.-T.; Sun, W.; Zhang, J.-T.; Fan, Y.-Z. Cancer-associated Fibroblast Regulation of Tumor Neo-angiogenesis as a Therapeutic Target in Cancer (Review). *Oncology Letters* **2019**, *17*, 3055–3065, doi:10.3892/ol.2019.9973.

55. Mao, X.; Xu, J.; Wang, W.; Liang, C.; Hua, J.; Liu, J.; Zhang, B.; Meng, Q.; Yu, X.; Shi, S. Crosstalk between Cancer-Associated Fibroblasts and Immune Cells in the Tumor Microenvironment: New Findings and Future Perspectives. *Molecular Cancer* **2021**, *20*, 131, doi:10.1186/s12943-021-01428-1.

56. Monteran, L.; Erez, N. The Dark Side of Fibroblasts: Cancer-Associated Fibroblasts as Mediators of Immunosuppression in the Tumor Microenvironment. *Frontiers in Immunology* **2019**, *10*.

57. Glabman, R.A.; Choyke, P.L.; Sato, N. Cancer-Associated Fibroblasts: Tumorigenicity and Targeting for Cancer Therapy. *Cancers* **2022**, *14*, 3906, doi:10.3390/cancers14163906.

58. Sumpio, B.E.; Timothy Riley, J.; Dardik, A. Cells in Focus: Endothelial Cell. *The International Journal of Biochemistry & Cell Biology* **2002**, *34*, 1508–1512, doi:10.1016/S1357-2725(02)00075-4.

59. Ghosh, K.; Thodeti, C.K.; Dudley, A.C.; Mammoto, A.; Klagsbrun, M.; Ingber, D.E. Tumor-Derived Endothelial Cells Exhibit Aberrant Rho-Mediated Mechanosensing and Abnormal Angiogenesis in Vitro. *PNAS* **2008**, *105*, 11305–11310, doi:10.1073/pnas.0800835105.

60. Dudley, A.C. Tumor Endothelial Cells. *Cold Spring Harb Perspect Med* **2012**, *2*, a006536, doi:10.1101/cshperspect.a006536.

61. Maishi, N.; Annan, D.A.; Kikuchi, H.; Hida, Y.; Hida, K. Tumor Endothelial Heterogeneity in Cancer Progression. *Cancers* **2019**, *11*, 1511, doi:10.3390/cancers11101511.

62. Hida, K.; Maishi, N.; Annan, D.A.; Hida, Y. Contribution of Tumor Endothelial Cells in Cancer Progression. *International Journal of Molecular Sciences* **2018**, *19*, 1272, doi:10.3390/ijms19051272.

63. Lugano, R.; Ramachandran, M.; Dimberg, A. Tumor Angiogenesis: Causes, Consequences, Challenges and Opportunities. *Cell. Mol. Life Sci.* **2020**, *77*, 1745–1770, doi:10.1007/s00018-019-03351-7.

64. Hida, K.; Ohga, N.; Akiyama, K.; Maishi, N.; Hida, Y. Heterogeneity of Tumor Endothelial Cells. *Cancer Science* **2013**, *104*, 1391–1395, doi:https://doi.org/10.1111/cas.12251.

65. Maishi, N.; Hida, K. Tumor Endothelial Cells Accelerate Tumor Metastasis. *Cancer Science* **2017**, *108*, 1921–1926, doi:10.1111/cas.13336.

66. Forster, J.C.; Harriss-Phillips, W.M.; Douglass, M.J.; Bezak, E. A Review of the Development of Tumor Vasculature and Its Effects on the Tumor Microenvironment. *Hypoxia* **2017**, *5*, 21–32, doi:10.2147/HP.S133231.

67. Nagl, L.; Horvath, L.; Pircher, A.; Wolf, D. Tumor Endothelial Cells (TECs) as Potential Immune Directors of the Tumor Microenvironment – New Findings and Future Perspectives. *Frontiers in Cell and Developmental Biology* **2020**, *8*.

68. Nanda, A.; St. Croix, B. Tumor Endothelial Markers: New Targets for Cancer Therapy. *Current Opinion in Oncology* **2004**, *16*, 44.

69. Sakurai, Y.; Akita, H.; Harashima, H. Targeting Tumor Endothelial Cells with Nanoparticles. *International Journal of Molecular Sciences* **2019**, *20*, 5819, doi:10.3390/ijms20235819.

70. Martin, J.D.; Seano, G.; Jain, R.K. Normalizing Function of Tumor Vessels: Progress, Opportunities, and Challenges. *Annual Review of Physiology* **2019**, *81*, 505–534, doi:10.1146/annurev-physiol-020518-114700.

71. Frantz, C.; Stewart, K.M.; Weaver, V.M. The Extracellular Matrix at a Glance. *Journal of Cell Science* **2010**, *123*, 4195–4200, doi:10.1242/jcs.023820.

72. Ahrens, T.D.; Bang-Christensen, S.R.; Jørgensen, A.M.; Løppke, C.; Spliid, C.B.; Sand, N.T.; Clausen, T.M.; Salanti, A.; Agerbæk, M.Ø. The Role of Proteoglycans in Cancer Metastasis and Circulating Tumor Cell Analysis. *Frontiers in Cell and Developmental Biology* **2020**, *8*.
73. Henke, E.; Nandigama, R.; Ergün, S. Extracellular Matrix in the Tumor Microenvironment and Its Impact on Cancer Therapy. *Frontiers in Molecular Biosciences* **2020**, *6*.
74. Xu, M.; Zhang, T.; Xia, R.; Wei, Y.; Wei, X. Targeting the Tumor Stroma for Cancer Therapy. *Mol Cancer* **2022**, *21*, 208, doi:10.1186/s12943-022-01670-1.
75. Hoffmann, E.J.; Ponik, S.M. Biomechanical Contributions to Macrophage Activation in the Tumor Microenvironment. *Frontiers in Oncology* **2020**, *10*.
76. Pupa, S.M.; Ménard, S.; Forti, S.; Tagliabue, E. New Insights into the Role of Extracellular Matrix during Tumor Onset and Progression. *Journal of Cellular Physiology* **2002**, *192*, 259–267, doi:10.1002/jcp.10142.
77. Piperigkou, Z.; Kyriakopoulou, K.; Koutsakis, C.; Mastronikolis, S.; Karamanos, N.K. Key Matrix Remodeling Enzymes: Functions and Targeting in Cancer. *Cancers* **2021**, *13*, 1441, doi:10.3390/cancers13061441.
78. Brassart-Pasco, S.; Brézillon, S.; Brassart, B.; Ramont, L.; Oudart, J.-B.; Monboisse, J.C. Tumor Microenvironment: Extracellular Matrix Alterations Influence Tumor Progression. *Frontiers in Oncology* **2020**, *10*.
79. Leeming, D.J.; Bay-Jensen, A.C.; Vassiliadis, E.; Larsen, M.R.; Henriksen, K.; Karsdal, M.A. Post-Translational Modifications of the Extracellular Matrix Are Key Events in Cancer Progression: Opportunities for Biochemical Marker Development. *Biomarkers* **2011**, *16*, 193–205, doi:10.3109/1354750X.2011.557440.
80. Pickup, M.W.; Mouw, J.K.; Weaver, V.M. The Extracellular Matrix Modulates the Hallmarks of Cancer. *EMBO reports* **2014**, *15*, 1243–1253, doi:10.15252/embr.201439246.
81. Campbell, N.E.; Kellenberger, L.; Greenaway, J.; Moorehead, R.A.; Linnerth-Petrik, N.M.; Petrik, J. Extracellular Matrix Proteins and Tumor Angiogenesis. *Journal of Oncology* **2010**, *2010*, e586905, doi:10.1155/2010/586905.
82. Gordon-Weeks, A.; Yuzhalin, A.E. Cancer Extracellular Matrix Proteins Regulate Tumour Immunity. *Cancers* **2020**, *12*, 3331, doi:10.3390/cancers12113331.
83. Socovich, A.M.; Naba, A. The Cancer Matrisome: From Comprehensive Characterization to Biomarker Discovery. *Seminars in Cell & Developmental Biology* **2019**, *89*, 157–166, doi:10.1016/j.semcdb.2018.06.005.

84. Guimarães, C.F.; Gasperini, L.; Marques, A.P.; Reis, R.L. The Stiffness of Living Tissues and Its Implications for Tissue Engineering. *Nat Rev Mater* **2020**, *5*, 351–370, doi:10.1038/s41578-019-0169-1.

85. Zanotelli, M.R.; Reinhart-King, C.A. Mechanical Forces in Tumor Angiogenesis. In *Biomechanics in Oncology*; Dong, C., Zahir, N., Konstantopoulos, K., Eds.; Advances in Experimental Medicine and Biology; Springer International Publishing: Cham, 2018; pp. 91–112 ISBN 978-3-319-95294-9.

86. Luo, Q.; Kuang, D.; Zhang, B.; Song, G. Cell Stiffness Determined by Atomic Force Microscopy and Its Correlation with Cell Motility. *Biochimica et Biophysica Acta (BBA) - General Subjects* **2016**, *1860*, 1953–1960, doi:10.1016/j.bbagen.2016.06.010.

87. Discher, D.E.; Janmey, P.; Wang, Y. Tissue Cells Feel and Respond to the Stiffness of Their Substrate. *Science* **2005**, *310*, 1139–1143, doi:10.1126/science.1116995.

88. Deng, B.; Zhao, Z.; Kong, W.; Han, C.; Shen, X.; Zhou, C. Biological Role of Matrix Stiffness in Tumor Growth and Treatment. *J Transl Med* **2022**, *20*, 540, doi:10.1186/s12967-022-03768-y.

89. Barbazán, J.; Matic Vignjevic, D. Cancer Associated Fibroblasts: Is the Force the Path to the Dark Side? *Current Opinion in Cell Biology* **2019**, *56*, 71–79, doi:10.1016/j.ceb.2018.09.002.

90. Lampi, M.C.; Reinhart-King, C.A. Targeting Extracellular Matrix Stiffness to Attenuate Disease: From Molecular Mechanisms to Clinical Trials. *Science Translational Medicine* **2018**, *10*, eaao0475, doi:10.1126/scitranslmed.aao0475.

91. Gimbrone, M.A., Jr.; Cotran, R.S.; Leapman, S.B.; Folkman, J. Tumor Growth and Neovascularization: An Experimental Model Using the Rabbit Cornea2. *JNCI: Journal of the National Cancer Institute* **1974**, *52*, 413–427, doi:10.1093/jnci/52.2.413.

92. Folkman, J. The Vascularization of Tumors. *Scientific American* **1976**, *234*, 58–73.

93. Zetter, B.R. The Scientific Contributions of M. Judah Folkman to Cancer Research. *Nat Rev Cancer* **2008**, *8*, 647–654, doi:10.1038/nrc2458.

94. Morikawa, S.; Baluk, P.; Kaidoh, T.; Haskell, A.; Jain, R.K.; McDonald, D.M. Abnormalities in Pericytes on Blood Vessels and Endothelial Sprouts in Tumors. *The American Journal of Pathology* **2002**, *160*, 985–1000, doi:10.1016/S0002-9440(10)64920-6.

95. Bordeleau, F.; Mason, B.N.; Lollis, E.M.; Mazzola, M.; Zanotelli, M.R.; Somasegar, S.; Califano, J.P.; Montague, C.; LaValley, D.J.; Huynh, J.; et al. Matrix Stiffening Promotes a

Tumor Vasculature Phenotype. *PNAS* **2017**, *114*, 492–497, doi:10.1073/pnas.1613855114.

96. Ribatti, D.; Nico, B.; Crivellato, E.; Vacca, A. The Structure of the Vascular Network of Tumors. *Cancer Letters* **2007**, *248*, 18–23, doi:10.1016/j.canlet.2006.06.007.
97. Matuszewska, K.; Pereira, M.; Petrik, D.; Lawler, J.; Petrik, J. Normalizing Tumor Vasculature to Reduce Hypoxia, Enhance Perfusion, and Optimize Therapy Uptake. *Cancers* **2021**, *13*, 4444, doi:10.3390/cancers13174444.
98. Viallard, C.; Larrivée, B. Tumor Angiogenesis and Vascular Normalization: Alternative Therapeutic Targets. *Angiogenesis* **2017**, *20*, 409–426, doi:10.1007/s10456-017-9562-9.
99. Belotti, D.; Pinessi, D.; Taraboletti, G. Alternative Vascularization Mechanisms in Tumor Resistance to Therapy. *Cancers* **2021**, *13*, 1912, doi:10.3390/cancers13081912.
100. Jain, R.K. Normalization of Tumor Vasculature: An Emerging Concept in Antiangiogenic Therapy. *Science* **2005**, *307*, 58–62, doi:10.1126/science.1104819.
101. Hynes, R.O. The Extracellular Matrix: Not Just Pretty Fibrils. *Science* **2009**, *326*, 1216–1219, doi:10.1126/science.1176009.
102. Lu, P.; Weaver, V.M.; Werb, Z. The Extracellular Matrix: A Dynamic Niche in Cancer Progression. *J Cell Biol* **2012**, *196*, 395–406, doi:10.1083/jcb.201102147.
103. Kumar, S.; Weaver, V.M. Mechanics, Malignancy, and Metastasis: The Force Journey of a Tumor Cell. *Cancer Metastasis Rev* **2009**, *28*, 113–127, doi:10.1007/s10555-008-9173-4.
104. Kharaishvili, G.; Simkova, D.; Bouchalova, K.; Gachechiladze, M.; Narsia, N.; Bouchal, J. The Role of Cancer-Associated Fibroblasts, Solid Stress and Other Microenvironmental Factors in Tumor Progression and Therapy Resistance. *Cancer Cell Int.* **2014**, *14*, 41, doi:10.1186/1475-2867-14-41.
105. Levental, K.R.; Yu, H.; Kass, L.; Lakins, J.N.; Egeblad, M.; Erler, J.T.; Fong, S.F.T.; Csiszar, K.; Giaccia, A.; Weninger, W.; et al. Matrix Crosslinking Forces Tumor Progression by Enhancing Integrin Signaling. *Cell* **2009**, *139*, 891–906, doi:10.1016/j.cell.2009.10.027.
106. Schrader, J.; Gordon-Walker, T.T.; Aucott, R.L.; van Deemter, M.; Quaas, A.; Walsh, S.; Benten, D.; Forbes, S.J.; Wells, R.G.; Iredale, J.P. Matrix Stiffness Modulates Proliferation, Chemotherapeutic Response and Dormancy in Hepatocellular Carcinoma Cells. *Hepatology* **2011**, *53*, 1192–1205, doi:10.1002/hep.24108.
107. Zaman, M.H.; Trapani, L.M.; Sieminski, A.L.; MacKellar, D.; Gong, H.; Kamm, R.D.; Wells, A.; Lauffenburger, D.A.; Matsudaira, P. Migration of Tumor Cells in 3D Matrices Is

Governed by Matrix Stiffness along with Cell-Matrix Adhesion and Proteolysis. *PNAS* **2006**, *103*, 10889–10894, doi:10.1073/pnas.0604460103.

108. Handorf, A.M.; Zhou, Y.; Halanski, M.A.; Li, W.-J. Tissue Stiffness Dictates Development, Homeostasis, and Disease Progression. *Organogenesis* **2015**, *11*, 1–15, doi:10.1080/15476278.2015.1019687.

109. Reid, S.E.; Kay, E.J.; Neilson, L.J.; Henze, A.-T.; Serneels, J.; McGhee, E.J.; Dhayade, S.; Nixon, C.; Mackey, J.B.; Santi, A.; et al. Tumor Matrix Stiffness Promotes Metastatic Cancer Cell Interaction with the Endothelium. *The EMBO Journal* **2017**, *36*, 2373–2389, doi:10.15252/embj.201694912.

110. Carey, S.P.; Kraning-Rush, C.M.; Williams, R.M.; Reinhart-King, C.A. Biophysical Control of Invasive Tumor Cell Behavior by Extracellular Matrix Microarchitecture. *Biomaterials* **2012**, *33*, 4157–4165, doi:10.1016/j.biomaterials.2012.02.029.

111. Wolf, K.; te Lindert, M.; Krause, M.; Alexander, S.; te Riet, J.; Willis, A.L.; Hoffman, R.M.; Figdor, C.G.; Weiss, S.J.; Friedl, P. Physical Limits of Cell Migration: Control by ECM Space and Nuclear Deformation and Tuning by Proteolysis and Traction Force. *The Journal of Cell Biology* **2013**, *201*, 1069–1084, doi:10.1083/jcb.201210152.

112. Harjanto, D.; Maffei, J.S.; Zaman, M.H. Quantitative Analysis of the Effect of Cancer Invasiveness and Collagen Concentration on 3D Matrix Remodeling. *PLOS ONE* **2011**, *6*, e24891, doi:10.1371/journal.pone.0024891.

113. Provenzano, P.P.; Eliceiri, K.W.; Campbell, J.M.; Inman, D.R.; White, J.G.; Keely, P.J. Collagen Reorganization at the Tumor-Stromal Interface Facilitates Local Invasion. *BMC Med* **2006**, *4*, 38, doi:10.1186/1741-7015-4-38.

114. Provenzano, P.P.; Inman, D.R.; Eliceiri, K.W.; Trier, S.M.; Keely, P.J. Contact Guidance Mediated Three-Dimensional Cell Migration Is Regulated by Rho/ROCK-Dependent Matrix Reorganization. *Biophysical Journal* **2008**, *95*, 5374–5384, doi:10.1529/biophysj.108.133116.

115. Conklin, M.W.; Eickhoff, J.C.; Riching, K.M.; Pehlke, C.A.; Eliceiri, K.W.; Provenzano, P.P.; Friedl, A.; Keely, P.J. Aligned Collagen Is a Prognostic Signature for Survival in Human Breast Carcinoma. *Am J Pathol* **2011**, *178*, 1221–1232, doi:10.1016/j.ajpath.2010.11.076.

116. Zanotelli, M.R.; Goldblatt, Z.E.; Miller, J.P.; Bordeleau, F.; Li, J.; VanderBurgh, J.A.; Lampi, M.C.; King, M.R.; Reinhart-King, C.A. Regulation of ATP Utilization during Metastatic Cell Migration by Collagen Architecture. *Mol Biol Cell* **2018**, *29*, 1–9, doi:10.1091/mbc.E17-01-0041.

117. Han, W.; Chen, S.; Yuan, W.; Fan, Q.; Tian, J.; Wang, X.; Chen, L.; Zhang, X.; Wei, W.; Liu, R.; et al. Oriented Collagen Fibers Direct Tumor Cell Intravasation. *Proceedings of the National Academy of Sciences* **2016**, *113*, 11208–11213, doi:10.1073/pnas.1610347113.

118. Ray, A.; Slama, Z.M.; Morford, R.K.; Madden, S.A.; Provenzano, P.P. Enhanced Directional Migration of Cancer Stem Cells in 3D Aligned Collagen Matrices. *Biophysical Journal* **2017**, *112*, 1023–1036, doi:10.1016/j.bpj.2017.01.007.

119. Stylianopoulos, T.; Diop-Frimpong, B.; Munn, L.L.; Jain, R.K. Diffusion Anisotropy in Collagen Gels and Tumors: The Effect of Fiber Network Orientation. *Biophysical Journal* **2010**, *99*, 3119–3128, doi:10.1016/j.bpj.2010.08.065.

120. Riching, K.M.; Cox, B.L.; Salick, M.R.; Pehlke, C.; Riching, A.S.; Ponik, S.M.; Bass, B.R.; Crone, W.C.; Jiang, Y.; Weaver, A.M.; et al. 3D Collagen Alignment Limits Protrusions to Enhance Breast Cancer Cell Persistence. *Biophys J* **2014**, *107*, 2546–2558, doi:10.1016/j.bpj.2014.10.035.

121. Verzijl, N.; DeGroot, J.; Zaken, C.B.; Braun-Benjamin, O.; Maroudas, A.; Bank, R.A.; Mizrahi, J.; Schalkwijk, C.G.; Thorpe, S.R.; Baynes, J.W.; et al. Crosslinking by Advanced Glycation End Products Increases the Stiffness of the Collagen Network in Human Articular Cartilage: A Possible Mechanism through Which Age Is a Risk Factor for Osteoarthritis. *Arthritis & Rheumatism* **2002**, *46*, 114–123, doi:10.1002/1529-0131(200201)46:1<114::AID-ART10025>3.0.CO;2-P.

122. Branco da Cunha, C.; Klumpers, D.D.; Li, W.A.; Koshy, S.T.; Weaver, J.C.; Chaudhuri, O.; Granja, P.L.; Mooney, D.J. Influence of the Stiffness of Three-Dimensional Alginate/Collagen-I Interpenetrating Networks on Fibroblast Biology. *Biomaterials* **2014**, *35*, 8927–8936, doi:10.1016/j.biomaterials.2014.06.047.

123. Jones, C.A.R.; Liang, L.; Lin, D.; Jiao, Y.; Sun, B. The Spatial-Temporal Characteristics of Type I Collagen-Based Extracellular Matrix. *Soft Matter* **2014**, *10*, 8855–8863, doi:10.1039/C4SM01772B.

124. Raub, C.B.; Suresh, V.; Krasieva, T.; Lyubovitsky, J.; Mih, J.D.; Putnam, A.J.; Tromberg, B.J.; George, S.C. Noninvasive Assessment of Collagen Gel Microstructure and Mechanics Using Multiphoton Microscopy. *Biophysical Journal* **2007**, *92*, 2212–2222, doi:10.1529/biophysj.106.097998.

125. P. Carey, S.; E. Goldblatt, Z.; E. Martin, K.; Romero, B.; M. Williams, R.; A. Reinhart-King, C. Local Extracellular Matrix Alignment Directs Cellular Protrusion Dynamics and

Migration through Rac1 and FAK. *Integrative Biology* **2016**, *8*, 821–835, doi:10.1039/C6IB00030D.

126. Ferdman, A.G.; Yannas, I.V. Scattering of Light from Histologic Sections: A New Method for the Analysis of Connective Tissue. *Journal of Investigative Dermatology* **1993**, *100*, 710–716, doi:10.1111/1523-1747.ep12472364.

127. Franke, K.; Sapudom, J.; Kalbitzer, L.; Anderegg, U.; Pompe, T. Topologically Defined Composites of Collagen Types I and V as in Vitro Cell Culture Scaffolds. *Acta Biomaterialia* **2014**, *10*, 2693–2702, doi:10.1016/j.actbio.2014.02.036.

128. Cross, V.L.; Zheng, Y.; Won Choi, N.; Verbridge, S.S.; Sutermaster, B.A.; Bonassar, L.J.; Fischbach, C.; Stroock, A.D. Dense Type I Collagen Matrices That Support Cellular Remodeling and Microfabrication for Studies of Tumor Angiogenesis and Vasculogenesis in Vitro. *Biomaterials* **2010**, *31*, 8596–8607, doi:10.1016/j.biomaterials.2010.07.072.

129. Jansen, K.A.; Licup, A.J.; Sharma, A.; Rens, R.; MacKintosh, F.C.; Koenderink, G.H. The Role of Network Architecture in Collagen Mechanics. *Biophysical Journal* **2018**, *114*, 2665–2678, doi:10.1016/j.bpj.2018.04.043.

130. Yang, Y.; Motte, S.; Kaufman, L.J. Pore Size Variable Type I Collagen Gels and Their Interaction with Glioma Cells. *Biomaterials* **2010**, *31*, 5678–5688, doi:10.1016/j.biomaterials.2010.03.039.

131. Roeder, B.A.; Kokini, K.; Sturgis, J.E.; Robinson, J.P.; Voytik-Harbin, S.L. Tensile Mechanical Properties of Three-Dimensional Type I Collagen Extracellular Matrices with Varied Microstructure. *J Biomech Eng* **2002**, *124*, 214–222.

132. Roeder, B.A.; Kokini, K.; Voytik-Harbin, S.L. Fibril Microstructure Affects Strain Transmission Within Collagen Extracellular Matrices. *J Biomech Eng* **2009**, *131*, 031004-031004–031011, doi:10.1115/1.3005331.

133. Yang, Y.; Leone, L.M.; Kaufman, L.J. Elastic Moduli of Collagen Gels Can Be Predicted from Two-Dimensional Confocal Microscopy. *Biophys J* **2009**, *97*, 2051–2060, doi:10.1016/j.bpj.2009.07.035.

134. Fraley, S.I.; Wu, P.; He, L.; Feng, Y.; Krisnamurthy, R.; Longmore, G.D.; Wirtz, D. Three-Dimensional Matrix Fiber Alignment Modulates Cell Migration and MT1-MMP Utility by Spatially and Temporally Directing Protrusions. *Scientific Reports* **2015**, *5*, doi:10.1038/srep14580.

135. S. Shannon, G.; Novak, T.; Mousoulis, C.; L. Voytik-Harbin, S.; P. Neu, C. Temperature and Concentration Dependent Fibrillogenesis for Improved Magnetic Alignment of Collagen Gels. *RSC Advances* **2015**, *5*, 2113–2121, doi:10.1039/C4RA11480A.

136. Paszek, M.J.; Zahir, N.; Johnson, K.R.; Lakins, J.N.; Rozenberg, G.I.; Gefen, A.; Reinhart-King, C.A.; Margulies, S.S.; Dembo, M.; Boettiger, D.; et al. Tensional Homeostasis and the Malignant Phenotype. *Cancer Cell* **2005**, *8*, 241–254, doi:10.1016/j.ccr.2005.08.010.
137. Xie, J.; Bao, M.; Bruekers, S.M.C.; Huck, W.T.S. Collagen Gels with Different Fibrillar Microarchitectures Elicit Different Cellular Responses. *ACS Applied Materials & Interfaces* **2017**, *9*, 19630–19637, doi:10.1021/acsami.7b03883.
138. Sharma, A.; Licup, A.J.; Jansen, K.A.; Rens, R.; Sheinman, M.; Koenderink, G.H.; MacKintosh, F.C. Strain-Controlled Criticality Governs the Nonlinear Mechanics of Fibre Networks. *Nature Physics* **2016**, *12*, 584–587, doi:10.1038/nphys3628.
139. Ulrich, T.A.; de Juan Pardo, E.M.; Kumar, S. The Mechanical Rigidity of the Extracellular Matrix Regulates the Structure, Motility, and Proliferation of Glioma Cells. *Cancer Res* **2009**, *69*, 4167–4174, doi:10.1158/0008-5472.CAN-08-4859.
140. Wei, S.C.; Fattet, L.; Tsai, J.H.; Guo, Y.; Pai, V.H.; Majeski, H.E.; Chen, A.C.; Sah, R.L.; Taylor, S.S.; Engler, A.J.; et al. Matrix Stiffness Drives Epithelial–Mesenchymal Transition and Tumour Metastasis through a TWIST1–G3BP2 Mechanotransduction Pathway. *Nature Cell Biology* **2015**, *17*, 678–688, doi:10.1038/ncb3157.
141. Rice, A.J.; Cortes, E.; Lachowski, D.; Cheung, B.C.H.; Karim, S.A.; Morton, J.P.; del Río Hernández, A. Matrix Stiffness Induces Epithelial–Mesenchymal Transition and Promotes Chemoresistance in Pancreatic Cancer Cells. *Oncogenesis* **2017**, *6*, e352–e352, doi:10.1038/oncsis.2017.54.
142. Schwager, S.C.; Bordeleau, F.; Zhang, J.; Antonyak, M.A.; Cerione, R.A.; Reinhart-King, C.A. Matrix Stiffness Regulates Microvesicle-Induced Fibroblast Activation. *American Journal of Physiology-Cell Physiology* **2019**, *317*, C82–C92, doi:10.1152/ajpcell.00418.2018.
143. Calvo, F.; Ege, N.; Grande-Garcia, A.; Hooper, S.; Jenkins, R.P.; Chaudhry, S.I.; Harrington, K.; Williamson, P.; Moeendarbary, E.; Charras, G.; et al. Mechanotransduction and YAP-Dependent Matrix Remodelling Is Required for the Generation and Maintenance of Cancer-Associated Fibroblasts. *Nature Cell Biology* **2013**, *15*, 637–646, doi:10.1038/ncb2756.
144. Mason, B.N.; Starchenko, A.; Williams, R.M.; Bonassar, L.J.; Reinhart-King, C.A. Tuning Three-Dimensional Collagen Matrix Stiffness Independently of Collagen Concentration Modulates Endothelial Cell Behavior. *Acta Biomaterialia* **2013**, *9*, 4635–4644, doi:10.1016/j.actbio.2012.08.007.

145. Yeh, Y.-T.; Hur, S.S.; Chang, J.; Wang, K.-C.; Chiu, J.-J.; Li, Y.-S.; Chien, S. Matrix Stiffness Regulates Endothelial Cell Proliferation through Septin 9. *PLoS ONE* **2012**, *7*, e46889, doi:10.1371/journal.pone.0046889.

146. Acerbi, I.; Cassereau, L.; Dean, I.; Shi, Q.; Au, A.; Park, C.; Chen, Y.Y.; Liphardt, J.; Hwang, E.S.; Weaver, V.M. Human Breast Cancer Invasion and Aggression Correlates with ECM Stiffening and Immune Cell Infiltration. *Int Bio (Cam)* **2015**, *7*, 1120–1134, doi:10.1039/c5ib00040h.

147. Adlerz, K.M.; Aranda-Espinoza, H.; Hayenga, H.N. Substrate Elasticity Regulates the Behavior of Human Monocyte-Derived Macrophages. *Eur Biophys J* **2016**, *45*, 301–309, doi:10.1007/s00249-015-1096-8.

148. McWhorter, F.Y.; Davis, C.T.; Liu, W.F. Physical and Mechanical Regulation of Macrophage Phenotype and Function. *Cell. Mol. Life Sci.* **2015**, *72*, 1303–1316, doi:10.1007/s00018-014-1796-8.

149. Pyonteck, S.M.; Akkari, L.; Schuhmacher, A.J.; Bowman, R.L.; Sevenich, L.; Quail, D.F.; Olson, O.C.; Quick, M.L.; Huse, J.T.; Teijeiro, V.; et al. CSF-1R Inhibition Alters Macrophage Polarization and Blocks Glioma Progression. *Nat Med* **2013**, *19*, 1264–1272, doi:10.1038/nm.3337.

150. Bordeleau, F.; Califano, J.P.; Negrón Abril, Y.L.; Mason, B.N.; LaValley, D.J.; Shin, S.J.; Weiss, R.S.; Reinhart-King, C.A. Tissue Stiffness Regulates Serine/Arginine-Rich Protein-Mediated Splicing of the Extra Domain B-Fibronectin Isoform in Tumors. *Proc. Natl. Acad. Sci. U.S.A.* **2015**, *112*, 8314–8319, doi:10.1073/pnas.1505421112.

151. Miroshnikova, Y.A.; Rozenberg, G.I.; Cassereau, L.; Pickup, M.; Mouw, J.K.; Ou, G.; Templeman, K.L.; Hannachi, E.-I.; Gooch, K.J.; Sarang-Sieminski, A.L.; et al. Α5β1-Integrin Promotes Tension-Dependent Mammary Epithelial Cell Invasion by Engaging the Fibronectin Synergy Site. *MBoC* **2017**, *28*, 2958–2977, doi:10.1091/mbc.e17-02-0126.

152. Wang, W.; Lollis, E.M.; Bordeleau, F.; Reinhart-King, C.A. Matrix Stiffness Regulates Vascular Integrity through Focal Adhesion Kinase Activity. *The FASEB Journal* **2018**, *33*, 1199–1208, doi:10.1096/fj.201800841R.

153. Wang, W.; Miller, J.P.; Pannullo, S.C.; Reinhart-King, C.A.; Bordeleau, F. Quantitative Assessment of Cell Contractility Using Polarized Light Microscopy. *Journal of Biophotonics* **2018**, *11*, e201800008, doi:10.1002/jbio.201800008.

154. Lopez, J.I.; Kang, I.; You, W.-K.; McDonald, D.M.; Weaver, V.M. In Situ Force Mapping of Mammary Gland Transformation. *Integr Biol (Camb)* **2011**, *3*, 910–921, doi:10.1039/c1ib00043h.

155. Nicolas-Boluda, A.; Vaquero, J.; Vimeux, L.; Guilbert, T.; Barrin, S.; Kantari-Mimoun, C.; Ponzo, M.; Renault, G.; Deptula, P.; Pogoda, K.; et al. Tumor Stiffening Reversion through Collagen Crosslinking Inhibition Improves T Cell Migration and Anti-PD-1 Treatment. *eLife* **2021**, *10*, e58688, doi:10.7554/eLife.58688.

156. Tang, H.; Leung, L.; Saturno, G.; Viros, A.; Smith, D.; Di Leva, G.; Morrison, E.; Niculescu-Duvaz, D.; Lopes, F.; Johnson, L.; et al. Lysyl Oxidase Drives Tumour Progression by Trapping EGF Receptors at the Cell Surface. *Nat Commun* **2017**, *8*, 14909, doi:10.1038/ncomms14909.

157. Herring, C.A.; Banerjee, A.; McKinley, E.T.; Simmons, A.J.; Ping, J.; Roland, J.T.; Franklin, J.L.; Liu, Q.; Gerdes, M.J.; Coffey, R.J.; et al. Unsupervised Trajectory Analysis of Single-Cell RNA-Seq and Imaging Data Reveals Alternative Tuft Cell Origins in the Gut. *Cell Systems* **2018**, *6*, 37-51.e9, doi:10.1016/j.cels.2017.10.012.

158. Ma, L.; Hernandez, M.O.; Zhao, Y.; Mehta, M.; Tran, B.; Kelly, M.; Rae, Z.; Hernandez, J.M.; Davis, J.L.; Martin, S.P.; et al. Tumor Cell Biodiversity Drives Microenvironmental Reprogramming in Liver Cancer. *Cancer Cell* **2019**, *36*, 418-430.e6, doi:10.1016/j.ccell.2019.08.007.

159. Efremova, M.; Vento-Tormo, M.; Teichmann, S.A.; Vento-Tormo, R. CellPhoneDB: Inferring Cell–Cell Communication from Combined Expression of Multi-Subunit Ligand–Receptor Complexes. *Nat Protoc* **2020**, *15*, 1484–1506, doi:10.1038/s41596-020-0292-x.

160. Chen, B.; Ramirez-Solano, M.A.; Heiser, C.N.; Liu, Q.; Lau, K.S. Processing Single-Cell RNA-Seq Data for Dimension Reduction-Based Analyses Using Open-Source Tools. *STAR Protoc* **2021**, *2*, 100450, doi:10.1016/j.xpro.2021.100450.

161. Hafemeister, C.; Satija, R. Normalization and Variance Stabilization of Single-Cell RNA-Seq Data Using Regularized Negative Binomial Regression. *Genome Biology* **2019**, *20*, 296, doi:10.1186/s13059-019-1874-1.

162. Lawrence, T.; Natoli, G. Transcriptional Regulation of Macrophage Polarization: Enabling Diversity with Identity. *Nature Reviews Immunology* **2011**, *11*, 750–761, doi:10.1038/nri3088.

163. Murray, P.J. Macrophage Polarization. *Annual Review of Physiology* **2017**, *79*, 541–566, doi:10.1146/annurev-physiol-022516-034339.

164. Shiau, D.-J.; Kuo, W.-T.; Davuluri, G.V.N.; Shieh, C.-C.; Tsai, P.-J.; Chen, C.-C.; Lin, Y.-S.; Wu, Y.-Z.; Hsiao, Y.-P.; Chang, C.-P. Hepatocellular Carcinoma-Derived High Mobility Group Box 1 Triggers M2 Macrophage Polarization via a TLR2/NOX2/Autophagy Axis. *Scientific Reports* **2020**, *10*, 13582, doi:10.1038/s41598-020-70137-4.

165. Chang, C.-P.; Su, Y.-C.; Hu, C.-W.; Lei, H.-Y. TLR2-Dependent Selective Autophagy Regulates NF- κ B Lysosomal Degradation in Hepatoma-Derived M2 Macrophage Differentiation. *Cell Death & Differentiation* **2013**, *20*, 515–523, doi:10.1038/cdd.2012.146.
166. Yang, Z.F.; Ho, D.W.; Lau, C.K.; Lam, C.T.; Lum, C.T.; Poon, R.T.P.; Fan, S.T. Allograft Inflammatory Factor-1 (AIF-1) Is Crucial for the Survival and pro-Inflammatory Activity of Macrophages. *Int Immunol* **2005**, *17*, 1391–1397, doi:10.1093/intimm/dxh316.
167. Sánchez-Martín, L.; Estecha, A.; Samaniego, R.; Sánchez-Ramón, S.; Vega, M.Á.; Sánchez-Mateos, P. The Chemokine CXCL12 Regulates Monocyte-Macrophage Differentiation and RUNX3 Expression. *Blood* **2011**, *117*, 88–97, doi:10.1182/blood-2009-12-258186.
168. Bai, T.; Chen, C.-C.; Lau, L.F. Matricellular Protein CCN1 Activates a Proinflammatory Genetic Program in Murine Macrophages. *The Journal of Immunology* **2010**, *184*, 3223–3232, doi:10.4049/jimmunol.0902792.
169. Guo, H.; Jin, D.; Chen, X. Lipocalin 2 Is a Regulator Of Macrophage Polarization and NF-κB/STAT3 Pathway Activation. *Mol Endocrinol* **2014**, *28*, 1616–1628, doi:10.1210/me.2014-1092.
170. Doebel, T.; Voisin, B.; Nagao, K. Langerhans Cells - The Macrophage in Dendritic Cell Clothing. *Trends Immunol.* **2017**, *38*, 817–828, doi:10.1016/j.it.2017.06.008.
171. Ouchi, T.; Nakato, G.; Udey, M.C. EpCAM Expressed by Murine Epidermal Langerhans Cells Modulates Immunization to an Epicutaneously Applied Protein Antigen. *J. Invest. Dermatol.* **2016**, *136*, 1627–1635, doi:10.1016/j.jid.2016.04.005.
172. Stutte, S.; Jux, B.; Esser, C.; Förster, I. CD24a Expression Levels Discriminate Langerhans Cells from Dermal Dendritic Cells in Murine Skin and Lymph Nodes. *Journal of Investigative Dermatology* **2008**, *128*, 1470–1475, doi:10.1038/sj.jid.5701228.
173. Tsuge, T.; Yamakawa, M.; Tsukamoto, M. Infiltrating Dendritic/Langerhans Cells in Primary Breast Cancer. *Breast Cancer Res Treat* **2000**, *59*, 141–152, doi:10.1023/A:1006396216933.
174. Zhang, Y.-H.; He, M.; Wang, Y.; Liao, A.-H. Modulators of the Balance between M1 and M2 Macrophages during Pregnancy. *Front Immunol* **2017**, *8*, doi:10.3389/fimmu.2017.00120.
175. Mantovani, A.; Sozzani, S.; Locati, M.; Allavena, P.; Sica, A. Macrophage Polarization: Tumor-Associated Macrophages as a Paradigm for Polarized M2 Mononuclear

Phagocytes. *Trends in Immunology* **2002**, *23*, 549–555, doi:10.1016/S1471-4906(02)02302-5.

176. Cochain, C.; Vafadarnejad, E.; Arampatzi, P.; Pelisek, J.; Winkels, H.; Ley, K.; Wolf, D.; Saliba, A.-E.; Zernecke, A. Single-Cell RNA-Seq Reveals the Transcriptional Landscape and Heterogeneity of Aortic Macrophages in Murine Atherosclerosis. *Circ. Res.* **2018**, *122*, 1661–1674, doi:10.1161/CIRCRESAHA.117.312509.

177. Orecchioni, M.; Ghosheh, Y.; Pramod, A.B.; Ley, K. Macrophage Polarization: Different Gene Signatures in M1(LPS+) vs. Classically and M2(LPS–) vs. Alternatively Activated Macrophages. *Front. Immunol.* **2019**, *10*, doi:10.3389/fimmu.2019.01084.

178. Kamata, T.; Jin, H.; Giblett, S.; Patel, B.; Patel, F.; Foster, C.; Pritchard, C. The Cholesterol-Binding Protein NPC2 Restrains Recruitment of Stromal Macrophage-Lineage Cells to Early-Stage Lung Tumours. *EMBO Molecular Medicine* **2015**, *7*, 1119–1137, doi:10.15252/emmm.201404838.

179. Puolakkainen, P.; Koski, A.; Vainionpää, S.; Shen, Z.; Repo, H.; Kemppainen, E.; Mustonen, H.; Seppänen, H. Anti-Inflammatory Macrophages Activate Invasion in Pancreatic Adenocarcinoma by Increasing the MMP9 and ADAM8 Expression. *Med Oncol* **2014**, *31*, 884, doi:10.1007/s12032-014-0884-9.

180. Zhang, Y.; Du, W.; Chen, Z.; Xiang, C. Upregulation of PD-L1 by SPP1 Mediates Macrophage Polarization and Facilitates Immune Escape in Lung Adenocarcinoma. *Experimental Cell Research* **2017**, *359*, 449–457, doi:10.1016/j.yexcr.2017.08.028.

181. Liu, K.; Zhao, E.; Ilyas, G.; Lalazar, G.; Lin, Y.; Haseeb, M.; Tanaka, K.E.; Czaja, M.J. Impaired Macrophage Autophagy Increases the Immune Response in Obese Mice by Promoting Proinflammatory Macrophage Polarization. *Autophagy* **2015**, *11*, 271–284, doi:10.1080/15548627.2015.1009787.

182. Wang, L.; Zhang, S.; Wu, H.; Rong, X.; Guo, J. M2b Macrophage Polarization and Its Roles in Diseases. *Journal of Leukocyte Biology* **2019**, *106*, 345–358, doi:10.1002/JLB.3RU1018-378RR.

183. Moradi-Chaleshtori, M.; Shojaei, S.; Mohammadi-Yeganeh, S.; Hashemi, S.M. Transfer of miRNA in Tumor-Derived Exosomes Suppresses Breast Tumor Cell Invasion and Migration by Inducing M1 Polarization in Macrophages. *Life Sciences* **2021**, *282*, 119800, doi:10.1016/j.lfs.2021.119800.

184. Metcalf, D. The Colony-Stimulating Factors and Cancer. *Cancer Immunol Res* **2013**, *1*, 351–356, doi:10.1158/2326-6066.CIR-13-0151.

185. Cooper, J.; Giancotti, F.G. Integrin Signaling in Cancer: Mechanotransduction, Stemness, Epithelial Plasticity, and Therapeutic Resistance. *Cancer Cell* **2019**, *35*, 347–367, doi:10.1016/j.ccell.2019.01.007.

186. Puram, S.V.; Tirosh, I.; Parikh, A.S.; Patel, A.P.; Yizhak, K.; Gillespie, S.; Rodman, C.; Luo, C.L.; Mroz, E.A.; Emerick, K.S.; et al. Single-Cell Transcriptomic Analysis of Primary and Metastatic Tumor Ecosystems in Head and Neck Cancer. *Cell* **2017**, *171*, 1611-1624.e24, doi:10.1016/j.cell.2017.10.044.

187. Pelon, F.; Bourachot, B.; Kieffer, Y.; Magagna, I.; Mermet-Meillon, F.; Bonnet, I.; Costa, A.; Givel, A.-M.; Attieh, Y.; Barbazan, J.; et al. Cancer-Associated Fibroblast Heterogeneity in Axillary Lymph Nodes Drives Metastases in Breast Cancer through Complementary Mechanisms. *Nature Communications* **2020**, *11*, 1–20, doi:10.1038/s41467-019-14134-w.

188. Martinez, F.O.; Gordon, S. The M1 and M2 Paradigm of Macrophage Activation: Time for Reassessment. *F1000Prime Rep* **2014**, *6*, doi:10.12703/P6-13.

189. Solinas, G.; Schiarea, S.; Liguori, M.; Fabbri, M.; Pesce, S.; Zammataro, L.; Pasqualini, F.; Nebuloni, M.; Chiabrando, C.; Mantovani, A.; et al. Tumor-Conditioned Macrophages Secrete Migration-Stimulating Factor: A New Marker for M2-Polarization, Influencing Tumor Cell Motility. *The Journal of Immunology* **2010**, *185*, 642–652, doi:10.4049/jimmunol.1000413.

190. Kurahara, H.; Shinchi, H.; Mataki, Y.; Maemura, K.; Noma, H.; Kubo, F.; Sakoda, M.; Ueno, S.; Natsugoe, S.; Takao, S. Significance of M2-Polarized Tumor-Associated Macrophage in Pancreatic Cancer. *Journal of Surgical Research* **2011**, *167*, e211–e219, doi:10.1016/j.jss.2009.05.026.

191. Sica, A.; Schioppa, T.; Mantovani, A.; Allavena, P. Tumour-Associated Macrophages Are a Distinct M2 Polarised Population Promoting Tumour Progression: Potential Targets of Anti-Cancer Therapy. *European Journal of Cancer* **2006**, *42*, 717–727, doi:10.1016/j.ejca.2006.01.003.

192. Tripathi, C.; Tewari, B.N.; Kanchan, R.K.; Baghel, K.S.; Nautiyal, N.; Shrivastava, R.; Kaur, H.; Bhatt, M.L.B.; Bhadauria, S. Macrophages Are Recruited to Hypoxic Tumor Areas and Acquire a Pro-Angiogenic M2-Polarized Phenotype via Hypoxic Cancer Cell Derived Cytokines Oncostatin M and Eotaxin. *Oncotarget* **2014**, *5*, 5350–5368.

193. Chen, Y.; Zhang, S.; Wang, Q.; Zhang, X. Tumor-Recruited M2 Macrophages Promote Gastric and Breast Cancer Metastasis via M2 Macrophage-Secreted CHI3L1 Protein. *J Hematol Oncol* **2017**, *10*, 36, doi:10.1186/s13045-017-0408-0.

194. Ding, T.; Xu, J.; Wang, F.; Shi, M.; Zhang, Y.; Li, S.-P.; Zheng, L. High Tumor-Infiltrating Macrophage Density Predicts Poor Prognosis in Patients with Primary Hepatocellular Carcinoma after Resection. *Human Pathology* **2009**, *40*, 381–389, doi:10.1016/j.humpath.2008.08.011.

195. Takanami, I.; Takeuchi, K.; Kodaira, S. Tumor-Associated Macrophage Infiltration in Pulmonary Adenocarcinoma: Association with Angiogenesis and Poor Prognosis. *OCL* **1999**, *57*, 138–142, doi:10.1159/000012021.

196. Subimerb, C.; Pinlaor, S.; Khuntikeo, N.; Leelayuwat, C.; Morris, A.; McGrath, M.S.; Wongkham, S. Tissue Invasive Macrophage Density Is Correlated with Prognosis in Cholangiocarcinoma. *Molecular Medicine Reports* **2010**, *3*, 597–605, doi:10.3892/mmr_00000303.

197. Najafi, M.; Goradel, N.H.; Farhood, B.; Salehi, E.; Nashtaei, M.S.; Khanlarkhani, N.; Khezri, Z.; Majidpoor, J.; Abouzaripour, M.; Habibi, M.; et al. Macrophage Polarity in Cancer: A Review. *Journal of Cellular Biochemistry* **2019**, *120*, 2756–2765, doi:10.1002/jcb.27646.

198. Ohri, C.M.; Shikotra, A.; Green, R.H.; Waller, D.A.; Bradding, P. Macrophages within NSCLC Tumour Islets Are Predominantly of a Cytotoxic M1 Phenotype Associated with Extended Survival. *Eur. Respir. J.* **2009**, *33*, 118–126, doi:10.1183/09031936.00065708.

199. Chaturvedi, P.; Gilkes, D.M.; Takano, N.; Semenza, G.L. Hypoxia-Inducible Factor-Dependent Signaling between Triple-Negative Breast Cancer Cells and Mesenchymal Stem Cells Promotes Macrophage Recruitment. *PNAS* **2014**, *111*, E2120–E2129, doi:10.1073/pnas.1406655111.

200. Hind, L.E.; Dembo, M.; Hammer, D.A. Macrophage Motility Is Driven by Frontal-Towing with a Force Magnitude Dependent on Substrate Stiffness. *Int Bio (Cam)* **2015**, *7*, 447–453, doi:10.1039/c4ib00260a.

201. Friedemann, M.; Kalbitzer, L.; Franz, S.; Moeller, S.; Schnabelrauch, M.; Simon, J.-C.; Pompe, T.; Franke, K. Instructing Human Macrophage Polarization by Stiffness and Glycosaminoglycan Functionalization in 3D Collagen Networks. *Advanced Healthcare Materials* **2017**, *6*, 1600967, doi:10.1002/adhm.201600967.

202. Sridharan, R.; Ryan, E.J.; Kearney, C.J.; Kelly, D.J.; O’Brien, F.J. Macrophage Polarization in Response to Collagen Scaffold Stiffness Is Dependent on Cross-Linking Agent Used To Modulate the Stiffness. *ACS Biomater. Sci. Eng.* **2019**, *5*, 544–552, doi:10.1021/acsbiomaterials.8b00910.

203. Sridharan, R.; Cavanagh, B.; Cameron, A.R.; Kelly, D.J.; O'Brien, F.J. Material Stiffness Influences the Polarization State, Function and Migration Mode of Macrophages. *Acta Biomaterialia* **2019**, *89*, 47–59, doi:10.1016/j.actbio.2019.02.048.

204. Okamoto, T.; Takagi, Y.; Kawamoto, E.; Park, E.J.; Usuda, H.; Wada, K.; Shimaoka, M. Reduced Substrate Stiffness Promotes M2-like Macrophage Activation and Enhances Peroxisome Proliferator-Activated Receptor γ Expression. *Experimental Cell Research* **2018**, *367*, 264–273, doi:10.1016/j.yexcr.2018.04.005.

205. Wu, S.; Yue, H.; Wu, J.; Zhang, W.; Jiang, M.; Ma, G. The Interacting Role of Physical Stiffness and Tumor Cells on the Macrophages Polarization. *Colloids and Surfaces A: Physicochemical and Engineering Aspects* **2018**, *552*, 81–88, doi:10.1016/j.colsurfa.2018.04.026.

206. Xue, Y.Z.B.; Niu, Y.M.; Tang, B.; Wang, C.M. PCL/EUG Scaffolds with Tunable Stiffness Can Regulate Macrophage Secretion Behavior. *Progress in Biophysics and Molecular Biology* **2019**, *148*, 4–11, doi:10.1016/j.pbiomolbio.2019.05.006.

207. Sapi, E. The Role of CSF-1 in Normal Physiology of Mammary Gland and Breast Cancer: An Update. *Exp Biol Med (Maywood)* **2004**, *229*, 1–11, doi:10.1177/153537020422900101.

208. Kuemmel, S.; Campone, M.; Loirat, D.; López, R.L.; Beck, J.T.; Laurentiis, M.D.; Im, S.-A.; Kim, S.-B.; Kwong, A.; Steger, G.G.; et al. A Randomized Phase II Study of Anti-CSF-1 Monoclonal Antibody Lacnotuzumab (MCS110) Combined with Gemcitabine and Carboplatin in Advanced Triple Negative Breast Cancer. *Clin Cancer Res* **2021**, doi:10.1158/1078-0432.CCR-20-3955.

209. Calvo, A.; Joensuu, H.; Sebastian, M.; Naing, A.; Bang, Y.-J.; Martin, M.; Roda, D.; Hodi, F.S.; Veloso, A.; Mataraza, J.; et al. Phase Ib/II Study of Lacnotuzumab (MCS110) Combined with Spartalizumab (PDR001) in Patients (Pts) with Advanced Tumors. *JCO* **2018**, *36*, 3014–3014, doi:10.1200/JCO.2018.36.15_suppl.3014.

210. Reid, S.E.; Kay, E.J.; Neilson, L.J.; Henze, A.-T.; Serneels, J.; McGhee, E.J.; Dhayade, S.; Nixon, C.; Mackey, J.B.; Santi, A.; et al. Tumor Matrix Stiffness Promotes Metastatic Cancer Cell Interaction with the Endothelium. *The EMBO Journal* **2017**, e201694912, doi:10.15252/embj.201694912.

211. Solinas, G.; Germano, G.; Mantovani, A.; Allavena, P. Tumor-Associated Macrophages (TAM) as Major Players of the Cancer-Related Inflammation. *Journal of Leukocyte Biology* **2009**, *86*, 1065–1073, doi:10.1189/jlb.0609385.

212. Kerbel, R.S. Tumor Angiogenesis. *New England Journal of Medicine* **2008**, *358*, 2039–2049, doi:10.1056/NEJMra0706596.
213. Sherwood, L.M.; Parris, E.E.; Folkman, J. Tumor Angiogenesis: Therapeutic Implications. *N Engl J Med* **1971**, *285*, 1182–1186, doi:10.1056/NEJM197111182852108.
214. Shayan, M.; Huang, M.S.; Navarro, R.; Chiang, G.; Hu, C.; Oropeza, B.P.; Johansson, P.K.; Suhar, R.A.; Foster, A.A.; LeSavage, B.L.; et al. Elastin-like Protein Hydrogels with Controllable Stress Relaxation Rate and Stiffness Modulate Endothelial Cell Function. *Journal of Biomedical Materials Research Part A* **2023**, *111*, 896–909, doi:10.1002/jbm.a.37520.
215. Byfield, F.J.; Reen, R.K.; Shentu, T.-P.; Levitan, I.; Gooch, K.J. Endothelial Actin and Cell Stiffness Is Modulated by Substrate Stiffness in 2D and 3D. *Journal of Biomechanics* **2009**, *42*, 1114–1119, doi:10.1016/j.jbiomech.2009.02.012.
216. Kelkhoff, D.; Downing, T.; Li, S. Mechanotransduction to Epigenetic Remodeling. In *Molecular and Cellular Mechanobiology*; Chien, S., Engler, A.J., Wang, P.Y., Eds.; Physiology in Health and Disease; Springer: New York, NY, 2016; pp. 163–173 ISBN 978-1-4939-5617-3.
217. Hu, B.; Zhou, D.; Wang, H.; Hu, N.; Zhao, W. Mechanical Cues Regulate Histone Modifications and Cell Behavior. *Stem Cells International* **2022**, *2022*, e9179111, doi:10.1155/2022/9179111.
218. Bird, A. Perceptions of Epigenetics. *Nature* **2007**, *447*, 396–398, doi:10.1038/nature05913.
219. Moore, L.D.; Le, T.; Fan, G. DNA Methylation and Its Basic Function. *Neuropsychopharmacol* **2013**, *38*, 23–38, doi:10.1038/npp.2012.112.
220. Jaenisch, R.; Bird, A. Epigenetic Regulation of Gene Expression: How the Genome Integrates Intrinsic and Environmental Signals. *Nat Genet* **2003**, *33*, 245–254, doi:10.1038/ng1089.
221. Li, P.; Liu, S.; Du, L.; Mohseni, G.; Zhang, Y.; Wang, C. Liquid Biopsies Based on DNA Methylation as Biomarkers for the Detection and Prognosis of Lung Cancer. *Clinical Epigenetics* **2022**, *14*, 118, doi:10.1186/s13148-022-01337-0.
222. Müller, D.; Győrffy, B. DNA Methylation-Based Diagnostic, Prognostic, and Predictive Biomarkers in Colorectal Cancer. *Biochimica et Biophysica Acta (BBA) - Reviews on Cancer* **2022**, *1877*, 188722, doi:10.1016/j.bbcan.2022.188722.
223. Moreno, E.; Martínez-Sanz, J.; Martín-Mateos, R.; Díaz-Álvarez, J.; Serrano-Villar, S.; Burgos-Santamaría, D.; Luna, L.; Vivancos, M.J.; Moreno-Zamora, A.; Pérez-Elías, M.J.;

et al. Global DNA Methylation and Telomere Length as Markers of Accelerated Aging in People Living with HIV and Non-Alcoholic Fatty Liver Disease. *BMC Genomics* **2023**, *24*, 567, doi:10.1186/s12864-023-09653-2.

224. Tu, J.; Chen, S.; Wu, S.; Wu, T.; Fan, R.; Kuang, Z. Tumor DNA Methylation Profiles Enable Diagnosis, Prognosis Prediction, and Screening for Cervical Cancer. *International Journal of General Medicine* **2022**, *15*, 5809–5821, doi:10.2147/IJGM.S352373.

225. Vietri, M.T.; D'Elia, G.; Benincasa, G.; Ferraro, G.; Caliendo, G.; Nicoletti, G.F.; Napoli, C. DNA Methylation and Breast Cancer: A Way Forward (Review). *International Journal of Oncology* **2021**, *59*, 1–12, doi:10.3892/ijo.2021.5278.

226. Dunn, J.; Qiu, H.; Kim, S.; Jjingo, D.; Hoffman, R.; Kim, C.W.; Jang, I.; Son, D.J.; Kim, D.; Pan, C.; et al. Flow-Dependent Epigenetic DNA Methylation Regulates Endothelial Gene Expression and Atherosclerosis. *J Clin Invest* **2014**, *124*, 3187–3199, doi:10.1172/JCI74792.

227. Dunn, J.; Thabet, S.; Jo, H. Flow-Dependent Epigenetic DNA Methylation in Endothelial Gene Expression and Atherosclerosis. *Arteriosclerosis, Thrombosis, and Vascular Biology* **2015**, *35*, 1562–1569, doi:10.1161/ATVBAHA.115.305042.

228. Jiang, Y.-Z.; Manduchi, E.; Stoeckert, C.J.; Davies, P.F. Arterial Endothelial Methylome: Differential DNA Methylation in Athero-Susceptible Disturbed Flow Regions in Vivo. *BMC Genomics* **2015**, *16*, 506, doi:10.1186/s12864-015-1656-4.

229. Goyal, D.; Goyal, R. Angiogenic Transformation in Human Brain Micro Endothelial Cells: Whole Genome DNA Methylation and Transcriptomic Analysis. *Frontiers in Physiology* **2019**, *10*, 1502, doi:10.3389/fphys.2019.01502.

230. Dudley, A.C. Tumor Endothelial Cells. *Cold Spring Harb Perspect Med* **2012**, *2*, doi:10.1101/cshperspect.a006536.

231. Hida, K.; Maishi, N.; Torii, C.; Hida, Y. Tumor Angiogenesis—Characteristics of Tumor Endothelial Cells. *Int J Clin Oncol* **2016**, *21*, 206–212, doi:10.1007/s10147-016-0957-1.

232. Maishi, N.; Ohba, Y.; Akiyama, K.; Ohga, N.; Hamada, J.; Nagao-Kitamoto, H.; Alam, M.T.; Yamamoto, K.; Kawamoto, T.; Inoue, N.; et al. Tumour Endothelial Cells in High Metastatic Tumours Promote Metastasis via Epigenetic Dysregulation of Biglycan. *Scientific Reports* **2016**, *6*, 28039, doi:10.1038/srep28039.

233. Plodinec, M.; Loparic, M.; Monnier, C.A.; Obermann, E.C.; Zanetti-Dallenbach, R.; Oertle, P.; Hyotyla, J.T.; Aebi, U.; Bentires-Alj, M.; Lim, R.Y.H.; et al. The Nanomechanical Signature of Breast Cancer. *Nature Nanotech* **2012**, *7*, 757–765, doi:10.1038/nnano.2012.167.

234. Xie, S.-A.; Zhang, T.; Wang, J.; Zhao, F.; Zhang, Y.-P.; Yao, W.-J.; Hur, S.S.; Yeh, Y.-T.; Pang, W.; Zheng, L.-S.; et al. Matrix Stiffness Determines the Phenotype of Vascular Smooth Muscle Cell in Vitro and in Vivo: Role of DNA Methyltransferase 1. *Biomaterials* **2018**, *155*, 203–216, doi:10.1016/j.biomaterials.2017.11.033.

235. Liu, Y.; Lv, J.; Liang, X.; Yin, X.; Zhang, L.; Chen, D.; Jin, X.; Fiskesund, R.; Tang, K.; Ma, J.; et al. Fibrin Stiffness Mediates Dormancy of Tumor-Repopulating Cells via a Cdc42-Driven Tet2 Epigenetic Program. *Cancer Research* **2018**, *78*, 3926–3937, doi:10.1158/0008-5472.CAN-17-3719.

236. Zhao, X.-B.; Chen, Y.-P.; Tan, M.; Zhao, L.; Zhai, Y.-Y.; Sun, Y.-L.; Gong, Y.; Feng, X.-Q.; Du, J.; Fan, Y.-B. Extracellular Matrix Stiffness Regulates DNA Methylation by PKCα-Dependent Nuclear Transport of DNMT3L. *Advanced Healthcare Materials* **2021**, *10*, 2100821, doi:10.1002/adhm.202100821.

237. Schellenberg, A.; Joussen, S.; Moser, K.; Hampe, N.; Hersch, N.; Hemeda, H.; Schnitker, J.; Denecke, B.; Lin, Q.; Pallua, N.; et al. Matrix Elasticity, Replicative Senescence and DNA Methylation Patterns of Mesenchymal Stem Cells. *Biomaterials* **2014**, *35*, 6351–6358, doi:10.1016/j.biomaterials.2014.04.079.

238. L. Sumey, J.; C. Johnston, P.; M. Harrell, A.; R. Caliari, S. Hydrogel Mechanics Regulate Fibroblast DNA Methylation and Chromatin Condensation. *Biomaterials Science* **2023**, *11*, 2886–2897, doi:10.1039/D2BM02058K.

239. Jang, M.; An, J.; Oh, S.W.; Lim, J.Y.; Kim, J.; Choi, J.K.; Cheong, J.-H.; Kim, P. Matrix Stiffness Epigenetically Regulates the Oncogenic Activation of the Yes-Associated Protein in Gastric Cancer. *Nat Biomed Eng* **2021**, *5*, 114–123, doi:10.1038/s41551-020-00657-x.

240. Qu, J.; Zhu, L.; Zhou, Z.; Chen, P.; Liu, S.; Locy, M.L.; Thannickal, V.J.; Zhou, Y. ERS Special Article.Reversing Mechanoinductive DSP Expression by CRISPR/dCas9–Mediated Epigenome Editing. *Am J Respir Crit Care Med* **2018**, *198*, 599–609, doi:10.1164/rccm.201711-2242OC.

241. Luo, C.-H.; Shi, Y.; Liu, Y.-Q.; Liu, Q.; Mao, M.; Luo, M.; Yang, K.-D.; Wang, W.-Y.; Chen, C.; Niu, Q.; et al. High Levels of TIMP1 Are Associated with Increased Extracellular Matrix Stiffness in Isocitrate Dehydrogenase 1-Wild Type Gliomas. *Lab Invest* **2022**, *102*, 1304–1313, doi:10.1038/s41374-022-00825-4.

242. Iijima, H.; Gilmer, G.; Wang, K.; Bean, A.C.; He, Y.; Lin, H.; Tang, W.-Y.; Lamont, D.; Tai, C.; Ito, A.; et al. Age-Related Matrix Stiffening Epigenetically Regulates α-Klotho

Expression and Compromises Chondrocyte Integrity. *Nat Commun* **2023**, *14*, 18, doi:10.1038/s41467-022-35359-2.

243. Wells, R.G. The Role of Matrix Stiffness in Regulating Cell Behavior. *Hepatology* **2008**, *47*, 1394–1400, doi:https://doi.org/10.1002/hep.22193.
244. Janmey, P.A.; Fletcher, D.A.; Reinhart-King, C.A. Stiffness Sensing by Cells. *Physiological Reviews* **2020**, *100*, 695–724, doi:10.1152/physrev.00013.2019.
245. Lang, N.R.; Skodzek, K.; Hurst, S.; Mainka, A.; Steinwachs, J.; Schneider, J.; Aifantis, K.E.; Fabry, B. Biphasic Response of Cell Invasion to Matrix Stiffness in Three-Dimensional Biopolymer Networks. *Acta Biomaterialia* **2015**, *13*, 61–67, doi:10.1016/j.actbio.2014.11.003.
246. Yuan, D.J.; Shi, L.; Kam, L.C. Biphasic Response of T Cell Activation to Substrate Stiffness. *Biomaterials* **2021**, *273*, 120797, doi:10.1016/j.biomaterials.2021.120797.
247. Peyton, S.R.; Putnam, A.J. Extracellular Matrix Rigidity Governs Smooth Muscle Cell Motility in a Biphasic Fashion. *Journal of Cellular Physiology* **2005**, *204*, 198–209, doi:10.1002/jcp.20274.
248. Lyko, F. The DNA Methyltransferase Family: A Versatile Toolkit for Epigenetic Regulation. *Nat Rev Genet* **2018**, *19*, 81–92, doi:10.1038/nrg.2017.80.
249. Bestor, T.H. The DNA Methyltransferases of Mammals. *Human Molecular Genetics* **2000**, *9*, 2395–2402, doi:10.1093/hmg/9.16.2395.
250. Edwards, J.R.; Yarychkivska, O.; Boulard, M.; Bestor, T.H. DNA Methylation and DNA Methyltransferases. *Epigenetics & Chromatin* **2017**, *10*, 23, doi:10.1186/s13072-017-0130-8.
251. Kohli, R.M.; Zhang, Y. TET Enzymes, TDG and the Dynamics of DNA Demethylation. *Nature* **2013**, *502*, 472–479, doi:10.1038/nature12750.
252. Garner, B.; Hodgson, A.J.; Wallace, G.G.; Underwood, P.A. Human Endothelial Cell a. *Journal of Materials Science: Materials in Medicine* **1999**, *10*, 19–27, doi:10.1023/A:1008835925998.
253. Nur, S.M.; Shait Mohammed, M.R.; Zamzami, M.A.; Choudhry, H.; Ahmad, A.; Ateeq, B.; Rather, I.A.; Khan, M.I. Untargeted Metabolomics Showed Accumulation of One-Carbon Metabolites to Facilitate DNA Methylation during Extracellular Matrix Detachment of Cancer Cells. *Metabolites* **2022**, *12*, 267, doi:10.3390/metabo12030267.
254. Iurlaro, M.; von Meyenn, F.; Reik, W. DNA Methylation Homeostasis in Human and Mouse Development. *Current Opinion in Genetics & Development* **2017**, *43*, 101–109, doi:10.1016/j.gde.2017.02.003.

255. Lampugnani, M.G.; Corada, M.; Andriopoulou, P.; Esser, S.; Risau, W.; Dejana, E. Cell Confluence Regulates Tyrosine Phosphorylation of Adherens Junction Components in Endothelial Cells. *Journal of Cell Science* **1997**, *110*, 2065–2077, doi:10.1242/jcs.110.17.2065.

256. Howell, G.J.; Herbert, S.P.; Smith, J.M.; Mittar, S.; Ewan, L.C.; Mohammed, M.; Hunter, A.R.; Simpson, N.; Turner, A.J.; Zachary, I.; et al. Endothelial Cell Confluence Regulates Weibel-Palade Body Formation. *Molecular Membrane Biology* **2004**, *21*, 413–421, doi:10.1080/09687860400011571.

257. Viñals, F.; Pouysségur, J. Confluence of Vascular Endothelial Cells Induces Cell Cycle Exit by Inhibiting P42/P44 Mitogen-Activated Protein Kinase Activity. *Mol Cell Biol* **1999**, *19*, 2763–2772.

258. Hayward, M.-K.; Muncie, J.M.; Weaver, V.M. Tissue Mechanics in Stem Cell Fate, Development, and Cancer. *Developmental Cell* **2021**, *56*, 1833–1847, doi:10.1016/j.devcel.2021.05.011.

259. Liu, C.; Li, M.; Dong, Z.-X.; Jiang, D.; Li, X.; Lin, S.; Chen, D.; Zou, X.; Zhang, X.-D.; Luker, G.D. Heterogeneous Microenvironmental Stiffness Regulates Pro-Metastatic Functions of Breast Cancer Cells. *Acta Biomaterialia* **2021**, *131*, 326–340, doi:10.1016/j.actbio.2021.07.009.

260. Khorana, A.A.; Tullio, K.; Elson, P.; Pennell, N.A.; Grobmyer, S.R.; Kalady, M.F.; Raymond, D.; Abraham, J.; Klein, E.A.; Walsh, R.M.; et al. Time to Initial Cancer Treatment in the United States and Association with Survival over Time: An Observational Study. *PLOS ONE* **2019**, *14*, e0213209, doi:10.1371/journal.pone.0213209.

261. Dudaryeva, O.Y.; Bernhard, S.; Tibbitt, M.W.; Labouesse, C. Implications of Cellular Mechanical Memory in Bioengineering. *ACS Biomater. Sci. Eng.* **2023**, doi:10.1021/acsbiomaterials.3c01007.

262. Schübeler, D. Function and Information Content of DNA Methylation. *Nature* **2015**, *517*, 321–326, doi:10.1038/nature14192.

263. Berdasco, M.; Esteller, M. Clinical Epigenetics: Seizing Opportunities for Translation. *Nat Rev Genet* **2019**, *20*, 109–127, doi:10.1038/s41576-018-0074-2.

264. Trepat, X.; Chen, Z.; Jacobson, K. Cell Migration. *Compr Physiol* **2012**, *2*, 2369–2392, doi:10.1002/cphy.c110012.

265. Hanahan, D.; Weinberg, R.A. The Hallmarks of Cancer. *Cell* **2000**, *100*, 57–70, doi:10.1016/S0092-8674(00)81683-9.

266. Yamaguchi, H.; Wyckoff, J.; Condeelis, J. Cell Migration in Tumors. *Current Opinion in Cell Biology* **2005**, *17*, 559–564, doi:10.1016/j.ceb.2005.08.002.

267. Friedl, P.; Gilmour, D. Collective Cell Migration in Morphogenesis, Regeneration and Cancer. *Nat Rev Mol Cell Biol* **2009**, *10*, 445–457, doi:10.1038/nrm2720.

268. Lintz, M.; Muñoz, A.; Reinhart-King, C.A. The Mechanics of Single Cell and Collective Migration of Tumor Cells. *Journal of Biomechanical Engineering* **2017**, *139*, doi:10.1115/1.4035121.

269. Sabeh, F.; Shimizu-Hirota, R.; Weiss, S.J. Protease-Dependent versus -Independent Cancer Cell Invasion Programs: Three-Dimensional Amoeboid Movement Revisited. *Journal of Cell Biology* **2009**, *185*, 11–19, doi:10.1083/jcb.200807195.

270. Emad, A.; Ray, T.; Jensen, T.W.; Parat, M.; Natrajan, R.; Sinha, S.; Ray, P.S. Superior Breast Cancer Metastasis Risk Stratification Using an Epithelial-Mesenchymal-Amoeboid Transition Gene Signature. *Breast Cancer Research* **2020**, *22*, 74, doi:10.1186/s13058-020-01304-8.

271. Dagogo-Jack, I.; Shaw, A.T. Tumour Heterogeneity and Resistance to Cancer Therapies. *Nat Rev Clin Oncol* **2018**, *15*, 81–94, doi:10.1038/nrclinonc.2017.166.

272. Melo, F.D.S.E.; Vermeulen, L.; Fessler, E.; Medema, J.P. Cancer Heterogeneity—a Multifaceted View. *EMBO reports* **2013**, *14*, 686–695, doi:10.1038/embor.2013.92.

273. Marusyk, A.; Polyak, K. Tumor Heterogeneity: Causes and Consequences. *Biochimica et Biophysica Acta (BBA) - Reviews on Cancer* **2010**, *1805*, 105–117, doi:10.1016/j.bbcan.2009.11.002.

274. Gambardella, V.; Tarazona, N.; Cejalvo, J.M.; Lombardi, P.; Huerta, M.; Roselló, S.; Fleitas, T.; Roda, D.; Cervantes, A. Personalized Medicine: Recent Progress in Cancer Therapy. *Cancers* **2020**, *12*, 1009, doi:10.3390/cancers12041009.

275. Roosmalen, W. van; Dévédec, S.E.L.; Golani, O.; Smid, M.; Pulyakhina, I.; Timmermans, A.M.; Look, M.P.; Zi, D.; Pont, C.; Graauw, M. de; et al. Tumor Cell Migration Screen Identifies SRPK1 as Breast Cancer Metastasis Determinant. *J Clin Invest* **2015**, *125*, 1648–1664, doi:10.1172/JCI74440.

276. Tajadura-Ortega, V.; Garg, R.; Allen, R.; Owczarek, C.; Bright, M.D.; Kean, S.; Mohd-Noor, A.; Grigoriadis, A.; Elston, T.C.; Hahn, K.M.; et al. An RNAi Screen of Rho Signalling Networks Identifies RhoH as a Regulator of Rac1 in Prostate Cancer Cell Migration. *BMC Biol* **2018**, *16*, 29, doi:10.1186/s12915-018-0489-4.

277. Bai, S.W.; Herrera-Abreu, M.T.; Rohn, J.L.; Racine, V.; Tajadura, V.; Suryavanshi, N.; Bechtel, S.; Wiemann, S.; Baum, B.; Ridley, A.J. Identification and Characterization of a

Set of Conserved and New Regulators of Cytoskeletal Organization, Cell Morphology and Migration. *BMC Biology* **2011**, *9*, 54, doi:10.1186/1741-7007-9-54.

278. Simpson, K.J.; Selfors, L.M.; Bui, J.; Reynolds, A.; Leake, D.; Khvorova, A.; Brugge, J.S. Identification of Genes That Regulate Epithelial Cell Migration Using an siRNA Screening Approach. *Nat Cell Biol* **2008**, *10*, 1027–1038, doi:10.1038/ncb1762.

279. Yang, J.; Fan, J.; Li, Y.; Li, F.; Chen, P.; Fan, Y.; Xia, X.; Wong, S.T. Genome-Wide RNAi Screening Identifies Genes Inhibiting the Migration of Glioblastoma Cells. *PLOS ONE* **2013**, *8*, e61915, doi:10.1371/journal.pone.0061915.

280. Smolen, G.A.; Zhang, J.; Zubrowski, M.J.; Edelman, E.J.; Luo, B.; Yu, M.; Ng, L.W.; Scherber, C.M.; Schott, B.J.; Ramaswamy, S.; et al. A Genome-Wide RNAi Screen Identifies Multiple RSK-Dependent Regulators of Cell Migration. *Genes Dev.* **2010**, *24*, 2654–2665, doi:10.1101/gad.1989110.

281. Koedoot, E.; Fokkelman, M.; Rogkoti, V.-M.; Smid, M.; van de Sandt, I.; de Bont, H.; Pont, C.; Klip, J.E.; Wink, S.; Timmermans, M.A.; et al. Uncovering the Signaling Landscape Controlling Breast Cancer Cell Migration Identifies Novel Metastasis Driver Genes. *Nat Commun* **2019**, *10*, 2983, doi:10.1038/s41467-019-11020-3.

282. Chen, Y.; Lu, B.; Yang, Q.; Fearns, C.; Yates, J.R., III; Lee, J.-D. Combined Integrin Phosphoproteomic Analyses and Small Interfering RNA–Based Functional Screening Identify Key Regulators for Cancer Cell Adhesion and Migration. *Cancer Research* **2009**, *69*, 3713–3720, doi:10.1158/0008-5472.CAN-08-2515.

283. Collins, C.S.; Hong, J.; Sapinoso, L.; Zhou, Y.; Liu, Z.; Micklash, K.; Schultz, P.G.; Hampton, G.M. A Small Interfering RNA Screen for Modulators of Tumor Cell Motility Identifies MAP4K4 as a Promigratory Kinase. *Proceedings of the National Academy of Sciences* **2006**, *103*, 3775–3780, doi:10.1073/pnas.0600040103.

284. Fokkelman, M.; Balcıoğlu, H.E.; Klip, J.E.; Yan, K.; Verbeek, F.J.; Danen, E.H.J.; van de Water, B. Cellular Adhesome Screen Identifies Critical Modulators of Focal Adhesion Dynamics, Cellular Traction Forces and Cell Migration Behaviour. *Sci Rep* **2016**, *6*, 31707, doi:10.1038/srep31707.

285. Naffar-Abu-Amara, S.; Shay, T.; Galun, M.; Cohen, N.; Isakoff, S.J.; Kam, Z.; Geiger, B. Identification of Novel Pro-Migratory, Cancer-Associated Genes Using Quantitative, Microscopy-Based Screening. *PLOS ONE* **2008**, *3*, e1457, doi:10.1371/journal.pone.0001457.

286. Seo, M.; Lee, W.-H.; Suk, K. Identification of Novel Cell Migration-Promoting Genes by a Functional Genetic Screen. *The FASEB Journal* **2010**, *24*, 464–478, doi:10.1096/fj.09-137562.

287. Hapach, L.A.; Carey, S.P.; Schwager, S.C.; Taufalele, P.V.; Wang, W.; Mosier, J.A.; Ortiz-Otero, N.; McArdle, T.J.; Goldblatt, Z.E.; Lampi, M.C.; et al. Phenotypic Heterogeneity and Metastasis of Breast Cancer Cells. *Cancer Research* **2021**, *81*, 3649–3663, doi:10.1158/0008-5472.CAN-20-1799.

288. Shatkin, G.; Yeoman, B.; Birmingham, K.; Katira, P.; Engler, A.J. Computational Models of Migration Modes Improve Our Understanding of Metastasis. *APL Bioengineering* **2020**, *4*, 041505, doi:10.1063/5.0023748.

289. Ribatti, D.; Tamma, R.; Annese, T. Epithelial-Mesenchymal Transition in Cancer: A Historical Overview. *Translational Oncology* **2020**, *13*, 100773, doi:10.1016/j.tranon.2020.100773.

290. Cao, R.; Yuan, L.; Ma, B.; Wang, G.; Qiu, W.; Tian, Y. An EMT-Related Gene Signature for the Prognosis of Human Bladder Cancer. *Journal of Cellular and Molecular Medicine* **2020**, *24*, 605–617, doi:10.1111/jcmm.14767.

291. Dai, W.; Xiao, Y.; Tang, W.; Li, J.; Hong, L.; Zhang, J.; Pei, M.; Lin, J.; Liu, S.; Wu, X.; et al. Identification of an EMT-Related Gene Signature for Predicting Overall Survival in Gastric Cancer. *Frontiers in Genetics* **2021**, *12*.

292. Hussey, G.S.; Link, L.A.; Brown, A.S.; Howley, B.V.; Chaudhury, A.; Howe, P.H. Establishment of a TGFβ-Induced Post-Transcriptional EMT Gene Signature. *PLOS ONE* **2012**, *7*, e52624, doi:10.1371/journal.pone.0052624.

293. Vasaikar, S.V.; Deshmukh, A.P.; den Hollander, P.; Addanki, S.; Kuburich, N.A.; Kudaravalli, S.; Joseph, R.; Chang, J.T.; Soundararajan, R.; Mani, S.A. EMTome: A Resource for Pan-Cancer Analysis of Epithelial-Mesenchymal Transition Genes and Signatures. *Br J Cancer* **2021**, *124*, 259–269, doi:10.1038/s41416-020-01178-9.

294. Krämer, A.; Green, J.; Pollard, J., Jr; Tugendreich, S. Causal Analysis Approaches in Ingenuity Pathway Analysis. *Bioinformatics* **2014**, *30*, 523–530, doi:10.1093/bioinformatics/btt703.

295. Tsafrir, D.; Bacolod, M.; Selvanayagam, Z.; Tsafrir, I.; Shia, J.; Zeng, Z.; Liu, H.; Krier, C.; Stengel, R.F.; Barany, F.; et al. Relationship of Gene Expression and Chromosomal Abnormalities in Colorectal Cancer. *Cancer Research* **2006**, *66*, 2129–2137, doi:10.1158/0008-5472.CAN-05-2569.

296. Carter, B.; Zhao, K. The Epigenetic Basis of Cellular Heterogeneity. *Nat Rev Genet* **2021**, *22*, 235–250, doi:10.1038/s41576-020-00300-0.

297. Gopi, L.K.; Kidder, B.L. Integrative Pan Cancer Analysis Reveals Epigenomic Variation in Cancer Type and Cell Specific Chromatin Domains. *Nat Commun* **2021**, *12*, 1419, doi:10.1038/s41467-021-21707-1.

298. Zhao, H.; Liu, H.; Yang, Y.; Wang, H. The Emerging Role of EVA1A in Different Types of Cancers. *International Journal of Molecular Sciences* **2022**, *23*, 6665, doi:10.3390/ijms23126665.

299. Zhen, Y.; Zhao, R.; Wang, M.; Jiang, X.; Gao, F.; Fu, L.; Zhang, L.; Zhou, X.-L. Flubendazole Elicits Anti-Cancer Effects via Targeting EVA1A-Modulated Autophagy and Apoptosis in Triple-Negative Breast Cancer. *Theranostics* **2020**, *10*, 8080–8097, doi:10.7150/thno.43473.

300. Zhen, Y.; Yuan, Z.; Zhang, J.; Chen, Y.; Fu, Y.; Liu, Y.; Fu, L.; Zhang, L.; Zhou, X.-L. Flubendazole Induces Mitochondrial Dysfunction and DRP1-Mediated Mitophagy by Targeting EVA1A in Breast Cancer. *Cell Death Dis* **2022**, *13*, 375, doi:10.1038/s41419-022-04823-8.

301. Yang, J.; Wang, B.; Xu, Q.; Yang, Y.; Hou, L.; Yin, K.; Guo, Q.; Hua, Y.; Zhang, L.; Li, Y.; et al. TMEM166 Inhibits Cell Proliferation, Migration and Invasion in Hepatocellular Carcinoma via Upregulating TP53. *Mol Cell Biochem* **2021**, *476*, 1151–1163, doi:10.1007/s11010-020-03979-1.

302. Lin, B.-Y.; Wen, J.-L.; Zheng, C.; Lin, L.-Z.; Chen, C.-Z.; Qu, J.-M. Eva-1 Homolog A Promotes Papillary Thyroid Cancer Progression and Epithelial-Mesenchymal Transition via the Hippo Signalling Pathway. *J Cell Mol Med* **2020**, *24*, 13070–13080, doi:10.1111/jcmm.15909.

303. Li, J.; Chen, Y.; Gao, J.; Chen, Y.; Zhou, C.; Lin, X.; Liu, C.; Zhao, M.; Xu, Y.; Ji, L.; et al. Eva1a Ameliorates Atherosclerosis by Promoting Re-Endothelialization of Injured Arteries via Rac1/Cdc42/Arpc1b. *Cardiovasc Res* **2021**, *117*, 450–461, doi:10.1093/cvr/cvaa011.

304. Castaneda, M.; den Hollander, P.; Kuburich, N.A.; Rosen, J.M.; Mani, S.A. Mechanisms of Cancer Metastasis. *Seminars in Cancer Biology* **2022**, *87*, 17–31, doi:10.1016/j.semcancer.2022.10.006.

305. Chen, M.; Huang, B.; Zhu, L.; Chen, K.; Liu, M.; Zhong, C. Structural and Functional Overview of TEAD4 in Cancer Biology. *OncoTargets and Therapy* **2020**, *13*, 9865–9874, doi:10.2147/OTT.S266649.

306. Yilmaz, M.; Christofori, G. EMT, the Cytoskeleton, and Cancer Cell Invasion. *Cancer Metastasis Rev* **2009**, *28*, 15–33, doi:10.1007/s10555-008-9169-0.

307. Torbet, J.; Ronzière, M.C. Magnetic Alignment of Collagen during Self-Assembly. *Biochemical Journal* **1984**, *219*, 1057–1059, doi:10.1042/bj2191057.

308. Vader, D.; Kabla, A.; Weitz, D.; Mahadevan, L. Strain-Induced Alignment in Collagen Gels. *PLOS ONE* **2009**, *4*, e5902, doi:10.1371/journal.pone.0005902.

309. Ng, C.P.; Swartz, M.A. Mechanisms of Interstitial Flow-Induced Remodeling of Fibroblast–Collagen Cultures. *Ann Biomed Eng* **2006**, *34*, 446–454, doi:10.1007/s10439-005-9067-3.

310. Wilks, B.T.; Evans, E.B.; Nakhla, M.N.; Morgan, J.R. Directing Fibroblast Self-Assembly to Fabricate Highly-Aligned, Collagen-Rich Matrices. *Acta Biomaterialia* **2018**, *81*, 70–79, doi:10.1016/j.actbio.2018.09.030.

311. Sawhney, R.K.; Howard, J. Slow Local Movements of Collagen Fibers by Fibroblasts Drive the Rapid Global Self-Organization of Collagen Gels. *Journal of Cell Biology* **2002**, *157*, 1083–1092, doi:10.1083/jcb.200203069.

312. Wang, J.H.-C.; Jia, F.; Gilbert, T.W.; Woo, S.L.-Y. Cell Orientation Determines the Alignment of Cell-Produced Collagenous Matrix. *Journal of Biomechanics* **2003**, *36*, 97–102, doi:10.1016/S0021-9290(02)00233-6.

313. Kim, A.; Lakshman, N.; Petroll, W.M. Quantitative Assessment of Local Collagen Matrix Remodeling in 3-D Culture: The Role of Rho Kinase. *Experimental Cell Research* **2006**, *312*, 3683–3692, doi:10.1016/j.yexcr.2006.08.009.

314. Piotrowski-Daspit, A.S.; Nerger, B.A.; Wolf, A.E.; Sundaresan, S.; Nelson, C.M. Dynamics of Tissue-Induced Alignment of Fibrous Extracellular Matrix. *Biophys J* **2017**, *113*, 702–713, doi:10.1016/j.bpj.2017.06.046.

315. Carey, S.P.; Goldblatt, Z.E.; Martin, K.E.; Romero, B.; Williams, R.M.; Reinhart-King, C.A. Local Extracellular Matrix Alignment Directs Cellular Protrusion Dynamics and Migration through Rac1 and FAK. *Integr. Biol.* **2016**, *8*, 821–835, doi:10.1039/C6IB00030D.

316. Wolf, K.; Alexander, S.; Schacht, V.; Coussens, L.M.; von Andrian, U.H.; van Rheenen, J.; Deryugina, E.; Friedl, P. Collagen-Based Cell Migration Models in Vitro and in Vivo. *Seminars in Cell & Developmental Biology* **2009**, *20*, 931–941, doi:10.1016/j.semcdb.2009.08.005.

317. Mason, B.N.; Califano, J.P.; Reinhart-King, C.A. Matrix Stiffness: A Regulator of Cellular Behavior and Tissue Formation. In *Engineering Biomaterials for Regenerative Medicine:*

Novel Technologies for Clinical Applications; Bhatia, S.K., Ed.; Springer: New York, NY, 2012; pp. 19–37 ISBN 978-1-4614-1080-5.

318. Mason, B.N.; Reinhart-King, C.A. Controlling the Mechanical Properties of Three-Dimensional Matrices via Non-Enzymatic Collagen Glycation. *Organogenesis* **2013**, *9*, 70–75, doi:10.4161/org.24942.

319. Chaudhari, N.; Findlay, A.D.; Stevenson, A.W.; Clemons, T.D.; Yao, Y.; Joshi, A.; Sayyar, S.; Wallace, G.; Rea, S.; Toshniwal, P.; et al. Topical Application of an Irreversible Small Molecule Inhibitor of Lysyl Oxidases Ameliorates Skin Scarring and Fibrosis. *Nat Commun* **2022**, *13*, 5555, doi:10.1038/s41467-022-33148-5.

320. Wang, W.; Hapach, L.A.; Griggs, L.; Smart, K.; Wu, Y.; Taufalele, P.V.; Rowe, M.M.; Young, K.M.; Bates, M.E.; Johnson, A.C.; et al. Diabetic Hyperglycemia Promotes Primary Tumor Progression through Glycation-Induced Tumor Extracellular Matrix Stiffening. *Science Advances* **2022**, *8*, eabo1673, doi:10.1126/sciadv.abo1673.

321. Sakamoto, K.; Schmidt, J.W.; Wagner, K.-U. Mouse Models of Breast Cancer. *Methods Mol Biol* **2015**, *1267*, 47–71, doi:10.1007/978-1-4939-2297-0_3.

322. Cai, Y.; Nogales-Cadenas, R.; Zhang, Q.; Lin, J.-R.; Zhang, W.; O'Brien, K.; Montagna, C.; Zhang, Z.D. Transcriptomic Dynamics of Breast Cancer Progression in the MMTV-PyMT Mouse Model. *BMC Genomics* **2017**, *18*, 185, doi:10.1186/s12864-017-3563-3.

323. Day, C.-P.; Merlino, G.; Van Dyke, T. Preclinical Mouse Cancer Models: A Maze of Opportunities and Challenges. *Cell* **2015**, *163*, 39–53, doi:10.1016/j.cell.2015.08.068.

324. Bode, K.J.; Mueller, S.; Schweinlin, M.; Metzger, M.; Brunner, T. A Fast and Simple Fluorometric Method to Detect Cell Death in 3D Intestinal Organoids. *BioTechniques* **2019**, *67*, 23–28, doi:10.2144/btn-2019-0023.

325. Bressan, D.; Battistoni, G.; Hannon, G.J. The Dawn of Spatial Omics. *Science* **2023**, *381*, eabq4964, doi:10.1126/science.abq4964.

326. Madissoon, E.; Oliver, A.J.; Kleshchevnikov, V.; Wilbrey-Clark, A.; Polanski, K.; Orsi, A.R.; Mamanova, L.; Bolt, L.; Richoz, N.; Elmentaite, R.; et al. A Spatial Multi-Omics Atlas of the Human Lung Reveals a Novel Immune Cell Survival Niche 2021, 2021.11.26.470108.

327. Chen, Y.; Pal, B.; Visvader, J.E.; Smyth, G.K. Differential Methylation Analysis of Reduced Representation Bisulfite Sequencing Experiments Using edgeR. *F1000Res* **2018**, *6*, 2055, doi:10.12688/f1000research.13196.2.

328. Wozniak, M.A.; Chen, C.S. Mechanotransduction in Development: A Growing Role for Contractility. *Nat Rev Mol Cell Biol* **2009**, *10*, 34–43, doi:10.1038/nrm2592.

329. Martino, F.; Perestrelo, A.R.; Vinarský, V.; Pagliari, S.; Forte, G. Cellular Mechanotransduction: From Tension to Function. *Frontiers in Physiology* **2018**, *9*.

330. Miroshnikova, Y.A.; Nava, M.M.; Wickström, S.A. Emerging Roles of Mechanical Forces in Chromatin Regulation. *Journal of Cell Science* **2017**, *130*, 2243–2250, doi:10.1242/jcs.202192.

331. Zuleger, N.; Robson, M.I.; Schirmer, E.C. The Nuclear Envelope as a Chromatin Organizer. *Nucleus* **2011**, *2*, 339–349, doi:10.4161/nucl.2.5.17846.

332. Mattout-Drubezki, A.; Gruenbaum, Y. Dynamic Interactions of Nuclear Lamina Proteins with Chromatin and Transcriptional Machinery. *CMLS, Cell. Mol. Life Sci.* **2003**, *60*, 2053–2063, doi:10.1007/s00018-003-3038-3.

333. Ribatti, D.; Tamma, R. Epigenetic Control of Tumor Angiogenesis. *Microcirculation* **2020**, *27*, e12602, doi:10.1111/micc.12602.

334. Potente, M.; Ghaeni, L.; Baldessari, D.; Mostoslavsky, R.; Rossig, L.; Dequiedt, F.; Haendeler, J.; Mione, M.; Dejana, E.; Alt, F.W.; et al. SIRT1 Controls Endothelial Angiogenic Functions during Vascular Growth. *Genes Dev* **2007**, *21*, 2644–2658, doi:10.1101/gad.435107.

335. Chang, S.; Young, B.D.; Li, S.; Qi, X.; Richardson, J.A.; Olson, E.N. Histone Deacetylase 7 Maintains Vascular Integrity by Repressing Matrix Metalloproteinase 10. *Cell* **2006**, *126*, 321–334, doi:10.1016/j.cell.2006.05.040.

336. Mottet, D.; Bellahcène, A.; Pirotte, S.; Waltregny, D.; Deroanne, C.; Lamour, V.; Lidereau, R.; Castronovo, V. Histone Deacetylase 7 Silencing Alters Endothelial Cell Migration, a Key Step in Angiogenesis. *Circulation Research* **2007**, *101*, 1237–1246, doi:10.1161/CIRCRESAHA.107.149377.

337. Turtoi, A.; Mottet, D.; Matheus, N.; Dumont, B.; Peixoto, P.; Hennequière, V.; Deroanne, C.; Colige, A.; De Pauw, E.; Bellahcène, A.; et al. The Angiogenesis Suppressor Gene AKAP12 Is under the Epigenetic Control of HDAC7 in Endothelial Cells. *Angiogenesis* **2012**, *15*, 543–554, doi:10.1007/s10456-012-9279-8.

338. Jiao, S.; Wang, H.; Shi, Z.; Dong, A.; Zhang, W.; Song, X.; He, F.; Wang, Y.; Zhang, Z.; Wang, W.; et al. A Peptide Mimicking VGLL4 Function Acts as a YAP Antagonist Therapy against Gastric Cancer. *Cancer Cell* **2014**, *25*, 166–180, doi:10.1016/j.ccr.2014.01.010.

339. Chin, Y.R.; Toker, A. Function of Akt/PKB Signaling to Cell Motility, Invasion and the Tumor Stroma in Cancer. *Cellular Signalling* **2009**, *21*, 470–476, doi:10.1016/j.cellsig.2008.11.015.

340. Dai, Y.; Wang, M.; Wu, H.; Xiao, M.; Liu, H.; Zhang, D. Loss of FOXN3 in Colon Cancer Activates Beta-Catenin/TCF Signaling and Promotes the Growth and Migration of Cancer Cells. *Oncotarget* **2016**, *8*, 9783–9793, doi:10.18632/oncotarget.14189.

341. Cai, J.; Du, S.; Wang, H.; Xin, B.; Wang, J.; Shen, W.; Wei, W.; Guo, Z.; Shen, X. Tenascin-C Induces Migration and Invasion through JNK/c-Jun Signalling in Pancreatic Cancer. *Oncotarget* **2017**, *8*, 74406–74422, doi:10.18632/oncotarget.20160.

342. Uribe, M.L.; Marrocco, I.; Yarden, Y. EGFR in Cancer: Signaling Mechanisms, Drugs, and Acquired Resistance. *Cancers* **2021**, *13*, 2748, doi:10.3390/cancers13112748.

343. Di, J.; Huang, H.; Qu, D.; Tang, J.; Cao, W.; Lu, Z.; Cheng, Q.; Yang, J.; Bai, J.; Zhang, Y.; et al. Rap2B Promotes Proliferation, Migration and Invasion of Human Breast Cancer through Calcium-Related ERK1/2 Signaling Pathway. *Sci Rep* **2015**, *5*, 12363, doi:10.1038/srep12363.

344. Zepecki, J.P.; Snyder, K.M.; Moreno, M.M.; Fajardo, E.; Fiser, A.; Ness, J.; Sarkar, A.; Toms, S.A.; Tapinos, N. Regulation of Human Glioma Cell Migration, Tumor Growth, and Stemness Gene Expression Using a Lck Targeted Inhibitor. *Oncogene* **2019**, *38*, 1734–1750, doi:10.1038/s41388-018-0546-z.

345. Pohorelic, B.; Singh, R.; Parkin, S.; Koro, K.; Yang, A.-D.; Egan, C.; Magliocco, A. Role of Src in Breast Cancer Cell Migration and Invasion in a Breast Cell/Bone-Derived Cell Microenvironment. *Breast Cancer Res Treat* **2012**, *133*, 201–214, doi:10.1007/s10549-011-1753-2.

346. Smith, H.A.; Kang, Y. Determinants of Organotropic Metastasis. *Annual Review of Cancer Biology* **2017**, *1*, 403–423, doi:10.1146/annurev-cancerbio-041916-064715.

347. Lu, X.; Kang, Y. Organotropism of Breast Cancer Metastasis. *J Mammary Gland Biol Neoplasia* **2007**, *12*, 153–162, doi:10.1007/s10911-007-9047-3.

348. Fidler, I.J.; Poste, G. The “Seed and Soil” Hypothesis Revisited. *The Lancet Oncology* **2008**, *9*, 808, doi:10.1016/S1470-2045(08)70201-8.

349. Liu, Y.; Cao, X. Characteristics and Significance of the Pre-Metastatic Niche. *Cancer Cell* **2016**, *30*, 668–681, doi:10.1016/j.ccell.2016.09.011.

350. Dellacasagrande, J.; Schreurs, O.J.F.; Hofgaard, P.O.; Omholt, H.; Steinsvoll, S.; Schenck, K.; Bogen, B.; Dembic, Z. Liver Metastasis of Cancer Facilitated by Chemokine Receptor CCR6. *Scandinavian Journal of Immunology* **2003**, *57*, 534–544, doi:10.1046/j.1365-3083.2003.01263.x.

351. Kuhlmann, L.; Cummins, E.; Samudio, I.; Kislinger, T. Cell-Surface Proteomics for the Identification of Novel Therapeutic Targets in Cancer. *Expert Review of Proteomics* **2018**, *15*, 259–275, doi:10.1080/14789450.2018.1429924.
352. Romani, P.; Valcarcel-Jimenez, L.; Frezza, C.; Dupont, S. Crosstalk between Mechanotransduction and Metabolism. *Nat Rev Mol Cell Biol* **2021**, *22*, 22–38, doi:10.1038/s41580-020-00306-w.
353. Chio, I.I.C.; Tuveson, D.A. ROS in Cancer: The Burning Question. *Trends in Molecular Medicine* **2017**, *23*, 411–429, doi:10.1016/j.molmed.2017.03.004.
354. Rehklau, K.; Hoffmann, L.; Gurniak, C.B.; Ott, M.; Witke, W.; Scorrano, L.; Culmsee, C.; Rust, M.B. Cofilin1-Dependent Actin Dynamics Control DRP1-Mediated Mitochondrial Fission. *Cell Death Dis* **2017**, *8*, e3063–e3063, doi:10.1038/cddis.2017.448.
355. Tharp, K.M.; Higuchi-Sanabria, R.; Timblin, G.A.; Ford, B.; Garzon-Coral, C.; Schneider, C.; Muncie, J.M.; Stashko, C.; Daniele, J.R.; Moore, A.S.; et al. Adhesion-Mediated Mechanosignaling Forces Mitohormesis. *Cell Metabolism* **2021**, *33*, 1322-1341.e13, doi:10.1016/j.cmet.2021.04.017.
356. Galloway, C.A.; Lee, H.; Yoon, Y. Mitochondrial Morphology – Emerging Role in Bioenergetics. *Free Radic Biol Med* **2012**, *53*, 10.1016/j.freeradbiomed.2012.09.035, doi:10.1016/j.freeradbiomed.2012.09.035.
357. Pelicano, H.; Carney, D.; Huang, P. ROS Stress in Cancer Cells and Therapeutic Implications. *Drug Resistance Updates* **2004**, *7*, 97–110, doi:10.1016/j.drup.2004.01.004.
358. Yun, J.; Finkel, T. Mitohormesis. *Cell Metabolism* **2014**, *19*, 757–766, doi:10.1016/j.cmet.2014.01.011.
359. Zanotelli, M.R.; Zhang, J.; Reinhart-King, C.A. Mechanoresponsive Metabolism in Cancer Cell Migration and Metastasis. *Cell Metab* **2021**, *33*, 1307–1321, doi:10.1016/j.cmet.2021.04.002.
360. Huynh, J.; Nishimura, N.; Rana, K.; Peloquin, J.M.; Califano, J.P.; Montague, C.R.; King, M.R.; Schaffer, C.B.; Reinhart-King, C.A. Age-Related Intimal Stiffening Enhances Endothelial Permeability and Leukocyte Transmigration. *Sci Transl Med* **2011**, *3*, 112ra122, doi:10.1126/scitranslmed.3002761.